STUDY OF CHARGE-COLLECTING INTERLAYERS FOR SINGLE-JUNCTION AND TANDEM ORGANIC SOLAR CELLS

A Dissertation
Presented to
The Academic Faculty

by

Jae Won Shim

In Partial Fulfillment
of the Requirements for the Degree
Doctor of Philosophy in the
School of Electrical and Computer Engineering

Georgia Institute of Technology
May 2014

STUDY OF CHARGE-COLLECTING INTERLAYERS FOR SINGLE-JUNCTION AND TANDEM ORGANIC SOLAR CELLS

Approved by:

Dr. Bernard Kippelen, Advisor
School of Electrical and Computer Engineering
Georgia Institute of Technology

Dr. Samuel Graham
School of Mechanical Engineering
Georgia Institute of Technology

Dr. Ajeet Rohatgi
School of Electrical and Computer Engineering
Georgia Institute of Technology

Dr. Elsa Reichmanis
School of Chemical and Biomolecular Engineering
Georgia Institute of Technology

Dr. Oliver Brand
School of Electrical and Computer Engineering
Georgia Institute of Technology

Date Approved: [February 5, 2014]

ACKNOWLEDGEMENTS

First and foremost I would like to express my sincere gratitude to God. You have given me the power to believe in myself and pursue my dreams. I could never have done this without the faith I have in you, the Almighty.

I would like to express my highest and most profound gratitude to my supervisor, Dr. Bernard Kippelen, for his guidance, support, and encouragement during the entire period of my studies. His trust and advice motivated and encouraged me to maintain passion for my research activity. Furthermore, I am thankful to Dr. Ajeet Rohatgi, Dr. Samuel Graham, Dr. Oliver Brand, and Dr. Elsa Reichmanis for taking the time to serve on my committee and review and evaluate my work.

I would also like to thank my fellow group members of the Kippelen Research Group for their technical and emotional support. Much of this work would not have been possible without their help. I am particularly grateful to Dr. Canek Fuentes-Hernandez for his mentorship, and to Dr. Yinhua Zhou and Talha M. Khan for engaging in discussion and providing valuable ideas. It should be noted that most of the PEIE-related work in this thesis was achieved with the help of Dr. Yinhua Zhou.

I would like to thank Dr. William Potscavage and Dr. Sung-Jin Kim for their assistance with depositions using the SPECTROS system, Amir Dindar for taking XPS and AFM data, and Dr. Hyeunseok Cheun and Dr. Seungkeun Choi for discussions related to organic solar cells. I also wish to thank all my past and present coworkers for their assistance and friendship: Dr. Jungbae Kim, Dr. Do Kyung Hwang, Dr. Shree Prakash Tiwari, Dr. Asha Sharma, Alfred Ernst, Cheng-Yin Wang, Ehsan Najafabadi, James Hsu, Keith Knauer, Michael Gaj, Vladimir Kolesov, Dr. Minseong, Sangmoo Choi, Dr. Claudiu Cirloganu, Dr. Dan Owens, Dr. Dengke Cai, Dr. Mathieu Fenoll, Dr. Sanjeev

Singh, Dr. Wojciech Haske, Dr. Xiaohong Zhang, Dr. Yongjin Kim, Hyungchul Kim, Boyi Fu, and others.

I would like to thank Angie Hughes and Tina Moseley for their support as administrative managers in the Kippelen Research Group.

I would like to thank Prof. Antoine Kahn and his team members at Princeton University for their collaboration and great assistance.

The research conducted in this thesis was funded in part through the Center for Interface Science: Solar Electric Materials, an Energy Frontier Research Center funded by the U.S. Department of Energy, Office of Science, Office of Basic Energy Sciences under Award Number DE-SC0001084 and by the Office of Naval Research (Grant No. N00014-04-1-0313), and 2012 Center for Organic Photonics and Electronics (COPE) fellowship.

Finally, I owe my deepest gratitude to D. G. Shin, my sister and my parents, and many thanks to my friends in Korea. I truly appreciate their infinite affection, and I dedicate this thesis to them.

May God bless you!

TABLE OF CONTENTS

LIST OF TABLES

Page

LIST OF FIGURES

Page

LIST OF SYMBOLS AND ABBREVIATIONS

OSC	Organic solar cell
PCE	Power-conversion efficiency
WF	Work function
CRL	Charge recombination layer
ALD	Atomic layer deposition
P3HT	Poly (3-hexyl thiophene)
$IC_{60}BA$	Indene-C_{60} bisadduct
PVP	Poly (N-vinylpyrrolidone)
PEI	Polyethylenimine
PEIE	Polyethylenimine exothylated
PBDTTT-C	Poly(4,8-bis-alkyloxybenzo(1,2-b:4,5-b′)dithiophene-2,6-diyl-alt-(alkyl thieno(3,4-b) thiophene-2-carboxylate)-2,6-diyl)
$PC_{60}BM$	[6,6]-phenyl-C_{61} butyric acid methyl ester
PEDOT:PSS	Poly(3,4-ethylenedioxythiophene):poly(styrenesulfonate)
J	Current density
V	Voltage
AM	Air mass
G	Global
P	Power density
J_{SC}	Short-circuit current density
V_{OC}	Open-circuit voltage
FF	Fill factor

e	Elementary charge (1.6×10^{-19} coul)
λ	Wavelength
EQE	External quantum efficiency
N_{ph}	Spectral photon flux density
a-Si	Amorphous silicon
CdTe	Cadmium telluride
CI(G)S	Copper indium (gallium) selenide
GaAs	Gallium arsenide
DSSC	Dye-sensitized solar cell
HOMO	Highest occupied molecular orbital
LUMO	Lowest unoccupied molecular orbital
E_G	Energy band-gap
IE	Ionization energy
EA	Electron affinity
UV	Ultra violet
UPS	Ultra-violet photoemission spectroscopy
IPES	Inverse photoemission spectroscopy
HCE	Hole-collecting electrode
ECE	Electron-collecting electrode
ε	Dielectric permittivity
ε_o	Permittivity in free space (8.854×10^{-12} F/m)
R_S	Series resistance
R_P	Shunt resistance
n	Ideality factor
k	Boltzmann constant (8.617×10^{-5} eV/K)

PPV	Poly-phenylene vinylene
ITO	Indium tin oxide
CuPc	Copper phthalocyanine
BCP	Bathocuproine
PTC	Perylene tetracarboxylic derivative
H_2Pc	Metal-free phthalocyanine
PTCBI	3,4,9,10-perylene tetracarboxylic bis-benzimidazole
ME-PTC	N-type perylene tetracarboxylic derivative
MEH-PPV	Poly(2-methoxy-5-(2-ethyl-hexyloxy)-1,4-phenylene vinylene
CN-PPV	Cyano-polyphenylene vinylene
PTB7	Poly thieno[3,4-b]thiophene/benzodithiophene
C_{60}	Fullerene
$PC_{70}BM$	[6,6]-phenyl-C_{71} butyric acid methyl ester
CCI	Charge-collecting interlayer
PTTBT	Poly[3,6-di(4'-ethyloctyl)thieno [3,2-b] thiophene-2,5-diyl-2,1,3-benzothiadiazole-4,7-diyl]
CBD	Chemical bath deposition
TDAE	Tetrakis(dimethylamino)ethylene
MDMO-PPV	Poly[2-methoxy-5-(3',7'-dimethyloctyloxy)-1,4-phenylene vinylene]
PCPDTBT	Poly[2,6-(4,4-bis-(2-ethylhexyl)-4H-cyclopenta[2,1-b;3,4-b']dithiophene)-alt-4,7-(2,1,3-benzothiadiazole)]
PDTP-DFBT	poly[2,7-(5,5-bis-(3,7-dimethyl octyl)-5H-dithieno[3,2-b:20,30-d]pyran)-alt-4,7-(5,6-difluoro-2,1,3-benzothiadiazole)]
PFN	Poly[(9,9-dioctyl-2,7-fluorene)- alt -(9,9-bis(3′-(N, N-dimethylamino)propyl)-2,7-fl uorene)]
PBDTT-SeDPP	Poly{2,6′-4,8-di(5-ethylhexylthienyl)benzo[1,2-b;3,4-b] dithiophene-alt-2,5-bis(2-butyloctyl)-3,6-bis(selenophene-2-yl) pyrrolo[3,4-c]pyrrole-1,4-dione}

PDPP5T	Poly diketopyrrolopyrroleoligothiophene
PSBTBT	Poly[(4,4′-bis(2-ethylhexyl)dithieno[3,2-b:2′,3′-d]silole)-2,6-diyl-alt-(2,1,3-benzothiadiazole)-4,7-diyl]
SubNc	Chloroboron subnaphthalocyanine
PF10TBT	Poly[9,9-didecanefluorenealt-(bis-thienylene)benzothiadiazole]
PFTBT	Poly[2,7-(9,9-didecylfluorene)-alt-5,5-(40,70-di-2-thienyl-20,10,30-benzothiadiazole)]
PBBTDPP2	Poly[3,6-bis(40-dodecyl-[2,20]bithiophenyl-5-yl)-2,5-bis(2-ethylhexyl)-2,5-dihydropyrrolo[3,4-]pyrrole-1,4-dione]
PTBEHT	Poly{5,7-di-2-thienyl-2,3-bis(3,5-di(2-ethylhexyloxy)phenyl) – thieno[3,4-b]pyrazine}
PBnDT-FTAZ	Polybenzodithiophene 2-alkyl-benzo[d][1,2,3]triazoles
BTI-BDT	Bithiophene imide Benzodithiophene
Alq3	Tris-(8-hydroxyquinoline)aluminum
DiNPB	N,N ′-diphenyl-N,N′-bis(4′-(N,N-bis(naphth-1-yl)-amino)-biphenyl-4-yl)-benzidine
DCV6T	Dicyanovinyl-capped sexithiophene derivative
PES	Polyethersulfone
IPA	2-propanol
PDMS	Polydimethylsiloxane
DMSO	Dimethyl sulfoxide
DCB	1,2-dichlorobenzene
CB	Chlorobenzene
DIO	1,8-diiodooctane
v	Volume
DEZ	Diethylzinc
Ni-AMD	Nickel alkyl amidinate

PVD	Physical vacuum deposition
ω	Angular frequency
C	Capacitance
HOPG	Highly ordered pyrolytic graphite
XPS	X-ray photoemission spectroscopy
AFM	Atomic force microscopy
PSC	Polymer solar cell
wt.	Weight
A	Absorbance
I_{ph}	Spectral photon irradiance
HPF6	Fluorophosphoric acid
k	Extinction coefficient
n	Refractive index
RMS	Root mean square

SUMMARY

In the past few years, organic solar cells (OSCs) have gained much interest due to their unique electrical and optical properties, as well as for their potential for simple and low-cost processing. In spite of progress in the performance of OSCs, further improvement in device stability and power conversion efficiency (PCE) is still needed for OSCs to compete with other emerging photovoltaic technologies. Conventionally, the use of low work function (WF) metals, such as LiF/Al and Ca/Al, for the top electrode has caused issues with device instability. Recently, so-called inverted solar cells have been proposed and developed with better air stability and comparable PCE to conventional ones. However, stacked individual cells with complementary absorption ranges through a charge recombination layer (CRL), called tandem solar cells, are desired for realization of highly efficient solar cells by covering the emission spectrum of the sun more effectively.

This dissertation presents research work that advances the field of OSCs by studying hole- or electron-collecting interlayers and finally realizing new CRLs for efficient inverted tandem OSCs. As a first step toward the goal, a hole-collecting interlayer layer of OSCs, NiO processed by atomic layer deposition (ALD) was studied. The ALD system can offer well-controlled layer-by-layer growth of highly conformal and uniform films. A high-WF (5.4 ± 0.02 eV) of NiO-coated ITO when subjected to an O_2-plasma treatment provided effective hole-collecting properties from a bulk heterojunction photoactive layer and maximized the open-circuit voltage of the OSC. With an O_2-plasma-treated, 25-nm-thick NiO hole-collecting interlayer, the poly(3-hexyl

thiophene) P3HT:indene-C_{60} bisadduct ($IC_{60}BA$)-based conventional single-junction OSCs yielded an average PCE around 4%.

The second step toward the goal was a study of polymeric surface modifiers, poly (N-vinylpyrrolidone) (PVP) and polyethylenimine (PEI) derivatives as electron-collecting interlayers of OSCs. The surface modifiers were based on polymers containing simple aliphatic amine groups. The surface modifiers provided substantial and universal WF reduction on many different conductors, including metals, transparent conductive metal oxides, conducting polymers, and graphene. The WF reduction arose from chemisorption (PVP) or physisorption (PVP and PEI derivatives) of the neutral polymer, which turned the modified conductors into efficient electron-collecting electrodes. These surface modifiers were processed in air from a solution and at a relatively low temperature (≤ 100 °C), providing an appealing alternative to chemically reactive low−WF metals. With this modification, many different types of efficient inverted single-junction OSCs, including all-polymeric solar cells, were demonstrated. With PEI exothylated (PEIE)-modified ITO electron-collecting electrodes, poly(4,8-bis-alkyloxybenzo(1,2-b:4,5-b′)dithiophene-2,6-diyl-alt-(alkyl thieno(3,4-b) thiophene-2-carboxylate)-2,6-diyl) (PBDTTT-C): [6,6]-phenyl-C_{61} butyric acid methyl ester ($PC_{60}BM$)-based inverted single-junction OSCs showed an average PCE over 6%.

The last attempt to reach the goal of this dissertation was realization of new efficient CRLs of inverted tandem OSCs using the polymer surface modifier, PEIE. The use of PEIE modification in CRLs offered further reduced WF of the electron-collecting layer, leading to high WF contrast between two opposite CRL surfaces. Three CRLs

(PEIE-modified MoO_X/Ag, PEIE-modified MoO_X/Al_2O_3:ZnO nanolaminate, and PEIE-modified poly(3,4-ethylenedioxythiophene):poly(styrenesulfonate) (PEDOT:PSS)) were demonstrated. The high-WF MoO_X layer and PEDOT:PSS served as hole-collecting layers. The Ag layer (1 nm) improved the electrical connection of two subcells by reducing the WF of MoO_X. The Al_2O_3:ZnO nanolaminate provided an electron-collecting layer in the CRL, but the WF was not low enough to efficiently collect electrons from the bulk heterojunction photoactive layer. In all cases, the PEIE modification provided further reduced WF on the layer below, and consequently formed an efficient and air-stable CRL. The P3HT:IC_{60}BA and PBDTTT-C:PC_{60}BM-based inverted tandem OSCs with the new CRL of PEI-modified PEDOT:PSS showed fill factor over 70% and PCE over 8%.

CHAPTER 1

INTRODUCTION

1.1 Solar Cells

Providing sufficient quantities of safe and renewable energy to the general public is an essential prerequisite for a sustainable society. Currently, the burning of fossil fuels represents more than three-quarters of the world's energy consumption and has had detrimental effects on the environment. To assure the public's safety, a clean energy source is required for decreasing environmental contamination and greenhouse gas emissions. Photovoltaic technology– the conversion of solar energy to electric power– is believed to be one of the most promising alternative energy sources for reducing fossil fuel dependency. The initial photovoltaic effect can be traced back 119 years to 1893, when Alexandre-Edmund Becquerel observed light-dependent voltage from electrodes immersed in an electrolyte [1]. Since this discovery, a variety of materials has been studied. Chapin *et al.* announced the first silicon-based single p-n junction photovoltaic cell (also referred to as solar cell) with a power conversion efficiency (PCE) of 6%, a tipping point for photovoltaics considering the state of technology in 1954 [2]. Photovoltaic technology has been developing ever since, by employing various semiconducting materials and different cell geometries. The cumulative installed power capacity from photovoltaic technology was around 65 GW at the end of 2011, compared with only about 1.5 GW in 2000 [3]. Photovoltaic energy is very attractive because the average energy received on the earth in one hour (1.2×10^{17} Wh/m^2) is larger than the world's annual energy consumption (1.1×10^{17} Wh/m^2), thus having great potential as a solution for the global energy challenge [4].

1.2 Characterization of Solar Cells

Before starting this section, it should be noted that here and in the remainder of the dissertation, ‘‘solar cell’’ and ‘‘photovoltaic cell’’ are used interchangeably. This section introduces the basic electrical characteristics to evaluate the photovoltaic performance of solar cells. The photovoltaic performance of solar cells is characterized by measuring the current-density versus voltage (*J*-*V*) characteristics under illumination. To measure the *J*-*V* characteristics, standard test conditions have been designed. The simulated solar spectrum, AM 1.5G, with intensity on the order of 100 mW/cm^2 is used as a standard light irradiation condition (incident power). AM stands for air mass, and 1.5 corresponds to the inverse cosine of the angle defined between the incident light and the normal to the earth’s surface (Figure 1.1 (a)). The G represents global and means modified solar spectrum due to the small contribution that diffuse light has over the direct incident light [5]. Figure 1.1 (b) depicts the spectral irradiance of the AM 1.5G solar spectrum.

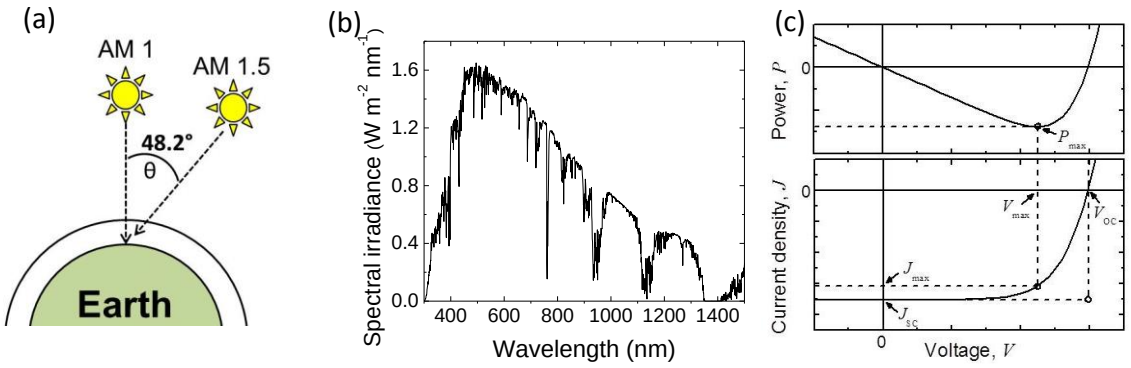

Figure 1.1 (a) Concept of air mass, (b) Spectral irradiance of the AM 1.5 G solar spectrum, and (c) Power and current-density as a function of applied voltage of a solar cell under illumination.

Figure 1.1 (c) shows a typical *J-V* characteristic of a solar cell under illumination and the power density (*P*), defined as the product of *J* and *V*, as a function of applied voltage. Here, note that a negative power density physically means that power is being generated by the solar cell. The PCE of a solar cell under a known illumination source is characterized by three parameters derived from the *J-V* characteristics under illumination: the short-circuit current density (J_{SC}), the open-circuit voltage (V_{OC}), and the fill factor (FF).

The V_{OC} is defined as the maximum voltage extractable from the solar cells, and is the measured voltage when no current is produced by the solar cell under illumination.

The J_{SC} is defined as the maximum current density drawn from a solar cell under illumination, and is measured at zero voltage. The J_{SC} is pertinent to generation rate and collection probability of charge carriers. The maximum J_{SC} can be expressed as follows:

$$J_{SC} = \int_{AM1.5} e\,EQE(\lambda)N_{ph}(\lambda)d\lambda \tag{1.1}$$

where *e* is the elementary charge (1.6×10^{-19} C), EQE is the external quantum efficiency and $N_{ph}(\lambda)$ is the spectral photon flux density under AM1.5 G illumination. The EQE, referred to as incident-photon-to-current efficiency, is defined as the number of electrons collected under a short-circuit condition divided by the number of incident photons.

$$EQE(\lambda) = \frac{n_e}{n_{ph}} = \frac{J_{SC}}{P_o}\frac{hc}{\lambda e} \tag{1.2}$$

where P_0 is the incident optical power density, *h* is Planck's constant (6.626×10^{-34} J·s), *c* is the speed of light, λ is the wavelength of light. The upper limit of the J_{SC} is attained by integrating the solar spectrum over the spectral region where light is being absorbed by

the solar cell. Experimentally, as shown in Figure 1.1 (c), the V_{OC} and J_{SC} can be obtained from intersects of the electrical characteristics with the vertical axis for the V_{OC} and the horizontal axis for the J_{SC}.

The V_{OC} and J_{SC} represent the maximum voltage and maximum current density, respectively. However, at these operating points, no power is generated. As shown in Figure 1.1 (c), the power density defined as the product between V and J reaches its maximum absolute value, P_{max}, at a point defined by the voltage value V_{max} and the corresponding current density J_{max}. The FF is a parameter that determines the maximum power density that can be extracted from a solar cell. The FF is defined as the ratio between P_{max} and the product of V_{OC} and $J_{SC.}$

$$FF = \frac{J_{max} \times V_{max}}{J_{SC} \times V_{OC}} \tag{1.3}$$

The PCE, which represents how much power can be generated from the solar cells with incident light, is defined as:

$$PCE = \frac{J_{max} \times V_{max}}{P_{inc}} = \frac{FF \times J_{SC} \times V_{OC}}{P_{inc}} \tag{1.4}$$

where P_{inc} denotes incident optical power density. All parameters used to describe the PCE are illustrated in Figure 1.1 (c).

1.3 Current Status of Photovoltaic Technologies

This section will briefly discuss the state-of-the-art in photovoltaic technologies. As mentioned in the previous section, photovoltaic cells can be formed in various ways with the ultimate goal of the photovoltaic technologies will always be maximum power at

minimum cost. In general, the photovoltaic technologies are categorized by the choice of the light-absorbing material.

Crystalline silicon is the most widely used semiconductor as a light-absorbing material, representing more than 80% of the market share because of their high PCE (~25% from mono-crystalline solar cells) and reliable yield. However, silicon solar cells require thick light-absorbing layers (several hundred μm) due to their relatively small absorption coefficients in the visible spectral range. Commonly, two types of crystalline silicon, mono-crystalline, from a high-purity single crystal boule, and multi-crystalline, from sawing a cast block of silicon, have been used in industry. Also, other silicon production technologies, such as growing silicon ribbons and melting silicon powder have been employed to overcome the inefficiencies from single crystal boule growth/casting and wafer sawing processes. Due to the high cost of crystalline silicon, there is a need for less expensive materials for the fabrication of solar cells [6].

Growth of the photovoltaic market depends upon price reductions, and competitive production needs to move to a thin film and away from bulk material. The thin film technologies enable reduction in the cost of photovoltaic devices by lowering material and manufacturing costs. Amorphous silicon (a-Si) and polycrystalline materials, such as cadmium telluride (CdTe), copper indium (gallium) selenide (CI(G)S) have been employed as thin film light-absorbing materials. These materials only need to be about 1 μm thick, have very strong light-absorbing properties, can be deposited on relatively large substrates and used for high throughput manufacturing. Furthermore, low temperature processing can be used for deposition of such thin films and more impurities can be tolerated because a shorter distance is required for charge carriers to travel in the active layer as compared to crystalline silicon-based solar cells. Advantages offered by thin film-based solar cells can lead to lower fabrication cost per unit area, but typically display lower PCE values than crystalline silicon-based solar cells [7].

Recently, numerous other photovoltaic technologies have emerged. These emerging technologies include organics-based approaches and those that do not depend on the conventional single p-n junction such as multi-junction gallium arsenide (GaAs)-based solar cells, dye-sensitized solar cells (DSSCs), organic solar cells (OSCs), and so forth [8]. GaAs-based solar cells with a multi-junction structure and a light concentrator is the most efficient solar cell, to date (PCE of 44 %) [9]. With the concentrator, solar cells can operate with increased light intensity. Also, with a multi-junction structure, nearly all of the solar spectrum can be used to generate electricity. Although the largest PCE value has been achieved with these kinds of solar cells, GaAs solar cells are only utilized on special applications such as space exploration and satellites because of their very high costs [10].

Two other technologies, DSSCs and OSCs use organic compounds as light-absorbing materials. The DSSC carries out light absorption and charge separation by combining an organic photo-sensitizer (dye) as the light absorbing material with a mesoporous or nanocrystalline semiconductor [11]. However, the reported highest PCE around 12 % from DSSC is still low compared to silicon-based solar cell [12]. In addition, the DSSCs use volatile solvents in their liquid electrolytes that can cause device instability [9,13].

Another organics-based emerging technology is the OSC. The OSCs use a thin-film of solid-state organic semiconductors, including polymers and small-molecule compounds for light absorption and charge transport to convert light into energy [8]. Since the OSC technology is so young, the highest reported PCE of the OSCs of about 12 % has not been able to match the PCE of the silicon-based solar cells and the air-stability is relatively poor [9,14]. However, the OSCs have huge potential as a future renewable energy source because of the unique ability to tune the electrical and optical properties of organic semiconductors and the viability for use low cost, simplified, and high throughput processing.

Among the photovoltaic technologies introduced above, this dissertation will deal with OSCs due to their interesting properties regarding the photo-conversion mechanism (from light absorption to charge generation) along with the prospect of low-cost and high throughout processing.

Figure 1.2 shows the summary of the highest PCEs from different types of solar cells throughout the years.

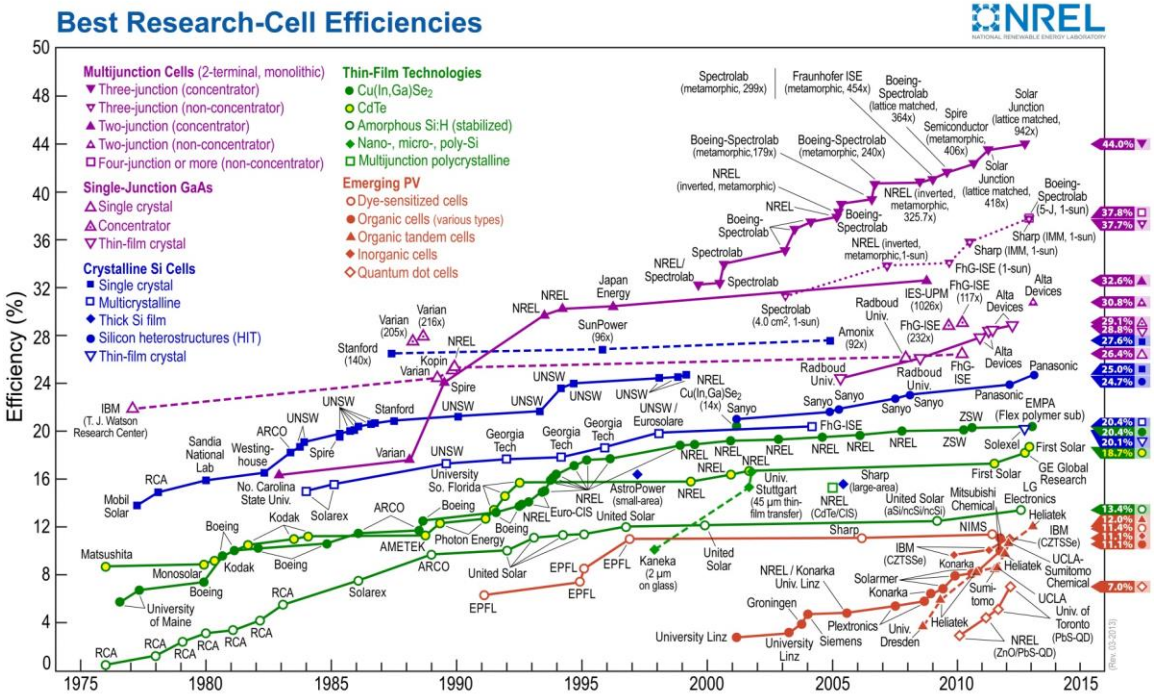

Figure 1.2. Reported timeline of the highest power conversion efficiencies from various solar cells [9].

1.4 Organic Solar Cells

The purpose of this section is to introduce the fundamental knowledge necessary to understand the operation of OSC and challenges faced by this technology. Finally, the aim and scope of this dissertation will be presented.

1.4.1 Organic Semiconductors

One of the most essential parts in solar cells is the light-absorbing layer, also referred to as the photoactive layer. The light-absorbing layer in an OSC comprises thin films of organic semiconductors. Many different properties of the thin film of the organic semiconductors make them very attractive for photovoltaic applications. The electro-chemical properties of the organic semiconductors such as energy levels, charge transport, and solubility can be tailored by modifying the chemical structure of organic molecules. Organic thin films can be formed using various low-temperature and high-throughput methods such as spin-coating and roll-to-roll processing that can reduce manufacturing costs. Only small amounts of organic materials are required to form a thin film (100 – 200 nm) since they typically display high absorption coefficients in the visible spectral range ($\geq 10^5$ cm^{-1}) [15,16].

Organic semiconductors can be broadly classified into two groups on the basis of their molecular weight and basic units [17]: small-molecules and polymers. The small molecules are low molecular weight organic compounds (< 1000 g/mol) in which carbon atoms form molecules usually with benzene rings. Polymers are high molecular weight organic compounds (> 1000 g/mol) comprising linked many small repeating units, called monomers. All organic semiconductors share common characteristics in their electronic structure that lead to similar optical and electronic properties [18]. These characteristics arise from electronic conjugation, the alternation of single and double bonds between

carbon atoms [19]. The details of the electronic configuration of the carbon atomes will be discussed in the following.

The carbon (C, atomic number 6) atom has an $1s^2 2s^2 2p^2$ electronic configuration in the ground state [18]. The two *s* orbitals, *1s* and *2s*, have two electrons each and are fully occupied. Hence, the C atom has only two unpaired electrons in its ground state and valence of 2 can be expected. However, the C atom prefers to form tetravalent compounds, resulting in valence of four. This can occur by promoting one electron of the *2s* orbital into the third *2p* orbital and enables C to have the electronic configuration $1s^2$, $2s^1$, $2p_x^1$, $2p_y^1$, $2p_z^1$. When the four valence electrons of a C atom interact with the valence electrons of other elements such as C, hydrogen (H), oxygen (O), and so forth, they form covalent bonds. The covalent bonds occur when pairs of electrons are shared between atoms. In other words, covalent bonds result from the overlap of atomic orbitals that describe the wave function of electrons, to produce molecular orbitals. When two atoms share a pair of electrons, it is called a single bond. Likewise, the cases that two or three pairs of electrons are shared between two atoms are called double or triple bonds.

Most cases of molecular bonds made in organic semiconductors have hybrid orbitals. This is different from the linear combination of one *2s* orbital and three *2p* orbitals. C atoms can form three different kinds of hybrid orbitals, sp^1, sp^2, and sp^3. The sp^2 orbital, for instance, hybridization happens between one *s* orbital and two *p* orbitals (p_x, p_y), resulting in three sp^2 orbitals and remaining one un-hybridized orbital (p_z) that is perpendicular to the plane spanned by the sp^2 orbitals. Figure 1.3 (a) describes the formation of the sp^2 hybridization in ethylene (C_2H_4) from two methyl radicals ($CH_3\cdot$).

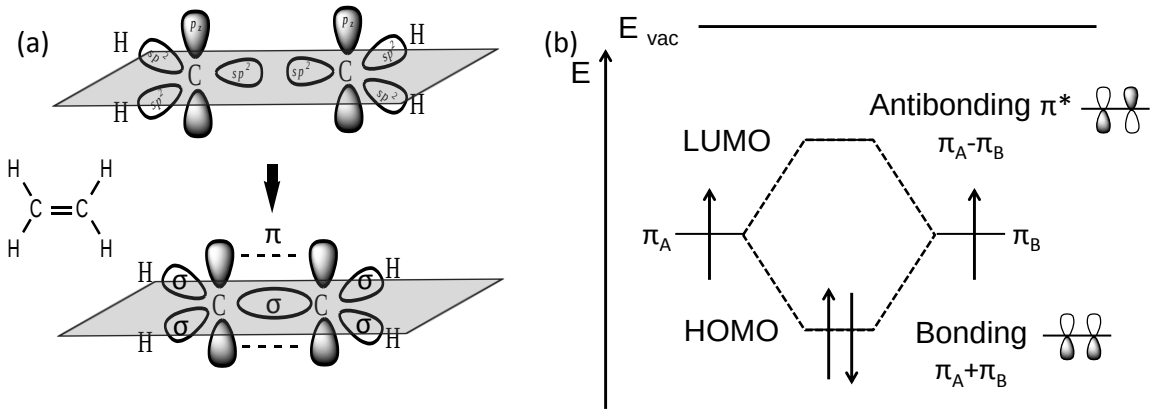

Figure 1.3 (a) Chemical structure and illustration of molecular orbital in two methyl radicals (CH_3·) and an ethylene (C_2H_4) and (b) HOMO and LUMO formation in an ethylene.

The double bond comprises two different overlaps: One is formed by overlapping two sp^2 hybrid orbitals between two C atoms and the other one is formed by overlapping two p_z orbitals between two C atoms. The bonding formed by overlapping the two sp^2 hybrid orbitals has a high degree of overlap, so-called σ bonding. Unlike the σ bonding, the bonding formed by overlapping the two p_z orbitals has a low degree of overlap, and is called π bonding. Because of the reduced overlap in π bonding, electrons, also referred to as π-electrons, are weakly coupled, thus more delocalized in space than electrons participating in σ bonds. The π-electrons are typically delocalized along the backbone comprising the alternation of single and double bonds and this delocalization provides a pathway for the π-electrons to move along a molecule or a polymer chain. This is the origin of the conductivity in the organic compounds.

The delocalized π molecular orbitals formed by overlapping π atomic orbitals along the backbone define the frontier electronic levels, highest occupied molecular orbital (HOMO, bonding orbital) and lowest unoccupied molecular orbital (LUMO, antibonding orbital), depending on the configuration of signs of the p_z orbitals. Figure 1.3 (b) illustrates the formation of the frontier orbitals (HOMO and LUMO) in an ethylene

molecule. The HOMO and LUMO are separated by an energy band-gap (E_G, also referred to as a transport gap) that makes such an organic compound a semiconductor. A rough analogy can be made these HOMO and LUMO with valence band and conduction band, respectively, in an inorganic semiconductor. A transition of an excited electron from the HOMO to the LUMO can only occur when a photon with energy larger than the E_G interacts with the material. At room temperature, an electron in the LUMO is not freely delocalized, and hence the difference between organic semiconductor and inorganic semiconductor.

1.4.2 Simplified Energy Level Diagram of Organic Solar Cells

Before starting this section, some energy levels used for electrical or optical characterization of OSCs are defined. An energy level diagram of an OSC is shown in Figure 1.4. It should be noted that the energy level diagram is before contacting all components. The ionization energy (IE) is the amount of energy needed to remove the most loosely bound electron from an atom or molecule to form a positive ion or a radical cation. The electron affinity (EA) is the amount of required energy released when an extra electron is added to a neutral atom or a molecule to form a negative ion or a radical anion. In OSCs, the IE (EA) is the energy level difference between HOMO (LUMO) and a vacuum level. Since HOMO and LUMO energies can only be calculated, these levels can be estimated by measuring IE and EA via experimental methods, such as ultra-violet (UV) photoemission spectroscopy (UPS) and inverse photoemission spectroscopy (IPES). The work function (WF) is the energy required to move an electron from the Fermi level into vacuum and can be estimated by using experimental methods, such as UPS or the Kelvin probe method. The Fermi level (E_F) is a hypothetical energy level of an electron that has a 50% probability of being occupied with electrons.

In general, two different organic semiconductors are employed to form the photoactive layer of an OSC. One has an electron-donating property (donor) and the other

one has an electron-accepting property (acceptor). The donor and acceptor materials have low IE and high EA, respectively. Also, the donor and acceptor materials provide for efficient hole and electron transport layers, respectively [18]. Two charge-collecting electrodes, a hole-collecting electrode (HCE) and an electron-collecting electrode (ECE) with different WF values are employed on either side of donor and acceptor material to collect photo-generated charge carriers.

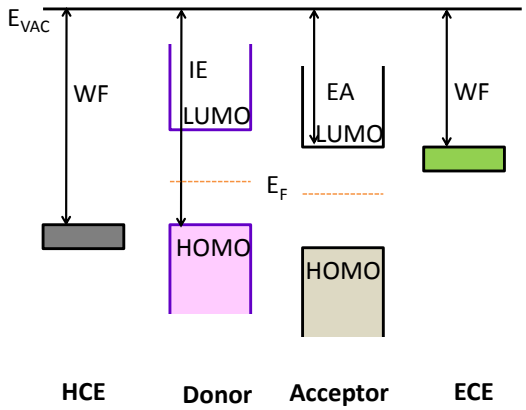

Figure 1.4 Energy level diagrams of donor and acceptor materials and charge-collecting electrodes in heterojunction organic solar cells (before contact is made).

1.4.3 Basic Operating Principles of Organic Solar Cells

The operating principles of an OSC are not yet fully understood. From light absorption to electric power generation, several scenarios have been suggested. This section briefly introduces one of the possible explanations for the operation of the OSC.

Firstly, photons with average photon energy larger than the optical band-gap of the photoactive layer are absorbed in the organic semiconductor active layer. It should be noted that the optical band-gap is different from the transport gap and roughly defined as the energy difference between the hole and electron in an exciton (the details of the exciton will be discussed soon). Organic semiconductors have a high absorption coefficient, above 10^7 m^{-1} that allows very thin layers, between 100-300 nm, to absorb

sufficient light. The absorbed photon energy excites an electron in the ground state up to a higher energy state. The promoted charge relaxes down to the bottom of the potential energy surface of the lowest excited state by a thermal energy loss. This excited state gets to its equilibrium geometry and an exciton is created [8]. These excitons are generally known as Coulomb-bound electron-hole pairs. The binding energy of the excitons can be expressed as follows:

$$E_{Exciton-binding} = \frac{2m_{red}e^4}{(4\varepsilon\varepsilon_0)^2 h^2} \tag{1.5}$$

where the reduced mass of the exciton, $m_{red} = m_e^* \cdot m_h^* / (m_e^* + m_h^*)$, ($m_{e,h}$* is the effective mass of an electron and a hole), is employed to explain the movement of electron and hole around their common center of mass, ε is the dielectric permittivity, and ε_o (8.854×10^{-12} F/m) is the permittivity in free space [20]. The excitons formed in organic semiconductors exhibit a binding energy on the order of 500 meV at room temperature, much higher than their thermal energy (25 meV) [18]. In OSCs, absorbed photons induce a generation of excitons and not free charge carriers directly. However, the exciton binding energy of inorganic semiconductors is much smaller than their thermal energy at room temperature due to their high dielectric permittivity ($\varepsilon > 10$). Thus, the excitons can be formed in inorganic semiconductors only at low temperature, and at room temperature photo-generated excitons are immediately thermally dissociated into free electrons and holes with the absorption of photons [20]. This is one of the main differences of the OSC to inorganic solar cells.

To dissociate an exciton into free charge carriers, excitons should move to the donor–acceptor interface where they can be separated into electrons and holes before they decay back to the ground state. Since excitons are neutral species, their movement to the interface is governed by their concentration gradient, namely by diffusion *via* random hops [8,18].

In general, excitons that reach the donor–acceptor interface can dissociate to free charge carriers if the band offset energy between the EA of the donor and acceptor is larger than the exciton binding energy. However, exciton dissociation is a more complex process than what is described here. Unfortunately, no clear description has emerged yet to explain the exciton dissociation process; one possible mechanism is as follows: The electrons of the excitons from the donor transfer to the acceptor. Likewise, the holes of the excitons from the acceptor transfer to the donor. After the charge transfer, the exciton needs to split to a positive polaron in the donor and a negative polaron in the acceptor. The polaron refers to a charge carrier with a distortion of the charge's environment. Since the positive and negative polarons still remain in close proximity, they are Coulombically-bound (charge-transfer state). Although this binding energy is not as strong as that of the excitons, the polaron pairs need to be separated to provide free charge carriers (charge-separated state). To explain the eventual charge separation, many different theories have been suggested. One of these scenarios indicates that the presence of disorder or dipoles at the interface, or help from the phonon energy can induce an increased charge separation rate compared to the charge recombination rate [18].

After successful charge separation, the positive and negative charge carriers (polarons) can reach their respective electrodes *via* drift and diffusion that is driven by the gradient of the electrochemical potential and are collected by the charge-collecting electrodes. Because of the properties of organic semiconductors, such as the large electron-vibration coupling and the disorder effect, the motion of the positive and negative carrier is somewhat different from that of inorganic semiconductor. In such disordered molecular materials, band-like transport is not always applicable. Instead, charge carrier transport is governed by a hopping mechanism between distributed localized sites. In addition, charge collection at the interface between the organic semiconductor and the charge-collecting electrodes is also intricate. Many factors such as energy level mismatch between the WF of charge-collecting electrodes and EA or IE of

the organic semiconductor, the interfacial charge distribution, *etc.* can affect charge collection at the interface [8].

1.4.4 Equivalent Circuit Model and Model Fitting

The device performance of the OSCs can be approximated with an equivalent circuit used for a conventional p-n junction solar cell [21]. Figure 1.5 shows a schematic of the equivalent circuit comprising a current source (J_{ph}), a diode (J_0), a series resistance (R_S), and a shunt resistance (R_P). The current source corresponds to the generated photocurrent, J_{ph}, under illumination. The diode takes account of the rectifying behavior of the OSC and is characterized by the reverse saturation current density J_0 and ideality factor n. The R_S is related to the resistance of the photoactive layer, the contact resistance at the interface between layers, and the resistance of charge-collecting electrodes and interconnections, *etc*. The R_S should be minimized. The R_P originates from the loss of carriers because of pinhole leakage in the film or carrier recombination caused by impurities, *etc*. The R_P has to be maximized [8,21].

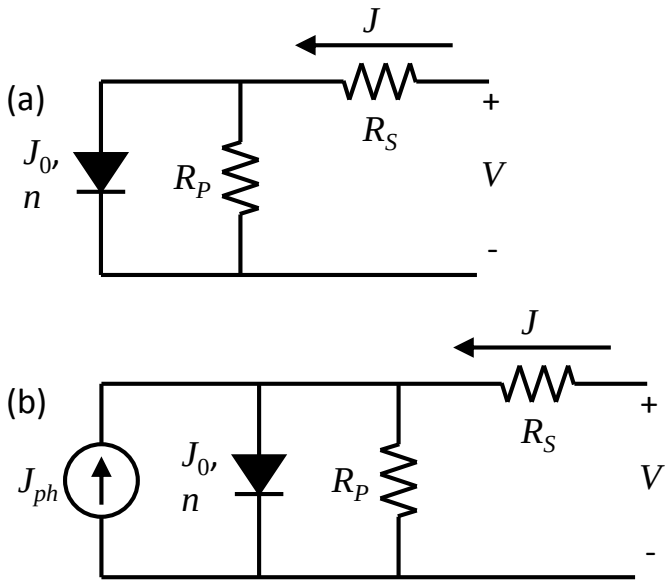

Figure 1.5 Equivalent circuits used to model OSCs (a) in the dark and (b) under illumination.

According to Shockley's theory, the current density of the diode as a function of the applied voltage is given by:

$$J = J_0\left\{\exp\left(\frac{eV}{nkT}\right)-1\right\} \tag{1.6}$$

where J_0 is the reverse saturation current density, e denotes the elementary charge, k denotes the Boltzmann constant (8.617×10^{-5} eV/K), and T denotes the temperature. By using the Shockley equation (Eq. 1.6), the equivalent circuits in the dark (Figure 1.5(a)) and under illumination (Figure 1.5(b)) can be solved analytically as follows:

$$J = \frac{1}{1+R_S/R_P}\left[J_0\left\{\exp\left(\frac{V-JR_SA}{nkT/e}\right)-1\right\}+\left(\frac{V}{R_PA}\right)\right] \tag{1.7}$$

$$J = \frac{1}{1+R_S/R_P}\left[J_0\left\{\exp\left(\frac{V-JR_SA}{nkT/e}\right)-1\right\}-\left(J_{ph}-\frac{V}{R_PA}\right)\right] \tag{1.8}$$

where A denotes the area of the cell. Furthermore, from Eq. 1.8, an equation for the V_{OC} can be derived with an assumption of J equal to zero, and the J_{SC} can be derived V equal to zero. Also, the derived equations for the V_{OC} and the J_{SC} can be expressed with an approximated form, where R_SA is very small, R_PA is large enough so that the effects can be ignored, and $J_{ph}/J_0 >> 1$. The V_{OC} and J_{SC} can be expressed as:

$$V_{OC} = \frac{nkT}{e}\ln\left\{1+\frac{J_{ph}}{J_0}\left(1-\frac{V_{OC}}{J_{ph}R_pA}\right)\right\} \approx \frac{nkT}{e}\ln\left\{1+\frac{J_{ph}}{J_0}\right\} \tag{1.9}$$

$$J_{SC} = -\frac{1}{1+R_S/R_P}\left[J_{ph} - J_0\left\{\exp\left(\frac{|J_{SC}|R_S A}{nkT/e}\right) - 1\right\}\right] \approx -J_{ph} \tag{1.10}$$

The equivalent circuit model reveals that the V_{OC} is influenced by n, J_{ph}, and J_0 and follows a logarithmic function of the ratio of the J_{ph} and the J_0. The J_{SC} is close to J_{ph} with a small R_SA value, a large R_PA value, and a much larger J_{ph} than J_0. *J-V* characteristics of solar cells can be fitted by using Eq. 1.8 and R_SA, R_PA, J_0, and n as the fitting parameters.

Another quantity needs to be calculated to evaluate the device performance is FF which is defined as $J_{max} \times V_{max}/J_{SC} \times V_{OC}$. Under ideal conditions where $R_S = 0$ and $1/R_P = 0$, the ideal FF_0 of a solar cell is given as [21,22]:

$$FF_0 = \frac{v_{OC} - \ln(v_{OC} + 0.72)}{v_{OC} + 1} \tag{1.11}$$

where $v_{OC} = eV_{OC}/nkT$. However, the FF_0 of an actual device can be affected by R_S and R_P, and thus should be lower than the ideal value. To incorporate the effects of R_S and R_P, a characteristic resistance for the device is defined as $R_{CH} = V_{OC}/(J_{SC}A)$ and normalized series resistance (r_S) and normalized shunt resistance (r_P) defined by $r_S = R_S/R_{CH}$ and $r_P = R_P/R_{CH}$, respectively. Using these quantities, the following semiempirical expressions have been shown to be good approximations to experimental values of the FF:

$$\begin{aligned} FF_S &= FF_0(1 - 1.1r_S) + 0.19r_S^2 \quad (0 \le r_S \le 0.4, 1/r_P = 0), \\ FF_{SP} &= FF_S\left\{1 - \frac{(v_{OC} + 0.7)}{v_{OC}}\frac{FF_S}{r_P}\right\} \quad (0 \le r_S + 1/r_P \le 0.4) \end{aligned} \tag{1.12}$$

It should be noted that the equations shown above yield good approximations which are close enough in most cases for v_{OC} >10, but more generally applicable equations over a range of smaller values of v_{OC} (relatively large n) should be investigated.

1.4.5 Photovoltage Generation in Organic Solar Cells

The operating principle discussed in Chapter 1.4.3 described the photocurrent generation process in OSCs. Another important parameter of solar cells is the V_{OC} which is the voltage that compensates the current flow through the external circuit. In general, the V_{OC} of an OSC is known to be determined by several factors.

Properties of materials that comprise the photoactive layer affect the $V_{OC.}$ In particular, the relative energies of the relevant energy levels at the junction between donor and acceptor materials play an important role in the generation of the V_{OC} [23-25]. In the dark, the OSC works as a diode. That is, in the absence of generated charge carriers, the OSC is in equilibrium and no V_{OC} is observed since *J*–*V* characteristics in the dark cross the origin. The electron and hole densities are specified by the position of the E_F, and the E_F of all components in an OSC are aligned in equilibrium (Figure 1.6 (a)).

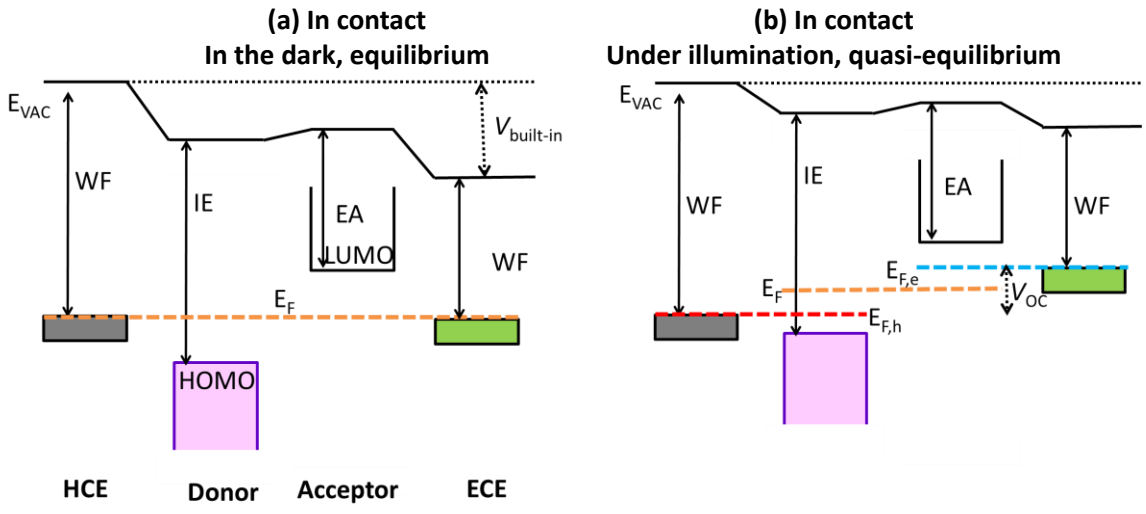

Figure 1.6 Energy level diagrams of donor and acceptor materials and charge-collecting electrodes in heterojunction organic solar cells (a) after contact in the dark, and (b) after contact under illumination.

Under illumination, additional electrons and holes in the OSC are produced by the absorption of photons. The concentration of both the electron of the acceptor and hole of the donor are larger than in the dark. In this quasi-equilibrium, the generated charge carriers can no longer be described by a single E_F [4]. Instead, the density of the generated electrons and holes can be expressed by quasi-Fermi levels ($E_{F,e}$ for electrons, $E_{F,h}$ for holes). Due to the increased electron density in the acceptor, the $E_{F,e}$ must be closer to the LUMO than in the dark. Likewise, the increased hole density in the donor leads to an $E_{F,h}$ that is closer to the HOMO than in the dark. The density of electrons in the LUMO is given by

$$n = N_C \exp(-\frac{EA - E_{F,e}}{kT}) \tag{1.13}$$

where n is electron concentration, N_C is the effective density of states (N_C=2[m_n^*(kT)/$\hbar^2$]$^{1.5}$, m_n^* is the effective mass of an electron) in the LUMO [26] . The density of holes in the HOMO is expressed by

$$p = N_V \exp(-\frac{E_{F,h} - IE}{kT}) \tag{1.14}$$

where p is hole concentration, N_V is the effective density of states in the HOMO (N_V=2[2$\pi\times m_p^*\times$(kT)/h^2]$^{1.5}$, m_p^* is effective mass of a hole) [26]. In quasi-equilibrium, the so-called law of mass action expressed below is no longer applicable.

$$n_i^2 = np \tag{1.15}$$

where n_i is the intrinsic carrier concentration. The np then follows that

$$np = n_i^2 \exp(\frac{E_{F,e} - E_{F,h}}{KT}) \tag{1.16}$$

That is, the concentration of generated charge carriers in the donor and acceptor determine the quasi-Fermi levels, and the V_{OC} of the OSC generally originates from the

quasi-Fermi level difference between the donor material and acceptor material under illumination at zero current (Figure 1.6 (b)).

$$V_{OC} = EA_{Acceptor} - IE_{Donor} - KT \ln(\frac{N_C^{Acceptor} N_V^{Donor}}{np}) \quad (1.17)$$

However, it should be noted that the estimation of V_{OC} with Eq. 1.17 only is applicable if there is no potential loss at the junction between the photoactive layer and the charge-collecting electrodes [8,18,27].

The WF difference between the two charge-collecting electrodes, the HCE and the ECE, also affects the V_{OC} of the OSC. Here, it is assumed that the charge-collecting electrodes are metals and are characterized by the chemical potential. The WF is known as the absolute value of the chemical potential. At the junction between an organic semiconductor and a metal, an electric potential difference arises, corresponding to the WF difference. Since the metal has a high concentration of electrons, the charge distribution in metal degenerates to a surface charge. Hence, the formed potential difference between the organic semiconductor and the metal is shown across the space charge layer of the organic semiconductor. If it is assumed that there is no charge at the contact except the surface charge of the metal, the electric potential is continuous across the interface. For example, the contact between an acceptor and an ECE (metal) under illumination, metals with a smaller WF value than $E_{F,e}$ of the acceptor material allow electrons to transfer into acceptor *via* thermal activation, resulting in an accumulation of electrons in the acceptor material (Figure 1.7 (a)). Hence, the $E_{F,e}$ of the acceptor is leveled and pinned to the WF of the ECE. Therefore, ECEs with small WF are favorable for transferring electrons and form a barrierless contact to acceptor materials. Conversely, HCEs with a large WF value are favorable to form a barrierless contact to donor materials. Consequently, in an OSC where barrierless contacts are formed, the V_{OC} is mainly determined by the interfacial kinetics at the heterojunction between a donor and

an acceptor, regardless of the WF of the charge-collecting electrodes. In other words, the V_{OC} is determined by Eq. 1.17.

On the other hand, ECEs with larger WF than $E_{F,e}$ of the acceptor material cause depletion of electrons in the acceptor material (Figure 1.7 (b)), and HCEs with smaller WF than $E_{F,h}$ of the donor material induce depletion of holes in the donor material. The $E_{F,e}$ of the acceptor is aligned with the WF of the ECE and $E_{F,h}$ of the donor is aligned with the WF of the HCE, However, in this case, the upper limit of $E_{F,e}$ is restricted to the WF of the ECE and the lower limit $E_{F,h}$ is constrained by the WF of the HCE. Consequently, the V_{OC} is limited by the WF difference between the HCE and the ECE [20,27].

$$V_{OC}^{\max} = V_{Built-in} = WF_{HCE} - WF_{ECE} \tag{1.18}$$

Furthermore, the depletion of the electrons in the acceptor material and that of the holes in the donor material induce potential barriers at either contact, resulting in an unavoidably high level of surface recombination at the interface [20]. This causes an S-shape kink in the *J-V* characteristics, resulting in reduced FF. Besides the two factor, many other effects such as band bending, temperature, *etc.* are also known to influence the V_{OC} [27,28].

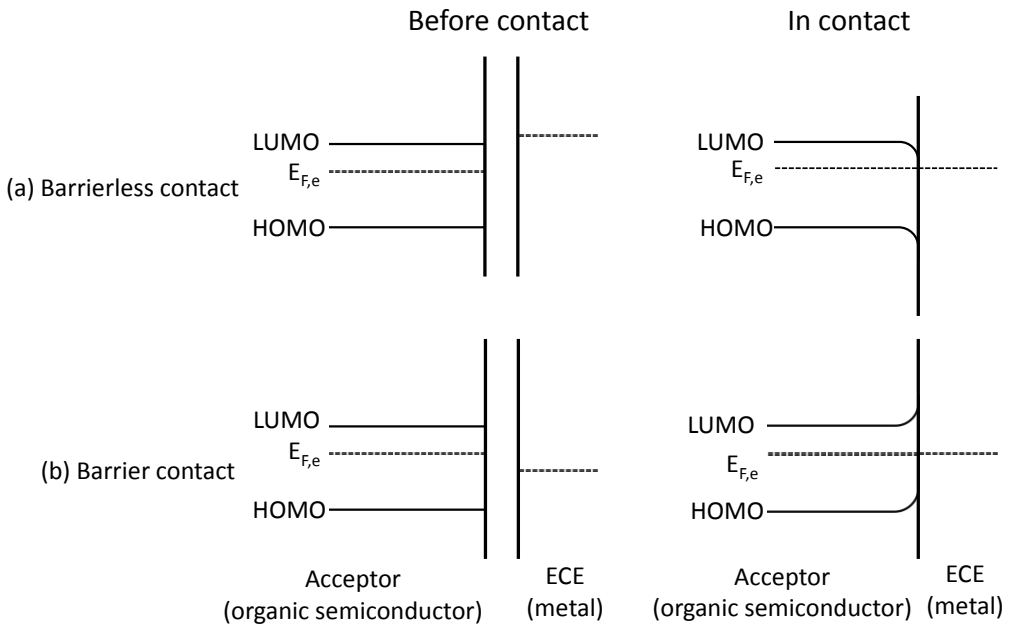

Figure 1.7 Energy level diagrams at the junction between an acceptor and an electron-collecting electrode. The electron-collecting electrode (a) has a smaller work function value and (b) has a larger work function than the quasi-Fermi level of the acceptor material under illumination (left column: before contact and right column: after contact).

1.4.6 Photoactive Layers in Organic Solar Cells

A major breakthrough in OSC technology was made when the bilayer heterojunction was used as the photoactive layer. The first bilayer heterojunction OSC was presented by C. W. Tang [29]. In this bilayer heterojunction OSC, the donor material, copper phthalocyanine (CuPc), and the acceptor material, a perylene tetracarboxylic derivative (Me-PTC), were sequentially stacked on top of each other. A PCE of around 1 % was achieved under simulated AM 2 illumination on this OSC. Figure 1.8 (a) shows a bilayer heterojunction OSC. In these kinds of OSCs, only the excitons created at a distance smaller than their diffusion length (typically 10-20 nm) from the heterojunction interface can contribute to the photocurrent. So this leads to exciton recombination when the exciton is generated at a location where the distance to

the heterojunction is longer than the exciton diffusion length, and consequently results in a low quantum efficiency and limited solar cell efficiency [30-32].

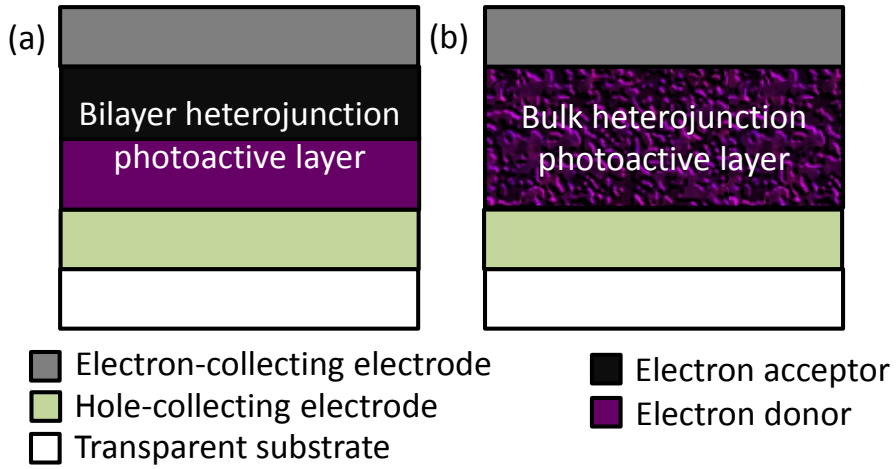

Figure 1.8 Types of photoactive layers for organic solar cells. (a) bilayer heterojunction, and (b) bulk heterojunction solar cells.

To overcome the limitation of small diffusion lengths in bilayer heterojunction-based devices, so-called bulk heterojunction OSCs comprising a blend of a donor material and an acceptor material emerged in 1991 [33]. A typical device configuration is shown in Figure 1.8 (b). In these kinds of OSCs, the donor and acceptor phase separate at 10-20 nm length scales. In this photoactive layer, the heterojunction interface between donor and acceptor phases can be made within the exciton diffusion length from the absorbing site, thus, the exciton decay process can be reduced [34]. The increased interface area in bulk heterojunction OSCs also improves the charge dissociation efficiency [33,35]. Unlike bilayer heterojunctions in which the donor and acceptor phases are completely separated from each other so that they can selectively contact the HCE or ECE, a mixture of the donor and acceptor phases in bulk heterojunction needs percolated pathways for the holes and electrons to transport to the HCE and ECE, respectively. Thus,

a good control of the morphology in the bulk heterojunction photoactive layer and the selection of charge-collecting electrodes are more sensitive in bulk heterojunction OSCs than bilayer heterojunction–based OSCs [18,34,36].

The first bulk heterojunction OSCs was demonstrated by Hiramoto *et al.* [37]. The photoactive layer comprised of three layers where a bulk heterojunction layer made by co-depositing the donor (metal-free phthalocyanine (H_2Pc)) and acceptor (Me-PTC) materials, was sandwiched between a single donor (H_2Pc) layer and a single acceptor (Me-PTC) layer. This structure yielded two times higher *J* compared to the OSC without the bulk heterojunction layer. Ever since, bulk heterojunction OSCs made with other small molecules such as copper phthalocyanine (CuPc) and 3,4,9,10-perylene tetracarboxylic bis-benzimidazole (PTCBI) were also demonstrated [38].

One of the first reported OSCs with a solution-processed bulk heterojunction photoactive layer was demonstrated by using a mixture of two polymers, poly(2-methoxy-5-(2-ethyl-hexyloxy)-1,4-phenylene vinylene) (MEH-PPV) as the donor with cyano-polyphenylene vinylene (CN-PPV) as the acceptor for the photoactive layer [39]. The interpenetrating network formed by the natural phase-segregation of the two polymers improved charge generation and charge carrier transport [39]. Yu *et al.* introduced the use of a soluble fullerene derivative, [6,6]-phenyl-C_{61} butyric acid methyl ester ($PC_{60}BM$) as an acceptor. An OSC using a blend of MEH-PPV and the $PC_{60}BM$ as a photoactive layer yielded a PCE of around 2.9 % under illumination (light intensity: 20 mW/cm^2) [33]. Shaheen *et al.* showed a solvent effect on the OSC performance. Use of a high boiling point solvent such as chlorobenzene enabled the bulk heterojunction film to gain more time for improved self-organization (phase separation) due to slow solvent

evaporation than the relatively low boiling point solvent, toluene. The enhanced phase separation induced more than twofold increase in the J_{SC} of PPV:PC_{60}BM-based OSCs [40].

Padinger *et al*. presented a photoactive layer with a conjugated donor polymer, poly(3-hexyl thiophene) donor (P3HT) in conjunction with PC_{60}BM. A further increase in PCE from 0.4% to 3.5% was achieved after a post-thermal annealing process at a temperature above the glass transition of the polymer. The following year, performance of OSCs steadily increased as research focused on optimization of bulk heterojunction devices with P3HT:PC_{60}BM photoactive layers. By optimizing the fabrication conditions, efficiencies in excess of 5% have been reported on P3HT:PC_{60}BM-based OSCs [36,41]. In recent years, as a result of tremendous efforts focusing on synthesizing new conjugated polymers and designing novel device architectures to increase absorption and carrier transport, OSCs have been reported with PCE up to 9.2 %. This highest PCE value reported on bulk heterojunction OSCs, was reported on poly thieno[3,4-b]thiophene/benzodithiophene (PTB7): [6,6]-phenyl C_{71}-butyric acid methyl ester (PC_{70}BM)-based organic solar cells [42,43].

1.4.7 Charge-collecting Interlayers in Organic Solar Cells

OSCs are commonly composed of a bulk heterojunction photoactive layer sandwiched by two charge-collecting electrodes: a HCE and an ECE. In a bulk heterojunction photoactive layer, two different types of materials: a donor material with a high HOMO and an acceptor material with a low LUMO are well dispersed in the bulk [8].

In the limit of a non-interacting metal/semiconductor interface, the Schottky-Mott limit, the barrier for electron (or hole) injection for an electrode with a WF within the semiconductor E_G, i.e. EA< WF < IE, is given by

$$\phi_B = WF_{ECE} - EA \text{ or } (\phi_B = IE - WF_{HCE}) \quad (1.19)$$

For charge collection, the height of this barrier appears to be relevant to the overall reduction of charge collection at that electrode/semiconductor interface. However, if the WF of the electrode approaches the limit of the E_G (IE or EA), it has been found that a substantial charge transfer can occur between the electrode and the semiconductor leading to interfacial dipoles and pinning of the Fermi level at an energy [44,45]. Hence, if the WF of an electrode can be modified to be WF ≥ IE of the donor material or WF ≤ EA of the acceptor material, then more efficient charge collection is speculated. Thus, the HCE should have sufficiently high WF and the ECE should possess sufficiently low WF to avoid the formation of a Schottky barrier between the donor and the HCE and between the acceptor and ECE.

In addition, as mentioned in Chapter 1.4.5, the V_{OC} of the OSC is known to be limited by the difference between EA of acceptor and IE of donor and the WF contrast between the HCE and ECE. Thus, these differences should be largest possible to maximize the V_{OC} of an OSC [23,24]. Since the difference between EA of acceptor and IE of donor in an OSC is determined by selection of donor and acceptor materials, to maximize the V_{OC}, and achieve efficient charge collection, the HCE and ECE should present a high WF contrast.

These charge-collecting electrodes are often realized by combining a conductor with a charge-collecting interlayer (CCI). The CCIs between the bulk heterojunction photoactive layer and electrode modifies the conductor to serve the roles of the charge-collecting electrodes (HCEs and ECEs) effectively. In general, to be efficient CCIs, they

should fulfill several requirements regarding electrical, optical, chemical, and mechanical properties. Above all, CCIs are required to have proper WF values, sufficiently high-WF for the HCE and low-WF for the ECE to enhance charge-collection efficiency. The charge-collection efficiency estimates the quality of charge collection with respect to charge generation in the photoactive layer [46]. Besides this, the CCIs should have high optical transparency to allow photons to reach the photoactive layer (if they are modifying a transparent electrode) and chemical compatibility with the adjacent layers to enhance device lifetime [47].

One of the most commonly used hole-collecting interlayer is a conducting polymer, poly(3,4-ethylenedioxythiophene):poly(styrenesulfonate) (PEDOT:PSS). PEDOT:PSS is solution processible and its conductivity can be varied by controlling its chemical composition from 10^{-6} to 10^{3} S/cm. Its WF of around 5.1 eV provides a good energy level matching with IE of various donor polymers [48,49]. However, a polymer with a larger HOMO level of 5.64 eV, such as poly[3,6-di(4'-ethyloctyl)thieno [3,2-b] thiophene-2,5-diyl-2,1,3-benzothiadiazole-4,7-diyl] (PTTBT) is not compatible with PEDOT:PSS. The electrical and structural inhomogeneities from the insulating PSS layer can reduce charge-collection efficiency, and acidic nature can cause chemical instability [47,50,51].

Another type of hole-collecting interlayer is transition metal oxides. N-type transition metal oxides such as vanadium oxide (V_2O_X), molybdenum oxide (MoO_X) and tungsten oxide (WO_X) have been widely employed to extract holes from the photoactive layer [52-54]. As n-type semiconductors, the enhanced hole-collecting properties of these metal oxides are induced by their high WF values and EA values, which are much larger than HOMO levels of common organic semiconductors used as electron-donor materials in OSCs. The holes of the electron-donor materials can be extracted via injection of electrons through the metal oxide layers. The EA values of V_2O_X, MoO_X and WO_X are 4.9 eV, 6.7 eV and 6.27 eV, respectively, and the IE values of V_2O_X, MoO_X and WO_X are

8.1 eV, 9.68 eV and 9.66 eV, respectively. The WF values of V_2O_X, MoO_X and WO_X are 5.6 eV, 6.86 eV and 6.47 eV, respectively [52,55,56].

A p-type transition metal oxide, nickel oxide (NiO) has been also employed to collect holes from the photoactive layers in OSCs. NiO possesses a relatively large E_G along with a sufficiently low EA (1.8 eV) than the EA values of both donor and acceptor materials so that they can effectively block electron transport through the metal oxide layers. Also, their high WF of around 5.0-5.4 eV provides a good energy level matching to the IE of the donor materials. These metal oxides can be deposited either by evaporation under vacuum, a solution process, or atomic layer deposition [41,57-59]. Besides these transition metal oxides, an oxidized derivative of graphene, graphene oxide (GO) has also been used as a hole-collecting interlayer [60,61].

Along with the hole-collecting interlayers, a variety of interlayers to enhance the electron-collection have been introduced. Conventionally, vacuum deposited thin layers of low-WF metals, such as Ca, have been employed on top of the photoactive layer to extract electrons. However, sensitivity of the low-WF metals to air and moisture contributes to device instability [62].

N-type metal oxides have been investigated for use as electron-collecting interlayers in OSCs. So far, titanium oxide (TiO_X) [63-66] and zinc oxide (ZnO) [67,68] have been most widely used as the electron-collecting interlayer by modifying the WF of conductors such as ITO. The low WF value of TiO_X (4.1 eV - 4.3 eV) [65,69] enabled a good energy level match with the LUMO level of acceptor materials, such as $PC_{70}BM$, leading to efficient electron-collection. The maximum light intensity can be redistributed by inserting the optical spacer, TiO_X, between the photoactive layer and the ECE [70]. TiO_X can be fabricated by various techniques, such as spin-coating nanoparticles, sol-gel methods (including a conversion of the titanium oxide precursor by hydrolysis), ALD, and chemical bath deposition (CBD) [65].

ZnO has a very similar electronic structure to that of TiO_X. That is, the low WF value of ZnO (4.0 eV - 4.2 eV) roughly matches with LUMO levels of acceptor materials commonly used in OSCs. In addition, its high optical transmittance in the visible range combined with a high electrical conductivity and a low cost make ZnO more attractive as an electron-collecting interlayer. So far, many different processing methods have been used to realize ZnO layers, including solution processed sol-gel [68,71], spin-coating nanoparticles [72], sputtering [73], and ALD [67].

In addition to these two metals oxides, an ultrathin (1 nm) layer of aluminum oxide (Al_2O_3) processed by ALD has been reported as an electron-collecting interlayer in OSCs [74]. However, further UV treatment is required to operate the OSCs efficiently.

Besides these metal oxides, alkali metal salts, such as cesium carbonate (Cs_2CO_3) have been deposited on top of conductors such as ITO to work as an electron-collecting interlayer. The Cs_2CO_3 layer is decomposed through thermal annealing, forming a doped n-type semiconductor. This decomposed Cs_2CO_3 has a sufficiently low-WF (from 3.45 eV to 3.06 eV), leading to efficient electron-collection [75].

In another approach, an ultrathin layer (less than 10 nm) of a surface modifier can be used to coat a conductor surface. These modifiers are adsorbed on the conductor surface by physisorption or chemisorption. They create strong interface or molecular dipole moments that induce a vacuum level shift and modulate the WF of the conductor surface. For example, the WF of ITO was decreased from 4.4 eV to 3.9 eV by a basic solution, tetrabutylammonium hydroxide ($N(C_4H_9)_4OH$) [76] and from 4.6 eV to 3.7 eV by amine containing conjugated small molecules such as tetrakis(dimethylamino)ethylene (TDAE) [77].

However, materials used as electron-collecting interlayers shown above have some issues that must be overcome. First, the Ca and TDAE are not stable in ambient air. Next, the WF values from the metal oxides mentioned above (4.0 eV – 4.3 eV) may not

be compatible with an acceptor with a low LUMO level [71]. Moreover, some materials such as Cs_2CO_3 need specific chemical reactions at relatively high temperatures [62].

Recently, the Kippelen Research Group discovered that surface modifiers based on polymers containing simple aliphatic amine groups substantially and universally reduce the WF of conductors including metals, transparent conductive metal oxides, conducting polymers and graphene. The WF reduction comes from physisorption of the neutral polymer, which turns the modified conductors into efficient ECEs. These polymer surface modifiers are processed in air from solution, providing an appealing alternative to chemically reactive low−WF metals. For example, the WF of ITO decreases up to 0.8 eV by a polymer surface modifier of poly (N-vinylpyrrolidone) (PVP) and up to 1.1 eV by another polymer surface modifier of ethoxylated polyethylenimine (PEIE). These polymer surface modifiers will be discussed in Chapter 4 in detail. The WF values of the hole- or electron-collecting interlayers are summarized in Table 1.1.

Table 1.1 Work functions of charge-collecting interlayers. (Materials firstly used from the Kippelen Research Group are in red)

Charge-collecting interlayers	Work functions (eV)	Ref.
Hole-collecting interlayers		
PEDOT:PSS	5.1 - 5.2	[41,47]
NiO_X	5.0 - 5.4	[41,57-59]
MoO_X	6.86	[52,56]
V_2O_X	5.5	[55]
WO_3	6.47	[52]
GO	4.9 - 5.1	[60,61]
Electron-collecting interlayers		
Ca	2.9	[47]
ZnO	4.0 - 4.3	[67,68,78]
TiO_2	4.3 - 4.14	[65,69]
Al_2O_3	4.3	[74]
Cs_2CO_3	3.06	[75]
$N(C_4H_9)_4OH$	3.9 (on ITO)	[76]
TDAE	3.7 (on ITO)	[77]
PVP	3.6 (on ITO)	[79]
PEIE	3.3 (on ITO)	[62]

1.4.8 Conventional and Inverted Geometries

One important characteristic that OSCs require is to achieve good air stability. This is a problem caused in part by the geometry of an OSC. As shown in Figure 1.9, OSCs can be realized based on two types of device geometries, the so-called conventional geometry and the inverted geometry, in which the polarity of the charge-collecting electrodes is reversed. In both cases, the OSC is generally made up with a photoactive layer and two charge-collecting electrodes. Charge carriers are created in the photoactive layer, and two charge-collecting electrodes, an ECE and a HCE collect electrons and holes from the photoactive layer, respectively. As mentioned in Chapter 1.4.7 to provide better extraction of the electrons and the holes from the photoactive layer, the WF of the HCEs should be sufficiently high to match the IE of the donor material in

the photoactive layer and the WF of the ECEs should be low enough to match with the EA of the acceptor material in the photoactive layer. Moreover, the HCE and the ECE should build an energy barrier to holes and electrons, respectively, inhibiting charge carriers from recombining in the contact while allowing the appropriate carriers through.

An OSC with the conventional geometry (hereon will be referred to as conventional OSC) is defined as an OSC wherein the HCE is made at the bottom of the cell and is typically transparent, and the ECE is reflective and is fabricated at the top of the cell. Whereas an OSC with the inverted geometry (hereon will be referred to as inverted OSC) is defined as an OSC wherein the HCE is reflective and generally made at the top of the cell, and the ECE is transparent and typically fabricated at the bottom of the cell.

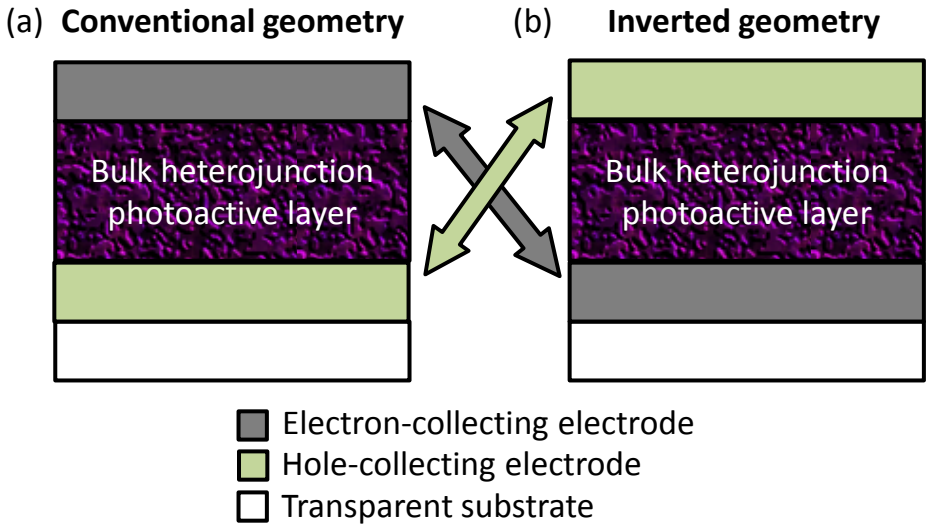

Figure 1.9 Organic solar cells with (a) a conventional geometry and (b) an inverted geometry.

In a conventional OSC, low-WF metals such as LiF/Al and Ca/Al as the ECE are typically used at the very top of the cells. Thereby, the HCE generally PEDOT:PSS-coated ITO, is fabricated at the bottom of the cell. However, the facile oxidation of the

low-WF metal is a major factor that contributes to limiting the air stability of solar cells and forces the use of encapsulation layers to improve their shelf stability [67,74,78,79]. In contrast to the conventional approach, in an inverted OSC, the ECE is commonly a modified ITO electrode with a low-WF electron-collecting interlayer, for example, surface modified ITO with amine containing polymer such as PEIE or low-WF metal oxides such as ZnO- or TiO_X- coated ITOs. The ECE in this type of cells is commonly fabricated at the bottom of the cell while the HCE, made of relatively high-WF metals such as Ag and Au, is fabricated at the top of the cell. Inverted OSCs avoid the use of the reactive low-WF metal electrodes at the top of the cell and therefore are attractive geometries, because the air stability can be improved.

1.4.9 Tandem Organic Solar Cells

Organic and inorganic solar cells suffer from two major losses, namely the sub-band-gap transmission and the thermalization of charge carriers. In addition, organic semiconductors suffer from narrow absorption bands and poor charge carrier transport [36]. One way to overcome these limitations simultaneously is the realization of tandem OSCs. Tandem solar cells contain several single-junction solar cells with different absorption ranges. A broader portion of the solar spectrum can be absorbed by multi-junction solar cells and thereby the PCE can be increased. Theoretically, an inorganic tandem solar cell with two sub-cells with band gaps of 1.9 eV and 1.0 eV, respectively, can allow achieving a PCE of 42 % which is exceeding the proposed detailed balance limit of a single p-n junction solar cell, 30 %, so-called the Shockley-Queisser limit [22,80]. Indeed, experimentally, a PCE as high as 36.9 % has been reported from GaInP/GaAs/GaInAs based solar cells under illumination of non-concentrated AM 1.5 G spectrum [81]. Similar to inorganic tandem solar cells, small molecules and polymers have been used in tandem solar cells geometries. Generally in tandem OSCs, two or more

single-junction OSCs are stacked and connected through charge recombination layers (CRLs). In the case of all sub-cells connected in series for a tandem OSC, the V_{OC} of the sub-cells adds up, the J_{SC} of the tandem cell is limited to the smallest J_{SC} generated in any of the sub-cells and consequently the PCE can be increased [80,82]. Figure 1.10 describes a tandem OSC with the conventional geometry.

To realize tandem OSCs, selecting photoactive materials for the bottom cell (the first light-absorbing sub-cell) and top cell (the second light-absorbing sub-cell stacked on top of the bottom cell through a CRL) with complementary absorption is essential to obtain a high J_{SC}. Matching the photo-generated current between sub-cells connected in series is also necessary to maximize the J_{SC} and consequently the PCE.

Another critical component to maximizing the PCE of a tandem OSC is the CRL that connects two OSC sub-cells in series. This layer allows holes to be collected, from one sub-cell, and be recombined with the electrons collected from the other sub-cell. Therefore, the WF of one side of the CRL is supposed to be high enough to provide good energy level alignment with the IE of the donor material, in the adjacent sub-cell, for a hole to be collected effectively at that interface. Also, the WF at the other side of the CRL should be low enough to provide adequate energy level alignment with the EA of the acceptor material in the adjacent sub-cell, for an electron to be collected efficiently at that interface. In addition, the CRL should work as an efficient recombination center for collected electrons and holes. Furthermore, materials for the CRL are required to have low optical absorption in the spectral region of interest. From a practical perspective, in tandem solar cells wherein the top active layer is solution-processed, the CRL also needs to be mechanically robust enough to prevent damage of the bottom cell and of the CRL itself during the processing of the top cell [80].

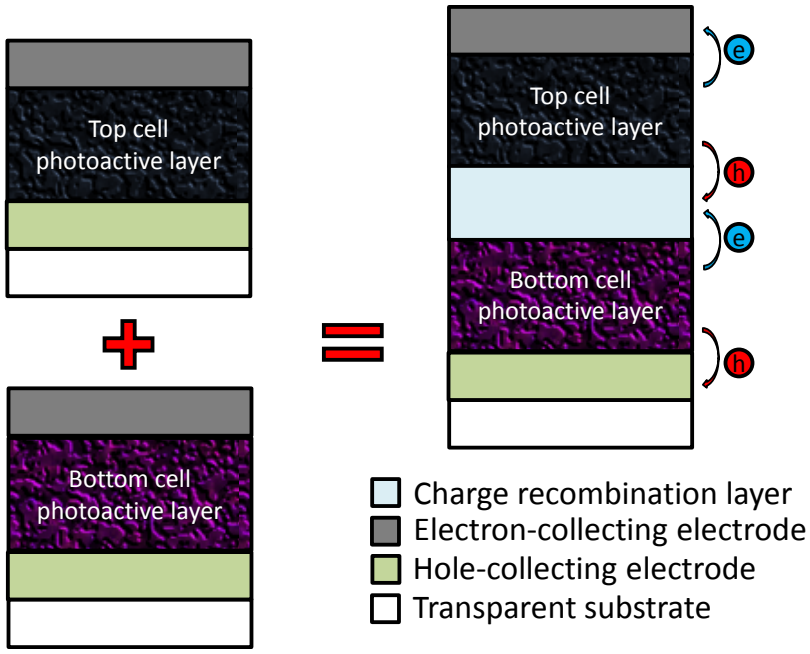

Figure 1.10 Formation of a tandem organic solar cell with a conventional geometry.

To date, a number of approaches to realize tandem OSCs either by different processing methods or device structures have been demonstrated. One of the first reported tandem OSC was made by Hiramoto *et al*.[83]. In this tandem OSC, H_2Pc and an n-type perylene tetracarboxylic derivative (Me-PTC) served as photoactive layers for the bottom and top cells identically and a thin Au layer was used as the CRL. The first tandem OSC exhibited almost doubling of the V_{OC} of each individual cell to reach a value of 0.78 V.

Yakimov *et al.* demonstrated the first tandem OSC with heterojunction photoactive layers wherein two, three, or five stacked thin photoactive layers comprising CuPc and PTCBI served as an electron-donor and –acceptor materials, respectively [84]. Ultrathin Ag clusters (5 Å) inserted between each sub-cells worked as the CRLs. The PCEs of the tandem OSCs with two and three heterojunctions photoactive layers under AM 1.5 illumination were about 2.5 % and 2.36 %, respectively. These PCE values were more than twice of that from single-junction OSC, 1.1 %. Also, the V_{OC}s from these two

tandem OSCs were 0.93 V (two sub-cells) and 1.20 V (three sub-cells), respectively while the 0.45 V was achieved from the single-junction OSC. These small molecule based tandem OSCs had the advantage that a number of layers including the photoactive layers and CRLs can be easily deposited with dry processes such as thermal evaporation. However, due to the lack of small molecules having different absorption ranges, hybrid tandem OSCs that used a polymer sub-cell and a small molecule sub-cell, and solution-processed tandem OSC that had two different polymer sub-cells emerged.

Dennler *et al*. demonstrated the first hybrid tandem OSCs composed of a polymer-based bottom cell comprising P3HT:PC_{60}BM and a small molecule-based top cell made with Zn-Pc:C_{60} [85]. For the P3HT:PC_{60}BM layer was processed from solution and the Zn-Pc:C_{60} layer was fabricated by vacuum deposition. Using photoactive layers with complementary absorption range (P3HT:PC_{60}BM: 375-630 nm Zn-Pc:C_{60}: 600-800 nm), a tandem OSC could utilize the whole visible range of the solar spectrum. For this tandem OSC, 1 nm-thick Au served as the CRL. The V_{OC} from the tandem OSCs (1.02 V) was almost equal to the sum of V_{OC}s from the single cells, 0.55 V from P3HT:PC_{60}BM cell and 0.47 V from Zn-Pc:C_{60} cell.

Kawano *et al.* showed one of the first polymer-based tandem OSCs with two identical bulk heterojunction photoactive layers comprising a blend of poly[2-methoxy-5-(3',7'-dimethyloctyloxy)-1,4-phenylene vinylene] (MDMO-PPV) and PC_{60}BM [25]. For this tandem OSC, ITO deposited by sputtering and PEDOT:PSS deposited by spin-coating were used for the CRL. The tandem OSCs showed about 1.6 times higher V_{OC} (1.34 V) than that of the single-junction reference OSC (0.84 V) with a structure of ITO/PEDOT:PSS/MDMO-PVP/Al. Although the V_{OC} from the tandem cell should be a sum of the V_{OC}s from sub-cells, the V_{OC} from this tandem OSC did not show doubled V_{OC} due to the increased series resistance introduced by the CRL. The J_{SC} (4.1 mA/cm^2) and FF (56 %) from the tandem OSC were slightly lower than those from the single-junction reference OSC (J_{SC}: 4.6 mA/cm^2 and FF: 59 %). These were attributed to the use of

identical photoactive layers which reduce light absorption at the top sub-cell, so different photoactive layers with complementary absorption ranges were believed to improve the device performance.

One major breakthrough in the tandem OSCs was realization of all solution processible polymer tandem OSC by Kim *et al.*[86]. In this tandem OSC, two mixtures of poly[2,6-(4,4-bis-(2-ethylhexyl)-4H-cyclopenta[2,1-b;3,4-b']dithiophene)-alt-4,7-(2,1,3-benzothiadiazole)] (PCPDTBT):$PC_{60}BM$ and P3HT:$PC_{70}BM$ were used as photoactive layers for the bottom and top sub-cells, respectively. Highly conductive PEDOT:PSS (PH 500) and TiO_X were spin-coated on top of the bottom sub-cell to serve as the CRL. The two polymers, PCPDTBT and P3HT, have complementary absorption ranges, so that the tandem cell could use a broader portion of the solar spectrum up to 850 nm. Under AM 1.5 G illumination, the tandem OSCs showed a J_{SC} of 7.8 mA/cm^2, a V_{OC} of 1.24 V, a FF of 0.67, and PCE of 6.5 %.

To avoid use of the low-WF metal at the top of the tandem OSCs, which is sensitive to oxygen and moisture, and causes device instability, inverted tandem OSCs have been demonstrated. One of the first report regarding inverted tandem OSCs were made by Sun *et al.* [87]. This inverted tandem OSC used two identical photoactive layers consisting of P3HT:$PC_{60}BM$ for the bottom and top cells, and a CRL composed of ultrathin multiple metal layers of Ca/Al/Ag and metal oxide MoO_3 that showed high transparency. The CRL in the tandem OSC showed effective charge recombination properties with V_{OC} values (1.18 V) corresponding to the sum of two sub-cells and a high FF of 0.618. The maximum PCE shown in this tandem OSC was 2.78 % under 100 mW/cm^2 AM 1.5 G illumination.

Ever since, tremendous efforts have been made towards providing new conjugated polymers with lower E_G and making more efficient CRLs with larger WF contrast between two opposite interfaces and lower optical loss. One of the most highly efficient CRLs was recently demonstrated by Zhou et al. from the Kippelen Research

Group [88]. In this work, efficient inverted tandem OSCs with an all-polymer CRL, comprising a conducting polymer PEDOT:PSS coated with an ultra-thin polymer surface modifier, PEIE were introduced for the first time. For the photoactive layers of the bottom and top cells, P3HT: indene-C_{60} bisadduct ($IC_{60}BA$) and poly(4,8-bis-alkyloxybenzo(1,2-b:4,5-b′)dithiophene-2,6-diyl-alt-(alkyl thieno(3,4-b) thiophene-2-carboxylate)-2,6-diyl) (PBDTTT-C): $PC_{60}BM$ were employed, respectively. The tandem OSCs with the polymer CRL exhibited high performance with a V_{OC} of 1.50 V, a J_{SC} of 7.7 mA/cm^2, a FF of 0.72, leading to a PCE of 8.2% under AM 1.5 100 mW/cm^2 illumination.

Recently, You *et al*. demonstrated inverted tandem OSCs with a PCE as high as 10.6 % [89]. In this inverted tandem cell, a low E_G (1.38 eV) conjugated polymer, poly[2,7-(5,5-bis-(3,7-dimethyl octyl)-5H-dithieno[3,2-b:20,30-d]pyran)-alt-4,7-(5,6-difluoro-2,1,3-benzothiadiazole)] (PDTP-DFBT) blended with $PC_{70}BM$ and relatively large band gap polymer P3HT mixed with $IC_{60}BA$ served as top and bottom photoactive layers. As the CRL, solution processible ZnO and PEDOT:PSS were employed. This was the first tandem OSC that broke the 10 % efficiency hurdle, which had been believed as a minimum required PCE for the commercialization of OSCs.

Although the device structures, including the photoactive layers and the CRL of the state-of-art tandem OSC have not been revealed by the inventor yet, PCE values as high as 12 % have been reported. A brief summary of the reports dealing with tandem OSCs with the conventional and inverted geometries is presented in Table 1.2.

Table 1.2 Summary of tandem OSCs with the conventional or inverted geometries. (PCE values were rounded off two digits after the decimal point.)

Bottom cells	CRLs	Top cells	PCE (%)	Year	Ref.
Conventional geometry					
PBDTT-FDPP-C12:$PC_{61}BM$	PFN/TiO_2/PEDOT	PBDTT-SeDPP :$PC_{71}BM$	7.3	2013	[90]
PCDTBT:$PC_{70}BM$	ZnO/PEDOT:PSS	PDPP5T:$PC_{60}BM$	7.5	2012	[91,92]
P3HT:$PC_{60}BM$	ZnO/PEDOT:GO	P3HT:$PC_{60}BM$	4.1	2011	[93]
P3HT:$IC_{60}BA$	TiO_2/m-PEDOT	PSBTBT:$PC_{70}BM$	7.0	2011	[94]
SubNc/C_{60}	PTCBI/Ag/MoO_3	SubNc/C_{60}	5.2	2010	[95]
PF10TBT:$PC_{60}BM$	ZnO/PEDOT:PSS	PF10TBT:$PC_{60}BM$	4.5	2010	[96]
PFTBT:$PC_{60}BM$	ZnO/N-PEDOT	PBBTDPP2:$PC_{60}BM$	4.9	2010	[50]
P3HT:$PC_{70}BM$	Al/TiO_2/ PEDOT:PSS	PSBTBT:$PC_{70}BM$	5.8	2010	[97]
P3HT:bis-$PC_{60}BM$	LiF/ITO/MoO_3	P3HT:$PC_{70}BM$	5.2	2010	[98]
P3HT:$PC_{60}BM$	Al/MoO_3	P3HT:$PC_{60}BM$	2.2	2009	[99]
P3HT:$PC_{60}BM$	LiF/Al/WO_3	CuPc:C_{60}	4.6	2007	[100]
P3HT:$PC_{60}BM$	Sm/Au/PTrFE/ Au/PEDOT:PSS	PTBEHT:$PC_{60}BM$	3.0	2007	[101]
PCPDTBT:$PC_{60}BM$	TiO_X/PEDOT:PSS	P3HT:$PC_{71}BM$	6.5	2007	[102]
MDMO-PPV:$PC_{60}BM$	ZnO/PEDOT:PSS	P3HT:$PC_{60}BM$	1.7	2007	[103]
P3HT:$PC_{60}BM$	BPen:Li/Au/MTDATA:F_4-TCNQ	CuPc/C_{60}	1.2	2006	[104]
P3HT:$PC_{60}BM$	C_{60}/Au	ZnPc/ZnPc:C_{60}/C_{60}	2.3	2006	[85]
MDMO-PPV:$PC_{60}BM$	ITO/PEDOT:PSS	MDMO-PPV:$PC_{60}BM$	3.1	2006	[25]
p-doped MeO-TPD/ blend ZnPc:C_{60}/n-doped C_{60}	Au	p-doped MeO-TPD/ blend ZnPc:C_{60}/n-doped C_{60}	3.8	2005	[105]
CuPc/CuPc:C_{60}/ C_{60}/PTCBI	Ag	m-MTDATA/CuPc/ CuPc:C_{60}/C_{60}/BCP	5.7	2004	[106]
CuPc/PTCBI	Ag	CuPc/PTCBI	2.5	2004	[107]
CuPc/PTCBI	Ag	CuPc/PTCBI	2.3	2002	[84]
Me-PTC/H_2PC	Au	Me-PTC/H_2PC	NA	1990	[108]
Inverted geometry					
PDTP-DFBT :$PC_{71}BM$	MoO_3/M-PEDOT:PSS/ZnO	PDTP-DFBT :$PC_{71}BM$	10.2	2013	[109]
P3HT:$IC_{60}BA$	PEDOT:PSS/ZnO	PDTP-DFBT :$PC_{71}BM$	10.6	2013	[89]
P3HT:$IC_{60}BA$	PEDOT:PSS/ZnO	PBDTT-SeDPP	9.5	2013	[110]

		:$PC_{71}BM$			
P3HT:$IC_{60}BA$	PEDOT:PSS/PEIE	PBDTTT-C: $PC_{60}BM$	8.2	2012	[88]
P3HT:$IC_{60}BA$	PEDOT:PSS/ZnO	PBDTT-DPP: $PC_{71}BM$	8.6	2012	[111]
P3HT:$IC_{60}BA$	PEDOT:PSS/ZnO	PDPP5T:$PC_{60}BM$	5.8	2012	[112]
P3HT:$PC_{60}BM$	MoO_X/Ag/PEIE	P3HT:$PC_{60}BM$	2.1	2012	[113]
P3HT:$IC_{60}BA$	PEDOT:Au/TiO_2:Cs	PSBTBT: $PC_{71}BM$	6.2	2012	[114]
F4-ZnPc:C_{60}	DiNPB/p-DiNPB 5%/p-DiNPB 10%/n-C_{60}/C_{60}	DCV6T:C_{60}	6.1	2011	[115]
P3HT:$PC_{60}BM$	MoO_3/Ag/Al/Ca	P3HT:$PC_{60}BM$	2.9	2011	[116]
P3HT:$PC_{60}BM$	MoO_3/Al/ZnO	PSBTBT:$PC_{70}BM$	5.1	2011	[117]
P3HT:$PC_{60}BM$	PEDOT:PSS/ZnO/ C_{60}-SAM	P3HT:$PC_{60}BM$	2.9	2010	[118]
P3HT:$PC_{60}BM$	MoO_3/Ag/Al/Ca	P3HT:$PC_{60}BM$	2.8	2010	[87]

1.4.10 State of The Art

The current status of OSCs, the reported highest values of photovoltaic parameters from OSCs with different geometries is summarized in this section (Table 1.3). Also, the device performances of the champion OSCs with different geometries fabricated in the Kippelen Research Group are introduced.

Table 1.3 A summary of the highest values of photovoltaic parameters in organic solar cells with different geometries. (The highest values are in red. Values of V_{OC}, FF, and device area were rounded off three digits after the decimal point and values of J_{SC} and PCE were rounded off two digits after the decimal point and device area values were rounded off three digits after the decimal point.)

Junction	Device polarity	Device structure	V_{OC} (V)	J_{SC} (mA/cm^2)	FF	PCE (%)	Area (cm^2)	Year ,Ref.
1	Conventional	ITO/PEDOT:PSS/PTB7:$PC_{71}BM$/PFN(Ca)/Al	0.76	15.8	0.70	8.4	0.16	2011 [119]
		ITO/PEDOT:PSS/PCDTBT:$PC_{71}BM$/ BCP/ Al	0.91	11.8	0.66	7.1	1.0	2011 [120]
		ITO/PEDOT:PSS/PBnDT-FTAZ:$PC_{61}BM$/Ca/Al	0.79	12.5	0.72	7.1	0.12	2011 [121]
		ITO/PEDOT:PSS/PBDTTT-C:$PC_{60}BM$/Ca/Al (The Kippelen Research Group)	0.67	14.3	0.62	6.0	0.1	2012 [62]
	Inverted	ITO/PFN/PTB7:$PC_{71}BM$/MoO_3/Ag	0.75	17.5	0.70	9.2	0.16	2012 [42]
		ITO/PEIE/P3HT:$IC_{60}BA$/MoO_X/Ag (The Kippelen Research Group)	0.81	7.9	0.73	4.7	0.1	2013
		ITO/ZnO/BTI-BDT:$PC_{71}BM$/MoOx/Ag	0.92	9.6	0.62	5.5	0.06	2012 [122]
		ITO/PEIE/PBDTTT-C:$PC_{60}BM$ /MoO_X/Ag (The Kippelen Research Group)	0.68	16.1	0.61	6.6	0.1	2012 [62]
2	Conventional	ITO/PEDOT:PSS/PCDTBT:$PC_{70}BM$ /ZnO/PEDOT:PSS/PDPP5T:$PC_{60}B$	1.44	8.8	0.59	7.5	0.16	2012 [91]

	M/Al						
	ITO/SubNc/C_{60}/PTCBI/Ag/MoO_3/SubNc/C_{60}/BCP/Ag	1.92	4.3	0.62	5.2	0.13	2010 [95]
	ITO/PEDOT:PSS/BP2T/AlClPc/ZnPc:C_{60}/C_{60}/Alq3/Al (Parallel tandem OSC)	0.54	12.2	0.53	3.5	0.03	2012 [123]
	ITO/PEDOT:PSS/P3HT:bis-PC_{60}BM/LiF/ITO/MoO_3/P3H:PC_{70}BM/LiF/Al[81]	1.14	6.1	0.74	5.2	0.06	2010 [98]
Inverted	ITO/ZnO/P3HT:ICBA/PEDOT:PSS/ZnO/PDTP-DFBT:PC_{60}BM/MoO_3/AG	1.53	10.1	0.69	10.6	0.01-0.10	2013 [89]
	ITO/n-C_{60}/C_{60}/F4-ZnPc:C_{60}/DiNPB/p-DiNPB 5%/p-DiNPB 10%/n-C_{60}/C_{60}/DCV6T:C_{60}/BPAPF/p-BPAPF 10%/p-BPAPF 5%/p-BPAPF 10%n-C_{60}/Al	1.59	6.2	0.62	6.1	2	2010 [115]
	ITO/PEIE/P3HT:IC_{60}BA/PEDOT:PSS/PEIE/PBDTTT-C:PC_{60}BM/MoO_X/Ag (The Kippelen Research Group)	1.50	7.7	0.72	8.2	0.09	2012 [88]
Proprietary (Heliatek)		-	-	-	12	1.1	2012 [81]

1.5 Objectives and Scope of the Dissertation

In spite of advancement in the field of OSCs, more progress needs to be accomplished to overcome challenges related to commercial applications. This section addresses several issues related to the aim of the research conducted in this dissertation and introduces the goals and scope of this dissertation.

As discussed in the previous section, the facile oxidation of the low-WF metal such as Ca used for the electron-collecting electrode is a major factor that contributes to limiting the environmental stability of OSCs and forces the use of encapsulation layers to

improve their shelf stability. Also, the energy level mismatching between the WF of electron-collecting interlayers or electrodes and LUMO level of acceptor materials, and hole-collecting interlayers or electrodes and HOMO level of donor materials can limit the V_{OC} and PCE as well. Moreover, even with recently developed small E_G polymers, less than 60% of the incident solar power is absorbed. Maximizing light absorption by increasing the thickness of the layers can reduce the carrier collection efficiency and make the cells too resistive, thus impacting its performance. Besides these challenges, some other issues such as processibility, scalability, *etc.* still exist. The research conducted in this dissertation aimed to overcome these issues.

The primary objective of this dissertation is to realize efficient charge-collecting interlayers for single-junction OSCs. The research related to the charge-collecting interlayers is divided into two main parts, a hole-collecting interlayer and an electron-collecting interlayer, and they are shown in the Chapter 3 and 4, respectively. Chapter 3 investigates use of a NiO layer processed by ALD for a hole-collecting interlayer in OSCs. The ALD process is firstly adopted for the NiO layer synthesis. The photovoltaic performance of the single-junction OSCs with the NiO hole-collecting interlayer is explored and a comparison with the widely used hole-collecting interlayer PEDOT:PSS is presented.

In Chapter 4, an investigation on the electron-collecting interlayers is described. The electron-collecting interlayers include TiO_2 nanoparticles and two polymeric materials, PVP and PEIE. Firstly, the use of the PVP for the dispersant for the TiO_2 nanoparticles is introduced. Then, a discovery of the polymeric interlayers (surface modifiers) during the optimization of the performance of OSC with the TiO_2:PVP layer is described. In the next chapters, the electron-collecting interlayers made only with polymeric materials, PVP and PEIE are investigated. The mechanism for the WF reduction of the conductor surface by the polymeric interlayers is introduced. Secondly,

several examples of conductors with reduced WF by the polymeric interlayer are introduced. Finally, with these polymeric interlayers, various types of efficient single-junction OSCs, including all-plastic solar cells, are demonstrated.

The second objective of this dissertation is to advance the field of OSCs by studying CRLs and finally realizing efficient inverted tandem OSCs. The work presented in Chapter 5 is related to tandem OSCs, especially the CRLs. Three different CRLs are introduced, including MoO_X/Ag/PEIE, MoO_X/Al_2O_3:ZnO nanolaminate/PEIE, and PEDOT:PSS/PEIE. Even though the hole-collecting layers in the CRLs are different, the PEIE layer is commonly used at one side of the CRLs for electron collection. In the first tandem OSCs with the CRL of the MoO_X/Ag/PEIE, two identical photoactive layers are used for bottom and top cells. The second tandem OSCs with CRL of the MoO_X/Al_2O_3:ZnO nanolaminate/PEIE and third tandem OSCs with the CRL of the PEDOT:PSS/PEIE have different photoactive layers for bottom and top cells with a complementary absorption range. The characterization of the CRLs themselves and photovoltaic performance of the tandem OSCs with the CRLs is described. Also, it should be noted that all the experimental details and methods regarding device fabrication and characterization are summarized in Chapter 2.

Chapter 6 summarizes the work presented in this dissertation and presents recommendations for future work.

CHAPTER 2

EXPERIMENTAL METHODS

2.1 Introduction

This chapter will show a detailed description of all experimental procedures used in this thesis. All steps included in device fabrication and characterization will be summarized in this chapter. The experimental method will be divided into two parts. The first part will illustrate critical steps for fabrication of OSCs, starting with the preparation of substrates used for the OSCs. Also, fabrication of thin films by various methods such as spin coating and ALD will be included. Finally, deposition of metal electrodes through thermal evaporation will be introduced. The second part will deal with the methods of characterizing OSCs used in this thesis. The techniques used for electrical and optical characterization of thin films will be shown first. Then, the measurement of the electrical characteristics of OSCs will be discussed.

2.2 Organic Solar Cell Fabrication

2.2.1 Substrate Preparation

Preparing substrates is exceptionally important for providing reproducibility of the device performance. For this thesis, two different substrates were used. The first was a glass coated with a transparent conducting oxide, ITO (hereafter referred as ITO-coated glass). While the ITO-coated glass was a rigid and non-flexible substrate, the other substrate was a plastic substrate made with polyethersulfone (PES). Moreover, patterning these substrates was required to define a photoactive area. In case of the ITO-coated glass, half of the substrate was deposited with a SiOx thin film or etched by an acidic solution.

In the case of the PES substrate, half of the substrate was covered with conducting polymer, PEDOT:PSS as a transparent electrode.

The preparation process for these substrates will be explained in more detail below.

ITO-coated glass substrate: ITO-coated glass (Colorado Concept Coatings LLC) with sheet resistivity of 15 Ω/sq was used as substrates. Substrates were cleaned in an ultrasonic bath of detergent (Liqui-Nox® Phosphate-Free Liquid Detergent, Alconox, Inc.) in water, rinsed with deionized water, and then cleaned in sequential ultrasonic baths of distilled water, acetone (VWR), and 2-propanol (VWR) (20 min each). Nitrogen was used to dry the substrates after each bath.

To define the photoactive area on ITO-coated glass substrate, two methods were employed. The first one is with deposition of SiO_X. On each ITO-coated glass substrate, a 300-nm-thick (estimated from the crystal thickness monitor) layer of SiO_X (Silicon Monoxide, Kurt J. Lesker) was deposited by electron-beam deposition (AXXIS, Kurt J. Lesker) through a shadow mask, at a rate of 0.4 - 0.6 nm/s and a base pressure of $\sim 8 \times 10^{-8}$ Torr to electrically isolate half of the ITO area.

Another way to isolate the half of ITO-coated glass substrate was etching with an acidic solution. Half of ITO-coated glass substrate was masked with Kapton tape (VWR, Radnor, PA) (1/2 inch wide) and the uncovered areas were etched with an acid solution of $HCl:HNO_3$ (1:3) at 75 °C for 5 min. After etching, the Kapton tape mask was removed, and substrates were cleaned in an ultrasonic bath of detergent in water, rinsed with deionized water, and then cleaned in sequential ultrasonic baths of distilled water, acetone, and 2-propanol (IPA) (20 min each). Nitrogen was used to dry the substrates after each bath.

PES substrate: The PES films (I-component, South Korea) were attached to rigid glass substrates with a piece of cured polydimethylsiloxane (PDMS, Gelest, Inc.,

Morrisville, PA). Next, a piece of PDMS as a shadow mask was put down on half of the PES substrates to keep its hydrophobic property prior to plasma treatment. Then 5 seconds of O_2-plasma treatment was performed on the PES substrates and the PDMS on half the substrate was peeled off. At this moment, half of the PES substrate is hydrophilic and the other half is hydrophobic. Then aqueous and high conductivity PEDOT:PSS PH1000 (CLEVIOS™ PH 1000, HC Stack Inc.) with 5% dimethyl sulfoxide (DMSO, VWR) was spin coated on PES substrates at a speed of 1000 rpm for 30 s and an acceleration of 1000 rpm/s and annealed at 140 °C for 10 min on a hot plate in air. Since the aqueous PH1000 solution only wets on the half PES substrates with hydrophilic property, PH1000 film was only deposited on half of the PES substrate.

2.2.2 Thin Films Deposition

An OSC comprises many thin layers with different functions, such as a photoactive layer, charge-collecting interlayers, etc. To form these layers, various techniques were used for this thesis.

2.2.2.1 Spin Coating

The first technique was spin coating. Spin coating is performed to deposit a uniform film on a flat substrate. A small amount of coating material is applied to the substrate, and then the material spreads out by centric force during the substrate spinning. The thickness of the film commonly depends on spin speed, viscosity, and concentration of the coating materials.[124] Spin coating was used for this thesis for depositions of photoactive layers, charge-collecting interlayers, and CRLs. The spin-coating process for these layers will be explained in more detail below.

Photoactive layers:

P3HT:$IC_{60}BA$: A solution of P3HT **(**Rieke Metals):$IC_{60}BA$ (Luminescence Technology Corp.) was made in 1,2-dichlorobenzene (DCB, Sigma Aldrich) with a weight ratio of 1:1 (P3HT:$IC_{60}BA$) and a total P3HT+$IC_{60}BA$ concentration of 40 mg/ml. The P3HT:$IC_{60}BA$ solution was stirred overnight in a nitrogen-filled glove box, and heated at a temperature of 70 °C for 8 hours before use. 200-nm-thick films of P3HT:$IC_{60}BA$ were deposited by spin coating at 800 rpm for 30 seconds, using a 0.2-μm-pore PTFE filter, and dried in covered glass Petri dishes for 5 hours under a nitrogen atmosphere. The films were then annealed at 150 ºC for 10 minutes under a nitrogen atmosphere (Chapter 3.1, 4.3, 5.2, and 5.3).

P3HT:$PC_{60}BM$: A solution of P3HT:$PC_{60}BM$ (Nano-C) was made in chlorobenzene (CB, Sigma Aldrich) with a weight ratio of 1:0.7 (P3HT:$PC_{60}BM$) and a total P3HT+$PC_{60}BM$ concentration of 20 or 34 mg/ml. The P3HT:$PC_{60}BM$ solution was stirred overnight in a nitrogen-filled glove box, and heated at a temperature of 45 °C for one hour before use. 90- or 180-nm-thick films of P3HT:$PC_{60}BM$ were deposited by spin coating at 700 rpm for 60 seconds, using a 0.2-μm-pore PTFE filter. The films were then annealed at 150 ºC for 10 minutes under a nitrogen atmosphere (Chapter 4.1, 4.2, and 5.1).

PBDTTT-C:$PC_{60}BM$: A solution of PBDTTT-C (Solarmer Materials):$PC_{60}BM$ was made in CB:1,8-diiodooctane (DIO) (97:3, volume (v):volume (v)) with a weight ratio of 1:1.5 (PBDTTT-C:$PC_{60}BM$) and a total PBDTTT-C +$PC_{60}BM$ concentration of 25 mg/ml. The PBDTTT-C:$PC_{60}BM$ solution was stirred overnight in a nitrogen-filled glove

box before use. 90-nm-thick films of PBDTTT-C:$PC_{60}BM$ were deposited by spin coating at 1000 rpm for 20 seconds (Chapter 4.3, 5.2, and 5.3).

The chemical structures of the materials used for the photoactive layers are shown in Figure 2.1.

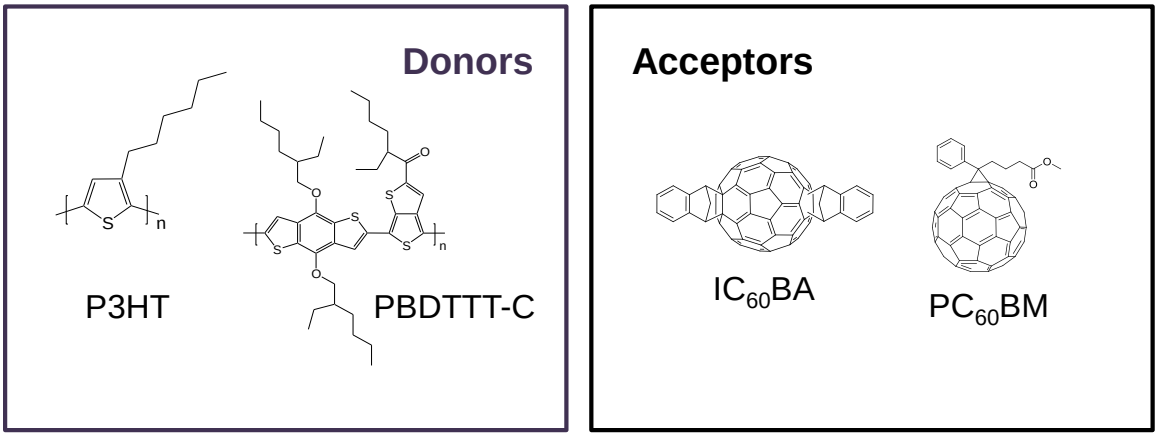

Figure 2.1 Chemical structures of donors and acceptor compounds for the photoactive layers in this dissertation.

Charge-collecting interlayers or charge-collecting electrodes:

TiO_2:PVP: Titanium dioxide (TiO_2) nanopowder (Sigma Aldrich) and PVP (Sigma Aldrich) was dispersed in distilled water with a total concentration of 0.14 wt.% (TiO_2 :0.07 (weight %) wt.% and PVP: 0.07 wt.%). The TiO_2:PVP solution was stirred overnight in air, and a ultrasonication for 30 minutes was performed on the solution. Then, the solution was centrifuged at a rotation speed of 3000 rpm for 5 minutes (Eppendorf Centrifuges 5804 R, Eppendorf AG). The taken solution from the top of the centrifuged solution was spin-coated onto ITO at 3000 rpm for one minute. The TiO_2:PVP film was then annealed at 80 ºC for 10 minutes in ambient air (Chapter 4.1).

PVP: PVP was dispersed in distilled water with a concentration of 0.07 wt.%. The PVP solution was stirred overnight in air, and a ultrasonication for 30 minutes was performed on the solution. The solution was spin-coated onto ITO at 3000 rpm for one minute. The PVP film was then annealed at 80 ºC for 10 minutes in ambient air (Chapter 4.2).

PEIE: PEIE (80% ethoxylated, Aldrich) was diluted into 2-methoxyethanol (Aldrich) to two different concentrations of 0.1 wt. % (for the CRL of PEIE-modified MoO_X/Ag) and 0.4 wt. % (for all except the CRL of PEIE-modified MoO_X/Ag). The PEIE solution was stirred overnight in air. The solution was spin-coated onto substrates at 5000 rpm for one minute. The PEIE film was then annealed at 100 ºC for 10 minutes in ambient air (Chapter 4.3, 5.1, 5.2, and 5.3).

PEDOT:PSS: Three different PEDOT:PSSs (H.C. Starck, Newton, MA), Clevios™ P VP AI 4083 (4083), Clevios™ PH 1000 (PH1000), and Clevios ™ CPP D105 (CPP) are used in this thesis. Each PEDOT:PSS has its distinctive functions such as conductivity and wettability. The PEDOT:PSS (4083) that has low conductivity ($\leq 10^{-3}$ S/cm) is used for hole-collecting interlayer on top of ITO. The PEDOT:PSS (PH 1000) that has high conductivity ($\approx 10^{3}$ S/cm) is employed as a transparent HCE on a bare glass (Chapter 4.3), or hole-collecting layer in the CRL of the PEIE-modified PEDOT:PSS (Chapter 5.3). The PEDOT:PSS (CPP) that has a good wettability on photoactive layer is used for hole-collecting interlayer and deposited on top of the photoactive layer followed by a metal electrode deposition.

PEDOT:PSS (4083): Prior to depositing PEDOT:PSS (4083), substrates such as SiO_X-patterned ITO-coated glass were first treated with O_2-plasma for 3 min to change the

surface to hydrophilic. Then, PEDOT:PSS (4083) was filtered through a 0.45 μm pore PVDF filter and spin-coated in air at 5000 rpm for 60 s. The substrates were then annealed for 10 min at 140 °C (Chapter 3.1).

PEDOT:PSS (CPP): PEDOT:PSS (CPP) was spin-coated in air at 2000 rpm for 45 s without any filtration. The substrates were then annealed for 10 min at 120 °C (Chapter 4.1 and 4.2).

PEDOT:PSS (PH 1000): PEDOT:PSS (PH 1000), substrates such as a glass, or a PES, and the bottom cell with photoactive layer were first treated with O_2-plasma for 5 sec and 1 sec, respectively, to change the surface to hydrophilic. Then, PEDOT:PSS (PH 1000) was filtered through a 0.45 μm pore PVDF filter and spin-coated in air at 5000 rpm for 60 s. The substrates were then annealed for 10 min at 110 °C (Chapter 4.3 and 5.3).

Mixed PEDOT:PSS (PH1000 + CPP, 3/1, v/v): PEDOT:PSS (PH 1000) and PEDOT:PSS (CPP) were blended and stirred overnight in air. Then, the mixed one was spin-coated in air at 1000 rpm for 30 s without any filtration. The substrates were then annealed for 10 min at 110 °C (Chapter 4.3).

The chemical structures of the materials used for the charge-collecting interlayers or electrodes are shown in Figure 2.2.

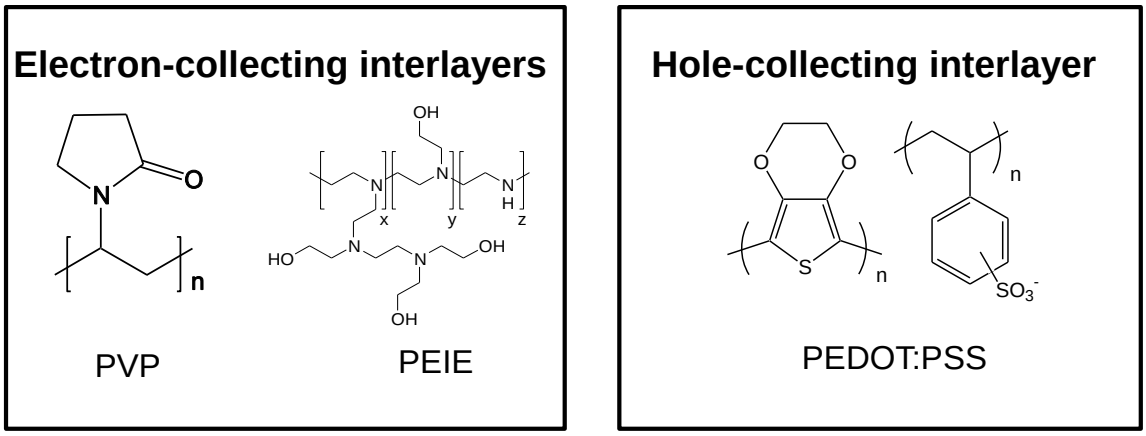

Figure 2.2 Chemical structures of electron- and hole-collecting interlayers used in this dissertation.

2.2.2.2 Atomic Layer Deposition (ALD)

The second deposition method is ALD (Savannah 100, Cambridge NanoTech, Cambridge). For this thesis, ALD was used for depositions of charge-collecting interlayers (ZnO and NiO) and CRL (Al_2O_3:ZnO nanolaminate). ALD uses sequential gas-phase chemical reaction. Due to its self-limiting and surface reaction characteristics, ALD can offer well-controlled layer-by-layer growth of highly conformal and uniform films. The thickness of the films deposited by ALD can be controlled at the nanometer scale by changing the number of deposition cycles. Also, since the ALD can be run in relatively low temperatures, temperature-limited substrates can be used [67]. In addition, high-speed ALD techniques have advanced to achieve deposition rates up to 1.2 nm/s, improving the industrial viability of this technology [125].

Figure 2.3 illustrates an ALD cycle for ZnO deposition. Si was used here as a substrate. One cycle of ZnO in the ALD system comprised sequential pulses of H_2O and

diethylzinc (DEZ) precursors injected into the ALD reactor, utilizing nitrogen as a carrier gas. First, a pulse of H_2O was injected into the ALD reaction chamber, utilizing nitrogen as a carrier gas, and adsorbed on the Si surface, forming hydroxyl group (-OH). Next, a diethylzinc (DEZ) precursor was introduced into the ALD reactor using the same carrier gas and chemisorbed on the hydroxylated Si surface, forming a uni-ethylzinc ($–ZnC_2H_5$). Because the DEZ does not react with itself, this process was finished with one layer formation. Then, the excess DEZ and reaction product (ethane, C_2H_6) were removed by inert nitrogen gas. Again, a pulse of H_2O was injected into the ALD reaction chamber and reacted with the dangling ethyl group. This reaction created a hydroxyl surface group on Zn as well as a Zn-O bridge. Also, the excess H_2O and the reaction product were pumped away by the nitrogen gas. This sequential process made one atomic layer, and the films could be made to the desired thickness by repeating this process [126]. The ZnO layer formed on the ITO substrate was made following the same process described above (Chapter 4.2).

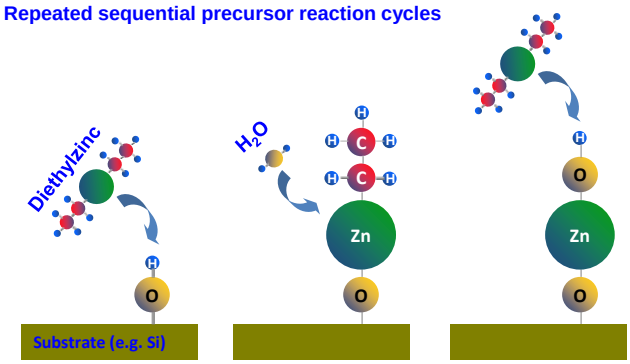

Chemical reaction for ZnO formation with diethylzinc and H_2O

$ZnOH + Zn(CH_2CH_3)_2 \rightarrow ZnOZn(CH_2CH_3) + CH_3CH_3$

$Zn(CH_2CH_3) + H_2O \rightarrow ZnOH + CH_3CH_3$

Figure 2.3 An illustration for ZnO formation by ALD and chemical reactions. (This figure was drawn by Hyeunseok Cheun)

The ALD process of NiO and Al_2O_3:ZnO nanolaminate was similar to that of ZnO but used slightly different conditions with different precursors. The detailed processing conditions for NiO and Al_2O_3:ZnO nanolaminate employed in this thesis are as follows.

NiO: NiO layers of three different thicknesses (6, 13, and 25 nm) were deposited by ALD. One cycle of NiO in the ALD system comprised sequential pulses of H_2O (15 ms pulse) and Ni-AMD (Nickel Alkyl Amidinate) (750 ms pulse) precursors injected into the ALD reactor, utilizing nitrogen as a carrier gas at a temperature of 150 °C. (Chapter 3.1).

Al_2O_3:ZnO nanolaminate: 10-nm-thick Al_2O_3:ZnO (1:20, 84 cycles) nanolaminate was deposited by ALD. One cycle of Al_2O_3 in the ALD system comprised sequential pulses of H_2O (15 ms pulse) and trimethylaluminum (15 ms pulse) precursors injected into the ALD reactor, utilizing nitrogen as a carrier gas at a temperature of 150 °C. One cycle of ZnO was made up of H_2O (15 ms pulse) and DEZ (15 ms pulse) pulse precursors. Finally, 10-nm-thick Al_2O_3:ZnO nanolaminate film was deposited with a series of ZnO cycles with interspersed Al_2O_3 cycles incorporated at a 1:20 ratio (Al_2O_3:ZnO) (Chapter 5.2).

2.2.2.3 Thermal Evaporation

The last deposition method used in this thesis was thermal evaporation (SPECTROS, Kurt J. Lesker). In this thermal evaporation system, the substrates and source materials were loaded in a chamber. Next, the chamber was pumped down to the proper vacuum level. Under vacuum, the source material contained in a crucible was heated until it was evaporated or sublimed. The evaporated particles traveled directly to the substrate. Deposition rate was controlled by applied power on the source crucible, and the thickness of the deposited film was monitored by quartz crystal microbalances. To pattern the deposited film, shadow masks were used.

The SPECTROS is a computer-controlled physical vacuum deposition (PVD) system. Conditions for deposition of individual materials such as deposition rate, base pressure, deposited layer thickness, etc., were recorded into a recipe and programmed for automatic deposition process. The SPECTROS was connected to an N_2-filled glove box from MBRAUN Company. This direct accessibility from the N_2-filled glove box protected the OSC from exposure to ambient air, which could cause performance degradation. The SPECTROS used a cryopump for high vacuum and roughing, and regeneration was conducted with a rotary vane pump. The base pressure for all deposition was lower than 1×10^{-7} Torr.

The SPECTROS system was equipped with two metal sources and four organic sources. For this thesis, only the metal sources were used for charge-collecting interlayers and metal electrodes. For use of a new crucible, the new empty crucible was baked at high temperature before loading metal sources to avoid contamination. Two metal sources were loaded in separated crucibles and evaporated. A shadow mask close to the substrate was employed to define a pattern in the deposited layers. The substrates were rotated during the film deposition to improve the uniformity. In this thesis, seven materials, Ca (Chapter 3.1), Al (Chapter 3.1), MoO_X (Chapter 4, 5), and Ag (Chapter 4, 5), phthalocyanine (CuPc) (Chpater 4.2), C_{60} (Chpater 4.2), bathocuproine (BCP) (Chpater 4.2) were deposited with a deposition rate around 1.0 Å/s.

2.3 Characterization

2.3.1 Thin Film Characterizations

The energy levels of the conductors and semiconductors reported in this dissertation were measured by Kelvin Probe (Besocke Delta Phi, with a probe diameter of around 3 mm) in air, and by UV photoelectron spectroscopy (UPS) and inverse photoemission spectroscopy (IPES) in ultra-high vacuum.

A Kelvin probe that measures the contact potential difference between surfaces of two conductors was used for WF measurements. For this Kelvin probe method, two conductors are brought into close proximity, but without electrical contact between the surfaces of the two conductors, like in a parallel plate capacitor. One of the conductors is vibrated with a certain frequency (ω). This periodic vibration induces a change in the distance between the two surfaces and results in AC current *i(t)* given by,

$$i(t) = V_{CPD}\omega\Delta C\cos(\omega t) \tag{2.1}$$

due to changes in capacitance (ΔC). To measure the CPD, an additional voltage having a polarity opposite that of the voltage induced by the CPD is applied between the two conductors until the *i(t)* equals zero. Also, it should be noted that true WF measurements need a reference with a known WF because the Kelvin probe can only measure the CPD [127]. For this dissertation, Kelvin probe measurements were done on three spots separated by ~1/2 inch and distributed across a 1×1 inch^2 substrate. Average values and standard deviations were generated over these spots. A highly ordered pyrolytic graphite (HOPG) sample with a WF of 4.5 eV was used as the reference sample.

UPS and IPES provided information on the energy distribution of occupied (IE: occupied states maximum) and unoccupied states (EA: unoccupied states minimum) at the surface of materials, respectively [128]. The UPS and IPES measurements in this dissertation were performed at Princeton University.

Figure 2.4 describes simplified processes of UPS and IPES. In the case of the UPS, information on the occupied states of the materials can be extracted from the analysis of kinetic energy spectra of photoelectrons emitted by materials that have absorbed UV photons. For the UPS measurements in this dissertation, a He I (21.22 eV) radiation line from a discharge lamp was used with an experimental resolution of 0.15 eV. It is worth mentioning that the UV illumination from the UPS lamp has been shown to cause variations of the WF of metal oxides, such as ITO, when continuously exposed for long periods of time. Exposure to UV light from the UPS lamp was minimized by exposing ITO-containing samples for only a very short period of time, and the results were confirmed by measuring several independent ITO samples. This effect was negligible on other substrates.

In case of the IPES, information on the unoccupied states of the materials can be obtained from the detection of emitted photon energy spectra when electrons are injected into high-lying (top) unoccupied states decay to low-lying (bottom) unoccupied states. For this dissertation, IPES was carried out in the isochromat mode, with a resolution of 0.45 eV [128]. UPS and IPES measurements were repeated two or three times per sample. The Fermi level reference was established by UPS and IPES measurements using an air-exposed Au surface.

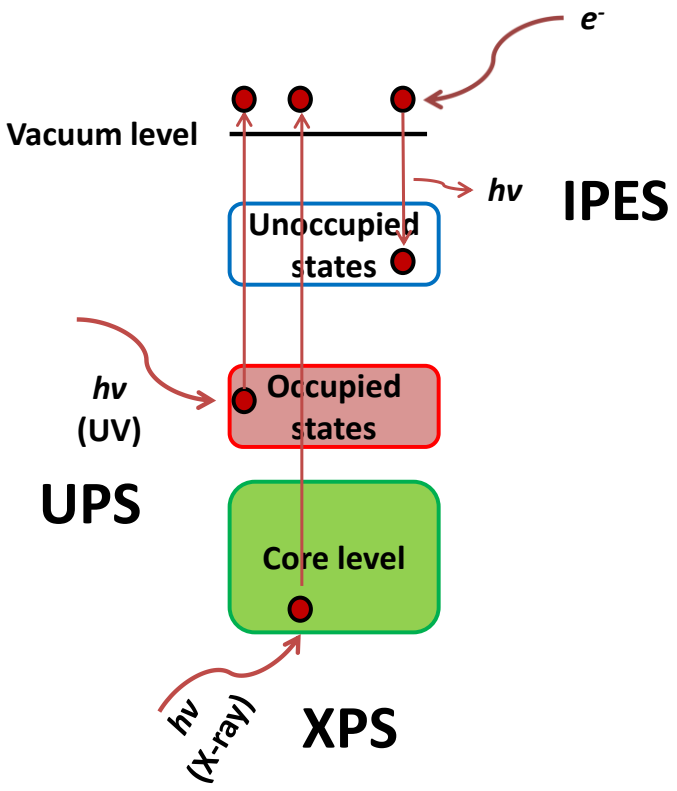

Figure 2.4 Simplified processes of UPS, IPES, and XPS measurements.

Besides these two photoemission spectroscopies, another photoemission spectroscopy is x-ray photoemission spectroscopy (XPS). XPS is a surface chemical analysis technique. For this dissertation, XPS (K-Alpha, Thermo Scientific) measurement was conducted to confirm the presence of each surface component by detecting the core levels of each component. A simplified process of XPS is illustrated in Figure 2.4. A basic mechanism for obtaining data (photoemission spectra) of XPS is similar to that of UPS. However, photons with larger energy (x-ray) than photons used in UPS (UV) are used in XPS. For this dissertation, an XPS system implemented with an Al K-alpha monochromatic source of photons with an energy of 1486.6 eV and a spot size of 300 μm was utilized to study the surface composition of ECEs, HECs, and CRLs.

Thicknesses and refractive indexes of films, including HCEs, ECEs, and photoactive layers, were derived from spectroscopic ellipsometry (J. A. Woollam Co., Inc.) data taken at incidence angles of 65°, 70° and 75°. Spectroscopic ellipsometry traces the evolution of polarization of light that reflects or transmits from a material. The change in polarization is derived from the optical properties and thickness of the material. Thus, such material properties as refractive indexes and thickness of the material can be derived from the spectroscopic ellipsometry [129]. In this dissertation, the data from spectroscopic ellipsometry were modeled by considering a single-layer model (without surface roughness) and Cauchy refractive index dispersion characteristics.

Surface morphology of films, including HCEs, ECEs, CRLs, and photoactive layers, was examined by atomic force microscopy (AFM). The basic operating principles of AFM are that a cantilever with a sharp tip (probe) is scanned over the surface of a sample with feedback mechanisms. These feedback mechanisms allow for the piezoelectric scanners to maintain the probe at a constant force to achieve height information, or at a constant height to acquire force information above the surface of the sample. The AFM can be operated in many different modes, depending on the application. Generally, modes for imaging the surface of a sample are divided into contact mode, non-contact mode, and tapping mode [130]. For this dissertation, the AFM (Dimension 3100, Veeco) studies were carried out using a MultiMode AFM equipped with a NanoScope III controller.

2.3.2 Device Characterization

2.3.2.1 Current Density - Voltage (*J*-*V*) Characterization

The J-V characteristics in the dark and under illumination of all OSCs discussed in this thesis were mainly conducted in an N_2-filled glove box (MBRAUN) using a source meter (2400, Keithley Instruments) controlled by a LabView program. Programs such as OriginLab and Matlab were used for data analysis. A four-wire configuration was adopted for the measurements. Two wires (one pair) were used for applying the current and another two wires (one pair) providing a low current were equipped to detect the voltage.

An AM 1.5 G solar simulator (Oriel 91160, Oriel instruments) with an irradiance of I_L = 100 mW cm^{-2} was used as a light source. For the calibration of the light source, a calibrated Si photodiode (S2386-44K, Hamamatsu) and a thermal detector (PM100, Thorlabs) were employed to estimate the irradiance of the source.

Prior to the electrical characterization, the photoactive areas of the devices were measured either by placing a shadow mask with a single aperture with an area of 0.092 cm^2 onto the glass substrate of the solar cell or by using a microscope for each individual device.

2.3.2.2 External Quantum Efficiency (EQE)

EQE measurements were conducted using a monochromator (CM110, CVI Spectral Products) coupled with 175 W xenon lamp (ASB-XE-175EX, CVI Spectral Products) and a calibrated photodiode (S2386-44K, Hamatsu). The light from the monochromator was passed through a diffuser to spread the light over the entire device and was illuminated through an aperture (size: 0.05 cm^2). To measure the EQE of the tandem OSCs (Chapter 5.2), light bias was used with two different wavelengths, 520 nm

and 750 nm. The current measurement was conducted by using a Keithley 2400 source meter in a four-wire scheme controlled by a LabView program. All EQE measurements were taken in ambient air.

2.3.2.3 Current Density Simulation for Tandem Organic Solar Cell

The absorptance of OSCs was measured and simulated by adjusting the thicknesses of individual layers using the transfer matrix method; a breakdown of the contribution to the total absorptance of each layer in the solar cell structure was carried out for reference single-junction OSCs with P3HT:$IC_{60}BA$ and PBDTTT-C:$PC_{60}BM$ using the transfer matrix method. The absorptance of the photoactive layer, $A_{PL}(\lambda)$ *(PL: photoactive layer)*, was multiplied by the spectral photon solar irradiance (AM 1.5G), $S_{AM1.5}(\lambda)\left[photons \cdot cm^{-2} \cdot s^{-1} \cdot nm^{-1}\right]$, and its product integrated spectrally. The internal quantum efficiency (*IQE*) was then approximated as a constant given by:

$$IQE = \frac{J_{SC,measured}}{e\int A_{PA}(\lambda)S_{AM1.5G}(\lambda)d\lambda} \tag{2.2}$$

where $J_{sc,measured}\left[A \cdot cm^{-2}\right]$ represents the average measured short circuit current and *e* is the elementary charge. In this way, IQE values of 0.61 and 0.86 were estimated for two OSC with structures of ITO/PEIE/P3HT:$IC_{60}BA$/MoO_X/Ag and ITO/PEIE/PBDTTT-C:$PC_{60}BM$/MoO_X/Ag, respectively. For tandem OSCs, the following expression was employed to estimate the J_{SC} in each subcell:

$$J_{SC,PAx} = e\int IQE_{PAx}A_{PAx}(\lambda)S_{AM1.5G}(\lambda)d\lambda \tag{2.3}$$

The J_{SC} of the tandem solar cell was taken as the minimum value between $J_{SC,AL1}$ and $J_{SC,AL2}$

CHAPTER 3

HOLE-COLLECTING INTERLAYERS

Previously, the roles of the charge-collecting interlayers in OSCs were introduced. In this chapter, the photovoltaic properties of OSCs with the conventional geometry using a hole-collecting interlayer, NiO processed by ALD will be discussed. First, various thicknesses (6-, 13-, and 25-nm-thick) of NiO layers were made on glass/ITO substrates. Next, electrical, optical, morphological properties of the NiO layers were characterized to see their viability as hole-collecting interlayer. Finally, the photovoltaic properties of P3HT:$IC_{60}BA$-based OSCs with a NiO layer were evaluated and compared with those of reference OSCs with PEDOT:PSS-coated glass/ITO as a hole-collecting electrode.

3.1 Nickel Oxide (NiO) as The Hole-collecting Interlayers

3.1.1 Introduction

Polymer-based OSCs, referred to as polymer solar cells (PSCs), are commonly composed of a bulk heterojunction photoactive layer sandwiched by a HCE and an ECE. As discussed in Chapter 1.4.7., to enhance the charge collection efficiency and maximize a V_{OC} of PSCs, a large WF contrast between the HCE and ECE is required. To optimize the photovoltaic performance of PSCs with the conventional geometry, the PSCs commonly have ECEs made of reflective and low-WF metals such as LiF/Al and Ca/Al at the top of the PSC. Also, they have HCEs composed of transparent high-WF components such as ITO generally modified with high-WF interlayer such as PEDOT:PSS at the bottom of the PSCs [47].

One candidate for a hole-collecting interlayer in PSCs is NiO. Stoichiometric NiO is known as an insulator with room temperature conductivity on the order of 10^{-13} S/cm. The conductivity of the NiO can be increased by p-doping with lithium (Li) or by the existence of nickel vacancy or interstitial oxygen in the NiO crystallite. P-type NiO is also a wide E_G (3.6 eV- 4.0 eV) semiconductor [57,131,132]. In recent reports, Irwin *et al.* and Steirer *et al.* showed PSCs with a NiO as the hole-collecting interlayer [41,57,132]. The NiO layers were made either by pulsed laser deposition (PLD) or spin coating; a WF value of 5.0 eV was found in both cases. PSCs with NiO hole-collecting interlayers yielded comparable photovoltaic performance to PSCs containing PEDOT:PSS interlayers but showed enhanced device air stability.

In this chapter ALD-processed NiO films are introduced as a hole-collecting interlayer in PSCs. As mentioned in Chapter 2, the ALD is suitable method for fabricating the charge-collecting interlayer of PSCs. It can offer well-controlled layer-by-layer growth of highly conformal and uniform films. Also, the thickness of the layer deposited by ALD can be controlled at the nanometer scale by changing the number of deposition cycles [67]. In this chapter, the structural, morphological, and optical properties of the ALD processed NiO were investigated by XPS, AFM, and spectroscopic ellipsometry. Optimized PSC composed of a P3HT:$IC_{60}BA$ photoactive layer and using an ITO/NiO HCE are shown to yield a PCE of 4.1 ± 0.2 % under a 100 mW/cm^2 AM 1.5G solar illumination.

3.1.2 NiO Layer Characterization

NiO films were found to grow at an average rate of 0.05 ± 0.01 nm/cycle on Si substrates. One cycle includes one pulse of H_2O and one pulse of AMD. The WF of the HCEs comprised by NiO-coated ITOs was studied with a Kelvin probe in air using different thicknesses of the NiO layer. The WF of a pristine 25 nm-thick NiO film

deposited on an ITO substrate had an initial value of 4.7 ± 0.05 eV and increased to a value of 5.4 ± 0.02 eV after a 3 min O_2-plasma treatment. NiO-coated ITO substrates with 6-nm and 13-nm-thick NiO layers exhibited similar WF values of 5.3 ± 0.02 eV and 5.3 ± 0.03 eV, respectively, after the 3 min O_2-plasma treatment. The value of the WF of bare ITO was 4.6 ± 0.02 eV. Figure 3.1 summarizes the WF values from different thicknesses of NiO layer on ITO and a bare ITO.

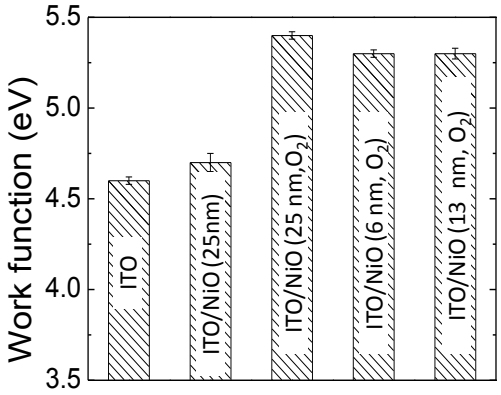

Figure 3.1 Work function values of a bare glass/ITO substrate, and pristine 25 nm-thick NiO films, O_2-plasma treated 25 nm-thick NiO films, O_2-plasma treated 13 nm-thick NiO films, and O_2-plasma treated 6 nm-thick NiO films on a glass/ITO substrate by a Kelvin probe.

XPS measurements were conducted on 25 nm-thick NiO film (as-deposited and with a 3 min O_2-plasma treatment) and bare ITO. It should be noted that the 25 nm-thick NiO films were selected for the XPS analysis because, as will be discussed later, they show PSCs with the best performance.

A comparison of an XPS survey from bare ITO and 25-nm-thick NiO coated ITOs (as-deposited and with O_2-plasma treatment) is shown in Figure 3.2(a). The high resolution XPS spectra of the O 1s and Ni 2p core levels of bare ITO and 25-nm-thick NiO coated ITOs (as-deposited and with O_2-plasma treatment) are shown in Figure 3.2

(b). The peaks above 850 eV (Ni 2p) clearly indicate presence of NiO on ITO. The complete disappearance of the peaks around 450 eV corresponding to In 3d and 490 eV corresponding to Sn 3d confirm that the conformal nature of the NiO layer.

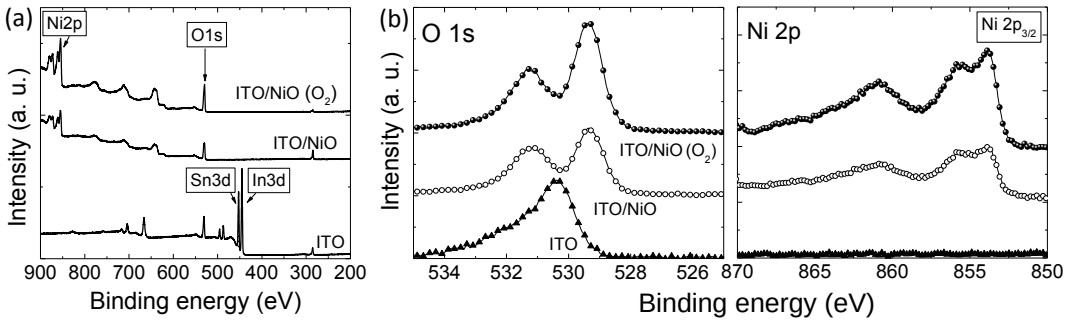

Figure 3.2 (a) A survey of XPS spectra for O_2-plasma treated 25 nm-thick NiO films (top) and pristine 25 nm-thick NiO films (middle) on a glass/ITO substrate, and a bare glass/ITO substrate (bottom), (b) XPS spectra of the O 1s and Ni 2p core levels for O_2-plasma treated 25 nm-thick NiO films (top, closed circle) and pristine 25 nm-thick NiO films (middle, open circle) on a glass/ITO substrate, and a bare glass/ITO substrate (bottom, closed triangle).

High resolution XPS data shown in Figure 3.2(b) also shows that at least two NiO species exist on the ALD-synthesized films, the low binding energy peaks at 853.9 eV (Ni 2p) and at 529.4 eV (O1s) correspond to the more abundant Ni^{+2} (NiO) [133,134] and the higher binding energy peaks at 855.6 eV(Ni 2p) and at 531.3 eV (O1s) corresponding to a less abundant species, likely corresponding to nickel hydroxide ($Ni(OH)_2$) [134] rather than commonly ascribed Ni_2O_3 [133]. The existence of ($Ni(OH)_2$) peaks around 855.6 eV can be related with the chemisorption of water from air or from unreacted hydroxylated Ni sites during the NiO deposition. Furthermore, the peaks near 280 eV indicate the presence of carbonaceous species on the surface of both ITO and as prepared ITO/NiO. Greiner *et al.* claimed that these $Ni(OH)_2$ and carbonaceous species on the surface of the as-deposited NiO film correlated with a significant WF reduction of the NiO films (6.73 eV to 5.5 eV, in air-exposed films, measured by UPS) [134]. Upon 3 min

O_2-plasma treatment, intensity of both $Ni(OH)_2$ and carbonaceous peaks were reduced and the NiO peaks in vicinity of 853.9 eV became even more dominant at the surface of the film. Thus, the measurable decrease of the strength of the $Ni(OH)_2$ and carbonaceous peaks made by the O_2-plasma treatment can explain the observation of the WF increase of the pristine NiO films after O_2-plamsa treatment.

In addition, the WF increase by the O_2-plamsa treatment can be attributed to p-doping. According to previous photoemission spectroscopy studies on solution-processed NiO films conducted by Steirer *et al*, the O_2-plasma treatment increased the IE and Fermi levels of the NiO layer linearly while it left the electron affinity constant. While the energy level difference between the IE and the E_F of the NiO remains unchanged before and after O_2-plasma treatment, the increase in the band gap after the O_2-plasma treatment can arise from p-doping of the NiO layer. Even though energy levels such as IE and EA have not been measured here, this effect cannot be ruled out by this study[132].

Figure 3.3 displays the complex refractive index of NiO derived after spectroscopic ellipsometric measurements on O_2-plasma treated 25 nm-thick NiO films coated glass/ITO substrates.

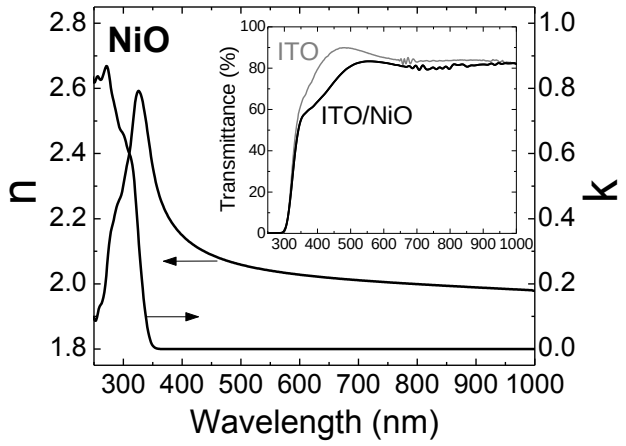

Figure 3.3 Refractive index and extinction coefficient of O_2-plasma treated 25 nm-thick NiO films on glass/ITO substrate. The inset shows optical transmission of O_2-plasma treated 25 nm-thick NiO films on a glass/ITO substrate (black) and a bare glass/ITO substrate (grey).

An E_G of 3.7 eV (335 nm) was extracted from these measurements. This value is in good agreement with literature values [133]. A comparison of the transmittance between the 25-nm-thick NiO-coated glass/ITO and bare glass/ITO is shown in the inset of Figure 3.3. As revealed by the optical extinction coefficient spectra, $k(\lambda)$, ALD NiO films display negligible absorption above 350 nm. Hence, reduced transmittance of the 25-nm-thick NiO-coated glass/ITO can be ascribed not to absorption loss from the NiO layer, but to the optical interference effects resulting in an increased reflectance.

To examine the surface morphology, ITO and 25-nm-thick NiO-coated ITO films were studied by AFM. Figure 3.4 shows AFM images of a bare glass/ITO substrate (Figure 3.4 (a)) and 25-nm-thick NiO-coated glass/ITO substrates, before (Figure 3.4(b)) and after O_2-plasma treatment (Figure 3.4(c)). The root-mean squared (RMS) surface roughness values derived from these images, with an area of 0.25 μm^2, in layers of glass/ITO, 25-nm-thick NiO-coated glass/ITO substrates (as-deposited), and 25-nm-thick NiO-coated glass/ITO substrates (with 3 min O_2-plasma treatment) are 4.7 nm, 4.4 nm, and 4.0 nm, respectively. As it is clear from these images, no significant changes related to the grain size and the film roughness between glass/ITO and NiO-coated glass/ITO were found.

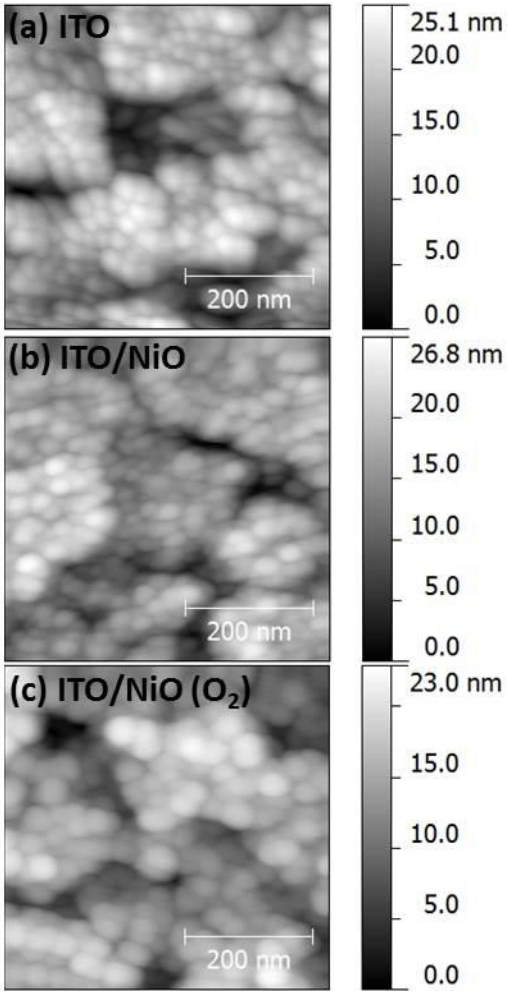

Figure 3.4 AFM images (height) of (a) a bare glass/ITO substrate, (b) 25 nm-thick NiO films on a glass/ITO substrate, and (c) O_2-plasma treated 25 nm-thick NiO films on a glass/ITO substrate.

3.1.3 Characterization of Solar Cells Performance

To evaluate photovoltaic performance of PSCs with 25-nm-thick NiO-coated glass/ITO as the HCE, PSCs with the structure of glass/ITO/NiO/P3HT:$IC_{60}BA$/Ca/Al were fabricated as shown in figure 3.5(a). PSCs with glass/ITO only shown in Figure 3.5(b), PEDOT:PSS-coated glass/ITO displayed in Figure 3.5(c), and different thicknesses (6 nm and 13 nm) of NiO-coated on the glass/ITO but using the same

photoactive layer and ECE were also fabricated to compare their photovoltaic performance.

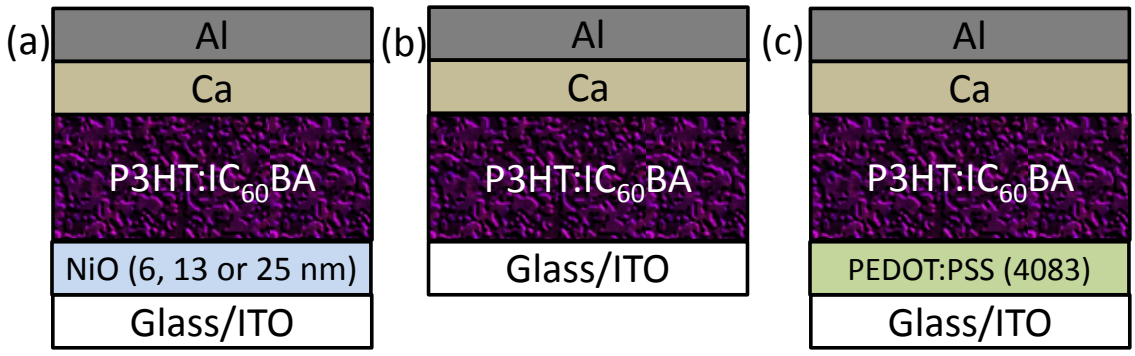

Figure 3.5 Device structures of conventional P3HT:$IC_{60}BA$ solar cells with (a) ITO/NiO, (b) ITO only, and (c) ITO/PEDOT:PSS as the hole-collecting electrodes.

Figure 3.6(a) shows a comparison between the *J-V* characteristics under illumination measured in PSCs with O_2-plasma treated NiO layers with different thicknesses. The PSCs with the 25-nm-thick NiO layer yielded V_{OC} of 827 ± 8 mV, J_{SC} of 7.4 ± 0.2 mA/cm^2, FF of 0.67 ± 0.03, and PCE of 4.1 ± 0.2 %. The PSCs with 6-nm-thick and 13-nm-thick NiO-coated glass/ITO showed slightly lower V_{OC} values (746 ± 17 mV from 6-nm NiO and 753 ± 9 mV from 13-nm NiO) and FF values (0.64 ± 0.01 from 6-nm NiO and 0.64 ± 0.02 from 13-nm NiO). These lower values might be attributed to the non-conformal coverage of NiO on ITO. Such non-conformal coverage leads to a spatial distribution of areas with higher (NiO-coated) and lower (bare ITO) WF values across the surface. Despite the apparently similar WF values from the different thickness of the NiO layers, locally, the nanometer scale areas with lower WF will provide poor energy-level alignment with the IE of P3HT and consequently will result in a reduced V_{OC} and FF [79]. Additionally, the PSCs having ITO-only HCE showed lower V_{OC} and FF values than those of 25-nm-thick NiO_X-coated ITO HCE. This poor photovoltaic performance arises from the small WF value of ITO compared with NiO.

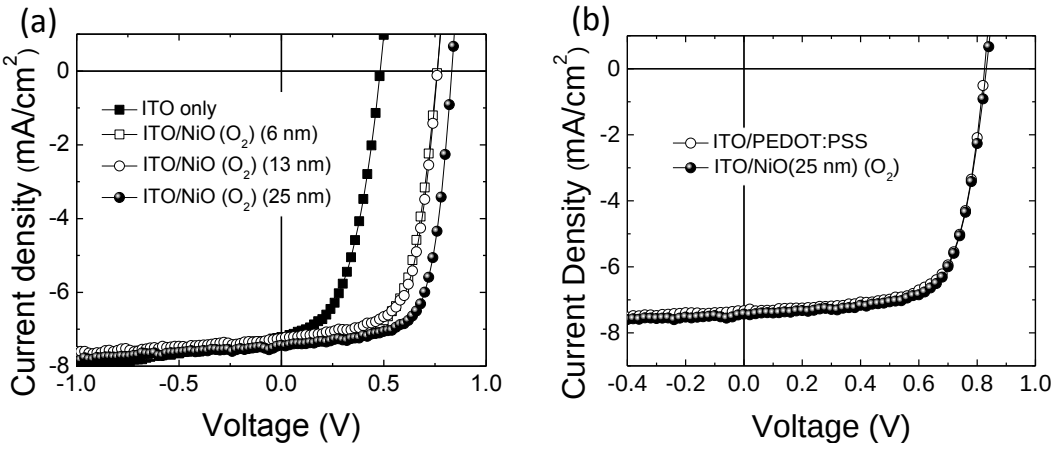

Figure 3.6 Representative *J-V* characteristics under illumination for a P3HT:$IC_{60}BA$-based polymer solar cell with hole-collecting electrodes of (a) ITO only (closed square) and O_2-plasma treated 6-nm-thick (open square), 13-nm-thick (open circle), and 25-nm-thick (closed circle) NiO-coated ITO, (b) PEDOT:PSS-coated ITO (open circle) and O_2-plasma treated 25-nm-thick NiO-coated ITO (closed circle).

Figure 3.6(b) shows a comparison of the *J-V* characteristics of PSCs with O_2-plama treated 25-nm-thick NiO-coated glass/ITO and the widely used HCE, PEDOT:PSS-coated glass/ITO. The latter showed an V_{OC} of 829 ± 6 mV, J_{SC} of 7.2 ± 0.3 mA/cm^2, FF of 0.70 ± 0.01, and PCE of 4.2 ± 0.1 %. This comparison reveals that the NiO_X-coated glass/ITO yields comparable hole collection to the PEDOT:PSS-coated glass/ITO.

Figure 3.7(a) presents photovoltaic performances of the PSC with 25-nm-thick NiO-coated glass/ITO before and after 3 minute of O_2-plamsa treatment. Without O_2-plasma treatment, the PSCs showed poor *J-V* characteristics with a PCE of 0.4 ± 0.1 %. However, the PCE increased appreciably (more than 10 times) when the NiO film was O_2-plasma treated. Interestingly, the values of J_{SC} (4.2 ± 1.3 mA/cm^2) and FF (0.21 ± 0.02) of the PSCs with a 25-nm-thick NiO-coated glass/ITO without O_2-plasma treatment are lower than those from PSCs using only ITO while both V_{OC} values are in a similar

range. Similar V_{OC} values are consistent with comparable values of WF measured in both types of HCEs (ITO/NiO: 4.7 ± 0.05 eV and ITO: 4.6 ± 0.02 eV). However, the lower FF and J_{SC} obtained in PSC with pristine NiO could be related its low conductivity.

To probe more in depth the conductivity issues, R_SA values from the PSCs with 25-nm-thick NiO-coated glass/ITO before and after 3 minute of O_2-plamsa treatment were extracted from *J-V* characteristics of the devices by fitting the equivalent circuit model (Eq. 1.8, rewritten in below) to experimental data. To compare the O_2-plasma treated NiO with the PEDOT:PSS, a R_SA value of the PSC with PEDOT:PSS was also extracted.

$$J = \frac{1}{1 + R_S / R_P}\left[J_0 \left\{ \exp\left(\frac{V - JR_S A}{nkT / e} \right) - 1 \right\} - \left(J_{ph} - \frac{V}{R_P A} \right) \right] \tag{3.1}$$

where R_S is the series resistance, R_P is the shunt resistance, J_0 is the reverse saturation current density, A is the device area, e is the elementary charge, k is the Boltzmann's constant, T is the temperature, n is the ideality factor of the diode, and J_{ph} is the photo current density. It should be noted that the R_SA values were obtained from the champion devices in all cases. The extracted R_SA values from the PSCs before and after the O_2-plamsa treatment were 677 Ω cm^2 and 5.4 Ω cm^2, respectively. This large difference in the R_SA values before and after the O_2-plamsa treatment can be attributed to both increased contact resistance caused by energy-level mismatching that induces the increased surface recombination and an increased conductivity of the NiO layer, itself. The increased conductivity leading to improved performance upon O_2-plasma treatment, would be consistent with reports in the literature that indicate that p-doping of NiO occurs upon O_2-plasma treatment [57,132]. Furthermore, the extracted R_SA value from the PSCs with the ITO/PEDOT:PSS HCE was 4.2 Ω cm^2. No big difference in R_SA values between PSCs with the ITO/PEDOT:PSS and ITO/O_2-plasma treated NiO HCEs was observed, as expected from the *J-V* characteristics.

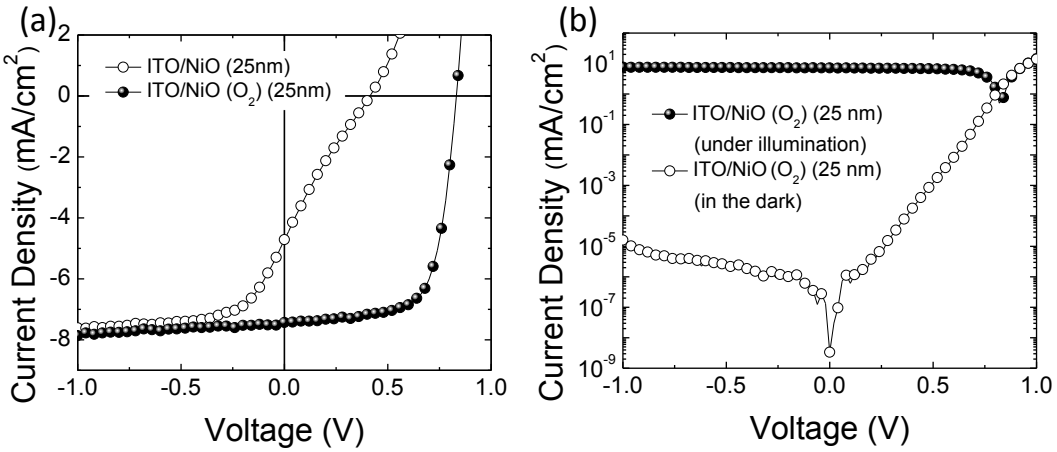

Figure 3.7 Representative *J-V* characteristics under illumination for a P3HT:$IC_{60}BA$-based polymer solar cell with hole-collecting electrodes of (a) pristine 25-nm-thick NiO-coated ITO (open circle) and O_2-plasma treated 25-nm-thick NiO-coated ITO (closed circle), and (b) representative semi-log *J-V* characteristics for a P3HT:$IC_{60}BA$-based polymer solar cell with hole-collecting electrodes of O_2-plasma treated 25-nm-thick NiO-coated ITO under illumination (closed circle) and in the dark (open circle).

Finally, Figure 3.7(b) shows semi-log *J-V* characteristics of the PSCs with the 25-nm-thick NiO-coated glass/ITO HCE in the dark and under illumination. The *J-V* characteristics in the dark reveal an excellent diode rectification and demonstrate a small leakage current. Table 1 summarizes the photovoltaic performance, averaged over five devices, of all PSCs evaluated.

Table 3.1 Summary of the averaged[a] device performance of P3HT:$IC_{60}BA$-based polymer solar cells with bare ITO, O_2-plasma treated 6-, 13-, and 25-nm-thick NiO-coated ITO, bare 25 nm-thick NiO-coated ITO, and PEDOT:PSS-coated ITO as a hole-collecting electrode.

Hole-collecting electrodes	V_{OC} (mV)	J_{SC} (mA/cm^2)	FF	PCE (%)
ITO only	428 ± 34	7.9 ± 0.4	0.49 ±0.01	1.7 ± 0.1
ITO/NiO (6 nm, O_2)	746 ± 17	7.4 ± 0.1	0.64 ± 0.01	3.5 ± 0.1
ITO/NiO (13 nm, O_2)	753 ± 9	7.2 ± 0.2	0.64 ± 0.02	3.5 ± 0.2
ITO/NiO (25 nm, O_2)	827 ± 8	7.4 ± 0.2	0.67 ±0.03	4.1 ± 0.2
ITO/NiO (25 nm)	423 ± 35	4.2 ± 1.3	0.21 ±0.02	0.4 ± 0.1
ITO/PEDOT:PSS	829 ± 6	7.2 ± 0.3	0.70 ±0.01	4.2 ± 0.1

[a] Average was calculated over five devices

3.1.4 Conclusions

A study of the properties of NiO films fabricated by ALD in the context of their use as hole-collecting interlayers in PSCs is described in this chapter. O_2-plasma treated NiO films deposited on ITO display a WF value of 5.4 ± 0.02 eV, allowing NiO-coated ITO to act as an efficient HCE. The PSCs based on P3HT:$IC_{60}BA$ with the O_2-plasma treated NiO-coated ITO HCE yield a PCE of 4.1 ± 0.2 % under simulated AM 1.5G 100 mW/cm^2 illumination, which is comparable to reference devices with PEDOT:PSS-coated ITO HCEs.

The study shown in this chapter provides several new insights into the physical, electrical and optical properties of NiO-coated ITO for PSC applications. All properties of the ALD-processed NiO such as a large WF value, a large E_G of 3.7 eV and the conformal nature of ALD NiO films reflect that the NiO layer is very attractive for use as a hole-collecting interlayer in PSCs. However, to be an efficient HCE, the NiO-coated ITO requires O_2-plasma treatment to increase its WF. The increase in WF of NiO-coated ITO when subjected to an O_2-plasma treatment is correlated with the reduction of strength of peaks of the $Ni(OH)_2$ and carbonaceous species from the surface of the as-

prepared ALD NiO films. In addition, p-doping induced by the O_2-plasma treatment seems to play an important role for the HCE by increasing conductivity of the NiO layer. Moreover, despite the similar WF values of NiO layers of varying thickness, non-conformal coverage induces a spatial distribution of areas with higher (NiO-coated) and lower (bare ITO) WF values across the surface. This non-conformal coverage was found to give detrimental effects such as poor energy-level alignment of the NiO work function with the P3HT ionization potential, resulting in reduced V_{OC} and FF. Based on this study, at least, a 25-nm-thick NiO should be formed on a ITO substrate to serve as an efficient HCE, avoiding the non-conformal coverage effect.

CHAPTER 4

ELECTRON-COLLECTING INTERLAYERS

This chapter will focus on the electron-collecting interlayers for PSCs with inverted geometry. In such inverted structures, the WF of ITO is reduced to a value that is low enough to be used as an electrode-selective layer. Reductions of the WF of ITO have been achieved either by coating its surface with a layer of semiconducting material, typically metal oxides having a lower WF value such as Al_2O_3 [135], ZnO [67,68], TiO_X [64,66], or an alkali metal salt, Cs_2CO_3 [75] generally deposited under vacuum or by spin-coating and post-fabrication thermal treatments, in the case of nano-particles. However, these ITO modification methods require vacuum deposition systems, which may not be compatible with high throughput fabrication methods, or require post thermal treatments at relatively high temperatures, which may not be compatible with flexible substrates. Hence, it is desirable to develop new methods that could be fabricated at lower temperatures, with environmentally friendly solvents and with large throughput fabrication methods.

Polymer-based surface modifiers containing simple aliphatic amide or amine groups, which substantially and universally reduce the WF of conductors including metals, transparent conductive metal oxides, conducting polymers, and graphene will be introduced. The WF reduction by the polymer surface modifiers comes from physisorption of the neutral polymer, which allows the modified conductors as efficient electron-collecting electrodes. These polymer surface modifiers are processed in air from solution, providing an appealing alternative to chemically reactive low−WF metals.

Two polymeric materials will be discussed. The first polymer is a poly(N-vinylpyrrolidone) (PVP). Initially, the PVP was employed as the dispersant of titanium dioxide (TiO_2) nanoparticles. An ITO coated with the TiO_2 nanoparticles dispersed by the PVP served as an ECE of inverted PSCs. However, it was found that the PVP itself can

reduce the WF of ITO. Even though the PVP-modified ITO shows lowered WF than that of a bare ITO, it still required a post treatment such as illumination from an UV-light source or a solar simulator for being used as the ECE of the OSCs. These UV treatments relate to the WF of the ITO and will be also discussed in this chapter.

The second is polyethylenimine (PEI) derivatives. Two different types of the PEI derivatives, PEI ethoxylated (hereon will be referred to as PEIE) and branched PEI (hereon will be referred to as PEI) will be used as the surface modifiers. Despite of the similar WF reduction mechanism to that of the PVP, PEIE and PEI can provide further reduced WF to conductor surface than that from PVP, thus can serve as an efficient ECE without UV post-treatments. The chemical structures of PVP, PEIE, and PEI are shown in Figure 4.1. With this modification, various types of efficient inverted PSCs, including all-plastic solar cells, will be demonstrated in this chapter.

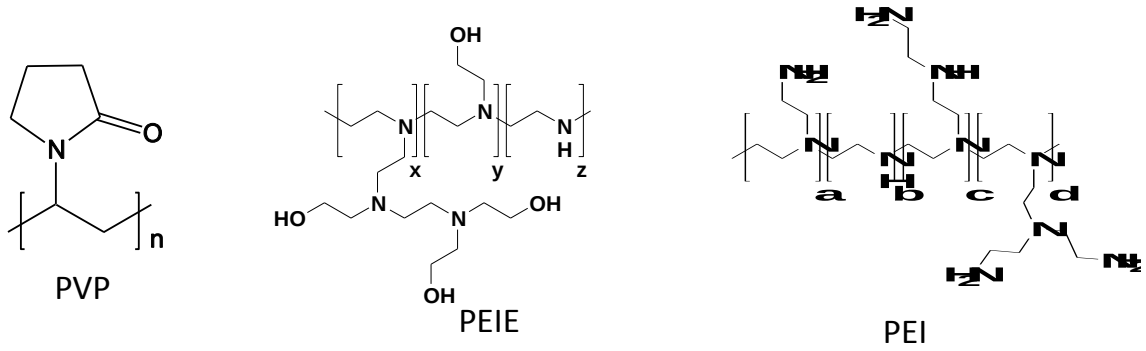

Figure 4.1 Chemical structures of poly (N-vinylpyrrolidone) (PVP), polyethylenimine ethoxylated (PEIE), and branched polyethylenimine (PEI).

4.1 Titanium Dioxide (TiO_2) Nanoparticles Dispersed in Poly (N-vinylpyrrolidone) (PVP) as the Electron-collecting Interlayers

4.1.1 Introduction

Prior to use of PVP as a surface modifier, PVP has been used as a dispersant of the nanoparticles. This section will briefly describe how the dispersant turned into a surface modifier. As mentioned previously, many different materials have been used to form the electron-collecting interlayer in PSCs. Among them, titanium oxide (TiO_2 or TiO_X) has been widely used. Even though titanium oxide has been synthesized from various techniques, such as ALD, sol-gel method, CBD, *etc.*, some of those techniques still require a high temperature sintering process, or a high vacuum process [136].

To avoid these issues, TiO_2 nanoparticle films processed from an aqueous solution at a low-temperature was studied. However, nanoparticles are often aggregated in solution making necessary to add a surfactant to hinder nanoparticle agglomeration. PVP has been known as a good surfactant for dispersing nanoparticles. The TiO_2 dispersion by the PVP begins with grafting the dispersant PVP, which has amphiphilic nature caused by the highly polar amide and non-polar methylene groups, onto the hydrophilic TiO_2 nanoparticles. Namely, the polar group of PVP is adsorbed onto the hydrophilic TiO_2 nanoparticles. Then, the repulsive force created by the surface charge of each nanoparticle prevents them to agglomerate. Recently, a mixture of ZnO nanoparticles and PVP, referred to as ZnO:PVP nanocomposite, was applied to an electron-collecting interlayer and shown to lead to better film uniformity as well as a lower density of defects in the film than those of a ZnO layer [137].

4.1.2 TiO_2:PVP Layer Characterization

Figure 4.2 displays a comparison of AFM topographic images (height images-top, three dimensional images-bottom) from TiO_2 and TiO_2:PVP (1:1 by weight) on ITO/glass substrates.

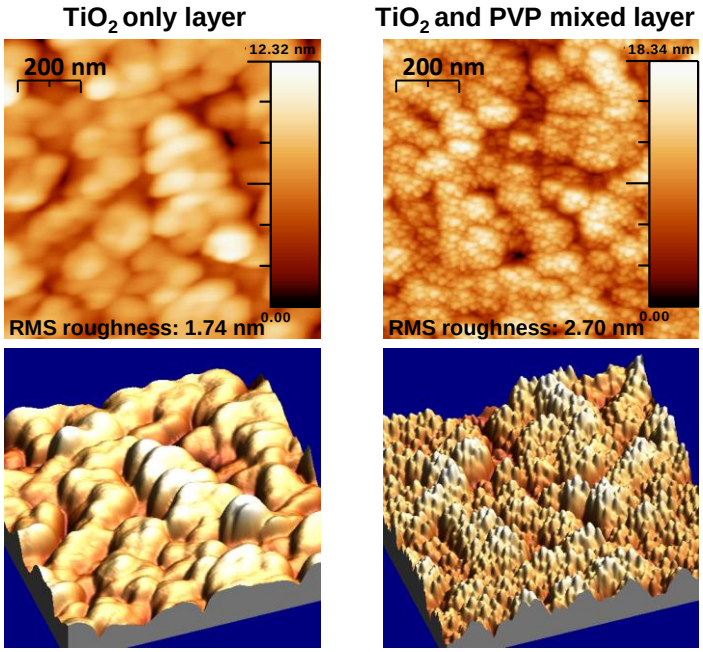

Figure 4.2 AFM images (top: height images, bottom: 3D images) of TiO_2 (left) and TiO_2:PVP (right) on glass/ITO substrates.

A noticeable difference was observed in morphology. Before mixing the TiO_2 nanoparticles with PVP, the dispersant, and TiO_2 nanoparticles stuck together while well-dispersed TiO_2 nanoparticles were found with the use of PVP. WF values from these two substrates were also compared. The WF values of TiO_2-coated and TiO_2:PVP-coated ITO were found to be 4.47 ± 0.02 eV and 4.33 ± 0.02 eV, respectively. A HOPG sample (WF

of 4.5 eV) and a bare ITO (WF of 4.65 ± 0.02 eV) were employed as references. All the WF values were averaged over three points.

XPS measurements were performed on TiO_2:PVP (1:1, by weight (wt.))-coated the glass/ITO substrate to confirm the presence of the each surface component. Samples with specific ratios TiO_2 and PVP were selected for the XPS study because, as will be shown later, they yield PSCs with the best performance. Figure 4.3 show a comparison of the XPS data obtained on a TiO_2:PVP-coated glass/ITO substrate and on a bare glass/ITO substrate. The peaks around 400 eV (N,1S), and 460 eV (Ti,2P), clearly indicate the presence of PVP and TiO_2.

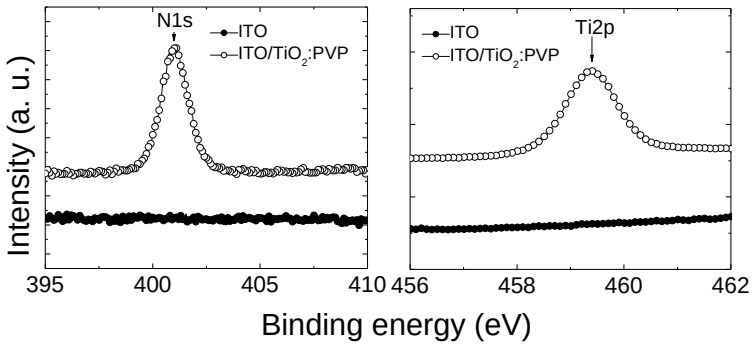

Figure 4.3 XPS spectrum of the N1s and Ti2p core level for ITO and ITO/TiO_2:PVP surfaces.

4.1.3 Characterization of Solar Cells Performance

To investigate the photovoltaic performance of PSCs with ECEs of TiO_2 or TiO_2:PVP-coated ITO/glass, inverted PSCs with device structures of ITO/TiO_2 or TiO_2:PVP/ P3HT:PC_{60}BM/PEDOT:PSS(CPP)/Ag were fabricated. As a reference device, PSCs with ITO-only ECE also made with the same photoactive layer and HCE. The device structures are shown in Figure 4.4. To find the optimum blend ratio between PVP

and TiO_2, PSC devices with ECEs of ITO coated with four different blend ratios PVP:TiO_2: none, 0.5:1 (0.035 wt. %: 0.07 wt.%, total 0.105 wt.% in distilled water), 1:1 (0.07 wt.%:0.07 wt.%, total 0.14 wt.% in distilled water), and 2:1 (0.14 wt.%:0.07 wt.%, total 0.21 wt.% in distilled water) were fabricated.

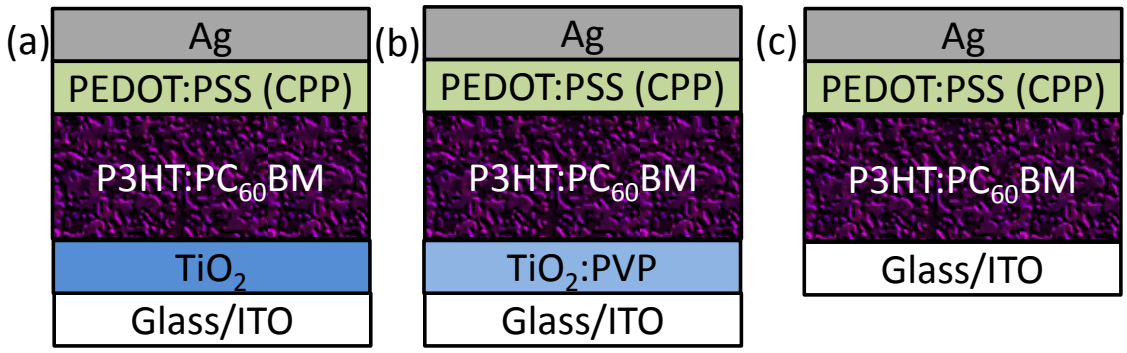

Figure 4.4 Device structures of inverted P3HT:PC_{60}BM solar cells with (a) TiO_2 only, (b) TiO_2:PVP, and (c) ITO only for the electron-collecting electrodes.

Figure 4.5 shows photovoltaic performance parameters of the PSCs, PCE, V_{OC}, and FF as a function of blend ratio between PVP and TiO_2. The parameters were measured after a 25-min treatment of solar simulator (AM 1.5G) irradiation because, as will be shown later, this treatment was found to improve the FF of the inverted PSCs. The photovoltaic performance of the PSCs was enhanced with increasing PVP concentration, up to the ratio of PVP to TiO_2, 1:1, but device performance degraded for the ratio of 2:1. The presence of PVP is found to improve the device performance. Although no major differences are found between devices having PVP/TiO_2 ratios of 0.5:1 and 1:1, a clear decrease in performance is observed for devices with a 2:1 ratio. This decrease in performance may be attributed to the excessive concentration of PVP

which is known to be an insulator. Hereafter, the properties of PSCs with the ECE of the PVP:TiO_2 (1:1) will be discussed.

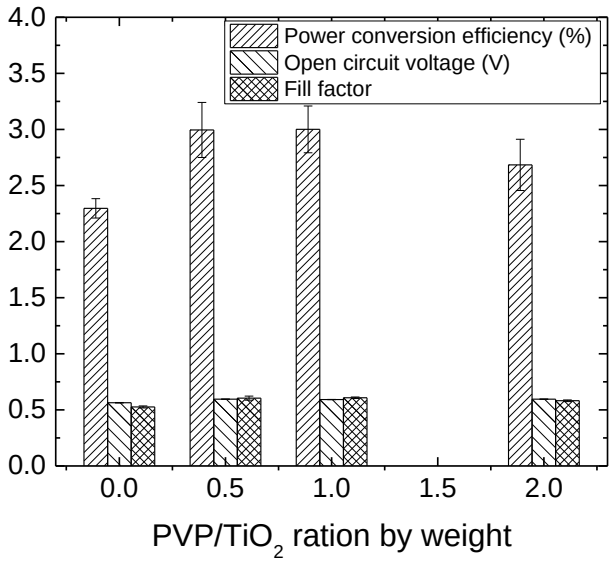

Figure 4.5 PCE, V_{OC}, and FF of inverted P3HT:$PC_{60}BM$ solar cells with ITO/TiO_2:PVP regarding various weight ratios between PVP and TiO_2.

Figure 4.6 shows the *J-V* characteristics of PSC with the ITO/TiO_2:PVP (1:1, by wt.) ECEs before and after the solar simulator treatment. The PSCs before the treatment showed an S-shaped kink in the *J-V* characteristics causing a low FF of 0.37, a small V_{OC} of 490 mV, and a PCE of 1.39 %. These untreated PSCs were subjected to the continuous illumination, inside a N_2-filled glove box, from the solar simulator. The S-shape kink disappeared within 10 minutes of the illumination treatment, and remained unchanged after up to 25 minutes of exposure. After illumination treatment, the PSCs with ECE of ITO/TiO_2:PVP yielded an V_{OC} of 592 ± 1 mV, a J_{SC} of 8.3 ± 0.5 mA/cm^2, a FF of 0.61 ± 0.01 and a PCE of 3.0 ± 0.2 %. Note that an S-shape kink in the *J-V* characteristics of PSCs due to poor charge selectivity of an electrode is often observed. Namely, this

phenomenon is related to increased contact recombination owing to the insufficiently low (high)-WF of electron (hole)-collecting electrode. R_SA values extracted from *J-V* characteristics displayed in Figure 4.6 by fitting them to equivalent circuit model with Eq. 4.1 were 14.7 Ω cm^2 (0 min of exposure), 4.9 Ω cm^2 (2 min), 1.6 Ω cm^2 (5 min), 1.2 Ω cm^2 (10 min), 1.1 Ω cm^2 (20 min), and 1.0 Ω cm^2 (25 min). The reduction of R_SA values depending on the exposure time also reflects the enhanced electron collection by the ECE. That is, the S-shape kink in case of the inverted geometry can disappear after UV or solar simulator treatment that reduces the WF or increase conductivity of ECE. In the section 4.2, this effect will be discussed in detail.

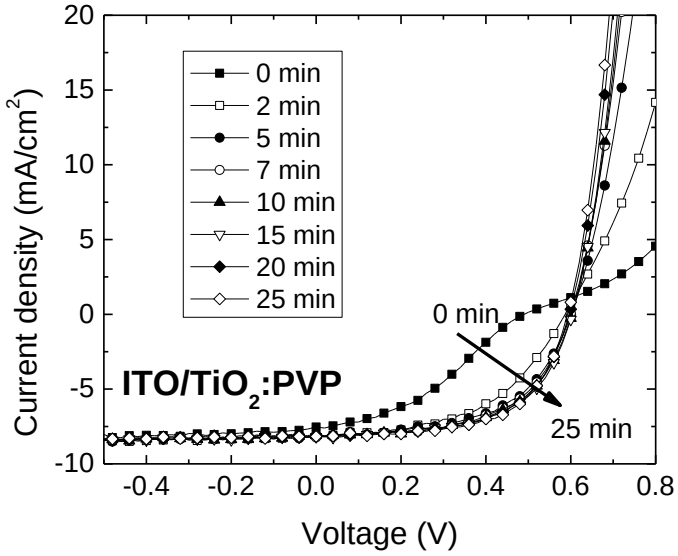

Figure 4.6 *J-V* characteristics under illumination for a P3HT:PC$_{60}$BM-based polymer solar cell with electron-collecting electrodes of ITO/TiO$_2$:PVP cells, as a function of light exposure time.

To confirm the WF reduction after solar simulator treatment, the WF values of all ECEs: ITO/TiO$_2$:PVP, ITO/TiO$_2$, and ITO only were measured before and after solar simulator treatment for 25 minutes. PSCs were exposed to solar simulator illumination

through the glass side (as PSC devices). The measured WF values by a Kelvin probe are summarized in Table 4.1.

The values of the WF (4.33 ± 0.02 eV) obtained from ITO/TiO_2:PVP before the solar simulator treatment seems to be low enough to produce good electron selectivity, given the EA of $PC_{60}BM$ (4.1 eV) [67]. However, it is expected that although the TiO_2:PVP layer appears to be homogeneous on the microscopic scale, it will not likely be fully conformal, and thus areas without TiO_2:PVP on ITO would be exposed. A non-conformal coverage would lead to a spatial distribution of areas with lower (TiO_2:PVP-coated) and higher (bare ITO) WF values across the surface. Therefore, regions with higher WF will offer poor electron-selectivity and consequently will show *J-V* characteristics with an S-shape kink. Upon solar simulator treatment, the electron-selectivity of these areas improves as the WF of ITO decreases, leading to an enhanced electron collection of the entire electrode.

Another interesting observation from these WF measurements is that PVP itself contributes to the WF reduction. The WF values of ITO/TiO_2 and ITO/TiO_2:PVP were found to be 4.47 ± 0.02 eV and 4.33 ± 0.02 eV, respectively. This difference indicates that about 0.14 eV WF reduction can come from the PVP itself. Also, the presence of PVP was confirmed by an XPS study. Although PVP was thought to be solely a dispersant for nanoparticles, its role as a surface modifier to reduce the WF of ITO was discovered on this study.

Table 4.1 Summary of the averaged[a] work function values of ITO only, TiO_2-coated ITO, and TiO_2:PVP (1:1 by weight)-coated ITO before and after solar simulator (AM 1.5G) treatment for 25 minutes.

Electron-collecting electrodes	**Work function (eV) by Kelvin probe**	
	Before treatment	**After treatment**
ITO only	4.65 ± 0.02	4.45± 0.02
ITO/TiO_2	4.47 ± 0.02	4.26 ± 0.02
ITO/TiO_2:PVP	4.33 ± 0.02	3.99 ± 0.02

[a] Average was calculated over three points

To compare the photovoltaic performance among PSCs with TiO_2/PVP-coated ITO electrode, pure TiO_2-coated ITO and bare ITO, two other inverted PSCs with a structure of glass/ITO/TiO_2/P3HT:PC_{60}BM/PEDOT:PSS/Ag and a structure of glass/ITO/P3HT:PC_{60}BM/PEDOT:PSS/Ag were fabricated by following identical processing conditions, with the exception of the electron-collecting interlayers. To make a fair comparison of the above PSCs with those having a TiO_2/PVP-coated ITO electrode, devices were subjected to 25 min of illumination under a solar simulator before measuring its electrical characteristics.

Figure 4.7 displays a comparison of the *J-V* characteristics of the three inverted PSCs, after the solar simulator treatment for 25 minutes under illumination. Table 4.1 summarizes the photovoltaic performances, averaged over five devices, of all the PSCs cells evaluated. The PSCs with ITO only as ECEs showed a V_{OC} of 522 ± 10 mV, a J_{SC} of 7.6 ± 0.2 mA/cm^2, a FF of 0.48 ± 0.01 and a PCE of 1.9 ± 0.1 % while the PSCs with ITO/TiO_2 as ECEs yielded a V_{OC} of 564 ± 2 mV, a J_{SC} of 7.7 ± 0.2 mA/cm^2, a FF of 0.53 ± 0.01 and a PCE of 2.3 ± 0.1 %.

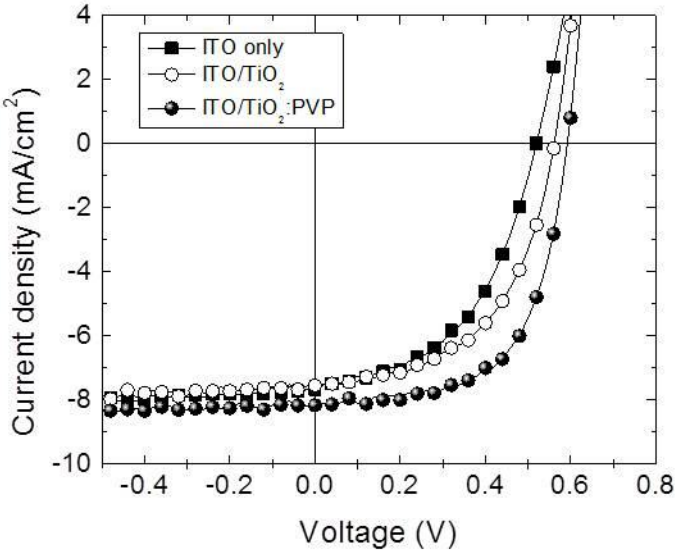

Figure 4.7 Representative *J-V* characteristics under illumination for a P3HT:$PC_{60}BM$-based polymer solar cell with electron-collecting electrodes of ITO only, TiO_2-coated ITO, and TiO_2:PVP(1:1 by weight)-coated ITO.

Table 4.2 Summary of the averaged[a] device performance of inverted P3HT:$PC_{60}BM$ solar cells with ITO only, TiO_2-coated ITO, and TiO_2:PVP (1:1 by weight)-coated ITO as an electron-collecting electrode.

Electron-collecting electrodes	V_{OC} **(mV)**	J_{SC} **(mA/cm^2)**	**FF**	**PCE (%)**
ITO only	522 ± 10	7.6 ± 0.2	0.48 ±0.01	1.9 ± 0.1
ITO/TiO_2	564 ± 2	7.7 ± 0.2	0.53 ±0.01	2.3 ± 0.1
ITO/TiO_2:PVP	592 ± 1	8.3 ± 0.5	0.61 ±0.01	3.0 ± 0.2

[a] Average was calculated over five devices

For PSCs with an ITO only ECE, in the absence of band-bending effects, even after the solar simulator treatment a relatively large energy level mismatch can be expected between the WF of the ITO (4.45 eV) and the EA (4.1 eV) of $PC_{60}BM$ [67].

While these PSCs work, the small value of the FF (0.48) and V_{OC} (522 mV) indicates that the electron-collecting properties of these electrodes is poor when compared with PSCs with the TiO_2:PVP-coated ITO ECE, having a FF of 0.61 and V_{OC} (592 mV). In the case of the PSCs with the TiO_2 layer, there is a slight enhancement in all the photovoltaic parameters of the PSC performance compared to PSC devices with bare ITO ECEs, leading to 20% higher PCE than PSCs with bare ITO ECEs, but the performance is inferior to that of PSCs with the TiO_2:PVP-coated ITO ECEs.

In addition to the use of PVP as a dispersant for TiO_2 nanoparticles, it was observed that PVP also provides an additional contribution to the WF reduction of the TiO_2/PVP-coated ITO ECE. A possibility that the PVP itself can reduce WF of ITO and thus serve as an electron-collecting interlayer was found through this study. A detailed study of the role of PVP as a surface modifier will be presented in the following section.

4.1.4 Conclusions

Although TiO_2 or TiO_X has been used widely as the electron-collecting interlayer in inverted PSCs, synthesizing techniques for the TiO_2 or TiO_X, have shown some issues in their processing conditions (high processing temperature, vacuum process, *etc.*). This study provides a new way to synthesize the TiO_2 nanoparticle films processed from an aqueous solution at a low-temperature in air.

The TiO_2 dispersion by PVP begins with grafting the dispersant PVP, which has an amphiphilic nature caused by the highly polar amide and non-polar methylene groups, onto the hydrophilic TiO_2 nanoparticles. The polar group of PVP is adsorbed onto the hydrophilic TiO_2 nanoparticles.

To achieve well-dispersed TiO_2 nanoparticles in the aqueous solution, the amphiphilic polymer, PVP, was used as a dispersant. The PVP was able to coordinate onto and disperse TiO_2 nanoparticles uniformly in films on top of ITO. More interestingly, the addition of PVP led to even larger reductions of the WF in TiO_2:PVP-coated ITO ECEs compared to TiO_2-coated ITO ECEs. Even though the PVP was believed to solely be a dispersant for nanoparticles, its new role as a surface modifier to reduce the WF of ITO was discovered from this study.

The TiO_2:PVP-coated ITO ECE was found to show good electron-collecting properties in inverted PSCs, after being exposed to light from a solar simulator for 10 min. The solar simulator treatment was shown to lead to reduction of the WF of ITO, TiO_2-coated ITO and TiO_2:PVP-coated ITO electrodes. The need for the solar simulator treatment prior to optimum device operation may be related to the non-conformal coverage in the nanometer scale of the spin-coated layers used to coat the ITO surface.

4.2 Poly (N-vinylpyrrolidone) (PVP) as the Electron-collecting Interlayers

4.2.1 Introduction

In the previous section, it was found that the PVP can serve not only as a dispersant, but also as a surface modifier. Even though surface modifications with polymeric materials are less common in the literature, electron-injection layer comprising of conjugated polymers and electron-collating interlayer with non-conjugated polymer have been proposed [138,139]. While frequently used electron-collecting interlayers such as metal oxides or alkali metal salt that require vacuum deposition systems or post thermal annealing at relatively high temperatures, polymer surface modifiers could be fabricated at lower temperatures from environmentally friendly solvents and be compatible with large throughput fabrication methods [64,66,67,74]. This section will focus on the role of PVP as the surface modifier that reduces the WF of ITO by up to 0.8 eV.

The molecular structure of PVP shown in Figure 4.1 (also shown in the inset of Figure 4.8) reveals an amphiphilic nature of the PVP. The amphiphilic due to the highly polar amide group and the non-polar methylene groups in the backbone and in the ring allows it to be soluble in polar solvents such as water [140]. For this study, the PVP is first dissolved in distilled water with a concentration of 0.07 wt. %. Then, an ultrathin PVP layer was prepared on an ITO substrate by spin coating in ambient air.

4.2.2 Poly (N-vinylpyrrolidone) Layer Characterization

The average thickness of the PVP layer, over nine points, was estimated to be 0.9 ± 0.1 nm by spectroscopic ellipsometry. To confirm the presence of PVP on ITO substrates, XPS measurement was conducted on a bare ITO and a PVP modified ITO by following the N1s peak of the PVP the In3d5 and the Sn3p3 of the ITO over nine points

across the substrate. A comparison of XPS spectra between PVP modified glass/ITO substrate and on a bare glass/ITO substrate is displayed in Figure 4.8 and the inset of the Figure 4.8. The detected N1s peak around 400 eV clearly reveals the presence of PVP (inset of Figure 4.8). This peak appeared from nine points on the surface consistently. However, as shown in Figure 4.8, the In3d5 and the Sn3p3 peaks were also found on both substrates.

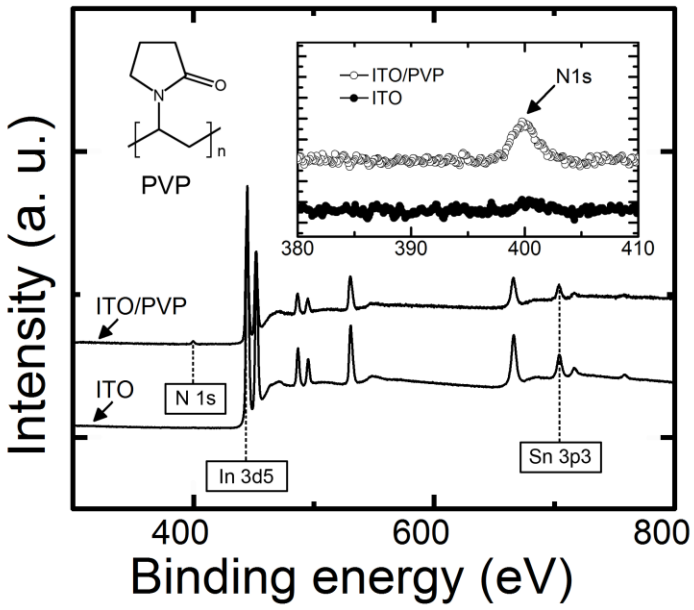

Figure 4.8 A survey of XPS spectra for ITO and PVP-modified ITO surfaces. The inset shows XPS spectra of the N1s core level for ITO and PVP-modified ITO surfaces, and the molecular structure of the PVP.

To investigate the change of surface morphology in PVP-modified ITO with respect to the thickness of PVP, phase and amplitude AFM images were taken. The images in the Figure 4.9 show a comparison of the phase and amplitude images of PVP-coated samples with different PVP thicknesses. The amplitude images shown on the right

column in Figure 4.9 reveal a decreasing RMS surface roughness with increasing PVP thickness. The obtained RMS surface roughness value from the bare ITO was found to be 5.0 nm, and 2.7 nm, 1.4 nm, and 0.8 nm from PVP layers with thickness values of 0.9 nm, 4.0 nm, and 8.8 nm, respectively.

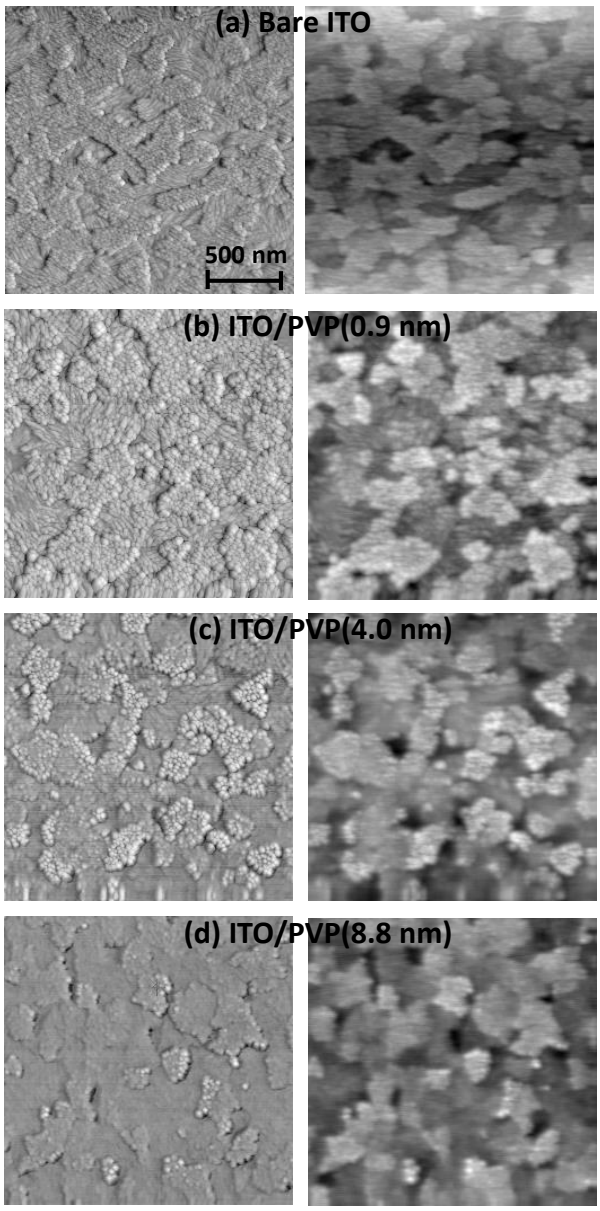

Figure 4.9 AFM images (phase-left column, amplitude-right column) of the bare ITO, ITO/PVP (0.9 nm), ITO/PVP (4.0 nm), and ITO/PVP (8.8 nm).

The phase images displayed in the left column of Figure 4.9 clearly reveal the surface distribution of PVP on the ITO surface. From the sample with 0.9 nm PVP-coated ITO substrates, non-conformal coverage of PVP on the ITO surface was found through a careful examination. However, these differences in two phases, ITO and PVP, were more clearly shown from the samples with 4.0 nm and 8.8 nm PVP-coated on the ITO surface. Also, the phase distribution shown in histograms of Figure 4.10 indicates the presence of a double-peak phase distribution in all PVP-coated ITO samples, and particularly for the 4.0 nm and 8.8 nm PVP-coated ITO samples, producing additional clue of the non-conformal coverage of PVP on the 0.9 nm PVP-coated ITO substrate.

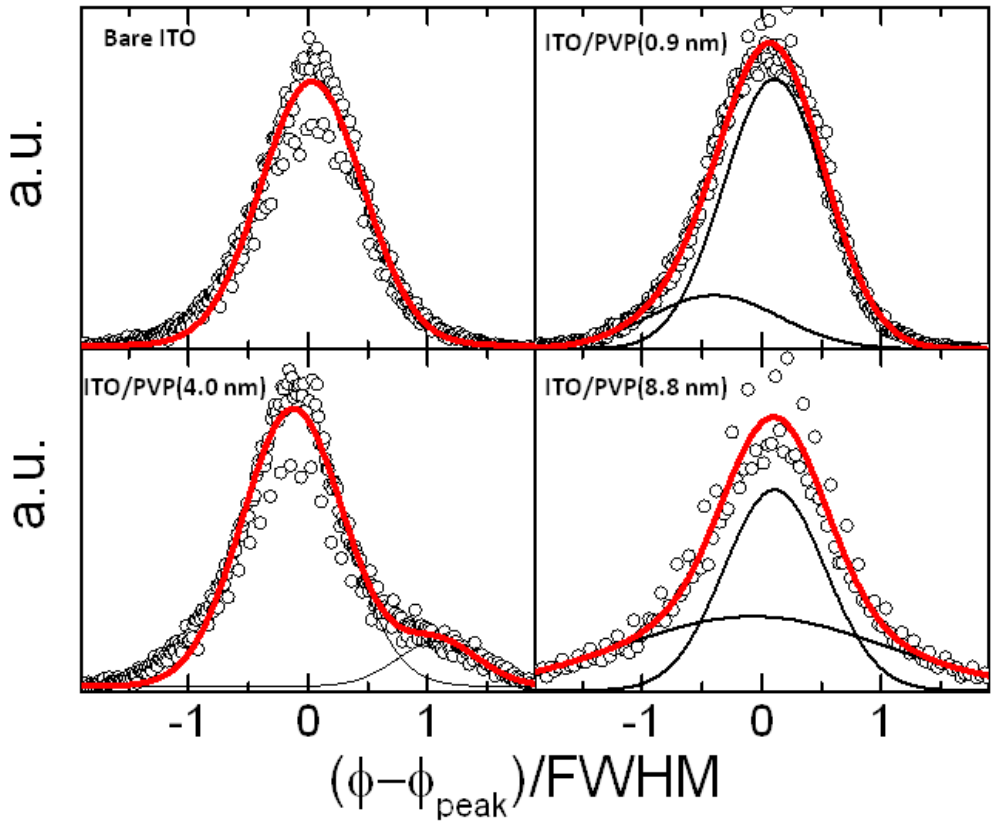

Figure 4.10 Histograms of the phase distribution measured by AFM on the bare ITO, ITO/PVP (0.9 nm), ITO/PVP (4.0 nm) and ITO/PVP (8.8 nm) substrates.

The WF values of bare ITO and PVP-modified ITO substrates were measured by using UPS. UPS was conducted in ultra-high vacuum, utilizing the He I (21.22 eV) and He II (40.8 eV) radiation lines from a He discharge lamp. The position of the photoemission onsets determines WF values. The energy resolution on WF measurements was 0.15 eV. Figure 4.11 (a) displays the UPS-He I spectra in which a vacuum level shift has been caused by the PVP modification of ITO. This vacuum shift induced a WF reduction of ITO from 4.4 eV to 3.6 eV.

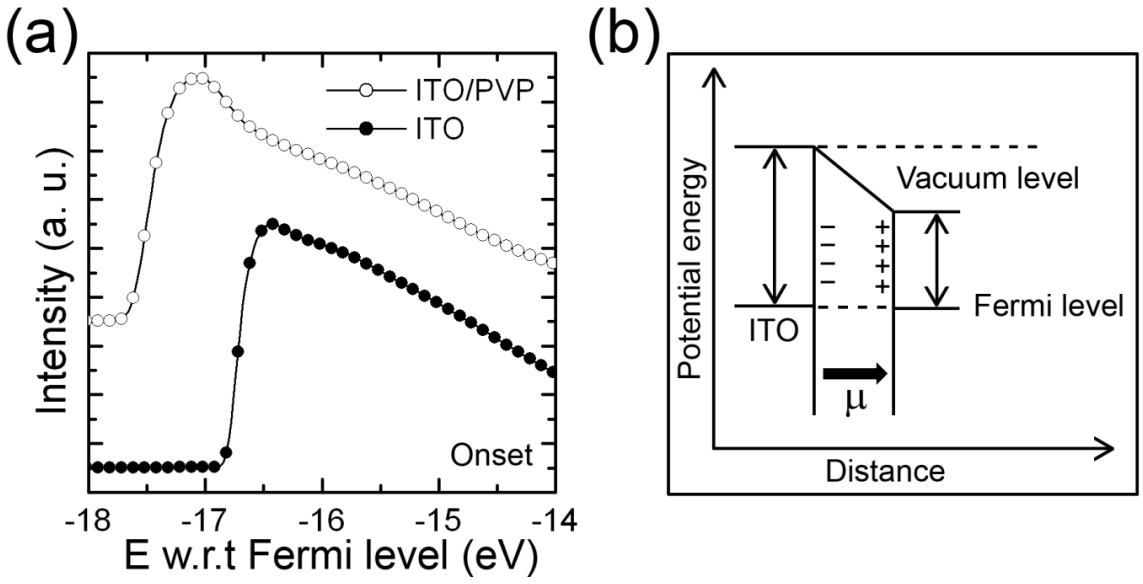

Figure 4.11 (a) Onset of photoemission used to calculate the surface work function, (b) work function changing mechanism due to the dipole moment from PVP modification.

The origin of this reduction is related to the presence of the pyrrolidone groups on PVP, which have partial electron-donating properties. The physical or chemical adsorption of PVP onto the ITO surface is believed to induce a partial electron transfer from the pyrrolidone group to ITO, thus creating a surface dipole μ on the ITO surface.

This surface dipole lowers the electrostatic potential at the surface of ITO, effectively reducing its WF, as shown in Figure 4.11 (b) [141,142].

4.2.3 Characterization of Solar Cells Performance

To investigate photovoltaic properties of PSCs with PVP modified ITO ECE, inverted PSCs with device structures of ITO/PVP/P3HT:$PC_{60}BM$/PEDOT:PSS(CPP)/ Ag were fabricated. Also, the photovoltaic properties of inverted PSCs with ITO/PVP ECE were compared with two reference cells: one with an ITO/ZnO (WF of 4.3 eV by Kelvin probe in air) ECE and other with a bare ITO ECE (WF of 4.7 eV by Kelvin probe in air). The device structures are shown in Figure 4.12.

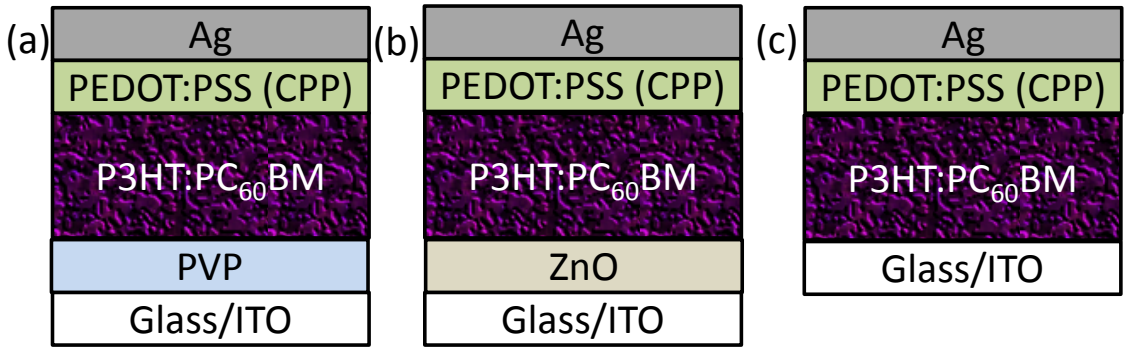

Figure 4.12 Device structures of inverted P3HT:$PC_{60}BM$ solar cells with (a) ITO/PVP, (b) ITO/ZnO, and (c) ITO only for the electron-collecting electrodes.

On pristine PSCs using ITO/PVP ECE, S-shape kinks were observed, leading to a poor device performance with a small FF of 0.33, small V_{OC} of 437 mV, and low PCE of 1.2%. Such S-shaped kinks in *J-V* characteristics have frequently emerged in metal-oxide

modified ITO electrodes. It has been believed that the advent of these S-shape kinks relates to oxygen traps within the metal-oxide interlayer, which can be eliminated by UV exposure or by the application of a high electric field, leading to improvements in the conductivity of the interlayers. For example, it has been reported that the conductivity of films of ZnO and SnO_2 is enhanced with a UV treatment [143]. However, this is not a plausible explanation in the case of the ITO/PVP ECE, because PVP is a non-conjugated polymer with good insulator properties. Interestingly, the S-shape kinks disappeared from the *J-V* characteristics after UV treatment in a N_2-filled glove box, through the glass substrate, for at least 20 min as shown in Figure 4.13. After this minimum exposure, the PSC performance remains unchanged, with an averaged PCE of 3.2% ± 0.1% while the samples are stored in the N_2-filled glove box.

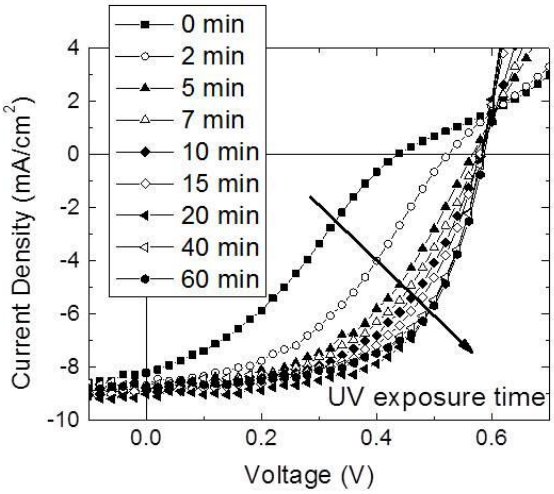

Figure 4.13 *J-V* characteristics under illumination for a P3HT:PC_{60}BM-based polymer solar cell with electron-collecting electrodes of ITO/PVP, as a function of UV-exposure time.

This process is also found to be reversible when samples are sequentially exposed to air and UV illumination, as shown in Figure 4.14. Namely, the S-shape kinks re-appeared when the samples were exposed to ambient air and disappeared again with UV treatment.

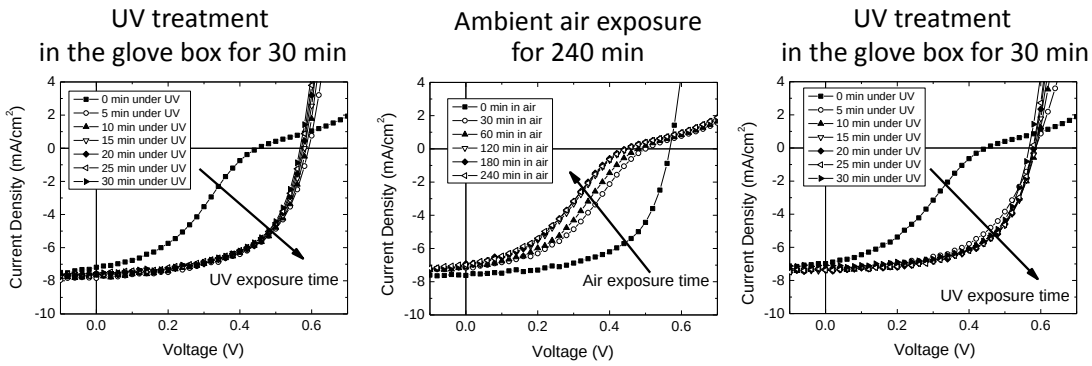

Figure 4.14 Reversible S-shape characteristics of P3HT:$PC_{60}BM$-based polymer solar cell with electron-collecting electrodes of ITO/PVP with sequentially exposed to air and UV illumination

Here, it should be noted that the appearance of the S-shape is not directly related to the magnitude of the spatially averaged WF of the PVP-modified ITO ECEs. This WF is sufficiently low to collect electrons efficiently since inverted PSCs with an ITO/ZnO ECE, having a WF of 4.3 eV measured by a Kelvin-probe in air [67], show a PCE of 3.1% ± 0.1%. As shown in Figure 4.15, since the absorption of the UV-radiation by the PVP layer is almost negligible, it is speculated that the observed evolution is related to ITO itself.

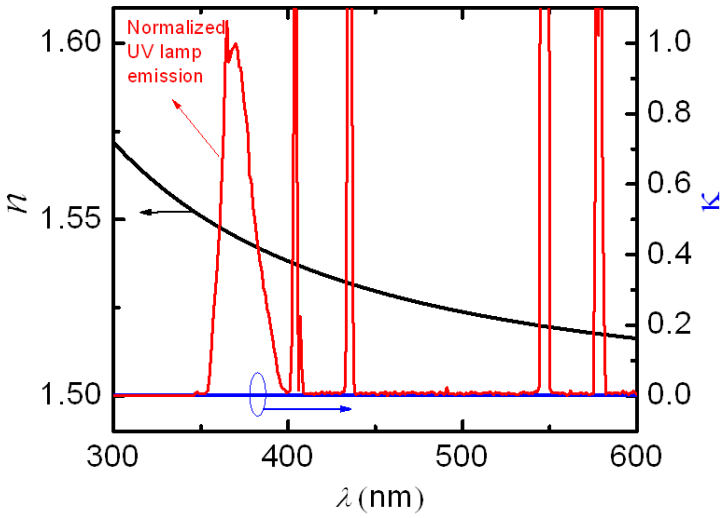

Figure 4.15 Refractive index and extinction coefficient derived from ellipsometric measurements on a PVP film deposited on a silicon wafer. In red, the normalized UV lamp emission used in the UV exposure experiments is also displayed as a reference.

Pristine inverted PSCs with an ITO-only ECE, having a WF of 4.4 eV measured by UPS and 4.6 eV measured with a Kelvin probe in air, were also found to exhibit S-shape characteristics. That situation was improved after a 20 minute UV treatment, leading to a PCE of 1.8 ± 0.1 %. A comparison of the *J-V* characteristics of these three types of PSCs is displayed in Figure 4.16 and its performance parameters summarized in Table 4.3.

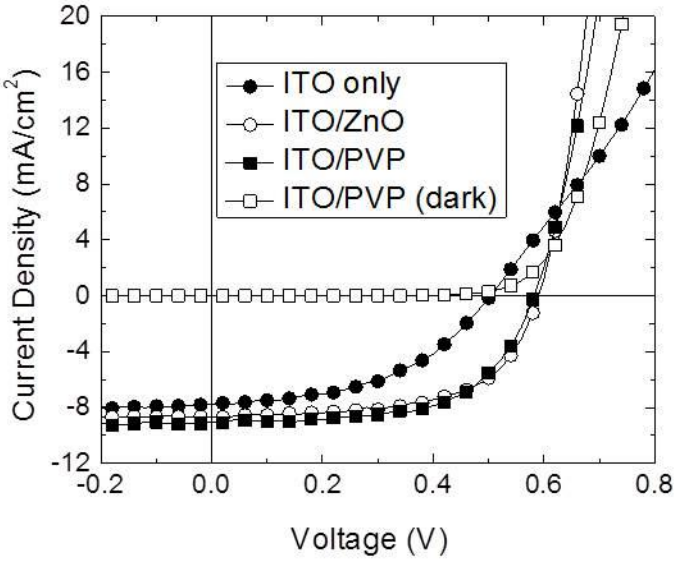

Figure 4.16 Representative *J-V* characteristics under illumination for a P3HT:$PC_{60}BM$-based polymer solar cell with electron-collecting electrodes of ITO only, ZnO (28 nm)-coated ITO, and PVP-coated ITO electrodes (including *J-V* characteristics in dark).

Table 4.3 Summary of the averaged[a] device performance of inverted P3HT:$PC_{60}BM$ solar cells with PVP-modified ITO, ZnO-coated ITO, and ITO only as an electron-collecting electrode.

Electron-collecting electrodes	V_{OC} **(mV)**	J_{SC} **(mA/cm^2)**	**FF**	**PCE (%)**
ITO/PVP	584±2	8.97±0.16	0.60±0.01	3.2±0.05
ITO/ZnO	585±5	8.73±0.37	0.60±0.01	3.1±0.11
ITO only	494±7	7.80±0.35	0.47±0.01	1.8±0.09

[a] Average was calculated over five devices

In pristine PSCs with ITO only ECE, in the absence of band-bending effects, an energetic mismatch exists between the WF of ITO and the EA of $PC_{60}BM$. This mismatching makes ITO a poor ECE since electron-hole recombination at this contact

could become significant. The increased contact recombination in this case would then lead to a slow rate of electron collection, leading to a low FF. This has been suggested to lead to s-shape characteristics in PSCs [143-145]. Upon UV illumination of glass/ITO substrates through glass (e.g. glass facing the illumination source) inside a N_2-filled glove box, it has been noticed that the WF of bare ITO can decrease from 4.6 eV to 4.3 eV. This reduction of the WF of the ITO would be sufficient to reduce the contact recombination; hence enhancing the electron-collection property of that electrode and the PCE. A similar test was also performed on PVP-modified ITO substrates and it showed a reduction of its WF from 4.3 eV to 4.0 eV upon UV exposure. This is a similar change than the one observed on bare ITO, suggesting that WF reduction upon UV illumination are related to changes in the WF of ITO itself.

To probe more in depth the influence of UV irradiation on the performance of PSCs, a separated study was performed. In this study, the appearance and disappearance of an S-shape kink was assumed to be related with an energetic mismatch between the WF of the ITO electrode and the relevant energy levels of the organic semiconductor in the photoactive layer of the PSC.

Two bilayer organic heterojunction-based solar cells with structures of ITO/copper phthalocyanine (CuPc)/C_{60}/bathocuproine (BCP)/Al (S1) and ITO/C_{60}/ CuPc/MoO_X/Al (S2) were fabricated. The CuPc served as an electron-donor and the C_{60} worked as an electron acceptor. The structure of the S1 has been previously reported in the literature [146] and showed efficient hole collection at the ITO electrode. Pristine S1 devices showed good photovoltaic performance, with a V_{OC} of 0.48 ± 0.01 V, a J_{SC} of 4.6 ± 0.1 mA/cm^2, a FF of 0.62 ± 0.01 and a PCE of 1.36 ± 0.03 %, averaged over 5 devices. However, the performance of S1 devices rapidly degrades upon continuous irradiation under a solar simulator. This degradation is characterized by the appearance of an S-shaped kink in the *J-V* characteristics after the devices have been exposed to the solar

simulator for a few minutes. For instance, when a device was exposed to the light from the solar simulator for 45 min, the FF dropped to 0.36, the V_{OC} dropped to 0.34 V, the J_{SC} dropped to 3.7 mA/cm^2, and the PCE dropped to 0.47% (Figure 4.17 (e)). Pristine S2 devices displayed very poor photovoltaic performance with a very pronounced S-shaped kink. However, the performance of S2 devices rapidly improved as a function of exposure to illumination from a solar simulator. Within 5 min of exposure, the S-shaped kink completely disappeared, yielding a FF of 0.60, a V_{OC} of 0.39 V, a J_{SC} of 3.9 mA/cm^2, and a PCE of 0.9% (Figure 4.17 (f)).

To investigate the origin of the S-shape characteristics of these PSCs, the WF of ITO was continuously monitored by a Kelvin probe under different exposure conditions, as described in Figure 4.17(a)-(d). WF value of a clean ITO is 4.66 eV (Figure 4.17). Independent glass/ITO substrates were exposed to light from either a UV lamp or the solar simulator, for a total period of 10 min. Similar to the treatment for the PSCs, glass/ITO substrates were exposed, inside a N_2-filled glove box, through the glass side.

Figure 4.17 (a) shows that both UV treatment and solar simulator treatment lead to a decreased WF value of ITO from 4.66 eV to a value around 4.17 eV. Then, the treated glass/ITO substrates were exposed to two different atmospheres, as shown in Figure 4.17 (b): ambient air and an O_2-rich atmosphere by placing the substrates in an O_2-filled vacuum oven. The WF of the glass/ITO substrates exposed to ambient air increased slowly to a value of 4.51 eV after 30 min. Likewise, the WF of the glass/ITO substrates exposed to the O_2-rich atmosphere increase to a value of 4.61 eV after 30 min. The faster WF increase observed from the glass/ITO substrates exposed to the O_2-rich atmosphere underscores the important role that O_2 seems to play in the observed behavior. This process is also shown to be reversible when the glass/ITO are sequentially exposed to air and UV illumination, a behavior that is consistent with the appearance and disappearance of the S-shape characteristics of the PSCs with ITO/PVP ECE as shown in Figure 4.14.

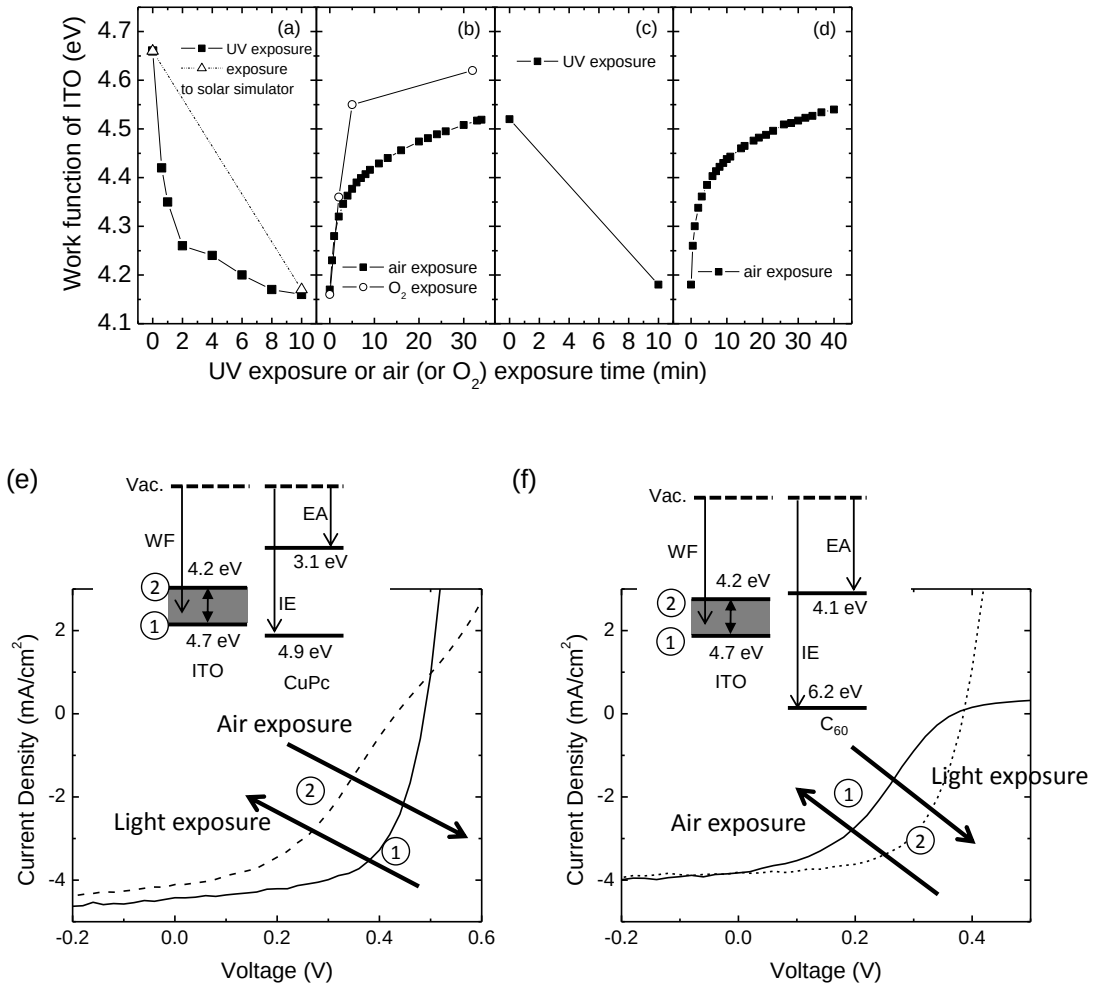

Figure 4.17 WF of ITO with continuous treatments: (a) exposed to a 365 nm-peaked UV lamp (10 mW/cm^2) or a AM 1.5G solar simulator (100 mW/cm^2) in a N_2-filled glove box and measured in the N_2-filled glove box; (b) further exposed to air and measured in air, or exposed to O_2 and measured in a N_2-filled glove box; (c) further exposed to a 365 nm-peaked UV lamp in a N_2-filled glove box and measured in air; (d) further exposed to air and measured in air. The lines connecting the points are present to better indicate the observed trends. Energy diagram and corresponding *J-V* characteristics under illumination of (e) ITO/CuPc and S1 and (f) ITO/C_{60} and S2. The shaded area represents the range of ITO WF values with air or UV exposure.

To figure out the role played by the use of different sources of illumination in producing the described changes, the optical properties of ITO were characterized. Figure 4.18 displays refractive index (*n*) and extinction coefficient (*k*) derived from ellipsometric measurements on an 150 nm–thick ITO film and the linear absorption of the ITO layer on glass, calculated using the transfer matrix method. Because of the strong UV absorption of the glass substrate, the ITO shows a bell-shaped absorption spectrum, with a central peak at 324 nm, having a maximum absorbance of 8%, and a 50 nm full-width at half-maximum. Given the spectral overlap between the light source's emission (Figure 4.18 (b)) and the ITO absorption spectrum, it is convenient to calculate the total (integrated) number of absorbed photons per unit time and area as,

$$A_{ITO-source} = \int d\lambda A_{ITO}(\lambda) I_{ph} = I_T \int d\lambda A_{ITO}(\lambda) \frac{I_{ph}(\lambda)}{I_T} = I_T \times K_{ITO-source} \qquad (4.1)$$

, where $A_{ITO}(\lambda)$ is the absorbance of ITO; $I_{ph}(\lambda)$ is the spectral photon irradiance in units of photons/(cm^2·s·nm); and I_T is the total (integrated) irradiance of the light source in units of mW/cm^2. For the UV lamp (spectrum shown in Figure 4.18 (b)), the overlap integral $K_{ITO\text{-}UVlamp}$, in equation (4.1), has a value of 3×10^{13} (photons/mW). Thus, the WF reduction observed for an exposure of 10 minutes at 10 mW/cm^2 under a UV lamp can be correlated with the absorption of about 1.8×10^{17} photons/cm^2 in ITO. A similar calculation for the solar simulator provides a $K_{ITO\text{-}solarsimulator}$ value of 7×10^{12} (photons/mW) and a total absorption of 4.2×10^{17} photons/cm^2, at 100 mW/cm^2 for 10 minutes. Thus, the absorbed-photon dose provided by the UV lamp and the solar simulator is estimated to be similar, in good agreement with the very similar change of WF observed.

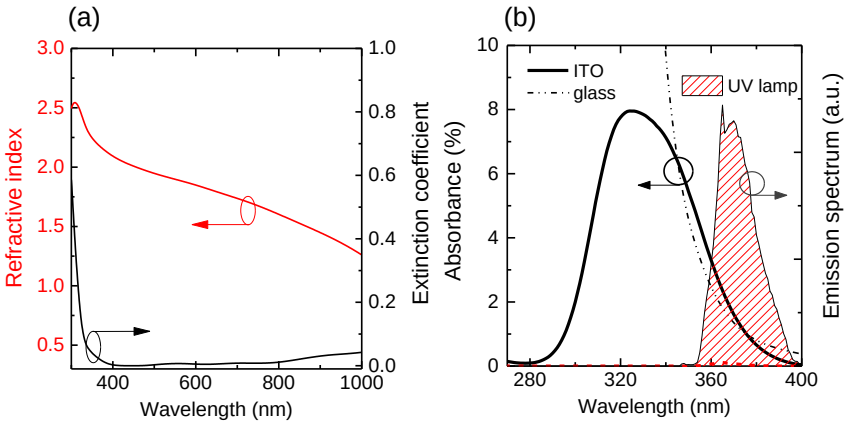

Figure 4.18 (a) Refractive index and extinction coefficient of ITO, (b) absorbance of ITO and glass, and emission spectrum of UV lamp used to illuminate the ITO samples to induce its work function change

As mentioned previously, the absorption of UV light has been related to the process of O_2 adsorption and desorption in metal-oxides. On the other hand, it was also found that the WF of metal-oxides decreased after UV treatment and the decrease of WF correlated with enhanced photovoltaic performance of PSCs with the inverted geometry [69]. These previous reports are consistent with the observation described in this section and may suggest that a similar behavior could be applied to other metal-oxide films. A detailed process is described below.

Free electrons are trapped at the surface or grain boundaries of ITO by atmospheric O_2 which leads to the formation of O_2^- and a surface dipole. This surface dipole increases the electrostatic potential at the ITO surface and consequently induces an upward shift of the vacuum level. Finally, the shift of the vacuum level leads to increase of the WF of ITO up to 4.66 eV. On the contrary, under UV or solar simulator illumination, photo-generated holes in ITO can recombine with the adsorbed O_2^- and promote the release of O_2. Consequently, this process induces the disappearance of the surface dipole and to the decrease in the WF of ITO to a value of 4.3 eV.

Figure 4.17 (e) and (f) displays a schematic representation of the energy levels at the ITO/semiconductor interfaces and the corresponding *J-V* characteristics on devices S1 and S2, respectively. The range of ITO WF values is represented by the shaded area. Note that the energy levels shown are those measured on independent samples and do not reflect any interaction that may exist between the materials when the interface is formed. Using these levels as a guideline, it is straightforward to correlate the photovoltaic behavior of devices S1 and S2 with the changes of WF of ITO upon exposure to the solar simulator. For instance, for S1 it is clear that the energy mismatch between the WF value of ITO and the IE of CuPc (4.9 eV) [62] increases by the photon absorption in ITO (Figure 4.17(e)). The increased mismatch leading to the appearance of the S-shaped kink may reveal that holes are being collected at a lower rate, and that holes are being accumulated at the ITO/CuPc interface [142]. Conversely, in S2 a reduction of the WF of ITO will decrease the energy mismatch between the WF of ITO and the EA of C_{60} (4.1 eV) [147]. Consequently, the rate of electron collection at these electrodes increases leading to the disappearance of the S-shape kink (Figure 4.17(f)). Upon exposing S2 devices to air, the WF of ITO increases leading to the reappearance of the S-shaped kink in their *J-V* characteristics (Figure 4.17 (f)).

The potential mechanism described above can offer a plausible explanation for the phenomena seen in the PSC with ITO/PVP ECE. This is that in the nanometer scale, the non-conformal coverage of PVP on ITO causes a spatial distribution of areas with higher (bare ITO) and lower (PVP-covered regions) WF values across the surface. That is, even though the spatially averaged WF of the PVP-modified ITO provides values that would appear to be sufficiently low for electrons to be effectively collected, locally, the nanometer scale areas with higher WF will show poor electron-selectivity and consequently will lead to S-shape kinks in *J-V* characteristics. As WF of these areas decreases after UV treatment, the electron-selectivity would be enhanced, leading to an

improved electron collection at this electrode. Here, it should be noted that the WF values of PVP-modified ITO substrates, measured by a Kelvin probe, were found to be 4.30 eV, 4.25 eV and 4.20 eV for PVP thicknesses of 0.9 nm, 4.0 nm and 8.8 nm, respectively. The small variations in WF reflect that not thickness variations, but non-conformal coverage is responsible for the observed effects.

4.2.4 Conclusions

The amide containing water-soluble polymer, PVP was found to reduce the WF of ITO up to 0.8 eV. The physisorption or chemisorption of PVP onto the ITO surface was thought to induce a partial electron transfer from the pyrrolidone group in PVP to ITO. The partial electron transfer was believed to form of a surface dipole on the ITO, consequently resulting in the ITO WF reduction. Inverted PSCs using PVP-modified ITO ECEs were demonstrated. These devices were as efficient as inverted PSCs using ITO/ZnO (by ALD deposition) ECEs, provided they are exposed to UV-illumination. In addition, it was also found that the UV-illumination by itself can also induce a WF reduction of ITO through O_2 desorption.

The use of the water soluble non-conjugated polymer for the electron-collecting interlayer is thought to be a big leap in the field of the polymeric electronic devices since it can be fabricated at lower temperatures from environmentally friendly solvents and is compatible with large throughput fabrication methods. However, despite the sufficiently lowered WF value of the ITO/PVP, without the UV treatment pristine PSCs showed poor photovoltaic performance with S-shape kinks in their *J-V* characteristics due to the inhomogeneous surface coverage of PVP on ITO. Thus, follow-up research that discovers new materials with more effective WF reduction properties must be performed.

4.3 Polyethylenimine Derivatives as the Electron-collecting Interlayers

Before starting this section, it should be noted that the study shown in this section was mostly led by Dr. Yinhua Zhou.

4.3.1 Introduction

In this section, another polymer-based surface modifier containing simple aliphatic amine groups will be introduced. This surface modifier is found to universally reduce the WF of a variety of conductors including metals, transparent conductive metal-oxides, conducting polymers, and graphene by up to 1.7 eV. Unlike π-conjugated amine-containing small molecules and polymers considered previously, the polymers discussed in this section are insulators with large band gap and should not be considered as charge injection layers but rather as surface modifiers. The polymer is physisorbed onto the conductor surface, and forms an ultrathin layer on the surface. The intrinsic molecular dipole moments induced by the neutral amine groups contained in such a polymer layer, and the charge-transfer character of their interaction with the conductor surface, lead to the WF reduction of a wide range of conductors. The polymer modifiers can be easily processed in air, from dilute solutions in eco-friendly solvents such as water or 2-methoxyethanol.

4.3.2 Polyethylenimine Derivatives Layer Characterization

Two polymer surface modifiers used in this section, polyethylenimine (PEI, branched) and polyethylenimine ethoxylated (PEIE) are shown in Figure 4.1. The high content of amine groups (primary, secondary, and tertiary) in the polymer structures yields high pH values in water and 2-methoxyethanol solutions. The measured pH values from these polymers in water and 2-methoxyethanol with a polymer concentration of 0.4 wt.% are summarized in Table 4.4.

Table 4.4 pH values of PEIE and PEI in water and 2-methoxyethanol solutions.

Polymers	Water	2-methoxyethanol
PEIE (0.4 wt.%)	10.3	10.1
PEI (0.4 wt.%)	10.5	10.3

To investigate WF change prior to and after the PEIE deposition on the conductor's surface, UPS measurement under high vacuum and independent Kelvin probe measurements in air were conducted. Figure 4.19 shows the results of UPS measurements on a series of conductors before and after deposition of 10-nm-thick PEIE layer; the spectra revealed WF reductions from 4.70 to 3.40 eV for Au, from 4.40 to 3.30 eV for ITO, and from 4.95 to 3.32 eV for PEDOT:PSS (PH1000).

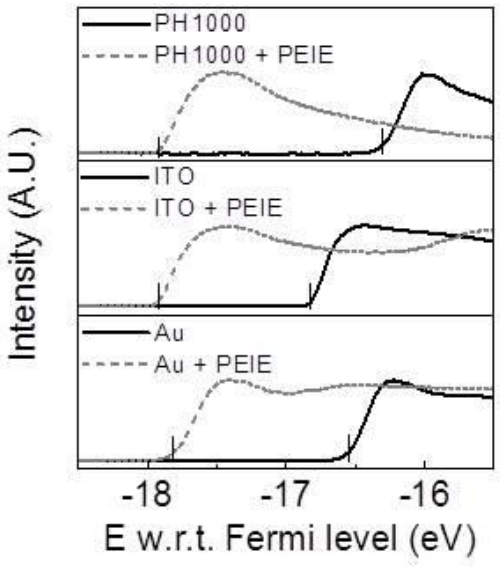

Figure 4.19 Photoemission cut-off obtained via UPS for ITO, Au and PEDOT:PSS (PH1000) samples, with and without PEIE.

Separate Kelvin probe measurements in air also showed WF reduction of metals oxides (ITO, FTO, ZnO), metals (Au, Ag and Al), as well as PEDOT:PSS PH1000 after PEIE deposition. Table 4.5 summarizes the WF values measured by Kelvin probe and UPS for several conductors modified with 10 nm-thick PEIE or PEI layers. Difference in WF values between the two techniques is likely due to differences in the measurement atmospheres.

Table 4.5 Work function values of conducting materials with and without PEIE or PEI modifications measured by Kelvin probe in air and by UPS under vacuum.

Conductors		**Work function (eV)**					
		By Kelvin prove in air			**By UPS under vacuum**		
		Pristine	**w/ PEIE**	**w/ PEI**	**Pristine**	**w/ PEIE**	**w/ PEI**
Metal oxides	ITO	4.62 ± 0.06	3.60 ± 0.06	3.50 ± 0.06	4.40	3.30	3.27
	ZnO	4.26 ± 0.06	3.28 ± 0.06	3.10 ± 0.06	3.96	3.55	3.17
	FTO	4.68 ± 0.06	3.80 ± 0.06	3.60 ±0.06	-	-	-
Metals	Au	5.10 ± 0.10	3.90 ± 0.06	3.94 ± 0.06	4.70	3.40	-
	Ag	4.60 ± 0.06	3.70 ± 0.06	3.60 ± 0.06	-	-	-
	Al	3.40 ± 0.06	2.75 ± 0.06	-	-	-	-
Polymer	PEDOT:PSS	4.90 ± 0.06	3.58 ± 0.06	3.88 ± 0.06	4.95	3.32	3.16

A study on the thermal stability of the WF of PEIE- and PEI-modified ITO substrates was conducted by Kelvin probe measurements in air. The WF of PEIE-modified ITO substrates did not make any change until a temperature of 190 °C, allowing them to be compatible with the processing of printed electronic devices on plastic substrates (Figure 4.20 (a)). Typically, the processing temperatures for the printed electronic device are below 200 °C. For PEI-modified ITO substrates, any change in the WF was found until 150 °C (Figure 4.20 (b)). PEIE-coated ITO substrates also remain fairly stable under normal ambient conditions for more than 4 weeks. During that period, the variation in WF was less than 0.2 eV (Figure 4.20 (c)). This small variation in WF might be caused by contamination from the ambient air, not by the degradation of PEIE

layer itself. Furthermore, PEIE or PEI solutions in distilled water are stable in air (i.e., remain effective agents for reducing the WF) for more than 1 year.

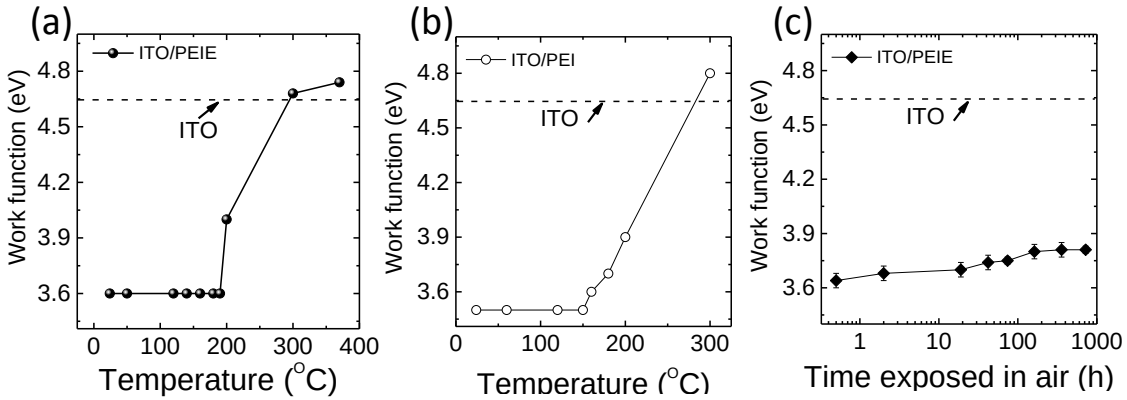

Figure 4.20 Work function of (a) ITO/PEIE and (b) ITO/PEI after annealing at different temperatures on a hot plate in air for 30 min, (c) evolution of the work function of ITO/PEIE for different air exposure times.

To further investigate the energy levels of PEIE, such as EA and IE, IPES (Figure 4.21 (a)) and UPS measurements (Figure 4.19) on PEIE-coated Au were performed. As mentioned in Table 4.5, the WF of PEIE on Au is 4.3 eV, and obtained EA and IE values from the IPES and UPS studies were 0.3 eV and 6.5 eV, respectively. An energy diagram of PEIE is illustrated in Figure 4.21(b). Unlike π-conjugated polymers that can show good electron-transporting properties [148], these results suggest that PEIE is likely to act as an insulator with a gap of 6.2 eV, and large barriers for both hole and electron injections.

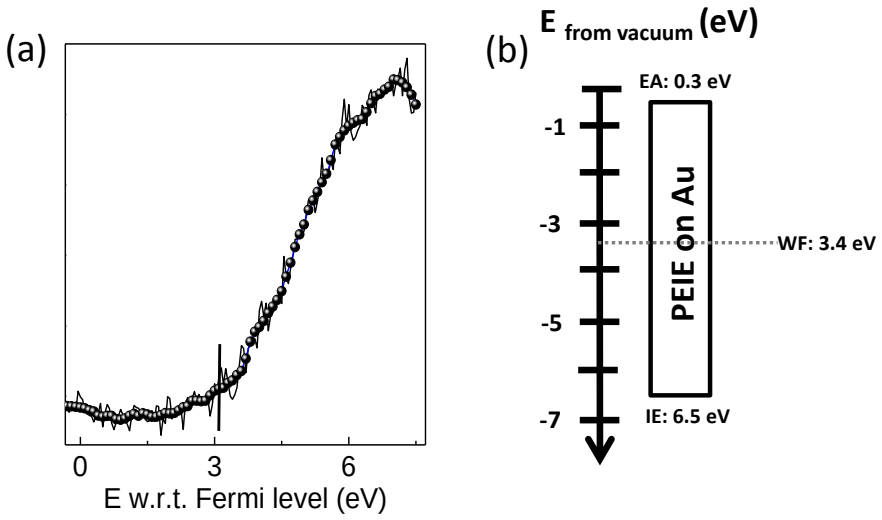

Figure 4.21(a) IPES spectrum of 10-nm-thick PEIE layer on top of Au, (b) the energy levels of PEIE.

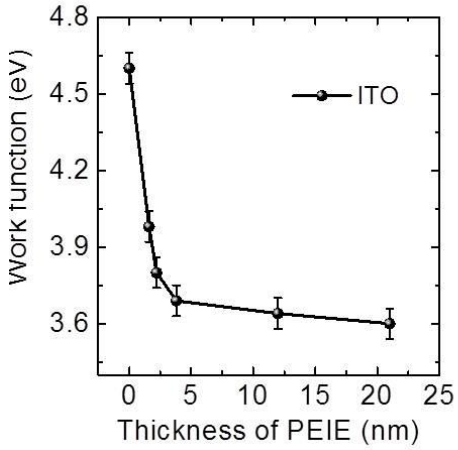

Figure 4.22 PEIE thickness dependence of the work function of PEIE-modified ITO substrates.

The PEIE thickness (from 2 to 22 nm) dependent WF reduction on ITO was studied and a variation was less than 10 % (Figure 4.22). However, even if the thickness of the PEIE layer did not influence ΔWF, its insulating nature would cause thicker

polymer layers to adversely affect PSC performance. The thicknesses of the PEIE layers were estimated by spectroscopic ellipsometry.

To explore the surface morphology of the PEIE-modified on ITO, amplitude and phase images were taken by AFM. As shown in Figure 4.23 (c)-(f), AFM measurements on PEIE-modified ITO reveal that a 10 nm-thick PEIE layer did not cover uniformly the ITO surface, but that islands formed are separated by areas with a much thinner PEIE coating. These PEIE islands could be easily washed away by subjecting the PEIE-modified ITO substrate to a mild flow of running distilled water for 1 min (Figure (g) and (h)). After washing, WF change decreased by less than 0.1 eV. This observation indicates that only an ultrathin layer of PEIE is required to produce a large WF reduction and that the processes leading to such modifications are truly confined to the very surface of the conductor.

To investigate the binding strength between PEIE and the surface of a conductor, the WF of a PEIE-modified ITO substrate was monitored over time as a function of controlled washing cycles with water. Figure 4.24 displays the evolution of WF change when the substrates were subjected to a total of 50 min of mild washing conditions. After such a period of time, the WF change was less than 0.34 eV. The apparent resilience of the PEIE layer on the surface of ITO might at first glance point to a strong binding interaction between the polymer and the conductor. However, the WF reduction entirely disappeared after subjecting the PEIE-modified ITO substrate to a 50 min water wash in an ultrasonic bath (Figure 4.24, closed circles). This observation indicates that PEIE layer is physisorbed on the surface of the conductor, which would be consistent with the seemingly universal ability of PEIE to substantially reduce the WF of many different conducting materials (Table 4.5).

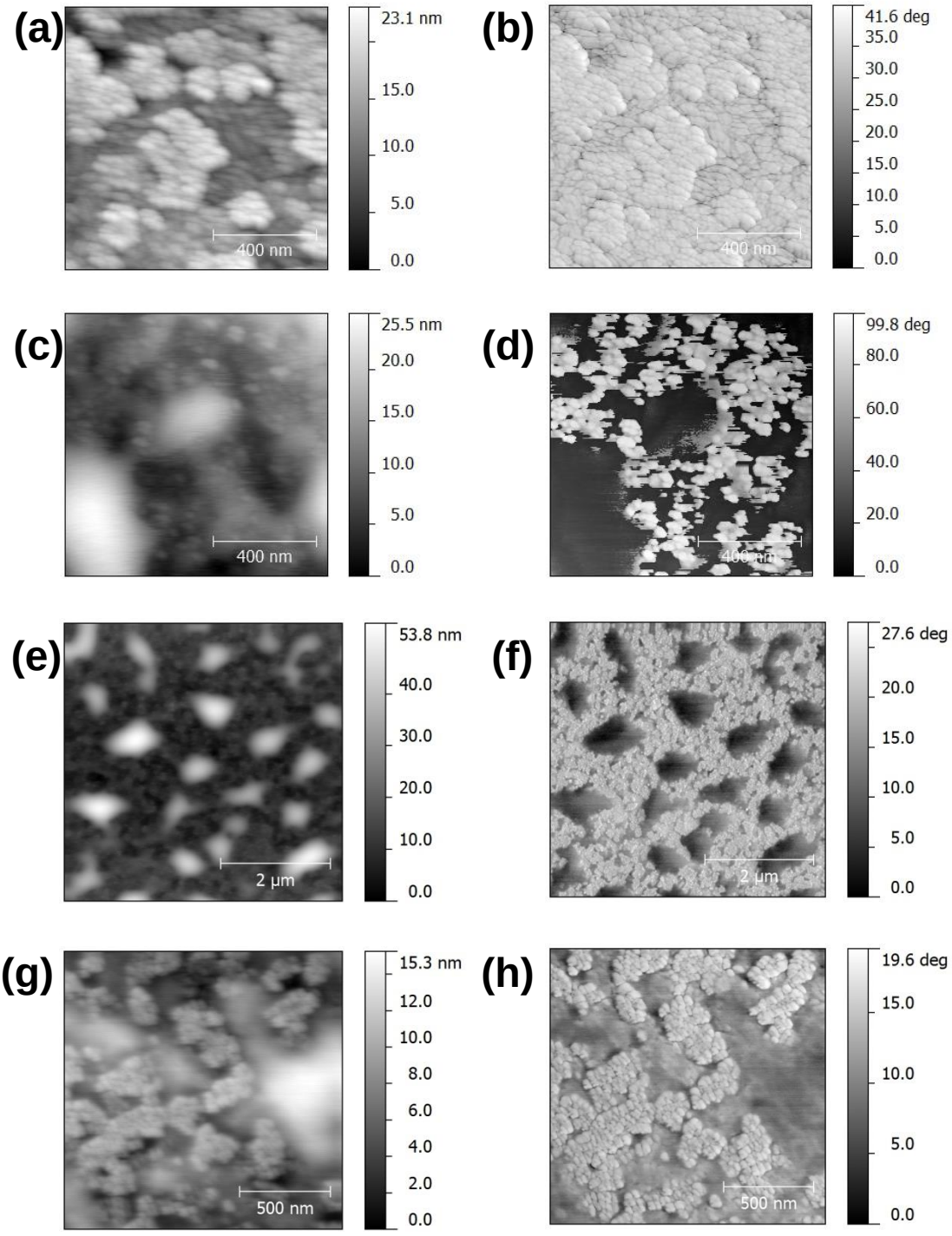

Figure 4.23 AFM image of ((a), (b)) ITO and ((c), (d)) ITO/PEIE in an area of 1 µm × 1 µm and ((e), (f)) ITO/PEIE in a larger area of 5 µm × 5 µm, ((g), (h)) ITO with 1 min mild washing. Figures (a), (c), (e), (g) are amplitude images and (b), (d), (f), (h) are phase images.

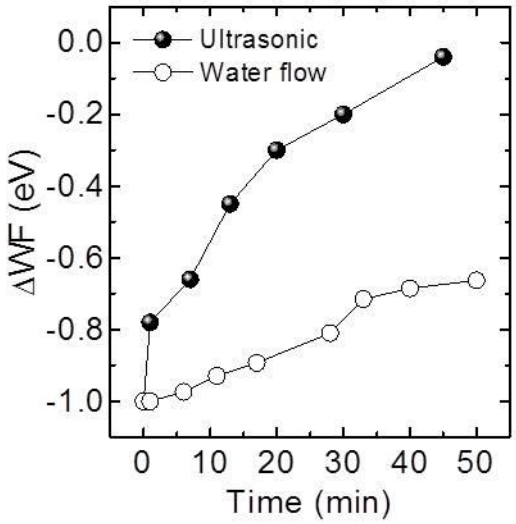

Figure 4.24 Change in work function relative to bare ITO of ITO/PEIE after different washing conditions.

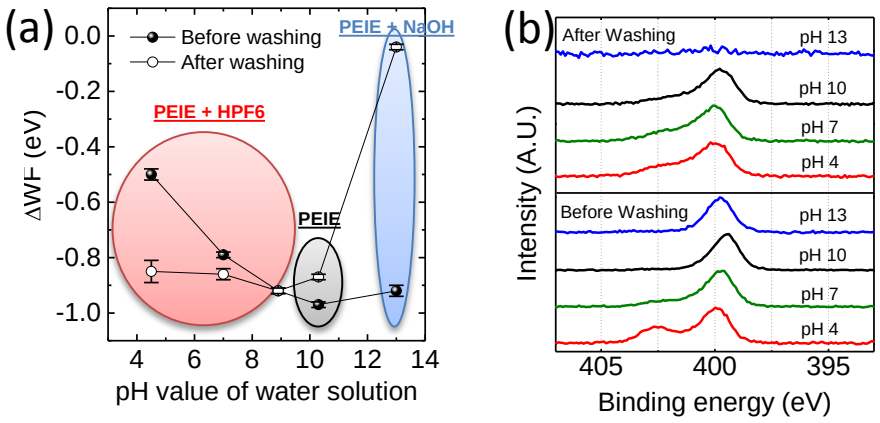

Figure 4,25 (a) Change in work function relative to bare ITO upon modification from PEIE water solution, PEIE with HPF6 water solution and PEIE with NaOH water solution before (filled circle) and after (open circle) water washing, (b) N1s core level recorded via XPS on the same samples.

To further investigate the nature of the interaction between PEIE and the conductor surface, the pH values of the original PEIE solution in water were modified by adding either fluorophosphoric acid (HPF6) or NaOH. PEIE layer was formed on ITO from solutions with pH values of 4.5, 7.1, 9.2, 10.3 or 13. Figure 4.25 (a) shows the change in WF value (ΔWF) induced prior to and after wash for one minute with running water.

Differences in the solution pH values were expected to mainly influence the degree of protonation of the amine groups in PEIE. The degree of PEIE protonation was followed with XPS by tracking the N1s peak position (Figure 4.25 (b)). When PEIE was processed from the most basic solution, ΔWF amounted to -0.92 eV and is related to the presence of neutral amine groups corresponding to the N1s peak at 399.8 eV (Figure 4.25 (b)). The same N1s peak was present in the PEIE layers processed from a pH of 10.3 solution that yields ΔWF of -0.97 eV. These results indicate that neutral amines groups are primarily involved in the interactions leading to the formation of the interface dipoles and the substantial changes in WF.

On the other hand, when the PEIE layers were processed from the more acidic solutions with a higher degree of protonated amines, smaller WF reductions were observed. In films processed from solutions with pH values of 7.1 and 4.1, the appearance of a second N1s peak at 402.5 eV (Figure 4.25 (b)) indicated the presence of protonated amines. After a 1-min water wash, with the exception of the PEIE layer made from the most basic solution (which was completely removed from the ITO surface), all layers showed similar ΔWF values around -0.86 eV. The XPS spectra of these layers show N1s peaks with a similar shape and a small shoulder at 402.5 eV. These results suggest that, in the case of PEIE, neutral amine groups are primarily responsible for the largest ΔWF observed.

4.3.3 Characterization of Solar Cells Performance

The PEIE-modified conductors for the low-WF ECEs were tested in a variety of PSCs geometries. PSCs were fabricated with PEIE-coated ITO, Ag, and PH1000 as the ECEs at the bottom of the devices to demonstrate their electron selectivity. In these cells, a blend of P3HT and $IC_{60}BA$ (1:1, wt. ratio) was employed as the photoactive layer. MoO_X/Ag served as the high-WF HCEs. Device structures are shown in Figure 4.26.

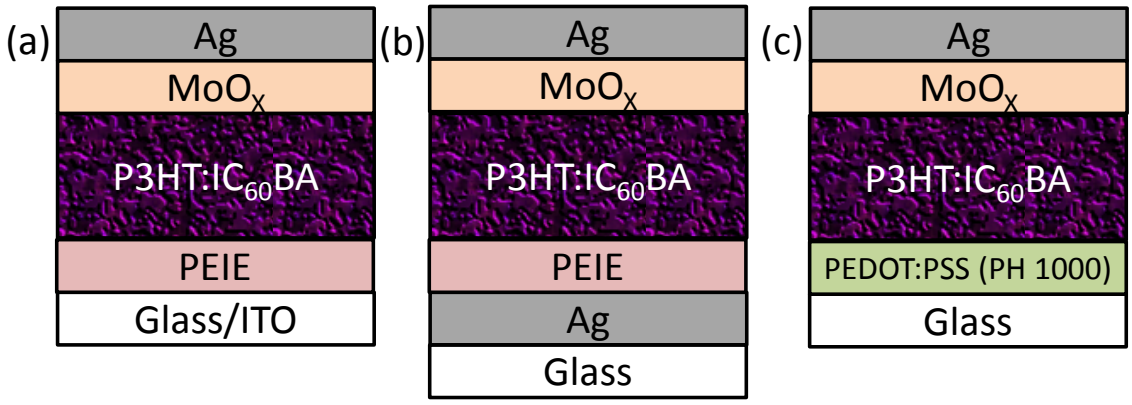

Figure 4.26 Device structures of inverted P3HT:$IC_{60}BA$ solar cells with (a) ITO/PEIE, (b) Ag/PEIE, and (c) PEDOT:PSS (PH1000)/PEIE for the electron-collecting electrodes.

Figure 4.27 (a) and (b) show the *J-V* characteristics of these solar cells in the dark and under illumination. In all cases, the *J-V* characteristics in the dark display a large rectification and small reverse saturation currents. This result reflects the excellent electron selectivity of the PEIE-modified ECEs. PSCs with PEIE-modified ITO ECE yielded a V_{OC} of 0.81 ± 10 V, a J_{SC} of 11.0 ± 0.8 mA/cm^2, a FF of 0.66 ± 0.01, and a PCE of 5.9 ± 0.3%, upon average over 10 devices. Relatively large FF value from these PSCs also provides indirect evidence of the excellent electron selectivity of the PEIE-modified ITO ECE [69,142]. It should be also noted that PCE values from these PSCs are

comparable with that previously reported in other inverted PSCs with the same photoactive layer.

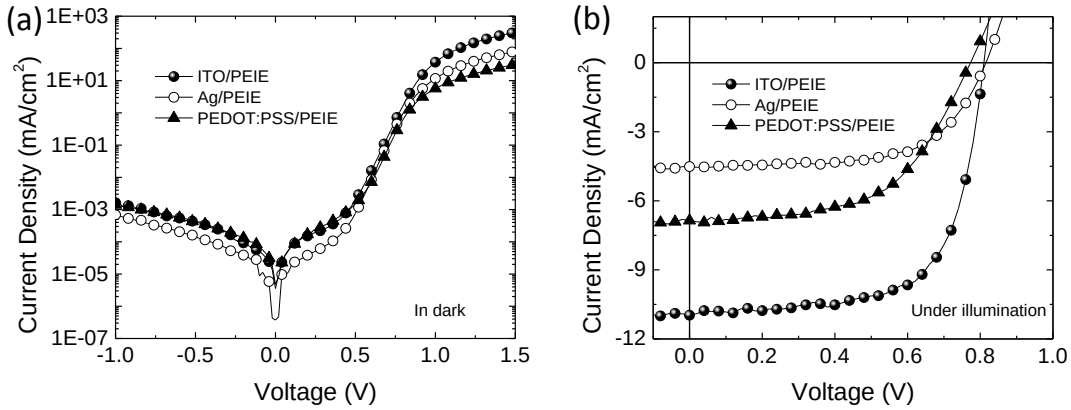

Figure 4.27 Representative *J-V* characteristics (a) in dark and (b) under illumination for a P3HT:$IC_{60}BA$-based polymer solar cell with electron-collecting electrodes of PEIE-modified ITO, PEIE-modified Ag, and PEIE-modified PEDOT:PSS (PH1000) electrodes.

A study on the shelf air stability of inverted PSCs with the ECE of PEIE-modified ITO was performed (Figure 4.28). For a comparison, conventional PSCs with the same photoactive layer, but a different ECE of a Ca/Al were also fabricated and tested. The PCE from the inverted PSCs was found to remain nearly constant after 30 days in air and was still about 70% of its initial value after 102 days, while device performance of the conventional PSCs degraded completely within 10 days.

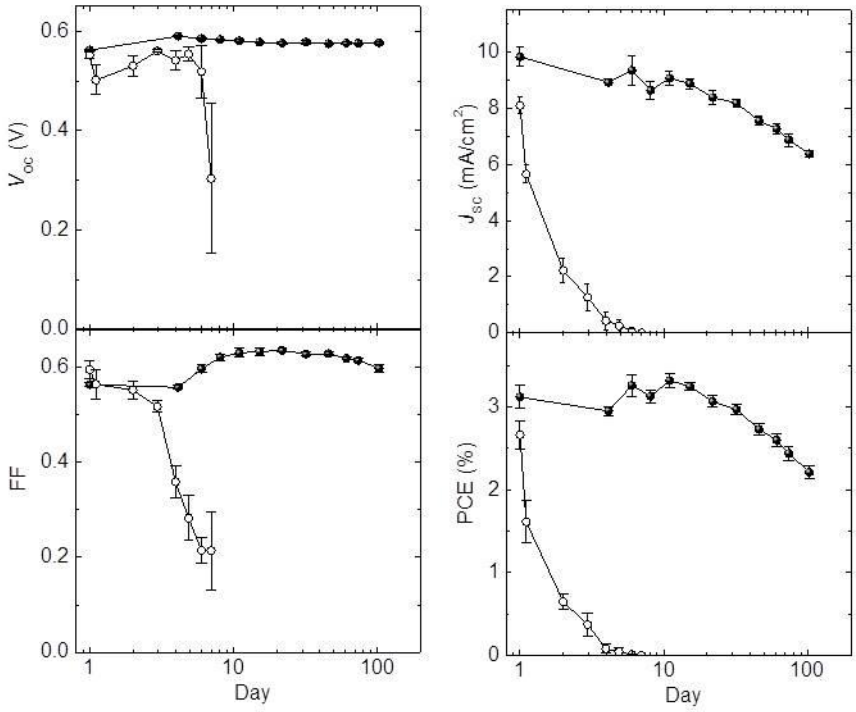

Figure 4.28 Device performance of solar cells with an inverted structure of glass/ITO/PEIE/P3HT: $PC_{60}BM$/PEDOT:PSS/Ag (filled circle, averaged over 5 devices) and a conventional structure of glass/ITO/PEDOT:PSS/P3HT:$PC_{60}BM$/Ca/Al (open circle, averaged over 9 devices), kept in air in the dark for up to 102 days.

In the case of the PSCs that use PEIE-modified Ag (80 nm) ECE at the bottom of the device, light illumination goes through the MoO_X (15 nm)/Ag (20 nm) HCE at the top of the device (Figure 4.26 (b)). In these devices, a relatively high FF of 0.60 is also measured but J_{SC} was lower (5.5 mA/cm^2) because of the low transmittance of the HCE at top of the device. As a result, the PCE was only 2.6%. PSCs with a PEIE-modified PEDOT:PSS (PH1000) ECE at the bottom of the device yielded a PCE of 3.5% (averaged over 5 devices), with a V_{OC} of 0.79 V, a FF of 0.57, and a J_{SC} of 7.6 mA/cm^2 (Figure 4.26 (c)). The slightly lower FF value is attributed to the increased R_S introduced by the relatively low conductivity of PH1000 (600 S/cm) compared to ITO or Ag, while the relatively small J_{SC} is mainly caused by the lower transmittance of PH1000 [74].

Table 4.6 summarizes the photovoltaic performances, averaged over ten devices, of all the PSCs evaluated.

Table 4.6 Summary of the averageda device performance of inverted P3HT:$IC_{60}BA$ solar cells with PEIE-modified ITO, PEIE-modified Ag, and PEIE-modified PEDOT:PSS (PH1000) as an electron-collecting electrode.

Electron-collecting electrodes	**V_{OC} (mV)**	**J_{SC} (mA/cm^2)**	**FF**	**PCE (%)**
ITO/PEIE	810±10	11.0±0.8	0.66±0.01	5.9±0.3
Ag/PEIE (Top illumination)	820±10	5.5±0.8	0.59±0.02	2.6±0.2
PEDOT:PSS (PH1000)/PEIE	790±30	7.6±0.2	0.57±0.02	3.5±0.3

[a] Average was calculated over ten devices

With the possibility to transform PEDOT:PSS into an efficient ECE upon modification, fully-polymeric solar cells on flexible substrates were fabricated; these highly flexible polymeric solar cells are fabricated in air on PES substrates using PEDOT:PSS as HCEs and PEI-modified PEDOT:PSS as ECEs. Figure 4.29 displays the *J-V* characteristics of the fully-polymeric solar cells in the dark and under illumination. The PSCs with PEI-modified PEDOT:PSS ECE showed excellent rectification in the dark. Under illumination, the PSCs with PEDOT:PSS/PEI ECE yielded an V_{OC} of 0.80 V, a J_{SC} of 7.1 mA/cm^2, a FF of 0.52, and a PCE of 3.0 %, averaged over 7 devices. The fully polymeric solar cells show similar V_{OC} to the PSCs with ITO/PEIE ECE (see Table 4.6). The smaller FF compared with the PSCs with ITO/PEIE ECE is attributed to the increased series resistance introduced by the relatively low conductivity of PH1000 compared to ITO or Ag (see Table 4.6), while the relatively small J_{SC} was mainly attributed to the lower transmittance of PH1000 and absence of the light reflector. However, PSCs without PEI layer did not show any rectification behavior because work function of PH1000 and PEDOT-blend are similar (Figure 4.29 (b)). The symmetric WF

of the two electrodes results in the symmetric *J-V* characteristics both in the dark and under illumination.

When a thick Ag layer (as a reflector) was placed behind the semitransparent fully-polymer solar cells, to make reflected light back into the photoactive layer, the J_{SC} increased to a value of 8.2 mA/cm^2, yielding a PCE of 3.4% (Figure 4.29 (c) and Table 4.7). These values are comparable to those measured in a device that uses a MoO_X/Ag HCE (see Table 4.6). Table 4.7 summarizes the photovoltaic performances, averaged over seven devices, of the evaluated fully polymeric solar cells with or without the Ag reflectors.

Table 4.7 Summary of the averageda device performance of P3HT:$IC_{60}BA$-based fully-polymeric solar cells with or without Ag reflector.

Ag reflector	V_{OC} **(mV)**	J_{SC} **(mA/cm^2)**	**FF**	**PCE (%)**
No	800±20	7.1 ± 0.4	0.52±0.02	3.0±0.1
Yes	800±20	8.3 ± 0.5	0.52±0.02	3.4±0.2

[a] Average was calculated over seven devices

Since the fully-polymeric PSCs only have polymer/polymer interfaces, good mechanical flexibility is expected. Figure 4.29 (d) shows the device performance of the fully polymeric devices with continuous bending averaged over three devices. The newly fabricated devices showed an average PCE of 2.55 %. After fixed on a radius of 5.4 mm and 3.9 mm for 30 min separately, devices exhibited an average PCE of 2.44 %. With continuous bending with radiuses of 6.3, 5.4 and 3.9 mm, 400 times for each, the average PCE was 2.40 %. It should be noted that the bending test was done after the device fabricated and kept in glove box for two weeks. The slight change of PCE of devices indicates that the devices have excellent mechanical flexibility.

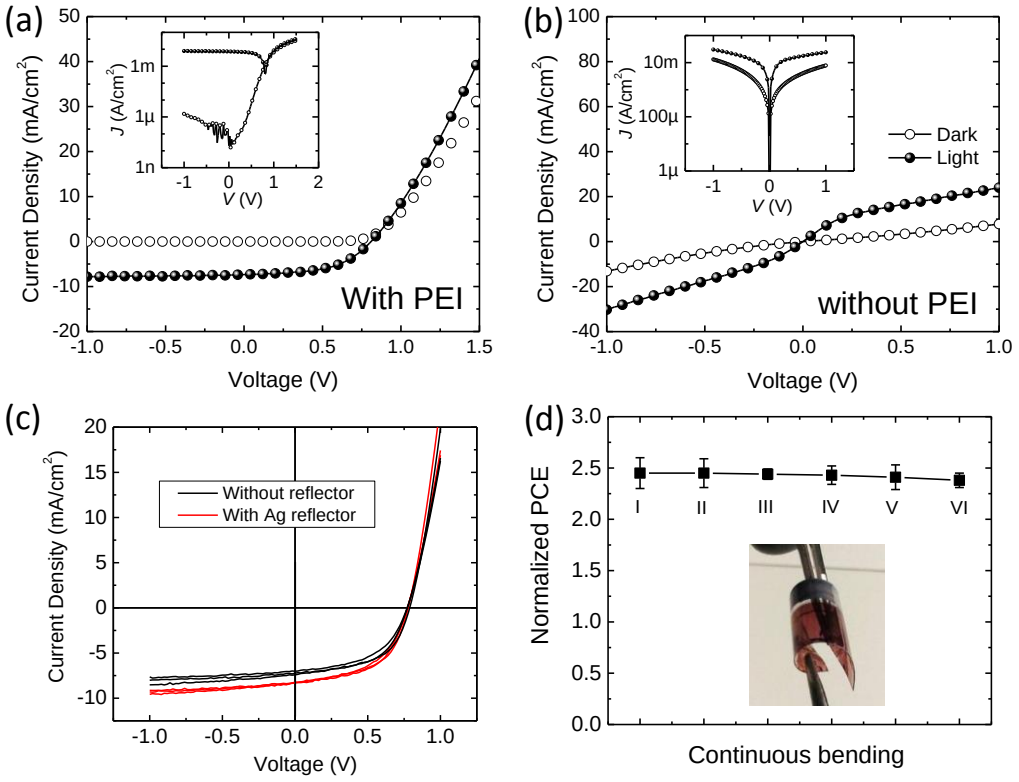

Figure 4.29 Representative *J-V* characteristics in dark (open circle) and under illumination (closed circle) for a P3HT:$IC_{60}BA$-based fully-polymeric solar cell (a) with or (b) without PEI modification on PEDOT:PSS layer at the bottom of the cells (c) *J-V* characteristics under illumination for P3HT:$IC_{60}BA$-based fully-polymeric solar cells with (red) or without (black) Ag reflector (d) Normalized PCE of fully-polymeric solar cells after continuous bending tests: Inset is a picture of bended cells. I: Newly fabricated, II: fixed on a roll with R = 5.4 mm, III: fixed on a roll with R = 3.5 mm, IV: bended 400 times with R = 6.3 mm, V: bended 400 times with R = 5.4 mm, and VI: bended 400 times with R = 3.9 mm

Finally, a study on the UV irradiation effect on the photovoltaic performance of the PSCs with the ITO/PEIE ECE was performed. Pristine PEIE-coated ITO samples displayed a WF value of 3.7 eV. Inverted PSCs with a structure of ITO/PEIE/C_{60}/CuPc/MoO_X/Ag were fabricated. One question that was raised after performing such surface modifications was how the WF of the combined ITO/PEIE

modifier electrode would be changed as a function of UV and air exposure. Figure 4.30 (a)-(d) display that the WF of the modified electrodes display a similar behavior to that observed in uncoated ITO electrodes (Figure 4.17 (a)-(d)). Also, it should be noted that PEIE has negligible absorption down to 300 nm, so absorption in this layer can be entirely neglected. Very interestingly, Figure 4.30 (a)-(d) shows that variations of the WF values of PEIE-coated ITO substrates remain below the minimum WF values of bare ITO under UV illumination and air exposure. Figure 4.30 (a)-(d) also shows that the change of the WF values induced by the UV illumination and air exposure are also reversible. As shown in Figure 4.30 (a) and (b) WF values of the ITO/PEIE electrode (3.5 eV – 3.7 eV) were smaller than the EA values of C_{60}. Therefore a better chance to be less sensitive to the effects produced by the absorption of photons in ITO can be expected.

Figure 4.30 (e) displays the temporal evolution of the *J-V* characteristics of the inverted PSCs (ITO/PEIE/C_{60}/CuPc/MoO_X/Ag) under 100 mW/cm^2 continuous illumination from a solar simulator (AM 1.5G). The PSCs before the solar simulator treatment yielded a V_{OC} of 0.41 V, a J_{SC} of 3.9 mA/cm^2, a FF of 0.60 and a PCE of 0.94%. As expected, after 51 minutes of the solar simulator treatment, the PSCs showed similar device performance with a V_{OC} of 0.41 V, a J_{SC} of 3.7 mA/cm^2, FF of 0.57 and PCE of 0.86% to those before the treatment.

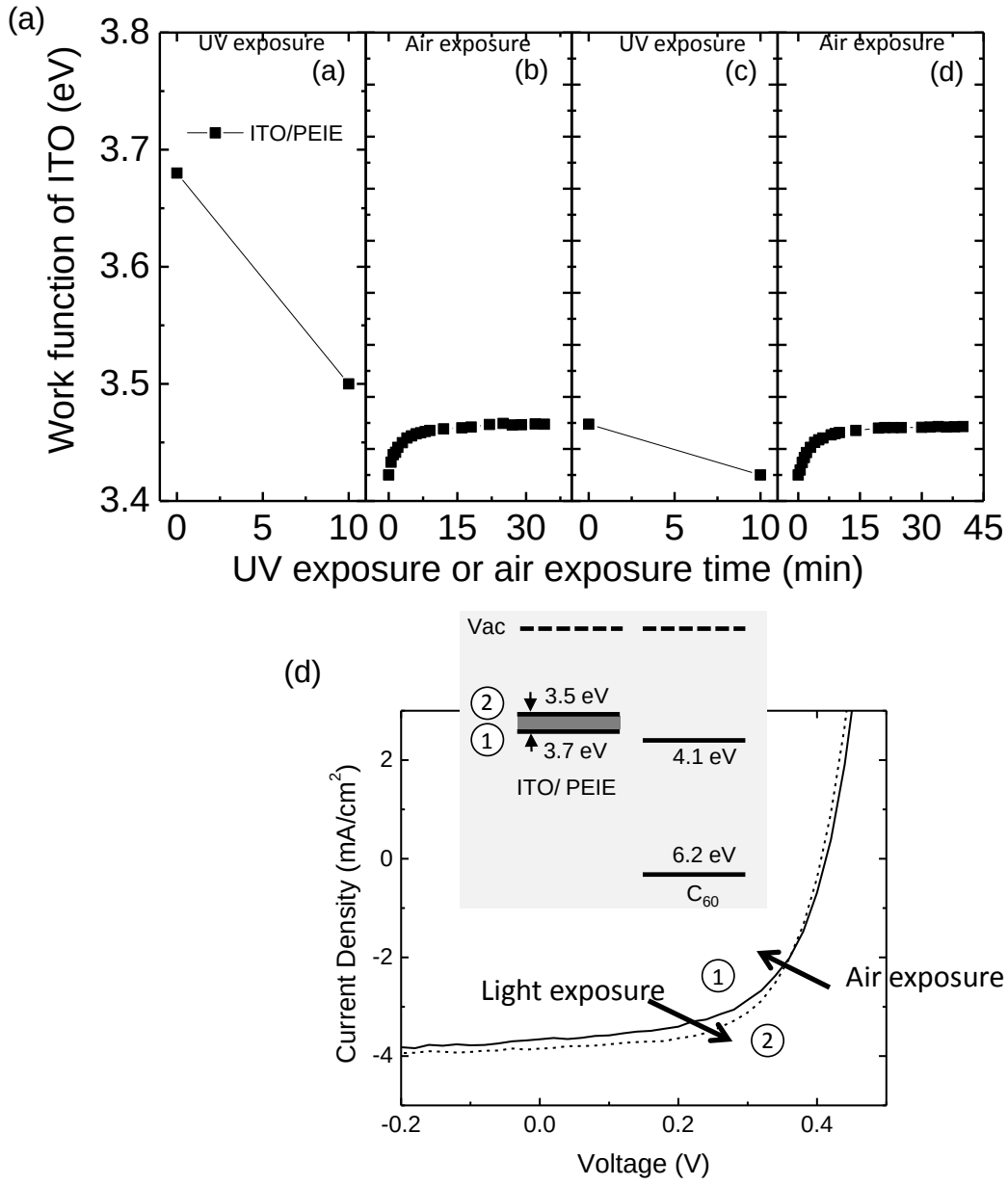

Figure 4.30 Work function of ITO/PEIE (filled square) with different treatments: (a) with simulated solar light exposure in a N_2-filled glove box and measured in air; (b) with air exposure and measured in air; (c) with simulated solar light exposure in a N_2-filled glove box and measured in air; (d) with air exposure and measured in air. (e) Energy diagram ITO/PEIE/C_{60} (band bending not considered when contact) where the shaded area represents the range of WF values of ITO/PEIE varying with air or UV exposure; Evolution of *J*-*V* curves under 100 mW/cm^2 AM1.5 illumination of devices soaked under solar simulator for different time with an inverted structure of ITO/PEIE/C_{60}/CuPc/MoO_X/Ag.

4.3.4 Conclusions

This section demonstrated a universal approach to reduce the WF of various conductors by applying polymer surface modifiers, such as PEIE and PEI, that contain simple aliphatic amine groups . The polymer surface modification enables the fabrication of air-stable low WF electrodes at very low cost from environmentally friendly solvents. With this modification, various types of efficient single-junction PSCs, including fully-polymeric solar cells, have been demonstrated. Besides the applications shown in this thesis, this polymer surface modification can be applicable to other applications with the further optimized specific properties of the polymers. Finally, this way should enable the mass production of low-WF electrodes from processes that are compatible with large-area roll-to-roll manufacturing techniques, and consequently the commercialization of PSCs.

CHAPTER 5

CHARGE RECOMBINATION LAYERS

In this chapter, new approaches for charge recombination layers (CRLs) in PSCs with an inverted tandem geometry will be discussed. As mentioned in Chapter 1, two major losses of solar cells such as sub-band-gap transmission and the thermalization of charge carriers, and two limitations typically shown in organic semiconductors such as narrow absorption bands and poor charge carrier transport can be overcome by realizing tandem solar cells. Tandem solar cells contain several single-junction solar cells with different absorption ranges. Broader solar spectrum can be absorbed by tandem solar cells and thereby the PCE can be increased. Generally in tandem OSCs, two or more single-junction OSCs have been stacked through CRLs. In the case of all sub-cells connected in series for a tandem OSC, the V_{OC} of all sub-cells can be added up, the J_{SC} of the tandem cell is limited to the smallest Jsc generated in any of the sub-cells, and consequently the PCE can be increased.

To realize efficient tandem PSC, selecting photoactive materials with complementary absorption is essential to obtain a high J_{SC}. Also, matching the photo-generated current between sub-cells connected in series is necessary to maximize the J_{SC} and consequently the PCE. In this thesis, two different polymers with different absorption ranges P3HT (E_G=2.52 eV) and PBDTTT-C (E_G=1.61 eV)) blended with fullerene derivatives ($PC_{60}BM$ or $IC_{60}BA$) will be employed as bottom cells (the first light-absorbing sub-cell) and top cells (the second light-absorbing sub-cell stacked on top of the bottom cell through a CRL) [49,149].

Another critical component to maximize the PCE of a tandem PSC is the CRL that connects two sub-cells in series. This layer allows holes to be collected, from one sub-cell, and be recombined with the electrons collected from the other sub-cell.

Therefore, the WF of one side of the recombination layer needs to be high enough to provide good energy level alignment with the IE of the donor material, in the adjacent sub-cell, for a hole to be collected effectively at that interface. The WF of the other side of the CRL should be low enough to provide adequate energy level alignment with the EA of the acceptor material, in the adjacent sub-cell, for an electron to be collected efficiently at that interface. In addition, the CRL should work as an efficient recombination center for collected electrons and holes. Furthermore, materials of a CRL are required to have low optical absorption in the spectral region of interest. From a practical perspective, in tandem solar cells wherein the top active layer is solution-processed, the CRL also needs to be mechanically robust enough to prevent damage of the bottom cell and of the CRL itself during the processing of the top cell.

In this thesis, three different CRLs will be introduced. Since the tandem PSCs discussed in this chapter use the inverted geometry, the high-WF layer is deposited first on top of the bottom cell and the low-WF layer is made on top of the high-WF layer. The first CRL will be composed of PEIE-modified MoO_X/Ag. In this CRL, the MoO_X serves as a hole selective layer, and the Ag layer is required to provide a better electrical connection between top and bottom cells. Finally, modification of the MoO_X/Ag with a polymeric surface modifier, PEIE, is found to further reduce the WF of MoO_X/Ag and significantly improve the performance of this CRL. The second CRL will comprise of PEIE-modified MoO_X/Al_2O_3:ZnO nanolaminates. The MoO_X works as a hole-collecting layer. Differently from the previous CRL, the Al_2O_3:ZnO nanolaminates serves as the electron-collecting layer in this CRL. The surface modification with PEIE on the MoO_X/Al_2O_3:ZnO nanolaminate improves the WF contrast leading to further enhanced the performance of tandem PSCs. The last CRL is made up with the conducting polymer PEDOT:PSS modified at one interface with PEIE. While the previous CRLs are made by stacking a low-WF layer on a high-WF layer, this CRL is realized by modifying one side

of a single layer. Furthermore, this CRL is made up with only polymeric materials and can be processed from solution. The PEDOT:PSS collects holes from the bottom cell and PEIE-modified side collects electrons from the top cells.

5.1 Polyethylenimine Ethoxylated (PEIE)-Modified Molybdenum Oxide (MoO_X) / Silver (Ag) as the Charge Recombination Layer

5.1.1 Introduction

The CRL is an essential component to maximize the PCE of a tandem PSC. To date, a common approach to realize a CRL is to use a first layer comprising materials with a high-WF, typically MoO_X or PEDOT:PSS, and a second layer comprising a low-WF metal such as Ca or a metal oxide such as ZnO. In some cases, an ultrathin (non-continuous) layer of a metal such as Al or Ag is inserted between the first and second layers [116,117]. The use of a reactive metal such as Ca is not desirable in an inverted structure. On the other hand, the use of ZnO, having a WF of around 4.3 eV, may limit the number of acceptor materials for which it provides efficient electron collection [67].

In this section, the first use of PEIE in a CRL of inverted tandem PSC structure is introduced. The tandem PSC uses a PEIE (12 nm)-modified MoO_X (6 nm)/Ag (1 nm) as a CRL. MoO_X serves as a hole-collecting layer since it displays a large value of IE and is strongly n-doped by oxygen vacancies. The EA, WF, and IE are 6.7 eV, 6.9 eV, and 9.7 eV, respectively [150]. These energy levels allow MoOx to efficiently collect holes from the bottom cell efficiently. The use of an ultrathin Ag layer has been claimed to provide better electrical connection between top and bottom cells [87,151]. The use of a polymer surface modifier, PEIE, induces a WF reduction on the Ag side of the MoO_X/Ag layer, allowing the interface to serve as an efficient electron collecting layer in the CRL.

In this study, an analysis of the optical, electrical, and morphological properties of the CRL is conducted. An investigation of the photovoltaic performance of P3HT:PC_{60}BM-based inverted tandem PSCs with this CRL is performed. The photovoltaic properties from the tandem PSCs are compared with those of single-junction

PSCs and tandem PSC with a CRL comprising only MoO_X/Ag layer. Finally, a shelf air stability study of the tandem PSC with the CRL of PEIE-modified MoO_X/Ag is conducted.

5.1.2 PEIE-modified MoO_X/Ag Charge Recombination Layer Characterization

Figure 5.1(a) displays the refractive index and extinction coefficient of MoO_X, Ag on MoO_X and the Ag/PEIE composite obtained by spectroscopic ellipsometry. Figure 5.1(b) shows a comparison of the measured transmittance of MoO_X, MoO_X /Ag and PEIE-modified MoO_X /Ag films deposited on glass substrates and the simulated transmittance values using the refractive index values shown on Figure 5.1(a).

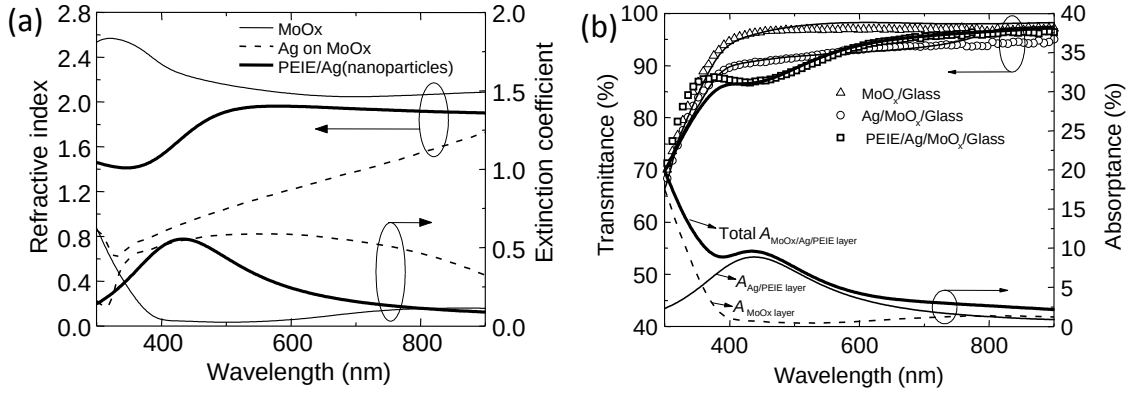

Figure 5.1 (a) Refractive index and extinction coefficient of MoO_X (6 nm) (thin solid line), Ag (1 nm) on MoO_X (6 nm) (thin dotted line), and PEIE (12 nm)/Ag (1 nm) (nanoparticles) (thick solid line) (b) Optical transmission and absorptance of the MoO_X (6 nm) (open triangle, thin dotted line), MoO_X (6 nm)/Ag (1 nm) (open circle, thin solid line), and MoO_X (6 nm)/Ag (1 nm)/PEIE (12 nm) (open square, thick solid line) layer.

Interestingly, the refractive index profile of the Ag layer initially deposited on MoO_X was derived assuming Bruggeman's effective medium approximation [152]. This type of approximation describes clusters or interconnected domains of nanoparticles with

broad plasmon resonances, as shown in Figure 5.1(a). However, as PEIE is spin-casted onto the Ag layer, the refractive index of the PEIE/Ag layer resembles that of isolated nanoparticles with a much narrower and well defined plasmon resonance. The refractive index of this layer was derived assuming spherical nanoparticles and using a Maxwell-Garnett approximation with an Ag fill factor of 0.14. It is clear from Figure 5.1(b) that both approximations yield very reasonable fits to the measured transmittance values. Hence, the spin-coating of PEIE has the effect of not only coating the Ag film underneath, but effectively changing the morphology of the Ag layer.

As a final remark on the optical properties of the CRL deposited on glass, the simulated absorptance of this layer is shown in Figure 5.1(b) along with the individual contributions to the absorptance coming from the MoO_X layer and the composite layer comprising Ag nanoparticles coated by PEIE. This shows that the Ag/PEIE layer present a parasitic absorptance (since it is not expected to give rise to any current but to be converted into heat) within the visible spectral range in air, reaching a peak absorptance of 9% at 438 nm. When embedded in a tandem PSC, this absorption can be expected to increase at certain wavelengths because some amount of the optical field will bounce back from the reflective electrode in the cell. However, since light will go first through the front cell, as long as the front cell heavily absorbs in the same spectral range as the nanoparticle layer, the amount of light absorbed in this layer will likely be reduced. For tandem PSCs using the proposed CRL and optimum material combinations with complementary absorption spectra, the refractive index (n) values shown in Figure 5.1(a) could serve as a guideline for simulations of the optical field distribution in those cells.

The change in the WF of the CRL was followed via UPS under vacuum and a Kelvin probe measurement in ambient. As reference samples, 70-nm-thick Au-coated glass slides and glass/ITO substrates were employed for UPS and Kelvin probe measurements, respectively. Figure 5.1(a) presents the dependence of the WF on layers

comprising the CRL. The WF values of the Au-coated glass and the glass/ITO substrates were 5.1 eV (by UPS) and 4.6 (by Kelvin probe), respectively. After depositing the 6-nm-thick MoO_X layer, the WF of the Au-coated glass remained around 5.0 eV (by UPS) while that of the glass/ITO substrate jumped up to 5.25 eV (by Kelvin probe). These WF values are considerably lower than WF values shown from freshly made MoO_X layers, which are usually higher than 6.5 eV [52]. The reason is that the present MoO_X films were exposed to ambient air for significant periods of time, either for Kelvin probe measurements in ambient air at Georgia Tech. or during transfer to Princeton for UPS, and ambient air contaminated MoO_X was found to exhibit the reduced WF value [56]. Yet, the important interface here is the buried MoO_X interface contacting the P3HT of the bottom cell, and this interface presumably involves "clean", unexposed, MoO_X with a significantly larger WF. In any case, even the reduced WF of the MoO_X is sufficiently high to produce effective hole-extraction from the donor polymer P3HT of the bottom cell, which has an IE of 4.7-4.9 eV [153] .

A 1-nm-thick Ag layer was found to produce no change of the WF with respect to a MoO_X film deposited on a Au-coated glass sample (5.0 eV by UPS). Although this ultrathin Ag layer does not form a continuous film on top of MoO_X layer, as confirmed by the optical characterization, it has been claimed to be required to provide a better electrical connection between the bottom and top cells [87,151].

In Chapter 4.3, it was found that the physisorption of neutral amine containing polymer, PEIE induces a WF reduction of large variety of conductors [62]. Consistent with previous observations, significantly reduced WF values, 3.6 eV (by UPS) and 3.8 eV (by Kelvin probe), were achieved after the PEIE modification on MoO_X/Ag layers. These WF values are sufficiently low to provide efficient electron selectivity since the EA of the $PC_{60}BM$, is around 3.8 eV [153].

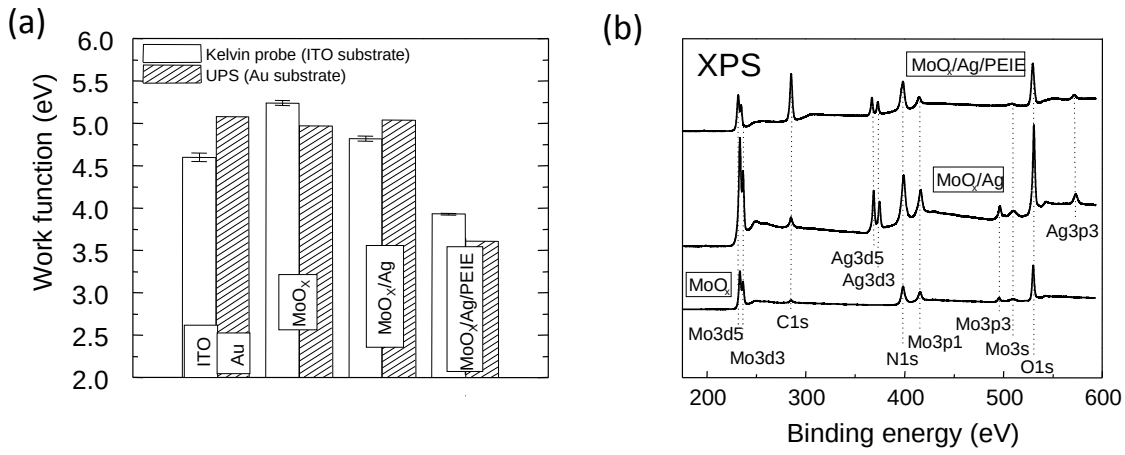

Figure 5.2 (a) Work function of MoO_X (6 nm), MoO_X (6 nm)/Ag (1 nm), and MoOX(6 nm)/Ag (1 nm)/PEIE (12 nm) layer on glass/ITO substrate by a Kelvin probe (blank column) and on glass/Au (70 nm) substrate by UPS (shaded column), (b) XPS data of MoO_X (6 nm) (bottom), MoO_X (6 nm)/Ag (1 nm) (middle), and MoO_X (6 nm)/Ag (1 nm)/PEIE (12 nm) layer (top).

To confirm the presence and surface homogeneity of MoO_X, Ag, and PEIE at the CRL, an XPS measurement on glass/MoO_X, glass/ MoO_X /Ag, and glass/ MoO_X /Ag/PEIE was performed. As shown in Figure 5.2(b), Ag core levels and some MoO_X peaks were still observed even after the PEIE deposition. This is indicative that the PEIE layer is thin-enough for the X-rays to penetrate through it, or, those regions with high- and low-WF values may be present at the top surface of the CRL.

5.1.3 Characterization of Solar Cells Performance

The performance of inverted tandem PSCs with the structure of glass/ITO/PEIE/P3HT:$PC_{60}BM$/MoO_X/Ag/PEIE/P3HT:$PC_{60}BM$/MoO_X/Ag, as shown in Figure 5.3(a), was investigated. To compare the photovoltaic performance, a single-junction PSC with structure: glass/ITO/PEIE/P3HT:$PC_{60}BM$/MoO_X/Ag (Figure 5.3(b)),

and a tandem PSC with structure: glass/ITO/PEIE/P3HT:$PC_{60}BM$/ MoO_X/Ag/P3HT:$PC_{60}BM$/MoO_X/Ag were fabricated as reference cells.

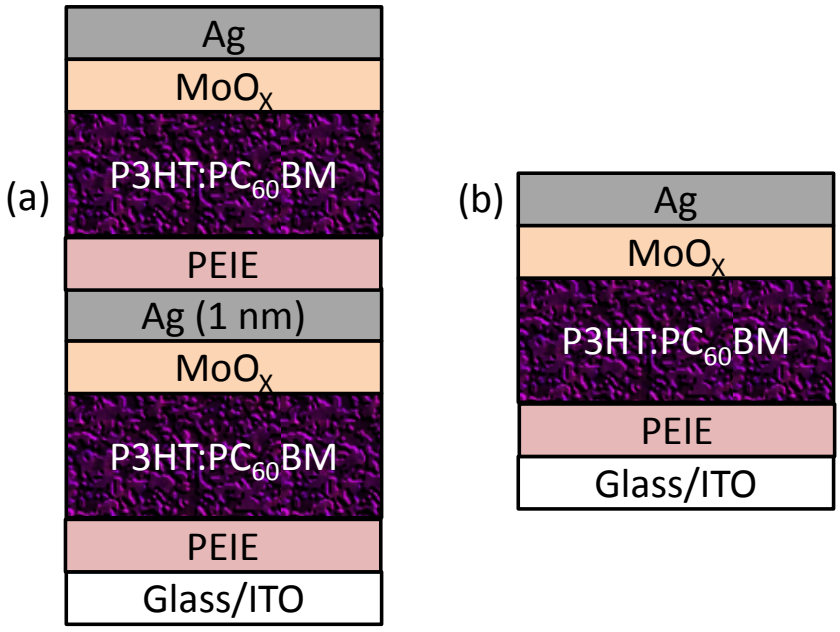

Figure 5.3 (a) Device structure of an inverted tandem P3HT:$PC_{60}BM$ solar cell with a charge recombination layer of PEIE modified MoOx/Ag layer and an inverted single-junction P3HT:$PC_{60}BM$ solar cell.

Figure 5.4(a) shows a comparison between the *J-V* characteristics under illumination measured on these reference cells and on the inverted tandem PSCs with the novel CRL. Table 5.1 summarizes the photovoltaic performance, averaged over five devices, of all PSCs cells evaluated.

Reference single-junction PSCs showed a PCE of 2.8 ± 0.1 % with a V_{OC} of 631 ± 5 mV, a J_{SC} of 7.0 ± 0.1 mA/cm^2, and a FF of 0.63 ± 0.02. Reference tandem PSCs, without a PEIE modification on the MoO_X/Ag layer, displayed a V_{OC} of 503 ± 31 mV

comparable to that of single-junction reference cells, indicating that the non-continuous Ag layer, by itself, does not provide adequate electron collection at the CLR. Hence, the reference tandem cell performs similarly to a single-junction cell with an increased R_S, reflected by the smaller FF of 0.52 ± 0.06; and consequently shows a poor PCE of 1.1 ± 0.3 %. In contrast, tandem PSCs with the CRL of a PEIE-modified MoO_X/Ag show an enhanced photovoltaic performance with a V_{OC} of 1042 ± 6 mV. Similar to prior results [87], these tandem PSCs achieve 83% of the ideal V_{OC} value (the addition of the V_{OC} of top and bottom cells). However, a high value of FF of 0.62 ± 0.01 (similar to single-junction cells) allows these tandem PSCs to achieve a PCE of 2.1 ± 0.1 %. As is clear from these results, the main limitation on the performance of the tandem PSC is therefore the small J_{SC} obtained by the use of the same photoactive layer for the top and bottom cells, and not the intrinsic properties of the CRL. Namely, by using the same thicknesses for the photoactive layers in the tandem and single-junction reference PSCs, the total absorption in both types of cells is expected to be very similar. However, the total absorption in the tandem cell is roughly split in half between the top and bottom cells. Consequently, the J_{SC} generated in each subcell, thereby in the tandem cell, is roughly half (3.2 mA/cm^2) of the J_{SC} generated in a single-junction reference cell (7.0 mA/cm^2). This issue can easily be overcome by employing photoactive layers with complementary absorption spectra for the bottom and top cells.

Although the use of the ECE of Ca/Al at the top of devices has been found to lead to tandem PSCs with high values of V_{OC} and FF, the limited environmental stability of Ca or LiF/Al constitutes a limitation for the environmental stability of PSCs in general [62]. Figure 5.4(b) displays the ambient air stability of tandem PSCs with PEIE modified MoO_X/Ag CRL. None of the photovoltaic performance parameters of the tandem PSCs, V_{OC}, J_{SC}, FF, and PCE, show any significant degradation when exposed to air for more than 140 hours.

Table 5.1. Summary of the averaged[a] device performance of inverted single-junction and tandem P3HT:$PC_{60}BM$-based solar cells with MoO_X/Ag/PEIE and MoO_X/Ag as a charge recombination layer.

Single-junction or Tandem (CRL)	V_{OC} **(mV)**	J_{SC} **(mA/cm^2)**	**FF**	**PCE (%)**
Single-junction	631 ± 5	7.0 ± 0.1	0.63 ± 0.02	2.8 ± 0.1
Tandem (MoO_X/Ag/PEIE)	1042 ± 6	3.2 ± 0.1	0.62 ± 0.01	2.1 ± 0.1
Tandem (MoO_X/Ag)	503 ± 31	4.0 ± 0.7	0.52 ± 0.06	1.1 ± 0.3

[a] Average was calculated over five devices

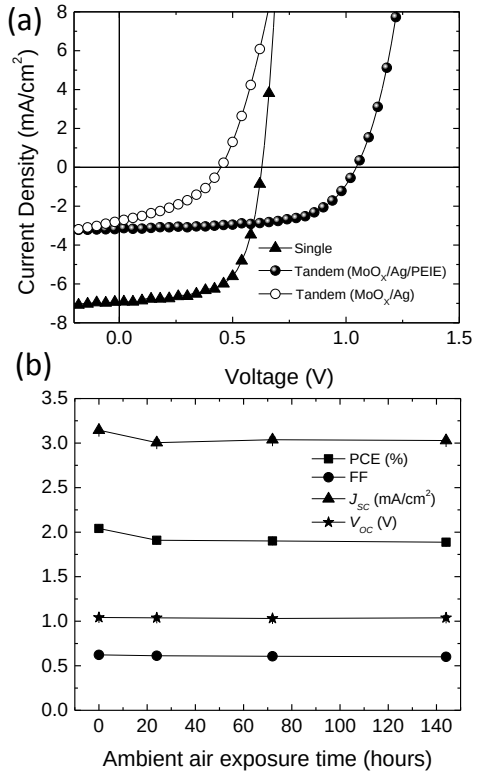

Figure 5.4 (a) Representative *J-V* characteristics under illumination for inverted P3HT:$PC_{60}BM$-based solar cells with a single-junction structure (triangle), a tandem structure with MoO_X/Ag/PEIE (closed circle), and a tandem structure with MoO_X/Ag (open circle), (b) PCE (%, square), fill factor (circle), J_{SC} (mA/cm^2,triangle), and V_{OC} (V, star) change of inverted tandem P3HT:$PC_{60}BM$-based solar cells with a MoO_X/Ag/PEIE charge recombination layer as a function of ambient air exposure time

5.1.4 Conclusions

Tandem cell geometries provide a potential solution to PSCs with high PCE. Inverted tandem PSCs studied in this section provided a proof-of-principle demonstration of the effectiveness of the PEIE-modified MoOx/Ag as a CRL. In particular, the importance of the WF contrast of CRLs was presented. Modification of bilayers of MoOx/Ag with PEIE was found to significantly improve the performance of these CRLs. The improvement was assigned to a significant reduction of the Ag WF by 1.5 eV with PEIE. The tandem cells yielded a V_{OC} of 1042 mV (83% of the addition of the V_{OC} of top and bottom cells) and a FF of 0.62, comparable to those of single-junction cells (0.63) under simulated AM 1.5G, 100 mW/cm^2 illumination.

However, the smaller than expected V_{OC} is an indication that the CRL will still need further optimization. A way to optimize the CRL will be to replace the ultrathin Ag layer with an electrically conductive and optically transparent material. In one hand, this material should provide a more uniformly covered MoO_X layer, and on the other hand, should not produce a large surface roughness, which is typical of non-continuous metal layers.

Lastly, no significant degradation of photovoltaic performance parameters was seen with more than 140 hours in ambient air, revealing that the inverted geometry avoiding the use of reactive low-work function metal electrodes are attractive for the air stability of PSC

5.2 Polyethylenimine Ethoxylated (PEIE)-Modified Molybdenum Oxide (MoO_X) / Aluminum Oxide (Al_2O_3):Zinc Oxide (ZnO) Nanolaminate as the Charge Recombination Layer

5.2.1 Introduction

Even though the CRL discussed in Chapter 5.2 exhibited efficient charge recombination properties in the tandem PSCs, it still has rooms for improvement. In particular, the low-WF component of the CRL comprising PEIE-modified ultrathin Ag layer in the CRL needs to be replaced with a film that provides uniform coverage, electrically high conductivity, and optical transparency. In addition, photoactive layers of the bottom and top cells should be substituted by two different materials with complementary absorption ranges. In this section, an inverted tandem PSC with a new low-WF component in the CRL and two photoactive layers with different absorption range is introduced.

To date, the most efficient inverted tandem PSCs have employed ZnO as the low-WF component in the CRL [89,111]. However, the electrical properties of ZnO, such as conductivity, differ depending on processing methods. For example, tandem PSCs with CRL containing ZnO nanoparticles, have shown S-shape kinks in the *J-V* characteristics due to the relatively low conductivity of the ZnO layer [154]. Among different processing methods, ALD provides one of the most reliable methods to consistently produce ZnO layers of high quality and presumably with larger conductivities than obtained by other methods [67,78,154,155]. The electrical conductivity of the ZnO layers processed by ALD is around 2×10^2 S/cm [67,78]. Recently, the Kippelen research group demonstrated that ALD-processed Al_2O_3:ZnO nanolaminate can display even higher conductivity values up to 1×10^3 S/cm and have optical transparency higher than 80 % in visible range. Nanolaminate films also retains a WF value of 4.0 ± 0.2 eV (by UPS) which is similar to

WF value of ZnO (3.96 eV by UPS) [78]. Hence, using the Al_2O_3:ZnO nanolaminate in the CRL can minimize the effects of having low conductivity values in its electron-collecting side. Moreover, since the ALD process can provide well-controlled layer-by-layer growth of highly conformal and uniform films, the use of an Al_2O_3:ZnO nanolaminate layer can resolve the issues induced by the ultrathin Ag in the PEIE-modified MoO_X/Ag CRL such as large surface roughness and reduced optical transparency [67,78]. As shown in Chapter 4.3, a surface modification with PEIE can provide a WF reduction of many different metal oxides including ITO, FTO, and ZnO. In particular, WF of ZnO decreased from 3.96 eV to 3.55 eV (by UPS) after the PEIE modification. The PEIE modification of Al_2O_3:ZnO nanolaminate could provide a lower WF value, and presumably lead to better electron-collection than that of Al_2O_3:ZnO nanolaminate only electron-collecting layer.

The CRL discussed in this section comprises a first layer of MoO_X followed by a second layer of Al_2O_3:ZnO (1:20) nanolaminate and a third layer of PEIE. Similarly to the role of the MoO_X in the PEIE-modified MoO_X/Ag CRL, the MoO_X here also works as a hole-collecting layer. The PEIE-modified Al_2O_3:ZnO nanolaminate serves as an electron-collecting layer.

To maximize the J_{SC} of tandem PSC, it is necessary to select two sets of photoactive materials having complementary absorption. In addition, the two photoactive layers need to generate similar currents when distributed in the tandem cell geometry. The tandem PSC discussed in this section uses a large E_G donor polymer of P3HT (E_G = 2.52 eV) [149] mixed with $IC_{60}BA$ and a small E_G donor polymer of PBDTTT-C (E_G=1.61 eV) [49] blended with $PC_{60}BM$ as the photoactive layers for the bottom cell and the top cell, respectively.

In this study, an analysis of the optical, electrical, and morphological properties of the CRL comprising MoO_X/Al_2O_3:ZnO nanolaminate/PEIE is conducted. An investigation of the photovoltaic performance of P3HT:$IC_{60}BA$ and PBDTTT-C:$PC_{60}BM$-based inverted tandem PSCs with the CRL is performed. A comparison of the photovoltaic properties of the tandem PSCs with those of two independent single-junction PSCs (having P3HT:$IC_{60}BA$ or PBDTTT-C:$PC_{60}BM$ photoactive layers), and three independent tandem PSCs, with different CRLs (MoO_X, PEIE-modified MoO_X/ZnO, or MoO_X/Al_2O_3:ZnO) is conducted.

5.2.2 PEIE-modified MoO_X/Al_3O_3:ZnO nanolaminate Charge Recombination Layer Characterization

An XPS study was performed by following the Mo3d peak to study the growth of the Al_2O_3:ZnO nanolaminate on MoO_X. Figure 5.5 shows a comparison of the XPS data obtained on none, 3, 5, and 10 nm-thick Al_2O_3:ZnO nanolaminates deposited on glass/ITO/PEIE/P3HT:$IC_{60}BA/MoO_X$ substrates. The Mo3d peak intensities are shown to decrease as the thickness of the Al_2O_3:ZnO nanolaminates increases. This indicates a gradual increase of the coverage of the Al_2O_3:ZnO nanolaminate on MoO_X. Disappearance of the Mo3d peaks from the 10-nm-thick Al_2O_3:ZnO nanolaminate sample clearly shows that the MoO_X layer is fully covered by the Al_2O_3:ZnO nanolaminate. Hence, at least 10-nm-thick Al_2O_3:ZnO nanolaminate is necessary to yield a uniform coverage of the MoO_X layer. Hereafter, the 10-nm-thick Al_2O_3:ZnO nanolaminate will be considered in this study.

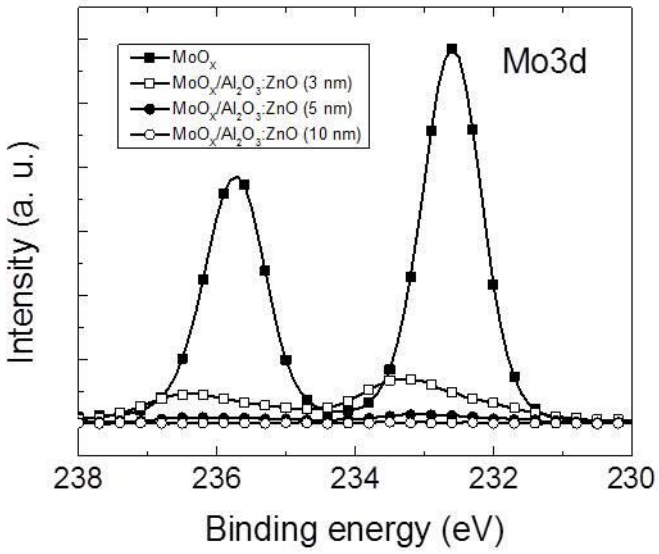

Figure 5.5 XPS spectra of the Mo3d core level for MoO_X (closed square), MoO_X/Al_2O_3:ZnO nanolaminates: 3 nm (open square), 5 nm (closed circle), and 10 nm (open circle) on glass/ITO/PEIE/P3HT:$IC_{60}BA$ substrates

Another XPS measurement was performed to confirm the presence of each layer in the CRL. For this XPS study, a glass substrate was used, rather than the glass/ITO/PEIE/P3HT:$IC_{60}BA/MoO_X$ substrates, to ease the identification of the nitrogen core level of PEIE. XPS studies on MoO_X films reveal the characteristic presence of the Mo3p3 and Mo3p1 peaks (Figure 5.6 (a)). Upon deposition of the Al_2O_3:ZnO nanolaminate, the Zn2p3 and Zn2p1 peaks appear on the XPS traces (Figure 5.6 (b)) as the Mo3d peak disappears from the survey (Figure 5.6 (d)), revealing good coverage and uniformity of the Al_2O_3:ZnO nanolaminates layer. Finally, the N1s peak from the amine groups in PEIE was easily detected (Figure 5.6 (c)). In this case, however, the Zn2p peak remained visible in the XPS surveys, revealing either the ultrathin nature of the PEIE layer or the non-uniform coverage of the PEIE layer.

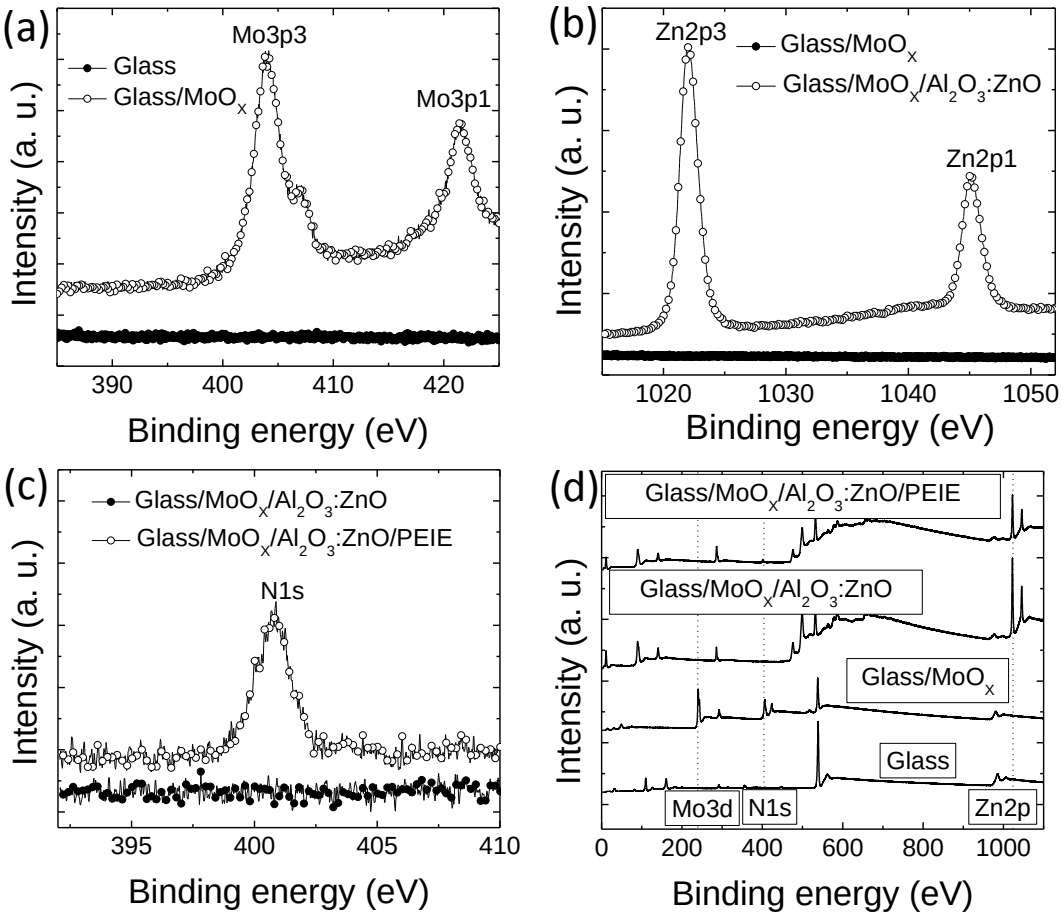

Figure 5.6 XPS spectra of (a) glass vs. glass/MoO_X, (b) glass/MoO_X vs. glass/MoO_X/Al_2O_3:ZnO nanolaminate, (c) glass/MoO_X/Al_2O_3:ZnO nanolaminate vs. glass/MoO_X/Al_2O_3:ZnO nanolaminate/PEIE, and (d) survey of glass, glass/MoO_X, glass/MoO_X/Al_2O_3:ZnO nanolaminate, and glass/MoO_X/Al_2O_3:ZnO nanolaminate/PEIE.

The topographic characterization of MoO_X, MoO_X/Al_2O_3:ZnO nanolaminate, and MoO_X/Al_2O_3:ZnO nanolaminate/PEIE films was conducted by AFM using glass/ITO/PEIE/P3HT:$IC_{60}BA$ substrates. AFM images of the surface of the different CRLs are shown in Figure 5.7. The surface roughness (RMS) values of the MoO_X, MoO_X/Al_2O_3:ZnO nanolaminate, and MoO_X/Al_2O_3:ZnO nanolaminate/PEIE films were 3.7, 3.2, and 0.6 nm, respectively. These results show that PEIE planarizes the surface of

the MoO_X/Al_2O_3:ZnO nanolaminate. The reduction of the surface roughness induced by PEIE modification is speculated to aid the electron selectivity of this interface [64].

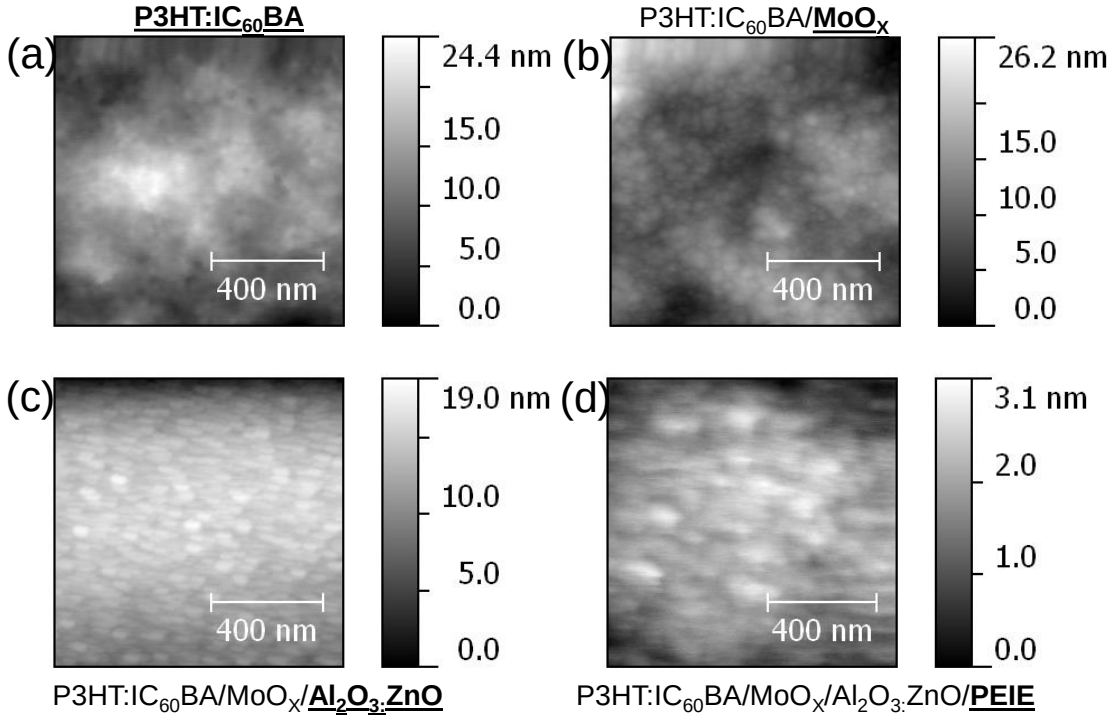

Figure 5.7 AFM images (height) of (a) glass/ITO/P3HT:$IC_{60}BA$, (b) glass/ITO/P3HT:$IC_{60}BA/MoO_X$ (20 nm), (c) glass/ITO/P3HT:$IC_{60}BA/MoO_X$ (20 nm)/Al_2O_3:ZnO nanolaminate (10 nm), (d) glass/ITO/P3HT:$IC_{60}BA/MoO_X$(20 nm)/Al_2O_3:ZnO nanolaminate (10 nm)/PEIE.

Figure 5.8 shows average values (over three spots in the sample) of the WF obtained in a MoO_X, MoO_X/Al_2O_3:ZnO nanolaminate, and MoO_X/Al_2O_3:ZnO nanolaminate/PEIE films deposited on ITO/glass substrates. For the WF studies, an ITO/glass substrate was used since the WF measurement by a Kelvin probe requires a conductive substrate. As a reference, the WF of clean ITO is included and shown to have

a value of 4.7 ± 0.05 eV. The MoO_X layer presented a WF of 5.3 ± 0.05 eV. After the deposition of the Al_2O_3:ZnO nanolaminate film the bilayer displayed a WF of 4.4 ± 0.03 eV. After spin coating the PEIE layer, the WF of the trilayer presented a value of 3.8 ± 0.05 eV. Using these values as a reference, it is expected that the MoO_X layer can provide good hole selectivity since its WF is larger than the IE of P3HT (5.1 eV). Therefore, reasonable device performance can be expected with the use of this CRL. This is because the WF of the Al_2O_3:ZnO nanolaminate layer is similar to that of ZnO and ZnO, despite having a WF that is larger than the EA of $PC_{60}BM$ (3.8 eV- 4.3 eV) [67,78], has been found to provide adequately efficient electron collection when employed in inverted single-junction PSC, and in the CRL of tandem PSC. However, the reduction of WF obtained by the introduction of the PEIE layer will be shown to play an important role in optimizing the CRL and the performance of the tandem PSC [71] .

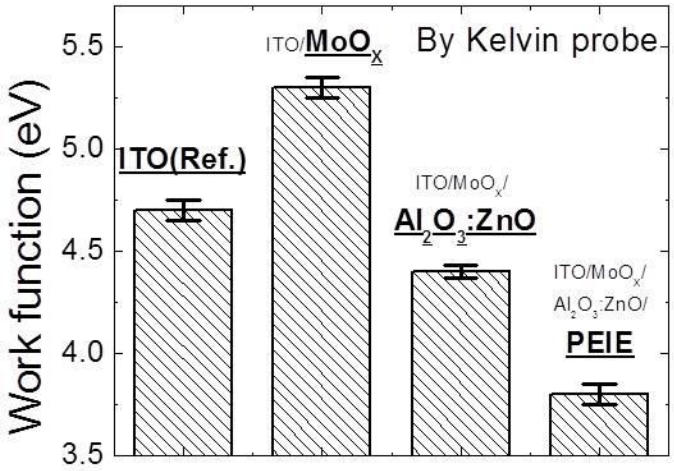

Figure 5.8 Work functions of glass/ITO (reference), glass/ITO/MoO_X, glass/ITO/MoO_X/Al_2O_3:ZnO nanolaminate, and glass/ITO/MoO_X/Al_2O_3:ZnO nanolaminate/PEIE by kelvin probe.

5.2.3 Characterization of Solar Cells Performance

Figure 5.9(a) displays the general device geometry of inverted tandem PSC introduced in this work. The photoactive layer of the bottom cell is a blend of P3HT and $IC_{60}BA$. The photoactive layer of the top cell is a mixture of PBDTTT-C and $PC_{60}BM$. Thicknesses of the photoactive layers of bottom and top cells were around 180 nm and 90 nm, respectively. The absorptance of two independent photoactive layers with P3HT:$IC_{60}BA$ and PBDTTT-C:$PC_{60}BM$ deposited on glass substrates is displayed in Figure 5.9(b). The absorptance of the P3HT:$IC_{60}BA$ film is strong in the range between 350 and 660 nm, which primarily arises from the π-π* transition in P3HT and only shows minor contributions from $IC_{60}BA$ in the UV range. In PBDTTT-C:$PC_{60}BM$ films, two relatively strong absorption bands near 400 nm appear due to $PC_{60}BM$ and at 660 nm due to PBDTTT-C. Therefore, the tandem PSC absorbs light from the visible range to the near-infrared (near-IR), up to around 800 nm.

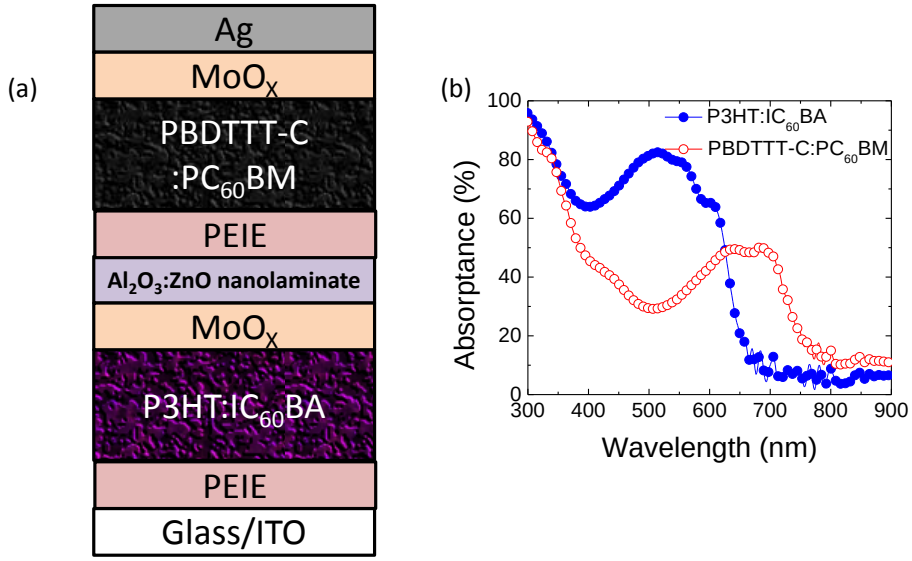

Figure 5.9 (a) Device structure of an inverted tandem P3HT:$IC_{60}BA$ (bottom cell) and PBDTTT-C:$PC_{60}BM$ (top cell) solar cell with a charge recombination layer of PEIE modified MoO_X/Al_2O_3:ZnO nanolaminate, (b) Absorptance of independent films of P3HT:$IC_{60}BA$ and PBDTTT-C:$PC_{60}BM$ deposited on glass substrates.

In this study, two single-junction PSCs and four tandem PSCs are introduced. The detailed device structures are described below:

Inverted single-junction PSCs:

- Glass/ITO/PEIE/P3HT:$IC_{60}BA$/MoO_X/Ag (**SB**)
- Glass/ITO/Al_2O_3:ZnO nanolaminate/PEIE/PBDTTT-C:$PC_{60}BM$/MoO_X/Ag (**ST**)

Inverted tandem PSCs:

- Glass/ITO/PEIE/P3HT:$IC_{60}BA$/MoO_X/Al_2O_3:ZnO nanolaminate/PEIE/PBDTTT-C:$PC_{60}BM$/MoO_X/Ag (**T1**)
- Glass/ITO/PEIE/P3HT:$IC_{60}BA$/MoO_X/Al_2O_3:ZnO nanolaminate/PBDTTT-C:$PC_{60}BM$/MoO_X/Ag (**T2**)
- Glass/ITO/PEIE/P3HT:$IC_{60}BA$/MoO_X/ZnO/PEIE/PBDTTT-C:$PC_{60}BM$/MoO_X/Ag (**T3**)
- Glass/ITO/PEIE/P3HT:$IC_{60}BA$/MoO_X/PBDTTT-C:$PC_{60}BM$/MoO_X/Ag (**T4**)

The *J-V* characteristics of 18 tandem PSCs of the devices **T1** were measured to exhibit its reproducibility. As shown in Figure 5.10, devices **T1** exhibit a V_{OC} = 1460 ± 14 mV, a J_{SC} = 8.2 ± 0.2 mA cm^{-2}, a FF = 0.58 ± 0.02, and a PCE = 6.9 ± 0.2%, averaged over 18 devices. The photoactive area of these devices was around 0.1 cm^2, but was determined accurately under a microscope for each individual device to extract their photovoltaic parameters. However, it should be noted that fringing effects caused by the highly conductive Al_2O_3:ZnO nanolaminate layer could impact the accuracy of the characterization of the photovoltaic parameters. A second batch of devices **T1** was characterized by using a 0.092 cm^2 aperture to define the active area. These, type T1 PSCs exhibited a PCE of 6.5 ± 0.1 % with a V_{OC} = 1481 ± 15 mV, a J_{SC} = 7.1 ± 0.1 mA cm^{-2}, and a FF = 0.62 ± 0.01. This second batch of devices **T1** yielded very comparable V_{OC} values to the first batch of devices **T1**. Slightly smaller J_{SC}, and consequently PCE

values, resulted from the improved accuracy of the characterization protocol used. Despite the small differences, when taken together these results underscore the high performance of the recombination layer and the good reproducibility of **T1** type devices.

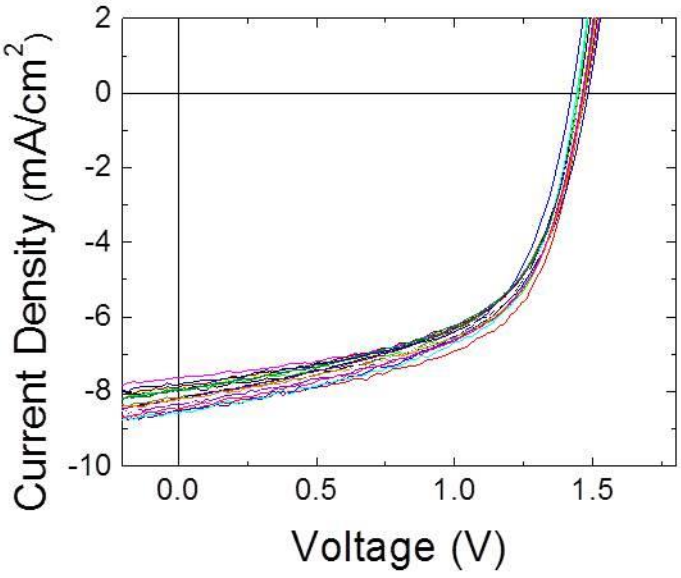

Figure 5.10 *J-V* characteristics under illumination of 18 devices **T1**. Note that the active area was around 0.1 cm^2 and determined accurately under a microscope for each individual device.

A comparison of the ***J-V*** characteristics under illumination and the semi-log |***J***|-***V*** characteristics in the dark of devices **SB**, **ST**, and **T1** is shown in Figure 5.11 (a) and (b). Devices **SB** displayed a PCE value of 4.7 ± 0.2 % with V_{OC} = 809 ± 4 mV, J_{SC} = 8.2 ± 0.1 mA cm^{-2}, and FF = 0.68 ± 0.03 while devices **ST** displayed a PCE value of 6.4 ± 0.1 % with V_{OC} = 677 ± 4 mV, J_{SC} = 15.3 ± 0.1 mA cm^{-2}, and FF = 0.62 ± 0.01. It is noteworthy that the V_{OC} of devices **T1** is statistically identical to the sum of the V_{OC} of two single cells (devices **SB**, **ST**). The photovoltaic performance parameters, averaged over 5 devices of each type, are summarized in Table 5.2.

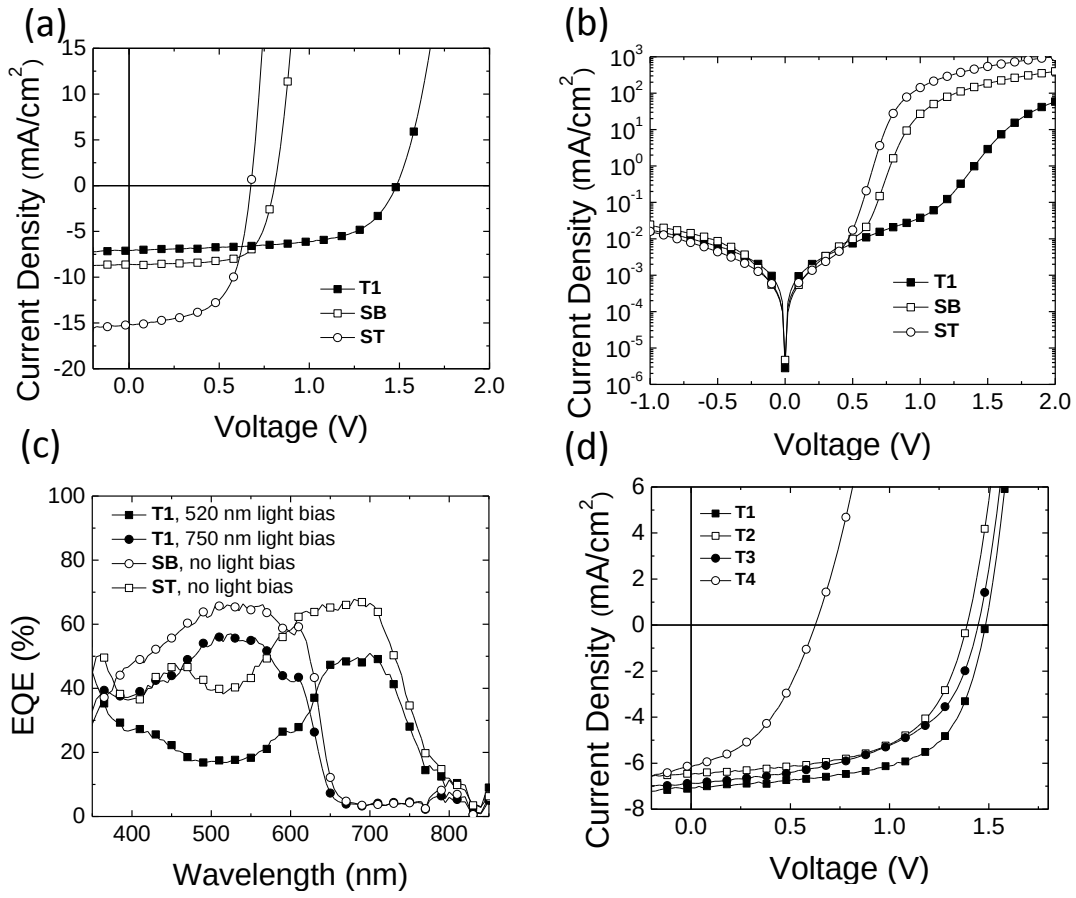

Figure 5.11 (a) Representative *J*-*V* characteristics under illumination for **SB** (open squares), **ST** (open circles), and **T1** (closed squares), (b) Representative |*J*|-*V* characteristics in the dark for **SB** (open squares), **ST** (open circles), and **T1** (closed squares), (c) EQEs of **T1** with 520 nm light bias (closed square) and with 750 nm light bias (closed circles), **SB** (open circles), and **ST** (open squares), and (d) Representative *J*-*V* characteristics under illumination for **T1** (closed squares), **T2** (open squares), **T3** (closed circle), and **T4** (open circles).

A comparison of the EQE spectra of two single-junction cells (devices **SB** and **ST**) and a tandem cell (devices **T1**) is shown in Figure 5.11 (c). The EQE spectra of the devices SB and ST are in good agreement with the absorptance spectra of the individual photoactive layers used in **SB** and **ST**, as shown in Figure 5.9 (b). Devices **SB** and **ST** showed maximum EQE values of around 66 % around 520 nm and around 67 % around 680 nm, respectively. The EQE spectrum of an individual sub-cell in a tandem cell geometry can also be extracted, and compared with that of single cells, if the devices are

illuminated with monochromatic light of constant intensity during the EQE measurement. By illuminating devices **T1** with light at 520 nm the bottom sub-cell can operate around the maximum power point while the top sub-cell present small absorption and photo-current; thus allowing for the EQE of top-subcell to be measured and compared with the values derived from device **SB**. Likewise, if device **T1** is illuminated with light at 750 nm, the EQE of the bottom sub-cell can be acquired and compared with that of device **ST**. As expected, the EQE of the two subcells in device **T1** closely follows the spectral shape of the single cells and demonstrate that **T1** can harvest photons up to 800 nm.

Table 5.2 Summary of the averaged photovoltaic performance parameters from single-junction (**SB** and **ST**) and tandem solar cells (**T1**, **T2**, **T3**, and **T4**). Averages taken over 5 devices for **SB**, **ST**, **T1**, **T2**, and **T4**, and 3 devices for **T3**.

Types	V_{OC} **(mV)**	J_{SC} **(mA/cm^2)**	**FF**	**PCE (%)**
SB	809 ± 4	8.2 ± 0.1	0.68 ± 0.03	4.7 ± 0.2
ST	677 ± 4	15.3 ± 0.1	0.62 ± 0.01	6.4 ± 0.1
T1	1481 ± 15	7.1 ± 0.1	0.62 ± 0.01	6.5 ± 0.1
T2	1410 ± 23	6.5 ± 0.1	0.58 ± 0.01	5.4 ± 0.3
T3	1439 ± 11	6.7 ± 0.2	0.52 ± 0.01	5.0 ± 0.2
T4	619 ± 13	6.4 ± 0.3	0.45 ± 0.02	1.8 ± 0.2

Figure 5.11(d) shows the EQE spectra of two single-junction cells (**SB** and **ST**) and the tandem cell (**T1**). The EQE spectra of the **SB** and **ST** are in good agreement with the absorptance spectra of the photoactive layers of the **SB** and **ST** shown in Figure 5.9(b). The **SB** and **ST** showed their maximum EQEs of around 66 % around the wavelength of 520 nm and around 67 % around the wavelength of 680 nm, respectively.

The application of a light bias was used to extract the EQE spectrum of an individual sub-cell from the tandem cell. With 520 nm of light bias, the **SB** can operate around the max-power point while the **ST** has negligible absorption, and thus the EQE of the **ST** can be obtained. Likewise, with 750 nm of light bias, the EQE of the **SB** can be acquired. The EQE of the **T1** revealed that the **T1** can harvest photons up to 800 nm and the bottom and top cells of the **T1** can contribute separately.

Finally, to see the effect of each layer at the CRL, the photovoltaic performances of four tandem PSCs, devices **T1**, **T2**, **T3**, and **T4**, were compared (Figure 5.11(d)). First, it is found that in the absence of an electron-collecting material in the CRL, devices **T4** (MoO_X CRL), two sub-cells in a tandem cell geometry act as a single cell. Devices **T4** show PCE values of 1.8 ± 0.2 % with V_{OC} of 619 ± 13 mV, J_{SC} of 6.4 ± 0.3 mA cm^{-2}, and FF of 0.45 ± 0.02. In the absence of PEIE, devices **T2** (MoO_X /Al_2O_3:ZnO CRL) display PCE values of 5.4 ± 0.3 % with V_{OC} of 1410 ± 23 mV, J_{SC} of 6.5 ± 0.1 mA cm^{-2}, and FF of 0.58 ± 0.01. The R_SA and R_PA values obtained from the *J-V* characteristics of **T2** were 3.1 ± 0.3 Ω cm^2 and 1100 ± 91 Ω cm^2, respectively. The performance of **T2** is worse than that of devices **T1**, which as previously reported reach PCE values of 6.5 ± 0.1 %. with V_{OC} of 1481 ± 15 mV, J_{SC} of 7.1 ± 0.1 mA cm^{-2}, FF of 0.62 ± 0.01. For devices **T1**, R_SA and R_PA are found to have values of 2.8 ± 0.2 Ω cm^2 and 1124 ± 28 Ω cm^2, respectively, which are very similar to those values found in devices **T2**. This demonstrates that the presence of PEIE in the CRL of devices **T1** does not introduce parasitic resistances to the cell but significantly improves the PCE value by 20% by increasing the values of V_{OC}, J_{SC} and FF. Although a detail description of the effects of PEIE in PSCs has not yet been fully understood it is speculated that the increased value of V_{OC} in devices **T1** induced by the presence of PEIE can arise by considering two effects: first that PEIE yields a significant reduction of the WF of the nanolaminate film, by 0.6 eV, bringing the value of the low-WF side of the CRL closer to the reported value of the EA (3.8 eV- 4.3 eV) [47]

of $PC_{60}BM$; and second that PEIE could potentially reduce trap-assisted recombination at the metal-oxide surface [71]. Both effects are believed to contribute to an improved electron collection efficiency by reducing recombination losses close to the CRL interface and would lead to increased V_{OC}, J_{SC} and FF values, as seen when comparing values in devices **T1** to those found in devices **T2**.

Lastly, giving the extensive use of ZnO as the low-WF layer in CRL reported in the literature, it is interesting to compare the performance of devices **T3**, comprising MoO_X/ZnO/PEIE as the CRL, with that of devices **T1**, comprising a MoO_X/Al_2O_3:ZnO nanolaminates/PEIE CRL. Devices **T3** show PCE values of 5.0 ± 0.2 % with V_{OC} of 1439 ± 11 mV, J_{SC} of 6.7 ± 0.2 mA cm^{-2}, and FF of 0.52 ± 0.01. The extracted R_SA and R_PA values from the *J*-*V* characteristics of device **T3** were 3.6 ± 0.2 Ω cm^2 and 619 ± 8 Ω cm^2, respectively. Here, the WF of both electron-collecting surfaces in the CRL is expected to be very similar in both types of devices [71]. Indeed, difference of V_{OC} values between devices **T1** and **T3** is only by 3%, while difference of the J_{SC} is by 6% and that of the FF is by 19%. It is believed that these differences come in part from the smaller electrical conductivity of ZnO compared to that of Al_2O_3:ZnO nanolaminates [78]. – inducing a larger series resistance in devices **T3.** While the exact origin of the much improved R_PA values in device **T1** compared to values in devices **T3** is unclear, according to previous reports [156,157], this can be ascribed to the improvement in the barrier properties of ALD nanolaminates compared to single-material ALD layers, leading to a CRL that chemically and mechanically more robust.

5.2.4 Conclusions

This section shows a new CRL for efficient inverted tandem PSCs. The CRL comprises a PEIE-modified bilayer of MoO_X/Al_2O_3:ZnO nanolaminates. Unlike the tandem PSC discussed in the previous section, the PSC demonstrated in this section uses two active layers with complementary absorption ranges, P3HT:$IC_{60}BA$ and PBDTTT-C:$PC_{60}BM$. This tandem PSCs displayed a PCE up to 6.5 % and almost perfectly summed V_{OC} from the sub-cells.

The CRL introduced here has several advantages. First, the use of the Al_2O_3:ZnO nanolaminate which has a higher electrical conductivity than that of ZnO, results in a lower R_sA, consequently providing about 6 % of J_{SC} increase and 19 % of FF increase. It should be noted that to date the most efficient inverted tandem PSCs have used ZnO as the electron collecting component in the CRL. Furthermore, the Al_2O_3:ZnO nanolaminate yields an increased R_PA that might be related to improved barrier properties from ALD nanolaminates than single-material ALD layers. In addition, the PEIE modification increases the WF contrast of the CRL by 0.6 eV, resulting in enhanced V_{OC} of the tandem PSC by 20 % than that of a tandem PSC without PEIE modification. Moreover, presumably, reduced trap-assisted recombination at the metal-oxide surface induced by the PEIE modification leads to increased electron selectivity.

However, further research related to device performance and processing methods is still needed. The photoactive layers employed in the bottom and top cells have a relatively big overlap in their absorption ranges. With new polymers utilizing the solar spectrum more efficiently, enhanced tandem device performance with this CRL is expected. Also, new techniques that can reduce processing time and cost are required. The fabrication processes of the MoO_X (thermal evaporation) and the Al_2O_3:ZnO nanolaminate (ALD) are done under vacuum and take a relatively long time (MoO_X:

more than 6 hours, Al_2O_3:ZnO nanolaminate: more than 3 hours). Despite their efficient charge collecting performance, these methods are still challenging. Thus, more cost-effective and less time-consuming fabrication methods such as solution processing should be considered.

5.3 Polyethylenimine Derivatives Modified PEDOT:PSS as the Charge Recombination Layer

5.3.1 Introduction

To date, some of low-WF components such as LiF, Ca, etc. and high-WF components such as MoO_X, etc. in CRLs in tandem PSCs need to be prepared in high vacuum [94,97,116,117,158,159]. More recently, all-solution processed CRLs such as PEDOT:PSS/ZnO [111,112] for the inverted geometry, and ZnO/PEDOT:PSS [103] and PFN/TiO_2/PEDOT:PSS [90] for the conventional geometry have been successfully applied to the tandem PSCs. Even though these all solution processable CRLs are highly desirable for large-area roll-to-roll manufacturing of PSCs, the use of crystalline inorganic materials may induce additional challenges regarding the mechanical flexibility of the PSCs. Furthermore, the use of PEDOT:PSS in combination with metal oxides with WF around 4.3 eV for the CRLs may not provide sufficiently high WF contrast between top and bottom interfaces of the CRL, which limits the range of photoactive materials that can be employed for realizing tandem PSCs.

As mentioned in Chapter 4.3, the PEIE or PEI can universally reduce the WF of conductors, including metals, metal oxides, conducting polymers and graphene [62]. Based on this discovery, PEIE-modified ITO, Ag and PEDOT:PSS (PH 1000) have been demonstrated as efficient ECEs (Chapter 4.3) in single-junction PSCs, and PEIE-modified MoO_X/Ag/PEIE (Chapter 5.1) and MoO_X/Al_2O_3:ZnO nanolaminates (Chapter 5.2) have been shown to work as efficient CRL in tandem PSCs. Furthermore, all-polymeric solar cells with a PEDOT:PSS HCEs and a PEI-modified PEDOT:PSS ECE has been introduced (Chapter 4.3).

Building upon these principles, this section demonstrates the use of conducting polymer PEDOT:PSS modified at one interface with PEIE as a simple, solution-processable all-polymeric CRL for inverted tandem PSC. In such CRL, the presence of a strong surface dipole induced by the PEIE leads to large WF contrast between the two opposite interfaces of the CRL in contact with the bottom and top cells in a tandem PSC where the sub-cells are connected in series. The surface of the PEDOT:PSS displays a high-WF of 4.9 eV, whereas the top surface shows a low-WF of 3.6 eV.

In this section, an analysis of electrical and optical properties of the CRL of PEIE-modified PEDOT:PSS (PH 1000) is conducted. An investigation of photovoltaic performance of P3HT:$PC_{60}BM$ and PBDTTT-C:$PC_{60}BM$-based inverted tandem PSCs with the CRL is performed. This is the same photoactive layers used in Chapter 5.2. A comparison of the photovoltaic properties of the tandem PSCs with those of two independent single-junction PSCs with P3HT:$IC_{60}BA$ or PBDTTT-C:$PC_{60}BM$ as the photoactive layers. Finally, investigation on photovoltaic performance of the inverted tandem PSCs with CRLs of PEI (branched PEI)-modified either highly conductive PEDOT:PSS (PH 1000) or lowly conductive (AI 4083) is performed.

5.3.2 PEIE-modified PEDOT:PSS Charge Recombination Layer Characterization

WF measurement by a Kelvin probe conducted on PEIE (10 nm)-modified PEDOT:PSS (PH1000) electrodes reveals that the WF of PEDOT:PSS (PH1000) decreases from 4.9 eV to 3.6 eV after the PEIE modification. Also, as demonstrated in Chapter 4.3, the thermally-annealed PEDOT:PSS (PH1000) layer is robust enough to avoid being dissolved by the aqueous PEIE solution. Hence, this chemical robustness as well as the large WF contrast in presented from the two opposite surfaces of the PEIE-midifed PEDOT:PSS make them very attractive for their use as a CRL. Furthermore, the

very low WF shown from the PEIE-modified interface should enable this CRL to work effectively with a wider range of acceptor materials, having even smaller EAs than typically-used fullerene derivatives.

The measured complex refractive index values ($N = n + ik$) of PEDOT:PSS (PH1000) and PEIE are shown in Figure 5.12. PEDOT:PSS (PH1000) displays complex refractive index dispersion characteristics that indicate its metallic nature. Namely, within the visible spectral region, the extinction coefficient (k) follows a spectral dispersion that is typical of a "free"-electron contribution, monotonically increasing with wavelength. Correspondingly, the refractive index (n) values are below 1 within this region. In contrast, PEIE shows the typical spectral dispersion for a lossless material (Cauchy dispersion characteristics) within the visible spectra.

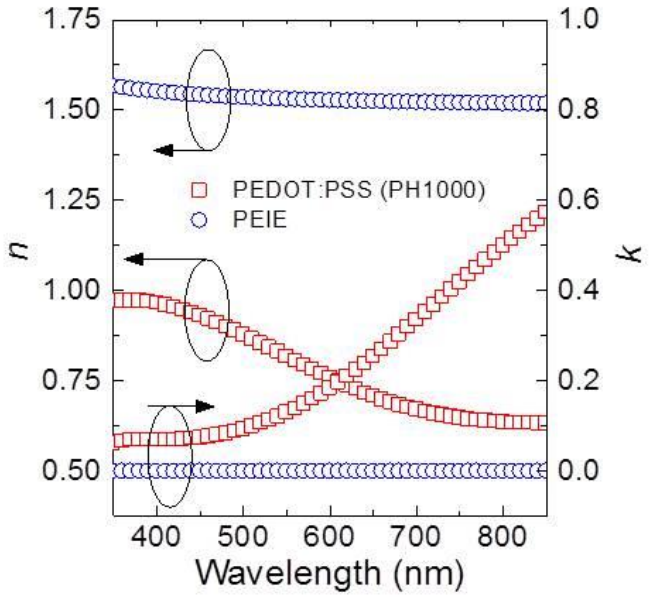

Figure 5.12 Refractive index (n) and extinction coefficient (k) spectra of PEDOT:PSS (PH1000) and PEIE films.

Simulations of the J_{SC} of the P3HT:$PC_{60}BM$ and PBDTTT-C:$PC_{60}BM$-based tandem PSCs were conducted to help out the selection of the thicknesses of the photoactive layers. Figure 5.13 (a) displays a simulation of the dependence of J_{SC} on the thicknesses of the photoactive layers.

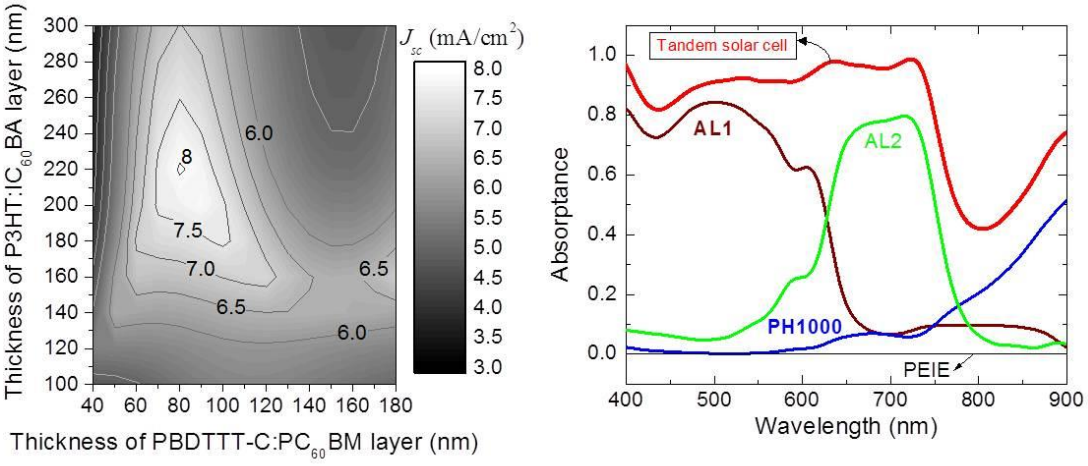

Figure 5.13 (a) Simulated J_{SC} generated in a P3HT:$IC_{60}BA$ and PBDTTT-C:$PC_{60}BM$-based tandem PSC as a function of the thicknesses of the photoactive layers. (b) Simulation of the absoprtance in a tandem solar cell with optimized geometry and a breakdown of the individual contributions of the P3HT/$IC_{60}BA$ (wine), PH1000(blue), PEIE (black) and PBDTTT-C/$PC_{60}BM$ (green) layers.

From these simulations, the J_{SC} reaches an optimum value, around 8.0 mA/cm^2, when the thicknesses of the P3HT:$IC_{60}BA$ and PBDTTT-C:$PC_{60}BM$ layers are around 220 nm and 80 nm, respectively. As shown in Figure 5.13 (b), in a tandem PSC with these photoactive layer thicknesses, a breakdown of the individual layer contributions to the total absorptance of the tandem cell shows that the PH1000 layer contributes less than 4.5% to the total absorptance of the tandem cell for wavelengths smaller than 800 nm.

From this optical simulation result, it was found that the contribution from the CRL to the total absorptance in the tandem cell is negligible.

5.3.3 Characterization of Solar Cells Performance

In this section, two single-junction PSCs and three tandem PSCs are discussed. It should be noted that the single-junction PSCs have the same device structures to those of single-junction PSCs introduced in Chapter 5.2, but they were newly fabricated for this study. Also, **T1**, **T2**, and **T3** are different tandem PSCs from the tandem PSCs studied in Chapter 5.2. The detailed device structures are described below and shown in Figure 5.14(a)-(c) and Figure 5.16 (a) and (b):

Inverted single-junction PSCs:

- Glass/ITO/PEIE/ PBDTTT-C:$PC_{60}BM$ /MoO_X/Ag (**SB**) (Figure 5.13 (a))
- Glass/ITO/PEIE/ P3HT:$IC_{60}BA$ /MoO_X/Ag (**ST**) (Figure 5.13 (b))

Inverted tandem PSCs

- Glass/ITO/PEIE/P3HT:$IC_{60}BA$/PEDOT:PSS (PH1000)/PEIE/PBDTTT-C:$PC_{60}BM$/MoO_X/Ag (**T1**) (Figure 5.13 (c))
- Glass/ITO/PEIE/P3HT:$IC_{60}BA$/PEDOT:PSS (PH1000)/PEI/PBDTTT-C:$PC_{60}BM$/MoO_X/Ag (**T2**) (Figure 5.15 (a))
- Glass/ITO/PEIE/P3HT:$IC_{60}BA$/PEDOT:PSS (AI4083)/PEI/PBDTTT-C:$PC_{60}BM$/MoO_X/Ag (**T3**) (Figure 5.15 (b))

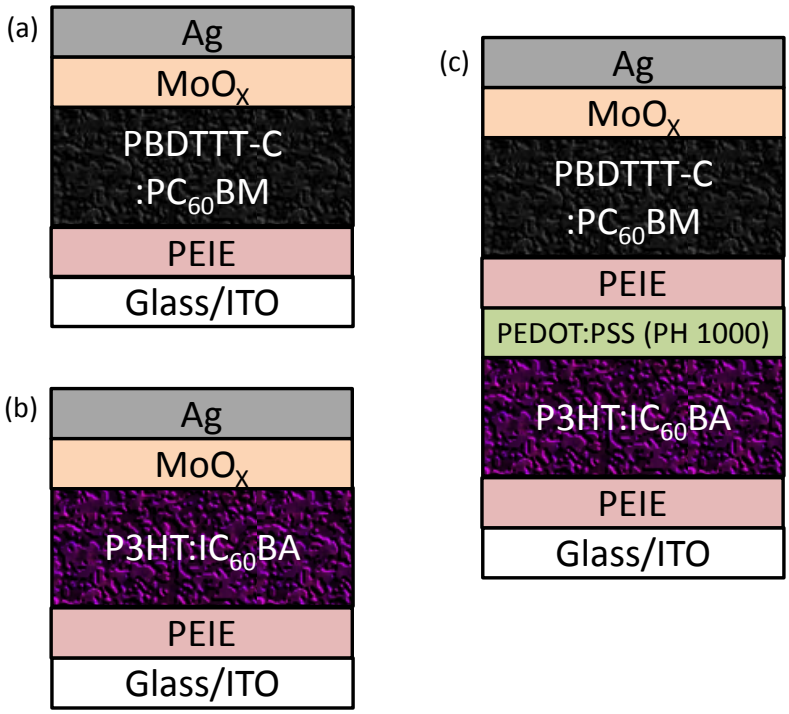

Figure 5.14 Device structures of inverted single-junction (a) **ST** and (b) **SB**, and tandem PCS (c) **T1**.

Figure 5.15 shows a comparison of the *J-V* characteristic ((a) under illumination and (b) in the dark) of **T1** and corresponding single-junction PSCs containing P3HT:$IC_{60}BA$ (**SB**) and PBDTTT-C:$PC_{60}BM$ (**ST**) photoactive layers. Device performance is summarized in Table 5.3. For single-junction cells, **SB** shows average values of V_{OC} of 820 mV, a J_{SC} of 8.8 mA/cm^2 and a FF of 0.63, resulting in a PCE of 4.5% (averaged over 20 devices). From **SB**, extracted R_SA and R_PA values from *J-V* characteristics are 2.9 Ω cm^2 and 2500 Ω cm^2, respectively. **ST** shows average values of V_{OC} of 671 mV, a J_{SC} of 15.2 mA/cm^2 and a FF of 0.57, resulting in a PCE of 5.9 % (averaged over 25 devices). From **ST**, extracted R_SA and R_PA values are 1.8 Ω cm^2 and 500 Ω cm^2, respectively. These results validate that the photoactive layers work reasonably well with the selected electrodes (ITO/PEIE and MoO_X/Ag).

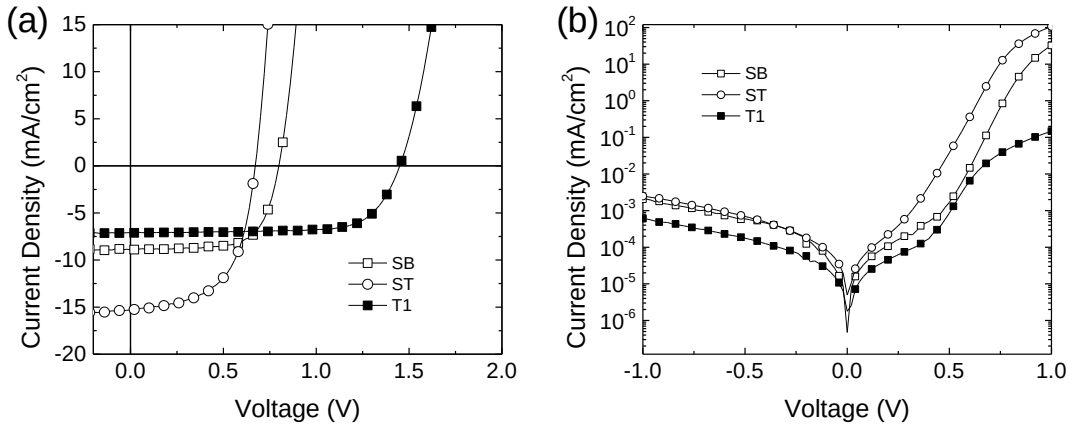

Figure 5.15 Representative *J-V* characteristics for **SB** (open squares), type **ST** (open circles), and type **T1** (closed squares) (a) under illumination and (b) in the dark.

Table 5.3 Summary of the averaged photovoltaic performance parameters from single-junction (**SB** averaged over 20 devices and **ST** averaged over 25 devices) and tandem solar cells (**T1** averaged over 25 devices).

Types	V_{OC} **(mV)**	J_{SC} **(mA/cm^2)**	**FF**	**PCE (%)**
SB	820± 10	8.8 ± 0.4	0.63 ± 0.01	4.5 ± 0.2
ST	671 ± 2	15.2 ± 0.8	0.57 ± 0.03	5.9 ± 0.3
T1	1480 ± 20	7.4 ± 0.4	0.68 ± 0.04	7.5 ± 0.7

As for tandem PSCs, **T1** shows averaged values of V_{OC} of 1480 mV, a J_{SC} of 7.4 mA/cm^2, a FF of 0.68 and a PCE of 7.5 % (averaged over 5 devices). For **T1**, R_SA and R_PA are found to have values of 3.3 Ω cm^2 and 3790 Ω cm^2, respectively. The champion tandem cell achieved a V_{OC} of 1458 mV, a J_{SC} of 7.2 mA/cm^2, and a high FF of 0.73, yielding a PCE of 8.5%. This result shows that the V_{OC} of tandem PSCs is the sum of the V_{OC} of the bottom and top cells; with no loss observed. This indicates that the energy alignment between the WF of the PH1000 interface and the IE of P3HT and of the PEIE-modied PEDOT:PSS (PH1000) interface and the EA of $PC_{60}BM$ is good enough to allow for the alignment of the quasi-Fermi levels of the bottom and top cells. The tandem PSCs

exhibit higher averaged FF (0.68) than both of the single-junction PSCs, 0.63 and 0.57, respectively. This performance can be analyzed using an equivalent circuit model with the following equation given below (Eq. 1.8 is rewritten.)

$$J = \frac{1}{1 + R_S / R_P}\left[J_0 \left\{ \exp\left(\frac{V - JR_S A}{nkT / e} \right) - 1 \right\} - \left(J_{ph} - \frac{V}{R_P A} \right) \right] \tag{5.1}$$

where R_S is the series resistance, R_P is the shunt resistance, J_0 is the reverse saturation current density, A is the solar cell area, e is the elementary charge, k is Boltzmann's constant, T is the temperature, n is the ideality factor of the diode, and J_{ph} is the photogenerated current density. First, it is worth noting that in the absence of R_S and for an infinite R_P, an upper-limit for the FF, FF_0 is defined by Eq. 5.2 (Eq. 1.11 is rewritten.)

$$FF_0 = \frac{v_{OC} - \ln\left(v_{OC} + 0.72\right)}{v_{OC} + 1} \tag{5.2}$$

$$\begin{aligned} FF_S &= FF_0(1 - 1.1 r_S) + 0.19 r_S^{\,2} \qquad \left(0 \le r_S \le 0.4, 1/r_P = 0\right), \\ FF_{SP} &= FF_S \left\{ 1 - \frac{\left(v_{OC} + 0.7\right)}{v_{OC}} \frac{FF_S}{r_P} \right\} \quad \left(0 \le r_S + 1/r_P \le 0.4\right) \end{aligned} \tag{5.3}$$

where $v_{OC} = eV_{OC}/nkT$. FF_0 yields values of 0.67, 0.62, and 0.74 for devices **SB**, **ST**, and **T1**, respectively. Namely, in the absence of R_S and for infinite R_P, a tandem cell will display a higher fill factor than any of the single-junction cells due to the increased V_{OC}. In devices **T1**, the extrated ideality factor n of 4.5 has a higher value which could reduce FF_0, however, this effect is not as strong as the increase arising from the higher value of V_{OC}. The extracted n values of **SB** and **ST** are 3.7 and 3.6, respectively. In devices, the FF is reduced by the values of R_S and R_P normalized to the characteristic resistance defined as $R_{CH} = V_{OC}/(J_{SC}A)$. After incorporating the normalized series resistance by following Eq. 5.3, $r_S = R_S / R_{CH}$, the fill factor (FF_S) yields values of 0.64, 0.60, and 0.72 for devices **SB**,

ST, and **T1**, respectively. Furthermore, with the additional incorporation of the normalized shunt resistance, $r_P = R_P / R_{CH}$, the fill factor (FF_{SP}) yields values of 0.63, 0.56, and 0.69 for devices **SB**, **ST**, and **T1**, respectively, consistent with the measured values, validating the effectiveness of the model in this case and the parameters derived from it. The equivalent circuit model provides a plausible explanation for the large fill-factor observed.

It is also worth mentioning that no S-shaped kinks were observed in the *J-V* characteristics under illumination (Figure 5.15 (a)), which further confirms the efficient recombination of carriers at the PEDOT:PSS (PH1000)/PEIE CRL. This observation is different from previous reports of tandem PSCs with CRL of TiO_2/Al/PEDOT:PSS[97] or ZnO/PEDOT:PSS[103] where S-shaped kinks were observed in the *J-V* characteristics which could be removed when the tandem PSCs are exposed to UV illumination. As discussed in Chapter 4, single-junction PSCs wherein the WF of the ECE is well matched, or ideally smaller, than the EA of the acceptor in the bulk hetrojunction photoactive layer, leads to PSCs that are insensitive to the UV treatment. Also, it was found that the effects induced by the UV exposure to PSCs containing metal-oxide layers, are related with a WF reduction of such metal oxides. When these metal-oxides are served as ECEs, the reduction of their WF leads to a better matching with the EA of the acceptor and consequently enhance the device performance. With the use of PEIE or PEI (shown later)-modified PEDOT:PSS for a CRL, the achieved WF of 3.6 eV at the PEIE-modified interface is ideal to produce efficient electron-collecting interfaces which are less sensitive to changes on the energy levels of the materials at that interface. The good electron selectivity of the PEIE-modified electrodes (ITO and PH1000) in the tandem PSCs here is also attested by the high rectification shown in the *J-V* characteristics acquired in the dark (Figure 5.15 (b)) on pristine devices, without the help of the UV-illumination.

While PEDOT:PSS (PH1000)/PEIE is demonstrated to be an efficient CRL for the tandem PSC, CRLs comprising PEDOT:PSS (PH1000)/PEI (branched) (**T2**) and a lowly conductive PEDOT:PSS (AI 4083)/PEI (**T3**) have been applied to inverted tandem PSCs with the same photoactive layers. The device structures of both cases are displayed in Figure 5.16. The PSCs with PEDOT:PSS (PH1000)/PEI CRL operate similarly to or slightly worse than those with PEDOT:PSS (PH1000)/PEIE with a averaged PCE of 7.1 %. This is consistent with the fact that both PEIE and PEI can yield WF reductions (with PEIE: 3.58 eV, with PEI: 3.88 eV measured by a Kelvin probe) of PEDOT:PSS (PH1000) as shown in Chapter 4.3. However, the tandem PSCs (**T3**) with a CRL of PEIE-modified PEDOT:PSS (AI 4083) showed poor device performance with an averaged V_{OC} of 1414 mV, J_{SC} of 6.6 mA/cm^2, FF of 0.46, and PCE of 4.3 %. These lower values might be attributed to the lower conductivity of PEDOT:PSS (AI 4083, electrical conductivity: 10^{-3} S/cm) layer than that of PDEOT:PSS (PH 1000, electrical conductivity: 600 S/cm) [62,160]. This low conductivity of the PEDOT:PSS may increase the R_S of the device which leads to low FF and J_{SC}, and consequently reduce the PCE. Device performance is summarized in Table 5.4.

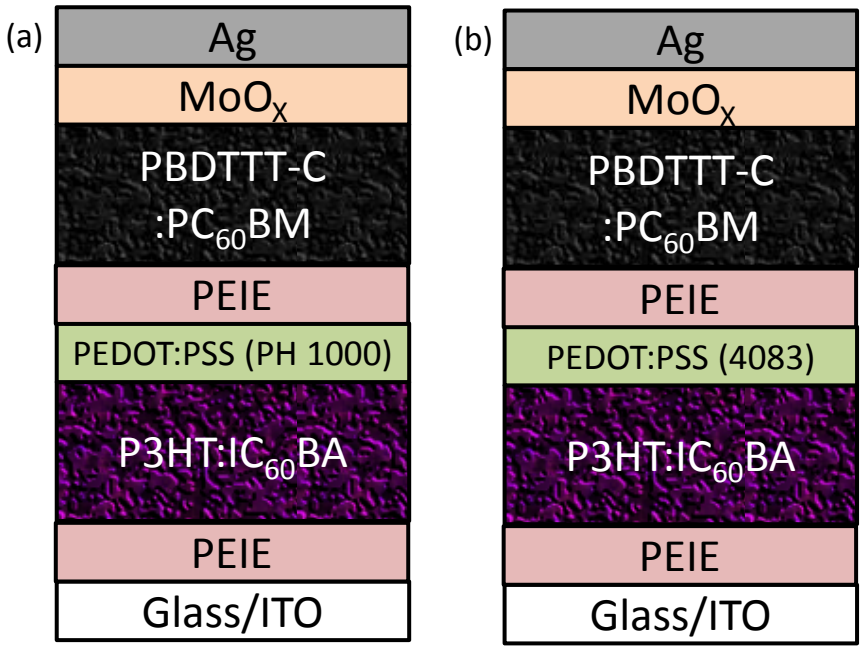

Figure 5.16 Device structures of inverted tandem (a) type T2 PSC and (b) type T3 PSC.

Table 5.4 Summary of the averaged[a] photovoltaic performance parameters from tandem solar cells (**T2** and **T3**).

Types	V_{OC} **(mV)**	J_{SC} **(mA/cm^2)**	**FF**	**PCE (%)**
T2	1490± 10	7.6 ± 0.4	0.63 ± 0.01	7.1 ± 0.4
T3	1414±52	6.6 ± 0.2	0.46 ± 0.06	4.3 ± 0.8

[a]Averaged over four devices

5.3.4 Conclusions

This section shows inverted tandem PSCs using an all-polymeric CRL of the PEIE-modified PEDOT:PSS (PH 1000). High PCE up to 8.5 % and large FF of 0.73 were achieved from the PSCs (**T1**) with the photoactive layers of P3HT:IC$_{60}$BA and PBDTTT-

C:PC_{60}BM. The device performance results validate the PEIE-modified PEDOT:PSS (PH1000) film as an excellent candidate as a CRL for highly efficient tandem PSCs.

Several factors make it very attractive as a CRL. First, a large WF contrast of 1.3 eV between the two opposite surfaces of the CRL result in excellent hole and electron collecting properties from the bottom and top cells. Next, while previously reported CRLs in tandem PSCs commonly comprised a combination of a low-WF and a high-WF components (layers), the CRL shown here is made up with a single layer of PEDOT:PSS modified at one interface with PEIE that showed adequate robustness for the fabrication of tandem PSCs from solution processes. This modified single layer of the CRL induced small absorption losses from the CRL, leading to an increased number of photons absorbed by the top cell. As a result, the tandem PSCs were able to yield the almost optimum J_{SC} value that was calculated from optical simulations.

With this CRL, higher PCE will be achieved if donor polymers with a broader and more complementary spectral absorption are employed in the tandem PSC. Furthermore, the fully solution processing and flexibility of the polymer CRL are compatible with roll-to-roll fabrication for large-area low-cost applications

CHAPTER 6

CONCLUSIONS AND RECOMMENDATIONS

6.1 Conclusions

OSC technologies have been the subject of active research and development over the past decades. Due to their ability to be processed at low temperature over large areas at potentially low cost, OSCs have experienced accelerated development in recent years and have the potential to spawn a new generation of products with thin and flexible form factors. However, in spite of steady progress in performance, there are many challenges and concerns about PCE and stability that must be resolved before this emerging technology can unleash its full potential. In particular, OSCs with the conventional structure that include low-WF metals, such as LiF/Al and Ca/Al, at the top electrode suffer from device instability due to the air sensitive low-WF top electrodes. Recently, OSCs with inverted structures, in which the top electrode is a relatively high-WF metal to collect holes, have been proposed and developed with better air stability and comparable PCE to conventional OSCs. However, OSCs with a tandem structure in which more than two individual cells with complementary absorption ranges are stacked through a CRL are desirable for the realization of highly efficient solar cells by covering the emission spectrum of the sun more effectively. In this dissertation, many efforts were geared towards improving the performance of the PSCs (polymer-based OSCs). In particular, extensive research has been conducted to overcome the issues in PSCs by studying charge-collecting interlayers of single-junction and CRLs of tandem PSCs.

This dissertation discussed several charge-collecting interlayers, one hole-collecting interlayer, NiO, and three electron-collecting interlayers, TiO_2:PVP, PVP, and PEIE. Although the role of the NiO (hole-collecting) was opposite to the others (electron-

collecting), these all were deposited on ITO to modify the WF of ITO to serve either as a HCE (conventional geometry) or ECE (inverted geometry). The NiO was processed by ALD and the other electron collecting interlayers were deposited by solution spin casting.

The goal of the conducted research with the charge-collecting interlayers was to investigate the origin of the WF evolution and the effect of WF values on the device performance. A rule of thumb is that the WF of the HCE has to be sufficiently high (higher than IE of donor) and that of ECE must be sufficiently low (lower than EA of acceptor) to maximize the charge-collection efficiency and the V_{OC} of PSCs.

In the case of NiO, the pristine NiO-coated ITO had an initial WF value of 4.7 ± 0.05 eV, and the WF value was not high enough to serve as a HCE in PSCs with P3HT (IE: 4.7-5.0 eV) as the donor [47,153]. Thus, P3HT:$IC_{60}BA$-based PSCs made with pristine NiO yielded poor photovoltaic performance with small FF and a low V_{OC}. However, subsequent O_2-plasma treatment further increased the WF up to 5.4 ± 0.02 eV as well as the conductivity of NiO, turning NiO-coated ITO into an efficient HCE. The XPS study showed that the origin of the WF increase after the O_2-plasma treatment was related to the reduction of the strength of peaks of the $Ni(OH)_2$ and carbonaceous species from the surface of the as-prepared ALD NiO films. Also, p-doping resulting from the O_2-plasma treatment could not be ruled out as a cause for the device performance improvement. After the O_2-plasma treatment, PSCs showed PCE of 4.1 ± 0.2 % with about two times increased V_{OC} and three times increased FF. Finally, non-conformal coverage of NiO on ITO showed detrimental effect on device performance. Despite the similar WF values NiO layers with different thickness, non-conformal coverage can cause a spatial distribution of areas with higher (NiO-coated) and lower (bare ITO) WF values across the surface. Thus, conformal coverage of the charge-collecting interlayer on the conductor surface should be achieved for better device performance.

Similarly to the hole-collecting interlayers, the sufficiently low-WF value of electron-collecting interlayers was important to collect electrons effectively. In addition

to the proper WF value, air stability is another key issue in electron-collecting interlayers since the reactive low-WF component often causes quick device degradation in air. In this dissertation, low-WF ECEs were introduced by modifying the surface of a conductor with a non-conjugated amine containing polymer. The ECEs have good air stability and sufficiently low WF. Also they could be achieved by using a simple and large throughput method at low temperature (< 120 °C) with environmental friendly solvents.

The first polymer surface modifier discussed in this dissertation was PVP. Initially, PVP was used as a dispersant for TiO_2 nanoparticles. As a dispersant, PVP was able to coordinate onto and disperse TiO_2 nanoparticles uniformly in films on top of ITO. An ECE comprising ITO coated with TiO_2 nanoparticles dispersed into PVP was employed in inverted PSCs and P3HT:PC_{60}BM-based PSCs yielded a PCE of 3.0 ± 0.2% after exposing the PSCs for 25 min under a 100 mW/cm^2 AM 1.5 G solar illumination.

The more important thing which was discovered from this study is that not only can the PVP help with the dispersion of the TiO_2 nanoparticles, but it can lead to even larger reductions of the WF in TiO_2:PVP-coated ITO ECEs (4.33 ± 0.02 eV) compared to TiO_2-coated ITO electrodes (4.47 ± 0.02 eV), and consequently to inverted PSCs with enhanced photovoltaic performance. From this discovery, it was found that pure PVP itself can induce a reduction of its WF up to 0.8 eV of ITO, allowing it to act as an ECE. The WF reduction induced by the PVP was found to originate from the electron-donating properties of pyrrolidone groups in PVP. That is, the physical or chemical adsorption of PVP onto the ITO surface was speculated to induce a partial electron transfer from the pyrrolidone group to the ITO, thus creating a surface dipole μ on the ITO surface. This surface dipole was thought to decrease the electrostatic potential on the surface of the ITO, effectively reducing its WF. This discovery provided a noticeable improvement in ECEs. So far, a reduction of the WF of conductors (in this dissertation, mostly ITO) to allow them to function as ECEs has been obtained by coating surface of ITO with a layer of semiconducting material, typically metal oxides [67,69] having a lower WF value, an

alkali metal salt [75] commonly fabricated under vacuum or by spin-coating and post-fabrication thermal treatments, in the case of nano-particles. However, these ITO modification methods need to be processed under vacuum, which may not be compatible with high throughput fabrication methods, or are in need of post thermal treatments at relatively high temperatures, which may not be compatible with flexible substrates. However, the polymer surface modification can be processed in air by spin-coating at low temperature, and provide similar WF reduction on the ITO surface.

Even though the use of PVP surface modification yielded a lowered WF value of ITO that was close to the EA of the acceptor material, it was found that further UV treatment was required due to the inhomogeneous surface coverage. Also, due to the insulating nature of the PVP, it was impossible to increase the thickness of the PVP like what was done for NiO layer. Hence, even if the polymer surface modification with the PVP provided an efficient way for realizing ECEs, using the only PVP for the surface modification still needs more improvements.

Another polymer surface modifier, PEI derivatives (PEI, PEIE), could overcome the issues of the PVP. These PEI derivatives, which are neutral polymers and contain simple aliphatic amine groups, were shown to provide universal WF reduction of many different conductors, including metals, transparent conductive metal oxides, conducting polymers, and graphene, by up to 1.7 eV. The mechanism for WF reduction by these polymers was found to be similar to that of the PVP. That is, the WF reduction arises from physisorption of such polymers onto the conductor surface, which form an ultrathin layer on the surface. The intrinsic molecular dipole moments created by the neutral amine groups contained in the polymer surface modifiers and the partial charge-transfer character of their interaction with the conductor surface induce WF reduction for a wide range of conductors. Therefore, many different types of low-WF ECEs such as ITO/PEIE (WF: 3.60 ± 0.06 eV), PEDOT:PSS/PEIE (WF: 3.58 ± 0.06 eV), Ag/ECE (WF: 3.70 ± 0.06 eV), *etc.* were successfully realized. These polymer surface modifiers are processed

in air from solution, providing an appealing alternative to chemically reactive low-WF metals. With ECEs made from the PEIE modification, various types of efficient single-junction PSCs, including all-polymeric solar cells, have been demonstrated. P3HT:$IC_{60}BA$-based PSCs with PEIE-modified ITO ECE yielded PCE of 5.9 ± 0.3 %, and fully polymeric solar cells with the same photoactive layer showed PCE of 3.4 ± 0.2 %.

This surface modification was also employed in CRLs of inverted tandem PSCs. The large WF contrast in a CRL of tandem cell is very important. The WF of one side of the CRL should be high enough to collect holes in the adjacent sub-cell effectively, and the WF of the other side of the CRL needs to be low enough to collect electrons in the adjacent sub-cell efficiently. In this dissertation, two different high WF materials, MoO_X (WF values of 5.3 ± 0.05 eV) and PEDOT:PSS (WF values of 4.9 ± 0.06 eV) served as hole-collecting layers in CRLs. And the PEIE modification was used to either reduce the WF of high-WF materials or provide further reduced WF of low-WF materials for the electron-selective interface.

The first CRL studied here was composed of PEIE-modified MoO_X/Ag. The 1-nm-thick Ag layer was shown to provide a better electrical connection between the top and bottom cells. In this CRL, the PEIE modification on the MoO_X/Ag was found to provide WF reduction of MoO_X/Ag from 4.8 ± 0.03 eV to 3.8 ± 0.01 eV, and consequently was used as the electron-selective interface. The CRL in the PSCs was shown to serve as a good recombination center for holes from the bottom cell and electrons from the top cell. While tandem PSCs without the PEIE modification in the CRL worked in essence as a single-junction cell with an increased R_S, PSCs having the PEIE-modified MoO_X/Ag CRL showed an improved photovoltaic performance with increased V_{OC} (83% of the ideal V_{OC} value) and a high value of FF similar to single-junction cells. However, the small J_{SC} due to the use of the same P3HT:$PC_{60}BM$ photoactive layer for the top and bottom cells limited the PCE of the tandem PSCs. In

addition to the enhanced device performance of the tandem PSCs, the inverted structure resulted in excellent air stability for exposure to ambient air for more than 140 h. However, the lack of optimized V_{OC} and J_{SC} from the tandem PSCs suggested that further study of the CRL and photoactive layers should be performed. Also, the deposition of the 1-nm-thick Ag with a thermal evaporator is challenging, thus another easy way to form the Ag layer or a new material that replaces the Ag layer should be considered.

The secondly discussed CRL was composed of PEIE-modified MoO_X/Al_2O_3:ZnO nanolaminates. In this CRL, a different electron-selective layer, Al_2O_3:ZnO nanolaminates was deposited on the MoO_X by ALD. Unlike the non-continuous Ag layer in the first CRL, the Al_2O_3:ZnO nanolaminate provided highly conformal and uniform films over the MoO_X layer, which could enhance not only the charge selectivity but also the V_{OC} of the tandem PSC. In addition, the use of the highly conductive Al_2O_3:ZnO nanolaminate (1×10^3 S/cm) [78] instead of the widely used electron-selective layer ZnO (2×10^2 S/cm) led to enhanced photovoltaic performance with higher FF (19%) and J_{SC} (6%) when compared to those of the PSC with the ZnO due to lower R_SA of the Al_2O_3:ZnO nanolaminate. However, the V_{OC} values difference between the two tandem PSCs were only by 3%, and it can be ascribed to similar WF values of PEIE-modified ZnO and Al_2O_3:ZnO nanolaminate. Lastly, the PEIE modification to the MoO_X/Al_2O_3:ZnO nanolaminate enlarged the WF contrast, leading to further enhanced performance of tandem PSCs with increased V_{OC}. Moreover, even though the exact origin of the increased R_PA after PEIE modification is unclear, the PEIE layer is believed to improve barrier properties of Al_2O_3:ZnO nanolaminate. This tandem PSC used two photoactive layers with different absorption ranges (P3HT:IC_{60}BA and PBDTTT-C:PC_{60}BM). The tandem PSCs could absorb light from the visible range to the near-IR, resulting in higher J_{SC} of 7.1 ± 0.1 mA/cm^2 compared to the J_{SC} (3.2 ± 0.1 mA/cm^2) from the previous tandem PSCs with same photoactive layers for bottom and top cells. However, there are still some issues with the proposed CRL, such as the crystalline

nature of Al_2O_3:ZnO nanolaminate limiting the mechanical flexibility of the PSCs, which needs to be resolved.

Lastly, the CRL consisting of the conducting polymer PEDOT:PSS (PH 1000) modified at one interface with PEIE was discussed. This was the first CRL made with fully polymeric materials and realized with a single PEDOT:PSS (PH 1000) layer with the surface modification. This CRL showed a large WF contrast between its two opposite surfaces, very small absorption losses and enough robustness to allow the fabrication of a top cell from solution processing. The photoactive layers P3HT:$IC_{60}BA$ and PBDTTT-C:$PC_{60}BM$ were applied to the tandem PSC containing the PEIE-modified PEDOT:PSS CRL. Interestingly, in this tandem PSCs, a higher FF of 0.68 than those of single-junction cells (bottom cell (FF: 0.63) and top cells (FF: 0.57)) was achieved, even though it has been generally known that a FF of tandem cell is lower than single-junction cell due to presumably increased R_S induced from two photoactive layer connected in series. However, this result clearly demonstrated that the increase in V_{OC} from the tandem geometry influences more effectively on FF than the impact induced by the increased R_S, and thus higher FF can be achieved. The photoactive layers of the bottom and top cells, however, still have some overlaps in their absorption range. Thus, provided donor polymers with a broader and more complementary spectral absorption are used in this tandem PSC, higher PCE will be obtained.

In short, surface modification with the polymeric materials discussed in this dissertation turns out to be an efficient way to provide air-stable low WF-electrodes for PSCs. This approach should allow the mass production of low-WF electrodes from processes that are compatible with the large-area roll-to-roll manufacturing techniques needed for the commercialization of low-cost, organic-based photovoltaic devices.

6.2 Recommendations for Future Work

This section provides several recommendations for future work.

First, in Chapter 3 the PCE of the PSC with the ITO/NiO HCE increased appreciably (more than 10 times) after O_2-plasma treatment of the NiO layer. Although it was assumed that one of the possible mechanisms behind this was the occurrence of p-doping of NiO film upon O_2-plasma treatment, no systematic study was performed on the p-doping effect. Also, even though a similar study on the solution-processed NiO layer was conducted by others in the research community [57,132], no research has been performed on the ALD-processed NiO layer yet. Thus, research on the doping effect and mechanism in ALD-processed NiO from the O_2-plasma treatment is recommended to further deepen understanding of the increased electrical conductivity of the NiO layer and the improved PCE of the PSC with the ITO/NiO HCE. Another recommendation for the PSCs with ITO/NiO HCE is the use of polymers with larger IE than that of the P3HT (4.65 eV – 5.0 eV) [47,149] used in this study. The WF of ITO/NiO with O_2-plasma treatment was around 5.4 eV. Hence, the polymers with larger IE than that of P3HT are capable of PSC with the ITO/NiO HCE, and consequently larger V_{OC} can be achieved. The maximum V_{OC} of the OSCs is commonly determined by the difference between the IE of the donor polymer and the EA of the acceptor material.

Secondly, in Chapter 4, it was shown that electrons could be injected from semiconductors to electrodes though the PEIE, although the PEIE was an insulator. Even though either tunneling or thermionic injection was assumed as the mechanism behind this charge transport, detailed studies of this were not conducted. Research on the charge transport of such modifiers is worth conducting. In addition, the polymer surface modification with either PVP or PEI derivatives was applied only for PSCs with inverted geometry. However, this surface modification may also be applicable to PSCs with conventional geometry. In a PSC with conventional geometry, the use of low-WF materials such as Ca, LiF, etc., on top of the PSC has shown to cause device instability in

air. The use of inverted geometry has been considered as one method of avoiding this issue. However, this stability issue can also be resolved by replacing the reactive materials with the air stable polymeric surface modifier at the top of the conventional PSCs, so that finally an air-stable PSC with conventional geometry will be achieved.

Finally, even though the PEIE-modified CRL shown in Chapter 5.3 exhibited an excellent charge recombination property in the tandem PSC, the comparatively low J_{SC} extracted from the tandem PSCs still left lots of room for improvement due to the relatively large overlap of absorption ranges between two polymers used, P3HT and PBDTTT-C. In order to take full advantage of this CRL, donor polymers with a broader and more complementary spectral absorption should be used in the tandem PSCs. Thus, it is worth fabricating tandem PSCs with new polymers to utilize the solar spectrum more efficiently. Finally, the tandem PSCs discussed in this thesis were made on a rigid substrate, glass/ITO. However, the fully polymeric CRL should be compatible with flexible tandem PSCs. Realizing fully polymeric tandem PSCs with the PEIE-modified PEDOT:PSS should be worthwhile.

6.3 List of Publications

Jae Won Shim, Canek Fuentes-Hernandez, Amir Dindar, Yinhua Zhou, Talha M. Khan, and Bernard Kippelen, "Polymer solar cells with NiO hole-collecting interlayers processed by atomic layer deposition," *Organic Electronics*, 14, 2802-2808, (2013)

Yinhua Zhou, **Jae Won Shim**, Canek Fuentes-Hernandez, Talha M. Khan, and Bernard Kippelen, "Inverted organic solar cells with polymer-modified fluorine-doped tin oxide as the electron-collecting electrode," *Thin Solid Films*, (2013), http://dx.doi.org/10.1016/j.tsf.2013.05.059

Yinhua Zhou, Canek Fuentes-Hernandez, Talha M. Khan, Jen-Chieh Liu, James Hsu, **Jae Won Shim**, Amir Dindar, Jeffrey P. Youngblood, Robert J. Moon, and Bernard Kippelen, "Recyclable organic solar cells oncellulose nanocrystal substrates," *Scientific Reports*, 3, 1536-1540, (2013)

Yinhua Zhou, Canek Fuentes-Hernandez, **Jae Won Shim**, Talha M. Khan, and Bernard Kippelen, "High performance polymeric charge recombination layer for organic tandem solar cells," *Energy & Environmental Science*, 5, 9827-9832, (2012)

Jae Won Shim, Hyeunseok Cheun, Amir Dindar, Yunsang Kim, Yinhua Zhou, Canek Fuentes-Hernandez, Do-Kyung Hwang, Joseph W. Perry, and Bernard Kippelen, "Indium tin oxide modified by titanium dioxide nanoparticles dispersed in poly(N-vinylpyrrolidone) for use as an electron-collecting layer in organic solar cells with an inverted structure," *Journal of Materials Research*, 27, 1-6, (2012).

Jae Won Shim, Yinhua Zhou, Canek Fuentes-Hernandez, Amir Dindar, Zelei Guan, Hyeunseok Cheun, Antoine Kahn, and Bernard Kippelen, "Studies of the

optimization of recombination layers for inverted tandem polymer solar cells," *Solar Energy Materials and Solar Cells*, 107, 51-55, (2012).

Jae Won Shim, Hyeunseok Cheun, Jens Meyer, Canek Fuentes-Hernandez, Amir Dindar, Yinhua Zhou, Do Kyung Hwang, Atoine Kahn, and Bernard Kippelen, "Polyvinylpyrrolidone-modified indium tin oxide as an electron-collecting electrode for inverted polymer solar cells," *Applied Physics Letters*, 101(7), 073303-073307, (2012).

Hong Li, Laura K. Schirra, **Jaewon Shim**, Hyeunseok Cheun, Bernard Kippelen, Oliver L. A. Monti, and Jean-Luc Bredas, "Zinc Oxide as a Model Transparent Conducting Oxide: A Theoretical and Experimental Study of the Impact of Hydroxylation, Vacancies, Interstitials, and Extrinsic Doping on the Electronic Properties of the Polar ZnO (0002) Surface," *Chemistry of Materials*, 24(15), 3044–3055, (2012).

Do Kyung Hwang, Raghunath R. Dasari, Mathieu Fenoll, Valérie Alain-Rizzo, Amir Dindar, **Jae Won Shim**, Nabankur Deb, Canek Fuentes-Hernandez, Stephen Barlow, David G. Bucknall, Pierre Audebert, Seth R. Marder, and Bernard Kippelen, "Stable Solution-Processed Molecular n -Channel Organic Field-Effect Transistors," *Advanced Materials*, 24(32), 4445-4450, (2012).

Yinhua Zhou[†], **Jae Won Shim,**[†] ([†]These authors contributed equally to this work.) Canek Fuentes-Hernandez, Asha Sharma, Keith A. Knauer, Anthony J. Giordano, Seth R. Marder, and Bernard Kippelen, "Direct correlation between work function of indium-tin-oxide electrodes and solar cell performance influenced by ultraviolet irradiation and air exposure," *Physical Chemistry Chemical Physics*, 14(34), 12014-12021, (2012).

Yinhua Zhou, Canek Fuentes-Hernandez, **Jaewon Shim**, Jens Meyer, Anthony J. Giordano, Hong Li, Paul Winget, Theodoros Papadopoulos, Hyeunseok Cheun, Jungbae Kim, Mathieu Fenoll, Amir Dindar, Wojciech Haske, Ehsan Najafabadi, Talha M. Khan, Hossein Sojoudi, Stephen Barlow, Samuel Graham, Jean-Luc Bredas, Seth R. Marder, Antoine Kahn, and Bernard Kippelen, "A Universal Method to Produce Low-Work Function Electrodes for Organic Electronics," *Science*, 336(6079), 327-332, (2012).

Hyeunseok Cheun, Canek Fuentes-Hernandez, **Jaewon Shim**, Yunnan Fang, Ye Cai, Hong Li, Ajaya K. Sigdel, Jens Meyer, Julia Maibach, Amir Dindar, Yinhua Zhou, Joseph J. Berry, Jean-Luc Bredas, Antoine Kahn, Kenneth H. Sandhage, and Bernard Kippelen, "Oriented Growth of Al_2O_3:ZnO Nanolaminates for Use as Electron-Selective Electrodes in Inverted Polymer Solar Cells," *Advanced Functional Materials*, 22(7), 1531-1538, (2012).

Hyeunseok Cheun, John D. Berrigan, Yinhua Zhou, Mathieu Fenoll, **Jaewon Shim**, Canek Fuentes-Hernandez, Kenneth H. Sandhage, and Bernard Kippelen, "Roles of thermally-induced vertical phase segregation and crystallization on the photovoltaic performance of bulk heterojunction inverted polymer solar cells," *Energy and Environmental Science*, 4(9), 3456-3460, (2011) .

Jianguo Mei, Kenneth R. Graham, Romain Stalder, Shree Prakash Tiwari, Hyeunseok Cheun, **Jaewon Shim**, Masafumi Yoshio, Colin Nuckolls, Bernard Kippelen, Ronald K. Castellano, and John R Reynolds, "Self-Assembled Amphiphilic Diketopyrrolopyrrole-Based Oligothiophenes for Field-Effect Transistors and Solar Cells," *Chemistry of Materials*, 23(9), 2285-2288, (2011).

Kenneth R. Graham, Jianguo Mei, Romain Stalder, **Jae Won Shim**, Hyeunseok Cheun, Fred Steffy, Franky So, Bernard Kippelen, and John R Reynolds,

"Polydimethylsiloxane as a Macromolecular Additive for Enhanced Performance of Molecular Bulk Heterojunction Organic Solar Cells," *ACS Applied Materials and Interfaces*, 3(4), 1210-1215, (2011).

Xuan Zhang, **Jae Won Shim**, Shree Prakash Tiwari, Qing Zhang, Joseph E. Norton, Pei-Tzu Wu, Stephen Barlow, Samson A. Jenekhe, Bernard Kippelen, Jean-Luc Bredas, and Seth R. Marder, "Dithienopyrrole-quinoxaline/pyridopyrazine donor-acceptor polymers: synthesis and electrochemical, optical, charge-transport, and photovoltaic properties," *Journal of Materials Chemistry*, 21(13), 4971-4982, (2011).

Hyeunseok Cheun, Canek Fuentes-Hernandez, Yinhua Zhou, William J., Jr. Potscavage, Sung-Jin Kim, **Jaewon Shim**, Amir Dindar, and Bernard Kippelen, "Electrical and Optical Properties of ZnO Processed by Atomic Layer Deposition in Inverted Polymer Solar Cells," *Journal of Physical Chemistry C*, 114(48), 20713-20718, (2010).

Hyeunseok Cheun, Jungbae Kim, Yinhua Zhou, Yunnan Fang, Yunnan, Amir Dindar, **Jaewon Shim**, Canek Fuentes-Hernandez, Kenneth H. Sandhage, Kenneth, and Bernard Kippelen, "Inverted polymer solar cells with amorphous indium zinc oxide as the electron-collecting electrode," *Optics Express*, 18(23), A506-A512, (2010).

REFERENCES

[1] E. Becquerel. (1839). Memoire sur les effets electriques produits sous l'influence des rayons solaires. *Comptes rendus de l'Académie des Sciences, 9*, 561-567.

[2] D.M. Chapin, C.S. Fuller, G.L. Pearson. (1954). A new silicon p-n junction photocell for converting solar radiation into electrical power. *Journal of Applied Physics, 25*, 676-677.

[3] I.E. Agency. Retrieved June 16, 2012 from http://www.iea.org/topics/solarpvandcsp/.

[4] A. Rohatgi. (2008). Lecture note, Solar Cells ECE 6456, Gerogia Institute of Technology.

[5] V. Shrotriya, G. Li, Y. Yao, T. Moriarty, K. Emery, Y. Yang. (2006). Accurate measurement and characterization of organic solar cells. *Advanced Functional Materials, 16*, 2016-2023.

[6] Solarbuzz. Retrieved May 23, 2012, from http://www.solarbuzz.com/node/19.

[7] L. El Chaar, L.A. lamont, N. El Zein. (2011). Review of photovoltaic technologies. *Renewable and Sustainable Energy Reviews, 15*, 2165-2175.

[8] B. Kippelen J.L. Bredas. (2009). Organic photovoltaics. *Energy & Environmental Science, 2*, 251-261.

[9] Y. Muraoka, N. Takubo, Z. Hiroi. (2009). Photoinduced conductivity in tin dioxide thin films. *Journal of Applied Physics, 105*, 103702.

[10] M. Bosi C. Pelosi. (2007). The potential of III-V semiconductors as terrestrial photovoltaic devices. *Progress in Photovoltaics, 15*, 51-68.

[11] M. Gratzel. (2004). Conversion of sunlight to electric power by nanocrystalline dye-sensitized solar cells. *Journal of Photochemistry and Photobiology a-Chemistry, 164*, 3-14.

[12] A. Yella, H.-W. Lee, H.N. Tsao, C. Yi, A.K. Chandiran, M.K. Nazeeruddin, E.W.-G. Diau, C.-Y. Yeh, S.M. Zakeeruddin, M. Grätzel. (2011). Porphyrin-Sensitized Solar Cells with Cobalt (II/III)–Based Redox Electrolyte Exceed 12 Percent Efficiency. *Science, 334*, 629-634.

[13] J. Gong, J. Liang, K. Sumathy. (2012). Review on dye-sensitized solar cells (DSSCs): Fundamental concepts and novel materials. *Renewable and Sustainable Energy Reviews, 16*, 5848-5860.

[14] M. Jorgensen, K. Norrman, F.C. Krebs. (2008). Stability/degradation of polymer solar cells. *Solar Energy Materials and Solar Cells, 92*, 686-714.

[15] J.-M. Nunzi. (2002). Organic photovoltaic materials and devices. *Comptes Rendus Physique, 3*, 523-542.

[16] H. Hoppe N.S. Sariciftci. (2004). Organic solar cells: An overview. *Journal of Materials Research, 19*, 1924-1945.

[17] V. Coropceanu, J. Cornil, D.A. da Silva Filho, Y. Olivier, R. Silbey, J.-L. Brédas. (2007). Charge transport in organic semiconductors. *Chemical Reviews, 107*, 926-952.

[18] C. Deibel V. Dyakonov. (2010). Polymer-fullerene bulk heterojunction solar cells. *Reports on Progress in Physics, 73*, 1-64.

[19] H. Shirakawa, E.J. Louis, A.G. Macdiarmid, C.K. Chiang, A.J. Heeger. (1977). Synthesis of electrically conducting organic polymers - Halogen derivatives of polyacetylene, $(CH)_X$ *Journal of the Chemical Society-Chemical Communications,* 578-580.

[20] P. Würfel, *Physics of Solar Cells: From Principles to New Concepts*, 2nd, updated and expanded edition ed. (WILEY-VCH, 2008).

[21] S. Yoo, B. Domercq, B. Kippelen. (2005). Intensity-dependent equivalent circuit parameters of organic solar cells based on pentacene and C60. *Journal of Applied Physics, 97*, 103706 - 103715.

[22] W. Shockley H.J. Queisser. (1961). Detailed balance limit of efficiency of p-n junction solar cells. *Journal of Applied Physics, 32*, 510-519.

[23] V.D. Mihailetchi, P.W.M. Blom, J.C. Hummelen, M.T. Rispens. (2003). Cathode dependence of the open-circuit voltage of polymer : fullerene bulk heterojunction solar cells. *Journal of Applied Physics, 94*, 6849-6854.

[24] M.C. Scharber, D. Wuhlbacher, M. Koppe, P. Denk, C. Waldauf, A.J. Heeger, C.L. Brabec. (2006). Design rules for donors in bulk-heterojunction solar cells - Towards 10 % energy-conversion efficiency. *Advanced Materials, 18*, 789-794.

[25] K. Kawano, N. Ito, T. Nishimori, J. Sakai. (2006). Open circuit voltage of stacked bulk heterojunction organic solar cells. *Applied Physics Letters, 88*, 073514-073517.

[26] R.F. Pierret, *Semiconductor Device Fundamentals*, 2nd edition ed. (Addison Wesley, 1996).

[27] B. Qi J. Wang. (2012). Open-circuit voltage in organic solar cells. *Journal of Materials Chemistry, 22*, 24315-24325.

[28] C.J. Brabec, A. Cravino, D. Meissner, N.S. Sariciftci, T. Fromherz, M.T. Rispens, L. Sanchez, J.C. Hummelen. (2001). Origin of the Open Circuit Voltage of Plastic Solar Cells. *Advanced Functional Materials, 11*, 374-380.

[29] C.W. Tang. (1986). 2-layer organic photovoltaic cell. *Applied Physics Letters, 48*, 183-185.

[30] S. Uchida, J.G. Xue, B.P. Rand, S.R. Forrest. (2004). Organic small molecule solar cells with a homogeneously mixed copper phthalocyanine: C_{60} active layer. *Applied Physics Letters, 84*, 4218-4220.

[31] S.A. Jenekhe S.J. Yi. (2000). Efficient photovoltaic cells from semiconducting polymer heterojunctions. *Applied Physics Letters, 77*, 2635-2637.

[32] M.G. Harrison, J. Gruner, G.C.W. Spencer. (1997). Analysis of the photocurrent action spectra of MEH-PPV polymer photodiodes. *Physical Review B, 55*, 7831-7849.

[33] G. Yu, J. Gao, J.C. Hummelen, F. Wudl, A.J. Heeger. (1995). Polymer photovoltaic Cells: enhanced efficiencies via a network of internal donor-acceptor heterojunctions. *Science, 270*, 1789-1791.

[34] S. Gunes, H. Neugebauer, N.S. Sariciftci. (2007). Conjugated polymer-based organic solar cells. *Chemical Reviews, 107*, 1324-1338.

[35] T. Yohannes, F. Zhang, A. Svensson, J.C. Hummelen, M.R. Andersson, O. Inganas. (2004). Polyfluorene copolymer based bulk heterojunction solar cells. *Thin Solid Films, 449*, 152-157.

[36] G. Dennler, M.C. Scharber, C.J. Brabec. (2009). Polymer-fullerene bulk-heterojunction solar cells. *Advanced Materials, 21*, 1323-1338.

[37] M. Hiramoto, H. Fujiwara, M. Yokoyama. (1991). Three-layered organic solar cell with a photoactive interlayer of codeposited pigments. *Applied Physics Letters, 58*, 1062-1064.

[38] P. Peumans, S. Uchida, S.R. Forrest. (2003). Efficient bulk heterojunction photovoltaic cells using small-molecular-weight organic thin films. *Nature, 425*, 158-162.

[39] J.J.M. Halls, C.A. Walsh, N.C. Greenham, E.A. Marseglia, R.H. Friend, S.C. Moratti, A.B. Holmes. (1995). Efficient photodiodes from interpenetrating polymer networks. *Nature, 376,* 498-500.

[40] S.E. Shaheen, C.J. Brabec, N.S. Sariciftci, F. Padinger, T. Fromherz, J.C. Hummelen. (2001). 2.5% efficient organic plastic solar cells. *Applied Physics Letters, 78,* 841-843.

[41] M.D. Irwin, D.B. Buchholz, A.W. Hains, R.P.H. Chang, T.J. Marks. (2008). P-type semiconducting nickel oxide as an efficiency-enhancing anode interfacial layer in polymer bulk-heterojunction solar cells. *Proceedings of the National Academy of Sciences, 105,* 2783-2787.

[42] Z.C. He, C.M. Zhong, S.J. Su, M. Xu, H.B. Wu, Y. Cao. (2012). Enhanced power-conversion efficiency in polymer solar cells using an inverted device structure. *Nature Photonics, 6,* 591-595.

[43] K. Lee, J.Y. Kim, S.H. Park, S.H. Kim, S. Cho, A.J. Heeger. (2007). Air-stable polymer electronic devices. *Advanced Materials, 19,* 2445-2449.

[44] S. Braun, W.R. Salaneck, M. Fahlman. (2009). Energy-Level Alignment at Organic/Metal and Organic/Organic Interfaces. *Advanced Materials, 21,* 1450-1472.

[45] A. Sharma, A. Haldi, W.J. Potscavage, P.J. Hotchkiss, S.R. Marder, B. Kippelen. (2009). Effects of surface modification of indium tin oxide electrodes on the performance of molecular multilayer organic photovoltaic devices. *Journal of Materials Chemistry, 19,* 5298-5302.

[46] I.D. Parker. (1994). Carrier tunneling and device characteristics in polymer light-emitting diodes. *Journal of Applied Physics, 75,* 1656-1666.

[47] H.L. Yip A.K.Y. Jen. (2012). Recent advances in solution-processed interfacial materials for efficient and stable polymer solar cells. *Energy & Environmental Science, 5,* 5994-6011.

[48] Y.Y. Liang, Z. Xu, J.B. Xia, S.T. Tsai, Y. Wu, G. Li, C. Ray, L.P. Yu. (2010). For the bright future-bulk heterojunction polymer solar cells with power conversion efficiency of 7.4%. *Advanced Materials, 22,* E135-E138.

[49] H.Y. Chen, J.H. Hou, S.Q. Zhang, Y.Y. Liang, G.W. Yang, Y. Yang, L.P. Yu, Y. Wu, G. Li. (2009). Polymer solar cells with enhanced open-circuit voltage and efficiency. *Nature Photonics, 3,* 649-653.

[50] J. Gilot, M.M. Wienk, R.A.J. Janssen. (2010). Optimizing polymer tandem solar cells. *Advanced Materials, 22,* E67-E71.

[51] J.C. Bijleveld, R.A.M. Verstrijden, M.M. Wienk, R.A.J. Janssen. (2010). Maximizing the open-circuit voltage of polymer: Fullerene solar cells. *Applied Physics Letters, 97*, 073304-073307.

[52] M. Kroger, S. Hamwi, J. Meyer, T. Riedl, W. Kowalsky, A. Kahn. (2009). P-type doping of organic wide band gap materials by transition metal oxides: A case-study on Molybdenum trioxide. *Organic Electronics, 10*, 932-938.

[53] S. Han, W.S. Shin, M. Seo, D. Gupta, S.J. Moon, S. Yoo. (2009). Improving performance of organic solar cells using amorphous tungsten oxides as an interfacial buffer layer on transparent anodes. *Organic Electronics, 10*, 791-797.

[54] C. Tao, S.P. Ruan, G.H. Xie, X.Z. Kong, L. Shen, F.X. Meng, C.X. Liu, X.D. Zhang, W. Dong, W.Y. Chen. (2009). Role of tungsten oxide in inverted polymer solar cells. *Applied Physics Letters, 94*, 043311-043314.

[55] I. Hancox, L.A. Rochford, D. Clare, M. Walker, J.J. Mudd, P. Sullivan, S. Schumann, C.F. McConville, T.S. Jones. (2012). Optimization of a high work function solution processed vanadium oxide hole-extracting layer for small molecule and polymer organic photovoltaic cells. *The Journal of Physical Chemistry C, 117*, 49-57.

[56] J. Meyer, A. Shu, M. Kroger, A. Kahn. (2010). Effect of contamination on the electronic structure and hole-injection properties of MoO_3/organic semiconductor interfaces. *Applied Physics Letters, 96*, 133308-133311.

[57] K.X. Steirer, J.P. Chesin, N.E. Widjonarko, J.J. Berry, A. Miedaner, D.S. Ginley, D.C. Olson. (2010). Solution deposited NiO thin-films as hole transport layers in organic photovoltaics. *Organic Electronics, 11*, 1414-1418.

[58] M.D. Irwin, J.D. Servaites, D.B. Buchholz, B.J. Leever, J. Liu, J.D. Emery, M. Zhang, J.H. Song, M.F. Durstock, A.J. Freeman, M.J. Bedzyk, M.C. Hersam, R.P.H. Chang, M.A. Ratner, T.J. Marks. (2011). Structural and electrical functionality of NiO interfacial films in bulk heterojunction organic solar cells. *Chemistry of Materials, 23*, 2218-2226.

[59] J.W. Shim, C. Fuentes-Hernandez, A. Dindar, Y. Zhou, T.M. Khan, B. Kippelen. (2013). Polymer solar cells with NiO hole-collecting interlayers processed by atomic layer deposition. *Organic Electronics, 14*, 2802-2808.

[60] S.S. Li, K.H. Tu, C.C. Lin, C.W. Chen, M. Chhowalla. (2010). Solution-processable graphene oxide as an efficient hole transport layer in polymer solar cells. *ACS Nano, 4*, 3169-3174.

[61] K.H. Tu, S.S. Li, W.C. Li, D.Y. Wang, J.R. Yang, C.W. Chen. (2011). Solution processable nanocarbon platform for polymer solar cells. *Energy & Environmental Science, 4*, 3521-3526.

[62] Y.H. Zhou, C. Fuentes-Hernandez, J. Shim, J. Meyer, A.J. Giordano, H. Li, P. Winget, T. Papadopoulos, H. Cheun, J. Kim, M. Fenoll, A. Dindar, W. Haske, E. Najafabadi, T.M. Khan, H. Sojoudi, S. Barlow, S. Graham, J.L. Bredas, S.R. Marder, A. Kahn, B. Kippelen. (2012). A universal method to produce low-work function electrodes for organic electronics. *Science, 336*, 327-332.

[63] R. Steim, F.R. Kogler, C.J. Brabec. (2010). Interface materials for organic solar cells. *Journal of Materials Chemistry, 20*, 2499-2512.

[64] R. Steim, S.A. Choulis, P. Schilinsky, C.J. Brabec. (2008). Interface modification for highly efficient organic photovoltaics. *Applied Physics Letters, 92*, 093303-093306.

[65] J.W. Shim, H. Cheun, A. Dindar, Y. Kim, Y.H. Zhou, C. Fuentes-Hernandez, D.K. Hwang, J.W. Perry, B. Kippelen. (2013). Indium tin oxide modified by titanium dioxide nanoparticles dispersed in poly(N-vinylpyrrolidone) for use as an electron-collecting layer in organic solar cells with an inverted structure. *Journal of Materials Research, 28*, 535-540.

[66] M.H. Habibi, M. Nasr-Esfahani, T.A. Egerton. (2007). Preparation, characterization and photocatalytic activity of TiO_2/Methylcellulose nanocomposite films derived from nanopowder TiO2 and modified sol-gel titania. *Journal of Materials Science, 42*, 6027-6035.

[67] H. Cheun, C. Fuentes-Hernandez, Y.H. Zhou, W.J. Potscavage, S.J. Kim, J. Shim, A. Dindar, B. Kippelen. (2010). Electrical and optical properties of ZnO processed by atomic layer deposition in inverted polymer solar cells. *Journal of Physical Chemistry C, 114*, 20713-20718.

[68] M.S. White, D.C. Olson, S.E. Shaheen, N. Kopidakis, D.S. Ginley. (2006). Inverted bulk-heterojunction organic photovoltaic device using a solution-derived ZnO underlayer. *Applied Physics Letters, 89*, 143517-143519.

[69] H. Schmidt, K. Zilberberg, S. Schmale, H. Flugge, T. Riedl, W. Kowalsky. (2010). Transient characteristics of inverted polymer solar cells using titaniumoxide interlayers. *Applied Physics Letters, 96*, 243305-243308.

[70] S.H. Park, A. Roy, S. Beaupre, S. Cho, N. Coates, J.S. Moon, D. Moses, M. Leclerc, K. Lee, A.J. Heeger. (2009). Bulk heterojunction solar cells with internal quantum efficiency approaching 100%. *Nature Photonics, 3*, 297-303.

[71] A.K.K. Kyaw, D.H. Wang, V. Gupta, J. Zhang, S. Chand, G.C. Bazan, A.J. Heeger. (2013). Efficient solution-processed small-molecule solar cells with inverted structure. *Advanced Materials, 25*, 2397-2402.

[72] W.J.E. Beek, M.M. Wienk, M. Kemerink, X.N. Yang, R.A.J. Janssen. (2005). Hybrid zinc oxide conjugated polymer bulk heterojunction solar cells. *Journal of Physical Chemistry B, 109*, 9505-9516.

[73] T. Shirakawa, T. Umeda, Y. Hashimoto, A. Fujii, K. Yoshino. (2004). Effect of ZnO layer on characteristics of conducting polymer/C_{60} photovoltaic cell. *Journal of Physics D-Applied Physics, 37*, 847-850.

[74] Y.H. Zhou, H. Cheun, W.J. Potscavage, C. Fuentes-Hernandez, S.J. Kim, B. Kippelen. (2010). Inverted organic solar cells with ITO electrodes modified with an ultrathin Al_2O_3 buffer layer deposited by atomic layer deposition. *Journal of Materials Chemistry, 20*, 6189-6194.

[75] H.H. Liao, L.M. Chen, Z. Xu, G. Li, Y. Yang. (2008). Highly efficient inverted polymer solar cell by low temperature annealing of Cs_2CO_3 interlayer. *Applied Physics Letters, 92*, 173303-173306.

[76] F. Nuesch, L.J. Rothberg, E.W. Forsythe, Q.T. Le, Y.L. Gao. (1999). A photoelectron spectroscopy study on the indium tin oxide treatment by acids and bases. *Applied Physics Letters, 74*, 880-882.

[77] W. Osikowicz, X. Crispin, C. Tengstedt, L. Lindell, T. Kugler, W.R. Salaneck. (2004). Transparent low-work-function indium tin oxide electrode obtained by molecular scale interface engineering. *Applied Physics Letters, 85*, 1616-1618.

[78] H. Cheun, C. Fuentes-Hernandez, J. Shim, Y.N. Fang, Y. Cai, H. Li, A.K. Sigdel, J. Meyer, J. Maibach, A. Dindar, Y.H. Zhou, J.J. Berry, J.L. Bredas, A. Kahn, K.H. Sandhage, B. Kippelen. (2012). Oriented growth of Al_2O_3:ZnO nanolaminates for use as electron-selective electrodes in inverted polymer solar cells. *Advanced Functional Materials, 22*, 1531-1538.

[79] J.W. Shim, H. Cheun, J. Meyer, C. Fuentes-Hernandez, A. Dindar, Y.H. Zhou, D.K. Hwang, A. Kahn, B. Kippelen. (2012). Polyvinylpyrrolidone-modified indium tin oxide as an electron-collecting electrode for inverted polymer solar cells. *Applied Physics Letters, 101,* 073303-073307.

[80] S. Sista, Z.R. Hong, L.M. Chen, Y. Yang. (2011). Tandem polymer photovoltaic cells-current status, challenges and future outlook. *Energy & Environmental Science, 4*, 1606-1620.

[81] M.A. Green, K. Emery, Y. Hishikawa, W. Warta, E.D. Dunlop. (2012). Solar cell efficiency tables (version 39). *Progress in Photovoltaics, 20,* 12-20.

[82] G. Dennler, M.C. Scharber, T. Ameri, P. Denk, K. Forberich, C. Waldauf, C.J. Brabec. (2008). Design rules for donors in bulk-heterojunction tandem solar cells-towards 15 % energy-conversion efficiency. *Advanced Materials, 20*, 579-583.

[83] M. Hiramoto, M. Suezaki, M. Yokoyama. (1990). Effect of thin gold interstitial-layer on the photovoltaic properties of tandem organic solar cell. *Chemistry Letters, 19*, 327-330.

[84] A. Yakimov S.R. Forrest. (2002). High photovoltage multiple-heterojunction organic solar cells incorporating interfacial metallic nanoclusters. *Applied Physics Letters, 80*, 1667-1669.

[85] G. Dennler, H.-J. Prall, R. Koeppe, M. Egginger, R. Autengruber, N.S. Sariciftci. (2006). Enhanced spectral coverage in tandem organic solar cells. *Applied Physics Letters, 89*, 073502-073505.

[86] J.S. Kim, M. Granstrom, R.H. Friend, N. Johansson, W.R. Salaneck, R. Daik, W.J. Feast, F. Cacialli. (1998). Indium--tin oxide treatments for single- and double-layer polymeric light-emitting diodes: The relation between the anode physical, chemical, and morphological properties and the device performance. *Journal of Applied Physics, 84*, 6859-6870.

[87] X.W. Sun, D.W. Zhao, L. Ke, A.K.K. Kyaw, G.Q. Lo, D.L. Kwong. (2010). Inverted tandem organic solar cells with a MoO_3/Ag/Al/Ca intermediate layer. *Applied Physics Letters, 97*, 053303-053306.

[88] Y.H. Zhou, C. Fuentes-Hernandez, J.W. Shim, T.M. Khan, B. Kippelen. (2012). High performance polymeric charge recombination layer for organic tandem solar cells. *Energy & Environmental Science, 5*, 9827-9832.

[89] J.B. You, L.T. Dou, K. Yoshimura, T. Kato, K. Ohya, T. Moriarty, K. Emery, C.C. Chen, J. Gao, G. Li, Y. Yang. (2013). A polymer tandem solar cell with 10.6% power conversion efficiency. *Nature Communications, 4*, 1-10.

[90] C.-C. Chen, L. Dou, J. Gao, W.-H. Chang, G. Li, Y. Yang. (2013). High-performance semi-transparent polymer solar cells possessing tandem structures. *Energy & Environmental Science, 6*, 2714-2720.

[91] V.S. Gevaerts, A. Furlan, M.M. Wienk, M. Turbiez, R.A.J. Janssen. (2012). Solution processed polymer tandem solar cell using efficient small and wide bandgap polymer:Fullerene blends. *Advanced Materials, 24*, 2130-2134.

[92] L. Burgi, M. Turbiez, R. Pfeiffer, F. Bienewald, H.J. Kirner, C. Winnewisser. (2008). High-mobility ambipolar near-infrared light-emitting polymer field-effect transistors. *Advanced Materials, 20*, 2217-2224.

[93] V.C. Tung, J. Kim, L.J. Cote, J. Huang. (2011). Sticky interconnect for solution-processed tandem solar cells. *Journal of the American Chemical Society, 133*, 9262-9265.

[94] J. Yang, R. Zhu, Z. Hong, Y. He, A. Kumar, Y. Li, Y. Yang. (2011). A robust inter-connecting layer for achieving high performance tandem polymer solar cells. *Advanced Materials, 23*, 3465-3470.

[95] D. Cheyns, B.P. Rand, P. Heremans. (2010). Organic tandem solar cells with complementary absorbing layers and a high open-circuit voltage. *Applied Physics Letters, 97*, 033301-033304.

[96] D.J.D. Moet, P. de Bruyn, P.W.M. Blom. (2010). High work function transparent middle electrode for organic tandem solar cells. *Applied Physics Letters, 96*, 153504-153507.

[97] S. Sista, M.-H. Park, Z. Hong, Y. Wu, J. Hou, W.L. Kwan, G. Li, Y. Yang. (2010). Highly efficient tandem polymer photovoltaic cells. *Advanced Materials, 22*, 380-383.

[98] J. Sakai, K. Kawano, T. Yamanari, T. Taima, Y. Yoshida, A. Fujii, M. Ozaki. (2010). Efficient organic photovoltaic tandem cells with novel transparent conductive oxide interlayer and poly (3-hexylthiophene): Fullerene active layers. *Solar Energy Materials and Solar Cells, 94*, 376-380.

[99] D.W. Zhao, X.W. Sun, C.Y. Jiang, A.K.K. Kyaw, G.Q. Lo, D.L. Kwong. (2009). An efficient triple-tandem polymer solar cell. *Electron Device Letters, IEEE, 30*, 490-492.

[100] A.G.F. Janssen, T. Riedl, S. Hamwi, H.H. Johannes, W. Kowalsky. (2007). Highly efficient organic tandem solar cells using an improved connecting architecture. *Applied Physics Letters, 91*, 073519-073522.

[101] A. Hadipour, B. de Boer, P.W.M. Blom. (2007). Solution-processed organic tandem solar cells with embedded optical spacers. *Journal of Applied Physics, 102*, 074506-074506.

[102] J.Y. Kim, K. Lee, N.E. Coates, D. Moses, T.Q. Nguyen, M. Dante, A.J. Heeger. (2007). Efficient tandem polymer solar cells fabricated by all-solution processing. *Science, 317*, 222-225.

[103] J. Gilot, M.M. Wienk, R.A.J. Janssen. (2007). Double and triple junction polymer solar cells processed from solution. *Applied Physics Letters, 90*, 143512-143515.

[104] A. Colsmann, J. Junge, C. Kayser, U. Lemmer. (2006). Organic tandem solar cells comprising polymer and small-molecule subcells. *Applied Physics Letters, 89*, 203506-203509.

[105] J. Drechsel, B. Mannig, F. Kozlowski, M. Pfeiffer, K. Leo, H. Hoppe. (2005). Efficient organic solar cells based on a double p-i-n architecture using doped wide-gap transport layers. *Applied Physics Letters, 86*, 244102-244105.

[106] J. Xue, S. Uchida, B.P. Rand, S.R. Forrest. (2004). Asymmetric tandem organic photovoltaic cells with hybrid planar-mixed molecular heterojunctions. *Applied Physics Letters, 85*, 5757-5759.

[107] B.P. Rand, P. Peumans, S.R. Forrest. (2004). Long-range absorption enhancement in organic tandem thin-film solar cells containing silver nanoclusters. *Journal of Applied Physics, 96*, 7519-7526.

[108] M. Hiramoto, M. Suezaki, M. Yokoyama. (1990). Effect of thin gold interstitial-layer on the photovoltaic properties of tandem organic solar-cell. *Chemistry Letters*, 327-330.

[109] J. You, C.-C. Chen, Z. Hong, K. Yoshimura, K. Ohya, R. Xu, S. Ye, J. Gao, G. Li, Y. Yang. (2013). 10.2% power conversion efficiency polymer tandem solar cells consisting of two identical sub-cells. *Advanced Materials, 25*, 3973-3978.

[110] L.T. Dou, C.C. Chen, K. Yoshimura, K. Ohya, W.H. Chang, J. Gao, Y.S. Liu, E. Richard, Y. Yang. (2013). Synthesis of 5H-Dithieno 3,2-b:2 ',3 '-d pyran as an electron-rich building block for donor-acceptor type low-bandgap polymers *Macromolecules, 46*, 4734-4734.

[111] J.Y. Letian Dou, Jun Yang, Chun-Chao Chen, Youjun He, SeiichiroMurase, K.E. Tom Moriarty, Gang Li and Yang Yang. (2012). Tandem polymer solar cells featuring a spectrally
matched low-bandgap polymer. *Nature Photonics, 6*, 180–185.

[112] S. Kouijzer, S. Esiner, C.H. Frijters, M. Turbiez, M.M. Wienk, R.A.J. Janssen. (2012). Efficient inverted tandem polymer solar cells with a solution-processed recombination layer. *Advanced Energy Materials, 2*, 945-949.

[113] J.W. Shim, Y.H. Zhou, C. Fuentes-Hernandez, A. Dindar, Z.L. Guan, H. Cheun, A. Kahn, B. Kippelen. (2012). Studies of the optimization of recombination layers for inverted tandem polymer solar cells. *Solar Energy Materials and Solar Cells, 107*, 51-55.

[114] J. Yang, J. You, C.-C. Chen, W.-C. Hsu, H.-r. Tan, X.W. Zhang, Z. Hong, Y. Yang. (2011). Plasmonic polymer tandem solar cell. *ACS Nano, 5*, 6210-6217.

[115] M. Riede, C. Uhrich, J. Widmer, R. Timmreck, D. Wynands, G. Schwartz, W.-M. Gnehr, D. Hildebrandt, A. Weiss, J. Hwang, S. Sundarraj, P. Erk, M. Pfeiffer, K. Leo. (2011). Efficient organic tandem solar cells based on small molecules. *Advanced Functional Materials, 21*, 3019-3028.

[116] D.W. Zhao, L. Ke, Y. Li, S.T. Tan, A.K.K. Kyaw, H.V. Demir, X.W. Sun, D.L. Carroll, G.Q. Lo, D.L. Kwong. (2011). Optimization of inverted tandem organic solar cells. *Solar Energy Materials and Solar Cells, 95*, 921-926.

[117] C.H. Chou, W.L. Kwan, Z.R. Hong, L.M. Chen, Y. Yang. (2011). A metal-oxide interconnection layer for polymer tandem solar cells with an inverted architecture. *Advanced Materials, 23*, 1282-1286.

[118] S.K. Hau, H.-L. Yip, K.-S. Chen, J. Zou, A.K.Y. Jen. (2010). Solution processed inverted tandem polymer solar cells with self-assembled monolayer modified interfacial layers. *Applied Physics Letters, 97*, 253307-253310.

[119] Z. He, C. Zhong, X. Huang, W.-Y. Wong, H. Wu, L. Chen, S. Su, Y. Cao. (2011). Simultaneous enhancement of open-circuit voltage, short-circuit current density, and fill factor in polymer solar cells. *Advanced Materials, 23*, 4636-4643.

[120] T.Y. Chu, S. Alem, S.W. Tsang, S.C. Tse, S. Wakim, J.P. Lu, G. Dennler, D. Waller, R. Gaudiana, Y. Tao. (2011). Morphology control in polycarbazole based bulk heterojunction solar cells and its impact on device performance. *Applied Physics Letters, 98*, 253301-253304.

[121] S.C. Price, A.C. Stuart, L.Q. Yang, H.X. Zhou, W. You. (2011). Fluorine substituted conjugated polymer of medium band gap yields 7% efficiency in polymer-fullerene solar cells. *Journal of the American Chemical Society, 133*, 4625-4631.

[122] N. Zhou, X. Guo, R.P. Ortiz, S. Li, S. Zhang, R.P.H. Chang, A. Facchetti, T.J. Marks. (2012). Bithiophene imide and benzodithiophene copolymers for efficient inverted polymer solar cells. *Advanced Materials, 24*, 2242-2248.

[123] W. Chen, X. Qiao, J. Yang, B. Yu, D. Yan. (2012). Efficient broad-spectrum parallel tandem organic solar cells based on the highly crystalline chloroaluminum phthalocyanine films as the planar layer. *Applied Physics Letters, 100*, 133302-133306.

[124] D.W. Schubert T. Dunkel. (2003). Spin coating from a molecular point of view: its concentration regimes, influence of molar mass and distribution. *Materials Research Innovations, 7*, 314-321.

[125] P. Poodt, A. Lankhorst, F. Roozeboom, K. Spee, D. Maas, A. Vermeer. (2010). High-speed spatial atomic-layer deposition of aluminum oxide layers for solar cell passivation. *Advanced Materials, 22,* 3564-3567.

[126] E. Guziewicz, M. Godlewski, L. Wachnicki, T.A. Krajewski, G. Luka, S. Gieraltowska, R. Jakiela, A. Stonert, W. Lisowski, M. Krawczyk, J.W. Sobczak, A. Jablonski. (2012). ALD grown zinc oxide with controllable electrical properties. *Semiconductor Science and Technology, 27,* 074011-074022.

[127] M. Nonnenmacher, M.P. O'Boyle, H.K. Wickramasinghe. (1991). Kelvin probe force microscopy. *Applied Physics Letters, 58,* 2921-2923.

[128] J. Hwang, A. Wan, A. Kahn. (2009). Energetics of metal-organic interfaces: New experiments and assessment of the field. *Materials Science & Engineering R-Reports, 64,* 1-31.

[129] J.A.W. Co. (2013). International Energy Agency, Retrieved September 18, 2012 from http://www.jawoollam.com/.

[130] G. Binnig, C.F. Quate, C. Gerber. (1986). Atomic force microscope. *Physical Review Letters, 56,* 930-933.

[131] H. Sato, T. Minami, S. Takata, T. Yamada. (1993). Transparent conducting p-type NiO thin-films propared by magnetron sputtering. *Thin Solid Films, 236,* 27-31.

[132] K.X. Steirer, P.F. Ndione, N.E. Widjonarko, M.T. Lloyd, J. Meyer, E.L. Ratcliff, A. Kahn, N.R. Armstrong, C.J. Curtis, D.S. Ginley, J.J. Berry, D.C. Olson. (2011). Enhanced efficiency in plastic solar cells via energy matched solution processed NiO_X interlayers. *Advanced Energy Materials, 1,* 813-820.

[133] M. Awais, M. Rahman, J.M. Don MacElroy, N. Coburn, D. Dini, J.G. Vos, D.P. Dowling. (2010). Deposition and characterization of NiOx coatings by magnetron sputtering for application in dye-sensitized solar cells. *Surface and Coatings Technology, 204,* 2729-2736.

[134] M.T. Greiner, M.G. Helander, Z.B. Wang, W.M. Tang, Z.H. Lu. (2010). Effects of processing conditions on the work function and energy-level alignment of NiO thin films. *Journal of Physical Chemistry C, 114,* 19777-19781.

[135] Y.H. Zhou, H. Cheun, S. Choi, W.J. Potscavage, C. Fuentes-Hernandez, B. Kippelen. (2010). Indium tin oxide-free and metal-free semitransparent organic solar cells. *Applied Physics Letters, 97,* 153304-153307.

[136] M.H. Park, J.H. Li, A. Kumar, G. Li, Y. Yang. (2009). Doping of the metal oxide nanostructure and its influence in organic electronics. *Advanced Functional Materials, 19*, 1241-1246.

[137] C.E. Small, S. Chen, J. Subbiah, C.M. Amb, S.W. Tsang, T.H. Lai, J.R. Reynolds, F. So. (2012). High-efficiency inverted dithienogermole-thienopyrrolodione-based polymer solar cells. *Nature Photonics, 6*, 115-120.

[138] F. Huang, Y.H. Niu, Y. Zhang, J.W. Ka, M.S. Liu, A.K.Y. Jen. (2007). A conjugated, neutral surfactant as electron-injection material for high-efficiency polymer light-emitting diodes. *Advanced Materials, 19*, 2010-2014.

[139] Y.H. Zhou, F.H. Li, S. Barrau, W.J. Tian, O. Inganas, F.L. Zhang. (2009). Inverted and transparent polymer solar cells prepared with vacuum-free processing. *Solar Energy Materials and Solar Cells, 93*, 497-500.

[140] A. Sionkowska, M. Wisniewski, J. Skopinska, S. Vicini, E. Marsano. (2005). The influence of UV irradiation on the mechanical properties of chitosan/poly(vinyl pyrrolidone) blends. *Polymer Degradation and Stability, 88*, 261-267.

[141] S. Khodabakhsh, D. Poplavskyy, S. Heutz, J. Nelson, D.D.C. Bradley, F. Murata, T.S. Jones. (2004). Using self-assembling dipole molecules to improve hole injection in conjugated polymers. *Advanced Functional Materials, 14*, 1205-1210.

[142] A. Wagenpfahl, D. Rauh, M. Binder, C. Deibel, V. Dyakonov. (2010). S-shaped current-voltage characteristics of organic solar devices. *Physical Review B, 82*, 115306-115314.

[143] F.C. Krebs, T. Tromholt, M. Jorgensen. (2010). Upscaling of polymer solar cell fabrication using full roll-to-roll processing. *Nanoscale, 2*, 873-886.

[144] A. Kumar, S. Sista, Y. Yang. (2009). Dipole induced anomalous S-shape I-V curves in polymer solar cells. *Journal of Applied Physics, 105*, 094512-094516.

[145] J. Nelson, J. Kirkpatrick, P. Ravirajan. (2004). Factors limiting the efficiency of molecular photovoltaic devices. *Physical Review B, 69*, 035337-035347.

[146] Z.R. Hong, C.J. Liang, X.Y. Sun, X.T. Zeng. (2006). Characterization of organic photovoltaic devices with indium-tin-oxide anode treated by plasma in various gases. *Journal of Applied Physics, 100*, 093711-093714.

[147] W.J. Potscavage, A. Sharma, B. Kippelen. (2009). Critical Interfaces in Organic Solar Cells and Their Influence on the Open-Circuit Voltage. *Accounts of Chemical Research, 42*, 1758-1767.

[148] F. Huang, H.B. Wu, Y. Cao. (2010). Water/alcohol soluble conjugated polymers as highly efficient electron transporting/injection layer in optoelectronic devices. *Chemical Society Reviews, 39*, 2500-2521.

[149] Z.L. Guan, J.B. Kim, Y.L. Loo, A. Kahn. (2011). Electronic structure of the poly(3-hexylthiophene):indene-C_{60} bisadduct bulk heterojunction. *Journal of Applied Physics, 110*, 043719-043724.

[150] J. Meyer, R. Khalandovsky, P. Gorrn, A. Kahn. (2011). MoO_3 films spin-coated from a nanoparticle suspension for efficient hole-injection in organic electronics. *Advanced Materials, 23*, 70-73.

[151] T.T. Larsen-Olsen, E. Bundgaard, K.O. Sylvester-Hvid, F.C. Krebs. (2011). A solution process for inverted tandem solar cells. *Organic Electronics, 12*, 364-371.

[152] D.A.G. Bruggeman. (1935). Calculation of various physics constants in heterogenous substances I Dielectricity constants and conductivity of mixed bodies from isotropic substances. *Annalen Der Physik, 24*, 636-664.

[153] Z.L. Guan, J.B. Kim, H. Wang, C. Jaye, D.A. Fischer, Y.L. Loo, A. Kahn. (2010). Direct determination of the electronic structure of the poly(3-hexylthiophene):phenyl- 6,6 -C_{61} butyric acid methyl ester blend. *Organic Electronics, 11*, 1779-1785.

[154] N. Li, T. Stubhan, D. Baran, J. Min, H.Q. Wang, T. Ameri, C.J. Brabec. (2013). Design of the solution-processed intermediate layer by engineering for inverted organic multi junction solar cells. *Advanced Energy Materials, 3*, 301-307.

[155] M. Caglar, S. Ilican, Y. Caglar, F. Yakuphanoglu. (2009). Electrical conductivity and optical properties of ZnO nanostructured thin film. *Applied Surface Science, 255*, 4491-4496.

[156] J. Meyer, P. Görrn, F. Bertram, S. Hamwi, T. Winkler, H.-H. Johannes, T. Weimann, P. Hinze, T. Riedl, W. Kowalsky. (2009). Al2O3/ZrO2 Nanolaminates as Ultrahigh Gas-Diffusion Barriers—A Strategy for Reliable Encapsulation of Organic Electronics. *Advanced Materials, 21*, 1845-1849.

[157] J. Meyer, H. Schmidt, W. Kowalsky, T. Riedl, A. Kahn. (2010). The origin of low water vapor transmission rates through Al2O3/ZrO2 nanolaminate gas-diffusion barriers grown by atomic layer deposition. *Applied Physics Letters, 96*, 243308-243311.

[158] A. Hadipour, B. de Boer, J. Wildeman, F.B. Kooistra, J.C. Hummelen, M.G.R. Turbiez, M.M. Wienk, R.A.J. Janssen, P.W.M. Blom. (2006). Solution-processed organic tandem solar cells. *Advanced Functional Materials, 16*, 1897-1903.

[159] D.W. Zhao, X.W. Sun, C.Y. Jiang, A.K.K. Kyaw, G.Q. Lo, D.L. Kwong. (2008). Efficient tandem organic solar cells with an Al/MoO_3 intermediate layer. *Applied Physics Letters, 93*, 083305-083307.

[160] S.I. Na, G. Wang, S.S. Kim, T.W. Kim, S.H. Oh, B.K. Yu, T. Lee, D.Y. Kim. (2009). Evolution of nanomorphology and anisotropic conductivity in solvent-modified PEDOT:PSS films for polymeric anodes of polymer solar cells. *Journal of Materials Chemistry, 19*, 9045-9053.